Roma Tre

Fisica

CORSO DI DOTTORATO DI RICERCA IN

XXXVIII

CICLO DEL CORSO DI DOTTORATO

The CYGNO Experiment for Directional Dark Matter Searches: Detector Characterization Based on Experimental Data and a Dedicated Monte Carlo Simulation

Pietro Meloni

Nome e Cognome del dottorando — Firma

Prof. Fabrizio Petrucci

Docente Guida/Tutor — Firma

Prof. Giorgio Matt

Coordinatore — Firma

Contents

Introduction

Astronomical and cosmological observations indicate that the vast majority of matter in the Universe does not emit or absorb light. This "dark matter" reveals itself only through its gravitational effects, from the rotation curves of galaxies to the large-scale structure of the cosmos. While the evidence for its existence is overwhelming, its fundamental nature remains one of the most profound mysteries in modern physics.

Among the various theoretical candidates proposed to explain dark matter, Weakly Interacting Massive Particles (WIMPs) have received particular attention. These hypothetical particles would interact with ordinary matter primarily through gravity and the weak nuclear force, making them extremely difficult to detect. However, if dark matter consists of WIMPs with masses in the GeV/c^2 range, occasional collisions with atomic nuclei in terrestrial detectors should produce faint but measurable signals in the form of nuclear recoils with energies of tens of keV.

Direct detection experiments search for these rare interactions by monitoring large volumes of ultra-pure materials in underground laboratories, shielded from cosmic rays and other backgrounds. A crucial challenge is distinguishing genuine dark matter signals from the overwhelming background of ordinary particle interactions. One particularly powerful discriminant is the *directional signature*: since the Solar System moves through the dark matter halo of our galaxy, WIMPs should exhibit a preferred incoming direction in the laboratory frame. Measuring the direction of nuclear recoils could therefore provide definitive evidence of a dark matter origin, even with a small number of events.

The CYGNO project pursues this directional approach by developing a gaseous Time Projection Chamber (TPC) with optical readout, with the goal of scaling up to volumes on the order of $O(30\,\mathrm{m}^3)$. The detector employs a gas mixture of helium and carbon tetrafluoride (CF_4) at atmospheric pressure. Helium maximizes the energy transfer in WIMP–nucleus scattering for low-mass WIMPs, while CF_4 provides abundant scintillation light that enables optical readout of the ionization tracks. This combination allows the detector to instrument large volumes with low noise, high spatial granularity, and sensitivity to both spin-independent and spin-dependent dark matter interactions through the fluorine content.

In the CYGNO TPC, ionization electrons produced by incoming particles drift toward a multi-stage amplification region consisting of three Gas Electron Multipliers (GEMs). The amplified charge produces secondary scintillation light, which is recorded by both scientific CMOS cameras and photomultiplier tubes (PMTs). This dual optical readout enables measurement of the energy deposited along the track and reconstruction of the complete three-dimensional track topology, which is essential for identifying the characteristic signatures of nuclear recoils and rejecting the dominant background from electron recoils.

Several prototypes have been constructed to validate the CYGNO detection concept for rare-event searches. The largest of these is LIME (Large Imaging Module Experiment), which is the primary focus of this thesis. After its initial commissioning at the Laboratori Nazionali di Frascati (LNF), LIME was installed at the Laboratori Nazionali del Gran Sasso (LNGS), where it began data taking in 2022 and continued operating for three years. The goals of the experiment include characterizing external backgrounds (from the laboratory environment and residual cosmic rays) and internal backgrounds (from radioactive contaminants in detector materials), as well as assessing the detector's response to nuclear recoils and validating its directional reconstruction capabilities.

Thesis Outline

- **Chapter 1 – Dark Matter.** Reviews the astrophysical and cosmological evidence for dark matter from galactic to cosmological scales and discusses leading theoretical candidates for its composition.
- **Chapter 2 – Direct Detection of Dark Matter.** Presents the theoretical framework of WIMP–nucleus scattering, the expected event rates and experimental signatures, and the principal challenges in rare-event searches, with emphasis on directional detection techniques.
- **Chapter 3 – The CYGNO Project.** Describes the CYGNO experiment, including its scientific goals, detection principle, and technological implementation.
- **Chapter 4 – LIME: The Largest Prototype.** Provides a comprehensive description of the LIME detector, including its design, commissioning, operation both overground and underground, and key performance results.
- **Chapter 5 – Simulation of the Detector Response.** Details the Monte Carlo simulation framework developed for CYGNO and LIME, describing the complete chain from primary particle generation to digitized detector response, including validation with overground data.
- **Chapter 6 – Electron Recoil Simulation Studies with LNGS Underground Data.** Presents the systematic optimization of simulation parameters and the characterization of detector stability through detailed comparison with experimental calibration data collected underground.
- **Chapter 7 – Validation of Nuclear Recoil Simulation with AmBe Source Data.** Describes the Monte Carlo simulation of neutron interactions from an AmBe source, the comparison between simulated and experimental data, and the characterization of electron/nuclear recoil discrimination capabilities.

Finally, the Conclusions present a comprehensive summary and discussion of the results obtained in this work.

Chapter 1

Dark matter

Over the past sixty years, an extensive array of astrophysical and cosmological observations has increasingly reinforced the hypothesis that the known forces and particles described by the Standard Model of particle physics are inadequate to fully explain all the matter in the Universe. These findings indicate the presence of a non-luminous and non-baryonic component, widely known as dark matter (DM), which interacts gravitationally like ordinary matter but remains invisible to electromagnetic interactions. While it constitutes a significant fraction of the Universe's total matter content, its nature remains elusive and unknown despite decades of intensive experimental and theoretical research.

Dark matter, making up about 84% of the total matter in the Universe, plays a fundamental role in the formation and evolution of cosmic structures. The hypothesis of dark matter stems from a variety of astrophysical and cosmological observations spanning multiple scales, from individual galaxies to the largest structures in the Universe. These observations suggest that an ingredient beyond the known particles and forces is required to explain phenomena such as the rotation curves of galaxies, the dynamics of galaxy clusters, and the patterns of anisotropies in the Cosmic Microwave Background (CMB).

1.1 Evidence for dark matter

Evidence for dark matter comes from a variety of astrophysical and cosmological observations, spanning multiple scales of the Universe. These include phenomena such as the flat rotation curves of spiral galaxies, the dynamics of galaxy clusters, and the anisotropies in the Cosmic Microwave Background (CMB). Each of these observations provides compelling support for the existence of dark matter, and they will be discussed in detail in the following sections.

1.1.1 Galactic scale

Galactic-scale observations provide some of the earliest and most direct evidence for dark matter. Two key phenomena stand out: the rotation curves of spiral galaxies, which reveal the presence of unseen mass in their outer regions, and gravitational lensing, where the bending of light by a galaxy's gravitational field exceeds what can be attributed to its visible matter. These observations strongly suggest the existence of a significant dark matter component within galaxies.

1.1.1.1 Galactic rotation curves

One of the earliest and, to date, most robust pieces of evidence for dark matter comes from the rotation curves of spiral galaxies, including our own Milky Way. In spiral galaxies, most stars reside in a central bulge, surrounded by spiral arms composed of additional stars and gas. The rotation curve of a galaxy specifies the circular velocity, $v(R)$, of these stars and gas clouds as a function of their distance R from the galactic center.

Under the simplifying assumption of Newtonian dynamics, the centripetal force required to maintain a circular orbit of a mass m at a radius R must balance the gravitational force from the total mass $M(R)$ enclosed within that radius:

$$\frac{m\,v^2(R)}{R} = \frac{G\,M(R)\,m}{R^2}, \tag{1.1}$$

where G is the universal gravitational constant. Simplifying Eq. (1.1), we obtain:

$$v(R) = \sqrt{\frac{G\,M(R)}{R}}. \tag{1.2}$$

In a simplified model, one typically assumes that most of a galaxy's mass is concentrated within some characteristic radius R_c (of a few kiloparsecs). For $R < R_\mathrm{c}$, the enclosed mass grows with volume if the density is roughly constant, implying that $v(R)$ increases proportionally to R. For $R \gg R_\mathrm{c}$, however, the mass $M(R)$ should be essentially constant, and the velocity $v(R)$ would then decrease as $1/\sqrt{R}$.

Rotation curves are typically measured via the Doppler shift of characteristic emission lines, particularly the 21 cm line of neutral hydrogen (H I). These observations often extend to large galactocentric distances, revealing a nearly universal feature: while the circular velocity increases as expected at small radii, at large R it remains approximately flat instead of falling off as $1/\sqrt{R}$.

This flat behavior (see Fig. 1.1) contradicts the expectation from Eq. (1.2) if only visible matter is present. It implies that the total mass $M(R)$ continues to grow with R, even beyond the luminous edge of the galaxy. The additional, invisible mass is interpreted as a dark matter halo, commonly assumed to be approximately spherical. Simple estimates show that the halo density profile must fall off roughly like $1/R^2$ to explain the flatness of the rotation curves [1].

1.1.1.2 Gravitational lensing

Gravitational lensing offers additional and compelling evidence for the presence of dark matter. According to General Relativity, massive objects distort the surrounding spacetime; in regions far from such masses, light rays follow straight paths in three-dimensional space, but in the vicinity of a large mass concentration, their trajectories are bent. Figure 1.2 illustrates this phenomenon: when a massive object (the lens) lies between an observer and a distant source, the potential well associated with the lens distorts the light rays originating from the source, often producing multiple images or visible arcs of the background object.

In a simplified description, the bending of a light ray passing at an impact parameter b from a lens of mass M can be approximated (in the weak-field limit of the Schwarzschild metric) by

$$\alpha \simeq \frac{4\,G\,M}{b\,c^2}, \tag{1.3}$$

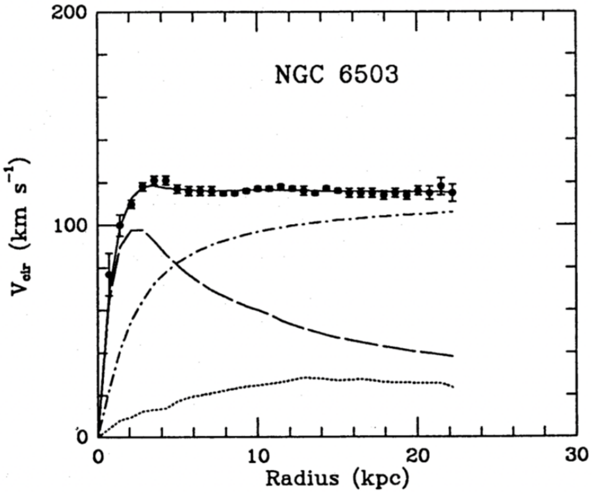

Figure 1.1: An example of the rotation curve measurement for the galaxy NGC6503, as presented in [2]. The solid line illustrates the overall fit to the data, while the dashed line represents the gas component, the dotted line corresponds to the visible matter, and the dash-dotted line indicates the dark matter (DM).

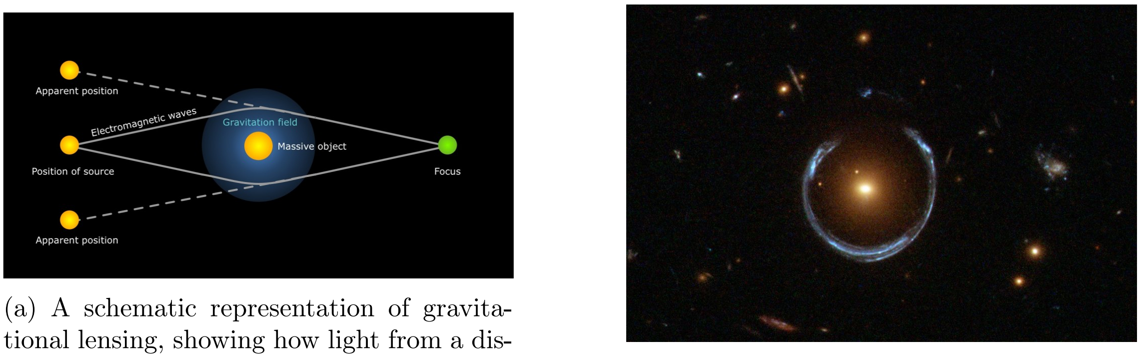

(a) A schematic representation of gravitational lensing, showing how light from a distant source is bent by the gravitational field of a massive object.

(b) An example of a horseshoe Einstein ring, captured by the Hubble Space Telescope.

Figure 1.2: On the left, a schematic showing the working principle of gravitational lensing. On the right, a Hubble image displaying a horseshoe Einstein ring [3].

where G is the gravitational constant and c is the speed of light in vacuum. By measuring the deflection angle α, it is possible to infer the mass responsible for the lensing. Different mass scales and distributions give rise to different lensing regimes. Strong lensing produces resolvable multiple images, arcs, or Einstein rings around massive clusters or galaxies. Weak lensing induces subtle distortions appearing as coherent shape deformations of background galaxies, requiring statistical analysis of many objects. Finally, microlensing occurs when small lenses (such as a star or compact object) cause little or no apparent distortion but temporarily alter the observed flux of the background source.

A particularly striking example supporting the dark matter hypothesis comes from observations of merging galaxy clusters, most famously the Bullet Cluster (1E 0657 − 558). X-ray measurements reveal the hot intracluster gas (which interacts electromagnetically), while gravitational lensing maps the total mass distribution, including dark matter (i.e.m̃aterial that does not emit electromagnetic radiation). Figure 1.3 illustrates how the X-ray emission (shown in red) does not align spatially with the strongest gravitational potential wells determined via lensing (depicted in green contours). This offset implies that the majority of the mass is in a form that does not interact significantly with the hot gas (which lags behind the collision), providing clear evidence for a non-collisional (or effectively collisionless) component consistent with dark matter [4].

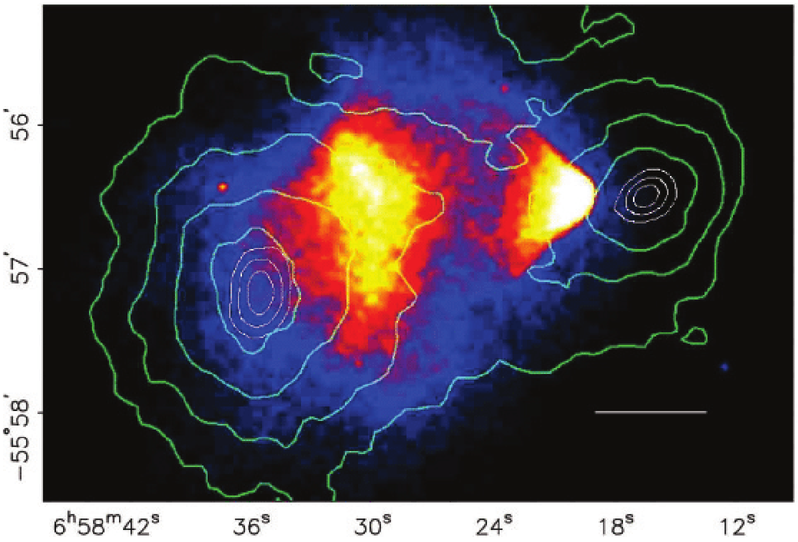

Figure 1.3: Composite image of the Bullet Cluster (1E 0657–558), illustrating the separation between the hot, X-ray-emitting gas (red) and the principal mass concentrations inferred from gravitational lensing (green contours). The observed displacement strongly supports the existence of dark matter that is effectively collisionless during cluster mergers [5].

Overall, gravitational lensing has enabled the reconstruction of mass distributions in numerous systems, from individual galaxies to massive clusters. These mass maps consistently require additional mass beyond that which is optically visible, reinforcing the conclusion that a significant fraction of matter in the Universe is dark and does not interact via the electromagnetic force.

1.1.2 Cosmological scale

Two complementary pillars reveal the presence of dark matter on the largest scales: the hierarchical growth of large-scale structure (LSS) and the fine-grained pattern of the Cosmic Microwave Background (CMB). Both are naturally interpreted within the Standard Model of Cosmology, the ΛCDM paradigm.

The ΛCDM Framework The standard model of Big Bang cosmology, known as the ΛCDM model, provides the most accurate description of the evolution and composition of the Universe on large scales. It is built upon the General Theory of Relativity (GR) applied to the cosmological scale and relies on the Cosmological Principle, which asserts that the Universe is homogeneous and isotropic on scales larger than $\sim 100\,\text{Mpc}$.

The model assumes the Universe is composed of four main energy components: radiation (ultra-relativistic particles like photons and neutrinos), ordinary matter (baryons), Cold Dark Matter (CDM), and Dark Energy (associated with a cosmological constant Λ).

The evolution of the background geometry and the statistics of primordial fluctuations are fully characterized by a minimal set of six independent parameters:

- $\Omega_b h^2$: The physical baryon density parameter.
- $\Omega_c h^2$: The physical cold dark matter density parameter.

- θ_s: The angular size of the sound horizon at the last scattering surface (related to the distance sound waves traveled before recombination).
- A_s: The amplitude of the primordial scalar power spectrum.
- n_s: The scalar spectral index (describing how density variations scale with distance).
- τ: The reionization optical depth (probability of a photon scattering during the reionization epoch).

The dynamics of the Universe are described by the Einstein field equations. Assuming the Friedmann-Lemaître-Robertson-Walker (FLRW) metric, which describes a flat, open, or closed spacetime, we derive the first Friedmann equation:

$$H^2(t) \equiv \left(\frac{\dot{a}}{a}\right)^2 = \frac{8\pi G}{3}\rho - \frac{kc^2}{a^2}, \tag{1.4}$$

where:

- $H(t)$ is the Hubble parameter, measuring the rate of cosmic expansion.
- $a(t)$ is the dimensionless scale factor (normalized such that $a(t_0) = 1$ today), describing the relative size of the Universe at time t.
- ρ is the total energy density of the fluid filling the Universe.
- k is the spatial curvature constant ($k = 0$ for flat, $k > 0$ for closed, $k < 0$ for open geometry).

To analyze the composition of the Universe, it is convenient to define the critical density ρ_c, which corresponds to the density required for a flat Universe ($k = 0$):

$$\rho_c = \frac{3H_0^2}{8\pi G} \approx 9.20 \times 10^{-27}\,\mathrm{kg\,m^{-3}}. \tag{1.5}$$

The abundance of each energy component i is then expressed as a dimensionless density parameter $\Omega_i \equiv \rho_i/\rho_c$.

By evaluating Eq. (1.4) at the present time (denoted by subscript '0') and normalizing by H_0^2, we can rewrite the expansion history as a sum of contributions from different components. Although the original equation groups all energy into ρ, the total density evolves as the sum of species with different equations of state: radiation ($\propto a^{-4}$), non-relativistic matter ($\propto a^{-3}$), and the cosmological constant ($\rho_\Lambda = \mathrm{const}$). Additionally, the curvature term $-kc^2/a^2$ can be treated as an effective energy density Ω_k. This yields the normalized Friedmann equation containing four distinct terms:

$$\frac{H^2(a)}{H_0^2} = \Omega_{r,0}\left(\frac{a_0}{a}\right)^4 + \Omega_{m,0}\left(\frac{a_0}{a}\right)^3 + \Omega_{k,0}\left(\frac{a_0}{a}\right)^2 + \Omega_\Lambda, \tag{1.6}$$

where:

- $\Omega_{r,0}$: Current radiation density (photons and neutrinos).
- $\Omega_{m,0} = \Omega_{b,0} + \Omega_{c,0}$: Current matter density (baryons + CDM).
- $\Omega_{k,0} = -kc^2/(a_0^2 H_0^2)$: Effective curvature density parameter.

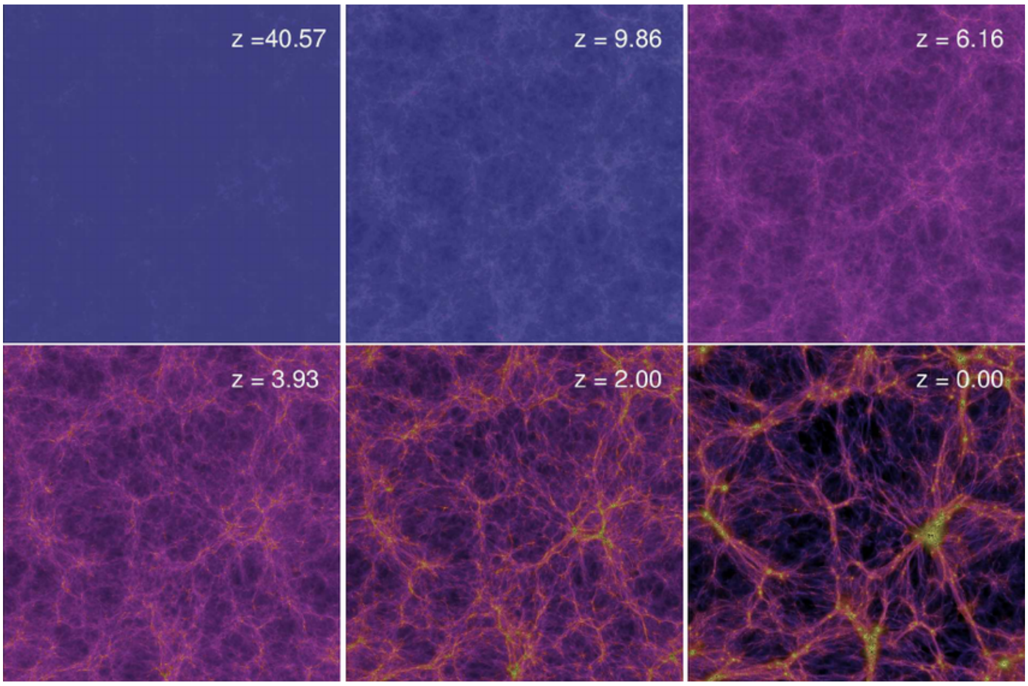

Figure 1.4: Snapshot from a cosmological simulation showing the projected matter density and temperature at different redshifts. Bright regions trace dense clusters; filaments connect them within the cosmic web [7].

- Ω_Λ: Dark Energy density parameter.

The constraint $\sum \Omega_{i,0} = 1$ applies; observations indicate a flat Universe ($\Omega_{k,0} \approx 0$), dominated today by Dark Energy ($\Omega_\Lambda \approx 0.69$) and Cold Dark Matter ($\Omega_c \approx 0.26$), with baryons constituting only $\approx 5\%$ of the critical density [6].

Large-scale structure (LSS). The observed web of galaxies and clusters provides compelling evidence for non-baryonic dark matter through its role in amplifying primordial overdensities and providing the gravitational scaffolding for structure formation.

Cosmological epochs are often referenced by their redshift z, which quantifies the stretching of photon wavelengths due to the expansion of space and is inversely related to the scale factor by $1 + z = 1/a(t)$. Since the Universe expands monotonically, higher redshifts correspond to earlier epochs. After matter–radiation equilibrium at $z \sim 3600$ (when the energy density of matter began to dominate over radiation), density fluctuations grew roughly in proportion to the cosmological scale factor $a(t)$ (normalized to unity today) until non-linear collapse led to the formation of virialised halos (see Fig. 1.4). Baryons subsequently fell into these gravitational potential wells, giving rise to stars and galaxies.

Cosmological N-body simulations, such as Millennium or Illustris, follow billions of particles from early initial conditions to the present epoch, successfully reproducing the filamentary structure and halo mass distribution observed in the Universe.

To this extent, a cold (non-relativistic) dark-matter component is essential: hot DM would erase small-scale power, producing a top-down formation history in conflict with observations [8, 9].

Cosmic Microwave Background (CMB). The Cosmic Microwave Background (CMB) is the remnant thermal radiation from the early Universe, providing one of the most powerful tools to constrain cosmological parameters and serving as the primary quantitative probe of the ΛCDM model.

In the early, hot Universe (before $z \simeq 1100$), photons were tightly coupled to baryons (protons and electrons) via Thomson scattering ($e^- + \gamma \to e^- + \gamma$), forming a thermal photon-baryon plasma. As the Universe expanded and cooled, the temperature eventually dropped below ∼3000 K, allowing electrons and nuclei to combine into neutral hydrogen atoms. This event, known as *recombination*, drastically reduced the free electron density and therefore the Thomson scattering rate Γ_S.

When Γ_S fell below the cosmic expansion rate H at $z \simeq 1100$ (corresponding to approximately 380,000 years after the Big Bang), photons *decoupled* from matter: their mean free path increased dramatically, and they began to stream freely through the Universe. This defines the *last scattering surface* (LSS), which we observe today as the CMB sky.

The measured spectrum of the CMB is that of a near-perfect black body with temperature $T_\gamma \simeq 2.7255\,\mathrm{K}$ [10]. However, the temperature is not perfectly uniform; it exhibits tiny anisotropies ($\Delta T/T \sim 10^{-5}$) that reflect primordial density fluctuations at the time of decoupling.

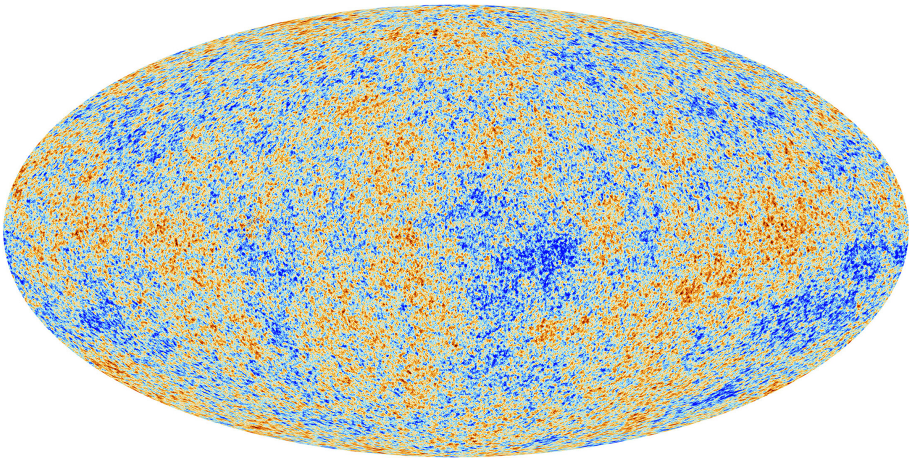

Figure 1.5: CMB temperature anisotropies measured by *Planck*. Image courtesy of ESA [11].

To analyze these fluctuations, the temperature field on the sky is expanded in spherical harmonics $Y_{lm}(\theta, \phi)$:

$$\frac{\Delta T}{T}(\theta, \phi) = \sum_{l=0}^{+\infty} \sum_{m=-l}^{+l} a_{lm} Y_{lm}(\theta, \phi), \tag{1.7}$$

where the expansion coefficients a_{lm} are given by:

$$a_{lm} = \int_{4\pi} \frac{\Delta T}{T}(\theta, \phi) Y_{lm}^*(\theta, \phi)\, d\Omega. \tag{1.8}$$

In practice, the monopole ($l = 0$, representing the mean temperature) and the dipole ($l = 1$, dominated by our motion relative to the CMB rest frame) are subtracted, and the analysis focuses on $l \geq 2$.

The statistical information is encoded in the angular power spectrum C_l, which measures the variance of the coefficients a_{lm}:

$$C_l \equiv \frac{1}{2l+1} \sum_{m=-l}^{l} |a_{lm}|^2. \tag{1.9}$$

The multipole l is inversely related to angular scale ($\theta \approx \pi/l$): low l corresponds to large angular scales, while high l represents fine details.

Physically, the peaks in the power spectrum (Figure 1.6) arise from acoustic oscillations in the photon-baryon fluid before recombination. Gravitational attraction (driven by dark matter potential wells) compressed the fluid, while photon pressure resisted, creating standing sound waves. The position of the first acoustic peak is highly sensitive to the spatial curvature of the Universe (Ω_k), while the relative heights of subsequent peaks constrain the baryon density (Ω_b) and cold dark matter density (Ω_c).

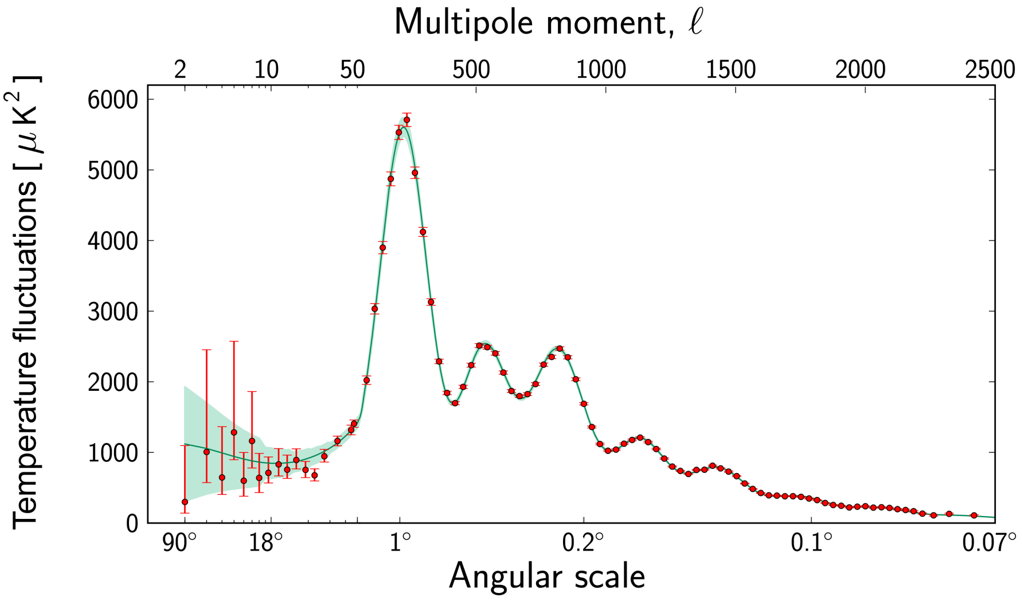

Figure 1.6: Angular power spectrum of CMB temperature anisotropies measured by *Planck* [12] (data points) and best-fit ΛCDM model (solid line).

In concert, the large-scale distribution of matter traced by galaxy surveys provides information on how structures grow over cosmic time, while the CMB anisotropies encode the initial conditions: the primordial density fluctuations and the composition of the Universe at the epoch of decoupling. These two probes provide mutually consistent, high-precision evidence that about 85% of the Universe's matter is a cold, non-luminous component interacting primarily through gravity, while a cosmological constant drives the present-day accelerated expansion. The angular power spectrum of CMB temperature anisotropies measured by *Planck* (Fig. 1.6) and its best-fit ΛCDM model stand as the primary quantitative result, precisely constraining the six cosmological parameters and confirming the necessity of cold dark matter.

The following section will present an overview of theoretical dark matter models, discussing their strengths and limitations. Subsequently, we will describe the experimental techniques used to search for or constrain these models, with a particular focus on direct detection experiments in underground laboratories.

1.2 Candidates for dark matter

Observational evidence from cosmological and astronomical studies, which is largely based on gravitational phenomena, is inconsistent with the current standard model describing the particles and forces in the Universe. This discrepancy indicates that an additional ingredient is necessary, or at least hypothesized, to adequately account for the measurements. Various theories have been proposed to explain these anomalies; the principal ones are discussed in the following sections.

1.2.1 Dark matter as a particle

The last few decades have witnessed the completion of the particle spectrum predicted by the Standard Model of particle physics, notably with the discovery of the Higgs boson at the LHC in 2012 [13]. Nevertheless, the Standard Model is known to exhibit several limitations, including the fine-tuning problem associated with the Higgs boson mass, neutrino masses, the strong CP problem, the matter-antimatter asymmetry, and the absence of gravitational interactions. Extensions of the Standard Model aim to predict the existence of new forces and particles, some of which possess characteristics suitable for dark matter candidates.

Based on the observational evidences discussed in Section 1.1, any viable particle dark matter model must satisfy the following properties:

1. **Non-baryonic:** CMB measurements from the Planck satellite imply that dark matter must be non-baryonic.

2. **Abundant:** Planck data indicate that the dark matter density is approximately 0.26, which is significantly greater than the density of ordinary baryonic matter.

3. **Neutral and Color-free:** The lack of interactions with photons precludes any electromagnetic interactions, and the absence of strong interactions ensures that dark matter does not lose energy and concentrate in galactic centers beyond what is observed.

4. **Weakly Interacting:** Although dark matter has been observed to interact gravitationally, any non-gravitational interaction must be extremely weak. This is necessary not only for the decoupling of dark matter from radiation and baryonic matter during Big Bang Nucleosynthesis (BBN), but also to allow for its potential detection. BBN refers to the epoch in which the temperature and density of the early Universe permitted the synthesis of light elements such as deuterium, helium, and lithium. Note that “weakly interacting” here does not necessarily refer to the Standard Model electroweak force, but to any interaction with a sub-weak strength.

5. **Stable or Extremely Long-lived:** In order to account for its current abundance and gravitational effects in the Universe, dark matter particles must be stable or have an extremely long lifetime.

6. **Warm or Cold:** Dark matter relics are categorized based on their energy at the moment of decoupling from baryonic matter. *Hot* dark matter models require relativistic particles (with masses typically on the order of $O(10)$ eV) at decoupling, but such models are incompatible with the observed formation of large-scale structures if their abundance is high. In contrast, *warm* and *cold* dark matter models, which involve particles with higher masses and lower kinetic energies (with cold dark matter being completely non-relativistic), support the formation of galaxies as observed. However, each scenario modifies the galactic structure in distinct ways, and current observations of galactic satellites are not yet conclusive in determining the precise nature of the dark matter population.

As a consequence of these stringent requirements, the modeling of a dark matter particle necessarily requires an extension of the Standard Model. No particle within the Standard Model satisfies all the listed properties, not even neutrinos. Although neutrinos are non-baryonic, neutral, and interact only weakly, their expected relic density does not match the observations [14].

1.2.1.1 WIMPs (Weakly Interacting Massive Particles)

One of the most widely studied and well-motivated classes of dark matter candidates are *Weakly Interacting Massive Particles* (WIMPs). Extensions of the Standard Model naturally predict new particles that can be produced in the correct abundance as thermal relics [15]. The basic assumptions behind WIMPs are that they are electrically neutral, massive, and interact with ordinary matter at or below the weak scale. Starting from these assumptions, it is possible to relate the WIMP mass and interaction cross section to the observed relic density.

Early in the history of the Universe, when temperatures were sufficiently high, WIMPs could annihilate into Standard Model particles (and vice versa) at rates fast enough to maintain thermal and chemical equilibrium. In this regime, the Boltzmann equation describing the WIMP number density n_χ can be written schematically as

$$\frac{dn_\chi}{dt} + 3H\, n_\chi \;=\; -\, \langle \sigma v \rangle \big(n_\chi^2 - n_{\chi,\mathrm{eq}}^2\big), \tag{1.10}$$

where H is the Hubble expansion rate, $\langle \sigma v \rangle$ is the thermally averaged annihilation cross section, and $n_{\chi,\mathrm{eq}}$ is the equilibrium number density [16]. As the Universe expanded and cooled, the WIMP interaction rate eventually became too small to keep up with the Hubble expansion, causing WIMPs to *freeze out* of equilibrium. After freeze-out, their comoving number density remained essentially constant until the present day.
In cosmology, the total entropy of the Universe is conserved during thermal equilibrium, making the comoving number density

$$Y_\chi \;=\; \frac{n_\chi}{s},$$

(where s is the entropy density) a convenient variable to track the relic abundance. After freeze-out, Y_χ stays constant as the Universe continues to expand.

Particles with the properties outlined above can arise in various extensions of the Standard Model. Two of the most popular theoretical frameworks that predict WIMP-like

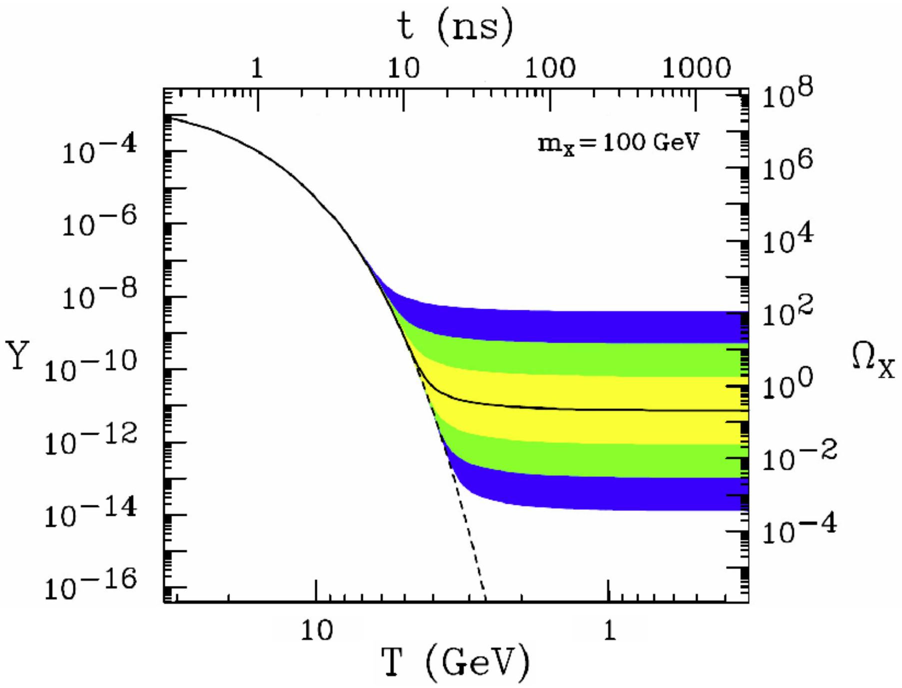

Figure 1.7: A schematic illustration of the comoving number density of WIMPs as a function of the inverse temperature (or cosmic scale factor). After a period of thermal equilibrium, the abundance of WIMPs *freezes out* once the annihilation rate drops below the expansion rate of the Universe [17].

particles are supersymmetry (SUSY) and models with extra dimensions (ED). In these scenarios, stable massive particles with weak-scale interactions naturally appear, providing compelling candidates for dark matter.

1.2.1.2 Sterile neutrinos

The Standard Model predicts three left-handed neutrinos with zero mass, yet neutrino oscillation experiments have confirmed that neutrinos possess a small but non-zero mass [18]. One elegant solution to this discrepancy is the introduction of a new particle, the *sterile neutrino*. Being a gauge singlet, the sterile neutrino interacts with Standard Model particles solely through a mixing matrix.

By employing the seesaw mechanism, the mixing between the sterile neutrino and the active neutrinos can be described by a symmetric mass matrix of the form

$$\mathcal{M} = \begin{pmatrix} 0 & m_D \\ m_D^T & M_R \end{pmatrix}, \tag{1.11}$$

where m_D represents the Dirac mass term and M_R is the large Majorana mass associated with the sterile state. In the seesaw limit ($M_R \gg m_D$), the resulting mass eigenvalues become hierarchical,

$$m_\nu \sim \frac{m_D^2}{M_R} \quad \text{and} \quad m_N \sim M_R,$$

so that the active neutrino masses are significantly suppressed relative to the sterile neutrino mass. If M_R is larger than approximately $1\,\mathrm{keV}/c^2$ and the mixing angles are sufficiently small, the sterile neutrino becomes non-relativistic early enough to yield a relic density in agreement with the cold dark matter hypothesis.

The extremely feeble interactions, mediated by the tiny mixing with active neutrinos, ensure that the sterile neutrino remains stable over cosmological timescales, thus qualifying as a candidate within the class of Feebly Interacting Massive Particles (FIMPs). In this scenario, the cross section for interactions with Standard Model particles is so low that even during the early Universe, sterile neutrinos were effectively decoupled. Their relic density gradually accumulated as the production processes were suppressed by the rapid expansion of the Universe.

A key experimental signature of sterile neutrino dark matter is its decay into a monochromatic photon. Searches for such a signal are currently ongoing [19].

1.2.1.3 Axions and ALPs (Axion-Like Particles)

Axions are hypothetical particles originally proposed to resolve the strong CP problem in Quantum Chromodynamics (QCD) [20]. The QCD Lagrangian allows a CP-violating term parametrized by θ, which experiments constrain to be extremely small. The Peccei–Quinn mechanism introduces a global chiral U(1) symmetry that is spontaneously broken at a scale f_a, dynamically driving θ to zero.

This mechanism gives rise to a pseudo-Nambu–Goldstone boson whose couplings to gluons and, via loops, to photons, depend on f_a. Despite their low mass, axions can form a coherent field that behaves as cold dark matter. Their photon coupling also enables experimental detection strategies, such as axion-to-photon conversion in strong magnetic fields [21].

1.2.1.4 Dark sector

The dark sector refers to hypothetical particles and interactions beyond the Standard Model that primarily couple among themselves and interact only weakly with visible matter [17]. These models may introduce new gauge symmetries and mediators, leading to rich phenomenology such as self-interactions and exotic radiation.

A common feature of dark sector models is the presence of a portal connecting the two sectors. Examples include kinetic mixing between a dark photon and the Standard Model photon [22], as well as Higgs and neutrino portals. These couplings motivate a broad range of searches, from direct detection to collider experiments, targeting potential signatures of dark sector physics.

1.2.1.5 Modified Newtonian dynamics (MOND)

Traditional astrophysical and cosmological evidence relies on the application of Newtonian dynamics and General Relativity. However, several alternative models suggest that the observed discrepancies can be explained by modifying the underlying assumptions of gravitational laws.

These theories, collectively known as *Modified Newtonian Dynamics* (MOND) [23], propose that the discrepancies in gravitational observations stem from a change in the behavior of gravity in regimes of very low acceleration. Central to the MOND hypothesis is the introduction of a new fundamental acceleration constant, denoted by a_0. This constant demarcates the transition between the standard Newtonian regime and the MOND regime. Specifically, when a system's acceleration a is less than a_0, the gravitational force deviates from the classical Newtonian prediction. Conversely, when $a \gg a_0$, standard Newtonian dynamics is recovered.

The value of a_0 is typically estimated from the rotation curves of galaxies, with a value on the order of $1.2 \times 10^{-10}\,\mathrm{m\,s^{-2}}$ [2]. Under MOND, the dynamics of galaxies and galaxy clusters are modified, while the dynamics at the scale of the solar system remain virtually unaffected.

MOND theories have proven to be quite successful at galactic scales, accurately predicting the dependence of rotation curves on the baryonic mass content of galaxies. However, challenges arise when attempting to extend these theories across different scales. For instance, describing the structure and behavior of galaxy clusters and the anisotropies in the Cosmic Microwave Background (CMB) necessitates a relativistic extension of MOND. These extended models often become less predictive as additional functions and parameters are required to properly account for the measurements.

While MOND-based theories can successfully describe the dynamics of some galaxy clusters and individual galaxies, they encounter significant difficulties with more complex structures and phenomena, such as those observed in the Bullet Cluster and the detailed features of the CMB [24]. Thus, although MOND provides an intriguing framework for addressing observational discrepancies, a complete and fully predictive theory remains an open challenge.

1.2.1.6 Primordial black holes

Gravitational observations indicating a missing component in the Universe can be explained without invoking modifications to the established laws of gravity. Instead, one may postulate the existence of astrophysical objects that have yet to be directly observed or identified. The hypothesis that black holes could form from the collapse of matter in the early Universe was originally proposed by Zel'dovich, Novikov, and Hawking during the 1960s [25]. These black holes are theorized to have been produced prior to the epoch of Big Bang Nucleosynthesis (BBN).

BBN refers to the period in which the temperature and density of the Universe permitted the nuclear fusion of light elements. During this epoch, the fusion products were not destroyed by the high-energy photons that were thermally coupled with matter. This phase enabled the synthesis of nuclei heavier than hydrogen and imposes constraints on the baryonic mass content of the Universe. Since these massive objects are formed before BBN, they are coupled with the remaining baryonic matter and are not included in the standard baryonic abundance calculations.

For these reasons, as these massive objects are not accounted for in the predictions of the Cosmic Microwave Background (CMB), they could represent the missing mass component of the Universe and may be consistent with the evidences discussed previously, such as galaxy rotation curves, gravitational lensing effects, and large-scale structure formation. In fact, primordial black holes (PBHs) with masses greater than $5 \times 10^{14}\,\mathrm{g}$ have lifetimes that exceed the current age of the Universe. Moreover, because PBHs do not originate from the collapse of massive stars, their masses are not bound by a strict upper limit and can span several orders of magnitude.

Although no direct discovery of primordial black holes has been made to date, observations from gravitational microlensing, gravitational wave detections, and CMB measurements are imposing stringent limits on the parameter space of the fraction of dark matter in the form of PBHs as a function of PBH mass. Currently, only a mass window between approximately 10^{17} and 10^{21} grams remains relatively unconstrained.

1.3 Experimental searches for dark matter

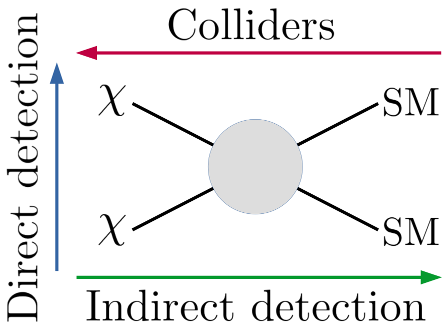

Figure 1.8: Schematic showing the possible Dark Matter detection channels.

The particle Dark Matter hypothesis remains the most compelling to date and can be tested through three complementary experimental approaches: production at particle accelerators, indirect detection through the search for annihilation or decay products, and direct detection via scattering off target nuclei. Figure 1.8 schematically illustrates the possible interactions between Dark Matter and ordinary matter particles. Reading the diagram from left to right, the annihilation of Dark Matter particles could produce Standard Model (SM) particle pairs; conversely, collisions at accelerators (such as electron-positron or proton-proton interactions) could generate Dark Matter particle pairs.

1.3.1 Direct detection

Direct detection (DD) experiments aim to observe interactions between dark matter particles and ordinary matter. In the case of Weakly Interacting Massive Particles (WIMPs), such interactions occur via elastic scattering off target nuclei within laboratory detectors. The key features of these experiments include:

- **Energy Measurement:** DD experiments measure the energy deposited by nuclear recoils, typically in the range of 10–100 keV, which results from the rare scattering events of WIMPs.

- **Low Background Environments:** Due to the extremely small interaction cross section of WIMPs, experiments are conducted deep underground using radiopure materials and appropriate shielding to minimize background from neutrons and other particles.

- **Kinematic Dependence:** The recoil energy spectrum depends on the mass of the target nuclei, and for spin-independent interactions, the signal normalization scales with the square of the mass number.

- **Detection Techniques:** Signals from DM-nuclei scatterings can be detected through:
  - *Scintillation light* from the excitation and subsequent de-excitation of nuclei.
  - *Ionization charge* generated by atomic ionization.
  - *Phonons (heat)* measured in crystal detectors.

Often, experiments employ a combination of these techniques to distinguish between potential WIMP signals (nuclear recoils) and background events (electron recoils).

Direct detection methods are particularly sensitive to Dark Matter candidates in the GeV-scale mass range and will be discussed in further detail in Section 2.1.

1.3.2 Indirect detection

Indirect detection searches aim to identify the secondary products of Dark Matter annihilation or decay occurring in astrophysical sources. The primary reaction considered is:

$$\mathrm{DM\,DM} \rightarrow \mathrm{SM\,SM},$$

where DM denotes a Dark Matter particle (e.g., a WIMP) and SM represents any Standard Model particle. The key points include:

- **Secondary Particle Detection:** Many SM particles produced in these processes are unstable and decay into detectable particles, such as gamma rays, neutrinos, or charged cosmic rays.
- **Thermal Relic Connection:** The cross section measured in indirect searches is directly related to the process that established the Dark Matter relic abundance in the early Universe, under the assumption that DM was once in thermal equilibrium.
- **Astrophysical Sources:** The most promising targets for indirect detection are regions with high Dark Matter density, such as the Galactic center, galactic halos, nearby galaxy clusters, and dwarf spheroidal galaxies.

Enhanced self-annihilation, scattering, or decay into Standard Model particles could generate a detectable flux, providing indirect evidence for the existence of Dark Matter.

1.3.3 Collider searches

Collider searches represent the third experimental strategy for WIMP detection. In high-energy collisions, such as those at the Large Hadron Collider (LHC), Dark Matter particles could be produced directly. The strategy is characterized by:

- **Missing Transverse Energy:** Many new physics searches at the LHC focus on events where, besides the visible hadronic or leptonic decay products, there is a significant amount of missing transverse energy. This missing energy is indicative of neutral, stable particles (potentially WIMPs) that escape detection.
- **Typical Reactions:** A representative collider process is:

  $$pp \rightarrow \chi\bar{\chi} + x,$$

  where χ represents a Dark Matter particle and x is a final state composed of hadronic jets, photons, or a leptonically decaying Z or W boson.
- **Complementarity with Direct Detection:** Collider searches and direct detection experiments probe different regions of the WIMP parameter space. While direct detection experiments lose sensitivity at very low WIMP masses (below a few GeV/c^2)

due to the reduced nuclear recoil energy, collider searches remain effective in this regime. Conversely, for higher WIMP masses, the production cross section at colliders decreases, making direct detection more competitive.

Detection of events with large missing momentum in association with visible particles would provide compelling evidence for the production of Dark Matter at colliders.

Chapter 2

Direct detection of dark matter

As discussed in Chapter 1, astronomical and cosmological observations indicate that our understanding of the fundamental particles and forces in the Universe remains incomplete. Many unexplained phenomena are consistent with the presence of missing mass. Under the assumption that dark matter is composed of particles with very weak, non-Standard-Model interactions beyond gravity, distinct experimental signatures arise that enable different search strategies to be pursued.

Dark matter may be indirectly detected by studying potential excesses of Standard Model particles produced from dark matter annihilation in space. Unpredicted fluxes of such particles, including positrons and other charged species, are actively sought in dedicated experiments. Alternatively, high-energy collider experiments, which are capable of producing new particles, are employed in dark matter searches either via direct production or beam dump approaches. In this thesis, we focus on an alternative approach based on the direct detection of dark matter by observing the elastic scattering of galactic dark matter particles off detector materials.

Observations of the Milky Way's rotational curves imply that our galaxy, like other spiral galaxies, is embedded in a dark matter halo [26]. Moreover, the peculiar motion of the Sun and the Earth relative to the galactic center introduces a preferred incoming direction for dark matter particles in the laboratory frame, a feature that can be exploited to boost signal detection and to characterize dark matter interactions in case of a positive signal. Unfortunately, astrophysical constraints suggest that the coupling between dark matter and Standard Model particles is extremely weak, leading to a very low expected signal rate. Given the multitude of phenomena capable of mimicking a dark matter signal, direct detection experiments are experimentally very challenging.

This thesis focuses on the direct detection of WIMPs (Weakly Interacting Massive Particles) through their nuclear recoil signatures. Section 2.1 outlines the phenomenology of WIMP interactions and the fundamental principles that govern direct dark matter detection. Section 2.3 then examines the experimental challenges associated with these searches and highlights the main features and advantages of directional detection techniques.

2.1 WIMPs–nuclei scattering

Within the framework of the WIMP model, the Milky Way is assumed to be embedded in a halo composed of cold, non-relativistic dark matter particles. The peculiar motion of the Sun around the Galactic center, combined with the Earth's orbit around the Sun, produces an apparent dark matter wind consisting of particles arriving from a preferred direction. This effect increases the kinetic energy of dark matter particles in the terrestrial reference frame and enhances the possibility of a detectable interaction between WIMPs and Standard Model (SM) particles, assuming such particles and interaction exist.

The basic idea behind direct detection experiments is to deploy a target volume of material capable of measuring the recoil of ordinary matter following an interaction with a WIMP. The constituents of ordinary matter are electrons and nuclei; while dark matter may potentially interact with both, the primary focus is on elastic interactions on nuclei. In fact, it is expected that WIMPs have a mass on the order of $O(10\,\mathrm{GeV}/c^2)$ and the kinematic coupling is more favorable for nuclei than for electrons [27]. The predicted rates depend on the assumed WIMP mass and scattering cross section, as well as on astrophysical parameters and target material properties.

2.1.1 DM halo

The observational data currently available regarding the actual WIMP velocity spectrum within our galaxy lacks the precision necessary to uniquely determine a specific distribution. Therefore, it is common practice to adopt a theoretical model for describing the galactic halo, building upon all the assumptions previously discussed in Chapter 1. The most widely adopted theoretical framework is known as the Standard Halo Model (SHM). According to this model, the dark matter halo of our galaxy is assumed to be an isotropic isothermal sphere. The density profile follows a power law $\rho \sim r^{-2}$, where r represents the radial distance from the galactic center. Within the rest frame of the galaxy, the normalized velocity distribution can be characterized by a Maxwellian distribution [28]:

$$f(\mathbf{v}) = \begin{cases} \frac{N}{(2\pi\sigma_v)^{3/2}} \exp\left(-\frac{|\mathbf{v}|^2}{2\sigma_v^2}\right) & \text{if } |\mathbf{v}| < v_{esc} \\ 0 & \text{if } |\mathbf{v}| > v_{esc} \end{cases} \tag{2.1}$$

In this expression, N represents a normalization constant. The velocity dispersion σ_v is connected to the circular speed via the relation $\sigma_v = \frac{v}{\sqrt{2}}$. At the Sun's location, the circular speed has been measured to be (229.0 ± 0.2) km/s [29]. Although the Maxwell distribution theoretically extends to arbitrarily large velocities, in practice the velocity distribution is truncated at a local escape velocity v_{esc}. This cutoff reflects the physical constraint that particles with velocities exceeding v_{esc} would not remain gravitationally bound to our Galaxy. Consequently, such particles cannot serve as potential sources of interaction. The RAVE survey has determined the escape velocity to be $v_{esc} = 533^{+54}_{-41}$ km/s [30].

Another crucial parameter in WIMP detection calculations is the local DM density. Its actual value depends significantly on which mass density profile model is adopted for the Milky Way. When considering a broad range of possible halo profiles, the resulting values span the range $\rho_0 = (0.2 - 0.6)$ GeV/cm^3 [31–34]. Interestingly, estimates of the local density obtained through methods that do not rely on detailed mass modeling of the Milky Way structure are consistent within this range. The value most commonly employed for the local density is $\rho_0 = 0.3$ GeV/cm^3, although this choice carries systematic uncertainties [35].

For the purpose of calculating the recoil spectrum in direct detection experiments, one must transform the velocity distribution from the galactic rest frame into the laboratory frame. Given that both the Earth's motion around the Sun and the Sun's motion around the galactic center are non-relativistic, a simple Galilean transformation is adequate for this purpose. Specifically, $f(\mathbf{v}_L) = f_{gal}(\mathbf{v} + \mathbf{v}_{lab}(t))$, where $\mathbf{v}_{lab}$ denotes the laboratory velocity with respect to the galactic rest frame. This transformation allows us to express the recoil rate in the laboratory rest frame. It should be noted that the gravitational potential of the Earth and the Sun would only influence very low energy WIMPs (those with $|\mathbf{v}| < 40$ km/s) [36], which constitute only a small fraction of the total population. The laboratory velocity, in this transformation, is obtained by vectorially summing the local circular speed, the Sun's velocity relative to the galactic rest frame, and the Earth's velocity relative to the Sun [28].

It is important to recognize that the SHM does not provide a fully accurate description of the Milky Way's dark matter halo. The assumption of an isotropic, isothermal sphere in perfect dynamical equilibrium is an idealization that does not capture the full complexity of reality. In cold dark matter cosmological scenarios, structures emerge through hierarchical formation processes. This leads to DM halos that exhibit triaxial geometry, anisotropic velocity distributions, and complex phase-space substructure [37]. High-resolution numerical simulations of galaxies comparable to the Milky Way show velocity distributions that deviate considerably from the simple Maxwellian form. Various functional forms that incorporate these deviations from the SHM have been proposed and investigated through detailed simulations [38–46]. Nevertheless, despite its limitations, the SHM continues to serve as a standard benchmark for computing the expected event rate in WIMP search experiments.

2.1.2 WIMP–nucleus scattering rate

According to [27], the expected rate per unit mass for an interaction between galactic WIMPs and atomic nuclei can be estimated by a simplified expression of the form:

$$dR = \frac{N_0}{A_{mol}} \sigma_{\chi A} \, v \, \frac{\rho_0}{m_\chi} f(\mathbf{v}) \, d^3v, \tag{2.2}$$

where N_0 is Avogadro's number, ρ_0 is the local dark matter density at Earth, A_{mol} is the molar mass of the target atom, $\sigma_{\chi A}$ is the WIMP–nucleus cross section, m_χ is the WIMP mass, and $f(\mathbf{v})$ is the velocity distribution of WIMPs in the galactic rest frame.

Integrating over the velocity distribution and assuming a standard isothermal halo with local density $\rho_0 = 0.3$ GeV cm^{-3} and a Maxwellian distribution (as described in Sect. 2.1.1), the total interaction rate for a WIMP of mass m_χ scattering elastically off a target can be approximated as

$$R \simeq \frac{\rho_0}{m_\chi} N_{\mathrm{T}} \langle \sigma_{\chi A} v \rangle \simeq 0.1 \, \frac{\text{events}}{\text{t yr}} \left(\frac{\rho_0}{0.3 \text{ GeV cm}^{-3}} \right) \left(\frac{100 \text{ GeV}}{m_\chi} \right) \left(\frac{\sigma_{\chi A}}{10^{-45} \text{ cm}^2} \right), \tag{2.3}$$

where $N_{\mathrm{T}} = N_0 M_{\mathrm{det}}/A_{mol}$ is the total number of target nuclei in a detector of mass M_{det}, and $\langle \sigma_{\chi A} v \rangle$ represents the velocity-averaged cross section:

$$\langle \sigma_{\chi A} v \rangle = \int \sigma_{\chi A}(v) \, v \, f(\mathbf{v}) \, d^3v. \tag{2.4}$$

For example, for a ^{132}Xe target, $N_{\mathrm{T}} \simeq 4.6 \times 10^{27}$ nuclei/tonne. Signals at the level of a few-tenths of an event per tonne and per year dictate stringent requirements on background suppression, typically requiring background rates at least one to two orders of magnitude below the expected signal in the recoil-energy window of interest.

To move beyond these simplified estimates, one needs a more complete expression for the differential scattering rate. Per unit target mass, it can be written (in double-differential form) as

$$\frac{d^2R}{dE_R\,d\Omega_R} \;=\; \frac{\rho_0}{m_\chi\,M_{\rm tot}} \int_{v\,\geq\,v_{\rm min}(E_R)} f(\mathbf{v})\,\frac{d^2\sigma_{\chi A}}{dE_R\,d\Omega_R}\,|\mathbf{v}|\;d^3v, \tag{2.5}$$

where:

- $f(\mathbf{v})$ is the normalized velocity distribution in the lab frame,
- $v_{\rm min}(E_R)$ is the minimum WIMP speed to induce a recoil of energy E_R,
- $\frac{d^2\sigma_{\chi A}}{dE_R\,d\Omega_R}$ is the differential cross section for WIMP–nucleus scattering,
- $M_{\rm tot}$ is the total detector mass (often factored out, depending on how R is defined).

The velocity integration is restricted to those WIMPs with $|\mathbf{v}| \geq v_{\rm min}$; this lower cut-off depends on the recoil energy and kinematics. The expected recoil spectrum depends not only on nuclear properties (such as mass, spin, and response functions) but also on astrophysical parameters related to the Galactic dark matter halo.

2.1.2.1 Scattering kinematics and recoil energy

Under the standard halo model (SHM) [47], WIMPs travel at non-relativistic speeds (on the order of a few hundred km/s). In the Earth/lab frame, the target nucleus is taken to be at rest before the collision, while the WIMP approaches with velocity $\mathbf{v}$. Because $v \ll c$, the energy and momentum transfer can be approximated via simple two-body elastic scattering formulas .

For a WIMP–nucleus system, the momentum transfer q is often expressed in terms of the reduced mass $\mu_{\chi A}$:

$$q \;\approx\; \mu_{\chi A}\,v, \tag{2.6}$$

where $\mu_{\chi A} = \frac{m_\chi M_A}{m_\chi + M_A}$ and M_A is the target nucleus mass. In the center-of-mass frame, the nucleus can recoil with an energy

$$E_R \;=\; \frac{\mu_{\chi A}^2}{M_A}\,v^2\,(1-\cos\theta_{\rm CM}), \tag{2.7}$$

where $\theta_{\rm CM}$ is the scattering angle in the center-of-mass frame. The initial WIMP kinetic energy is $E_i = \frac{1}{2}m_\chi v^2$, so one can rewrite E_R in terms of E_i and a dimensionless factor that depends on the scattering angle and the mass ratio:

$$E_R \;=\; \alpha\,E_i\;, \quad \text{where } 0 \leq \alpha \leq 1. \tag{2.8}$$

The maximum momentum transfer (and thus maximum recoil energy) occurs when $\theta_{\rm CM} \;=\; \pi$, corresponding to a head-on collision and optimal momentum transfer.

From these relations, one obtains the minimum velocity $v_{\rm min}(E_R)$ necessary to produce a recoil of energy E_R:

$$v_{\rm min}(E_R) \;=\; \sqrt{\frac{M_A\,E_R}{2\,\mu_{\chi A}^2}}. \tag{2.9}$$

This threshold velocity defines the lower limit of the integration in Eq. (2.5) .

2.1.2.2 Cross section

The WIMP–nucleus differential cross section encapsulates the underlying microscopic scattering process. At non-relativistic energies, one usually assumes that the total cross section can be factorized into a spin-independent (SI) term (often called scalar) plus a spin-dependent (SD) term [48], possibly with additional subdominant contributions depending on more exotic WIMP interactions:

$$\sigma_{\chi A} \;=\; \sigma_{\chi A}^{(\mathrm{SI})} + \sigma_{\chi A}^{(\mathrm{SD})}. \tag{2.10}$$

Because dark matter velocities are low, the momentum transfer is typically small enough that the WIMP interacts (to first approximation) coherently with the entire nucleus. However, nuclear structure effects reduce this coherence for larger q, as described by form factors.

In the SI scenario, the WIMP couples effectively to the total number of nucleons within the nucleus. At zero momentum transfer ($q = 0$), the scattering amplitude adds coherently, leading to a cross section proportional to A^2 if proton and neutron couplings are equal [48]. Thus, the SI component at $q = 0$ often takes the form

$$\sigma_{\chi A}^{(\mathrm{SI})}(q=0) \;=\; \sigma_{n}^{(\mathrm{SI})} \left(\frac{\mu_{\chi A}}{\mu_{\chi n}}\right)^{2} A^{2}, \tag{2.11}$$

where $\sigma_n^{(\mathrm{SI})}$ is the effective WIMP–nucleon cross section and $\mu_{\chi n}$ the reduced mass of the WIMP–nucleon system. Because of the A^2 scaling, heavier elements provide greater sensitivity to SI scattering for a fixed exposure.

For spin-dependent interactions, the WIMP couples to the net spin of the nucleus. Nuclei with even numbers of both protons and neutrons have total spin $J = 0$, so isotopes with an unpaired nucleon are required. The cross section at $q = 0$ can be written [48]:

$$\sigma_{\chi A}^{(\mathrm{SD})}(q=0) \;=\; \sigma_{n}^{(\mathrm{SD})} \left(\frac{\mu_{\chi A}}{\mu_{\chi n}}\right)^{2} \big[\text{nuclear spin factors}\big], \tag{2.12}$$

where the nuclear spin factors are determined from nuclear shell model calculations. Typically, $\sigma_n^{(\mathrm{SD})}$ is quoted separately for proton and neutron couplings, as target isotopes may be sensitive to one more than the other. In many theoretical models, the SD interaction is subdominant compared to SI, though targets with non-zero spin (such as ^{19}F or ^{127}I) are specifically chosen to explore this channel.

At finite momentum transfer, the cross sections in Eqs. (2.11) and (2.12) must be modified to account for nuclear structure effects. This is achieved by multiplying the zero-momentum-transfer cross section by the square of the appropriate form factor:

$$\sigma_{\chi A}(q^2) \;=\; \sigma_{\chi A}(q=0) \times F^2(q^2), \tag{2.13}$$

where $F(q^2)$ is normalized such that $F(0) = 1$. The momentum transfer q is related to the recoil energy through $q^2 = 2M_A E_R$, making the form factor an energy-dependent suppression factor. Consequently, the differential cross section entering Eq. (2.5) becomes

$$\frac{d^2\sigma_{\chi A}}{dE_R\, d\Omega_R}(E_R) \;=\; \left.\frac{d^2\sigma_{\chi A}}{dE_R\, d\Omega_R}\right|_{q=0} \times F^2(2M_A E_R). \tag{2.14}$$

The specific functional form of $F(q^2)$ depends on whether the interaction is spin-independent or spin-dependent, as discussed below.

Spin-independent form factor. For SI scattering, a widely adopted analytical approximation is the Helm form factor [49], written as

$$F_{\rm SI}(q^2) \;=\; 3\,\frac{j_1(qR_n)}{qR_n}\,\exp\!\Big[-\tfrac{1}{2}(qs)^2\Big], \tag{2.15}$$

where j_1 is the spherical Bessel function of the first kind, $R_n \simeq 1.2\,A^{1/3}\,\text{fm}$ approximates the nuclear "sharp" radius, and $s \approx 0.5\,\text{fm}$ is the nuclear skin thickness. Physically, $F_{\rm SI}(q^2) < 1$ at higher momentum transfers because the WIMP effectively probes smaller portions of the nucleus.

To estimate when significant loss of coherence occurs, one compares the de Broglie wavelength of the momentum transfer to the nuclear size. For typical targets with $A \geq 20$, form-factor suppression becomes relevant at recoil energies on the scale of tens of keV. Heavier nuclei (such as xenon or tungsten) experience stronger suppression at lower E_R since R_n is larger.

Spin-dependent form factor. For SD scattering, the situation is more involved. The nuclear spin is carried by unpaired nucleons, so nuclear shell models must be invoked to calculate detailed spin structure factors $S_p(q^2)$ and $S_n(q^2)$ for protons and neutrons [50]. These define

$$F_{\rm SD}^2(q^2) \;\sim\; \frac{S_p(q^2)\,\langle S_p\rangle^2 + S_n(q^2)\,\langle S_n\rangle^2}{(2J+1)}, \tag{2.16}$$

where J is the total nuclear spin. In general, the SD form factor falls off with increasing q, often faster than in the SI case, since only one or a few nucleons effectively contribute to the net spin.

2.1.3 Experimental signatures

When a Weakly Interacting Massive Particle (WIMP) scatters elastically off a nucleus in a terrestrial detector, three primary experimental features may be exploited to identify the resulting nuclear recoils (NR) as potential dark matter events: the recoil energy spectrum, the annual modulation of the event rate, and the angular dependence of the recoil distribution. Each of these observables provides a distinct experimental handle to discriminate a WIMP-induced signal from various backgrounds.

2.1.3.1 Recoil energy spectrum

The nuclear recoil spectrum induced by WIMPs typically follows an approximately exponential-like shape [27]. For a given WIMP kinetic energy E_i, the differential rate dR/dE_r can be parameterized as

$$\frac{dR}{dE_r} \;\propto\; e^{-\,E_r/E_0}, \tag{2.17}$$

where the characteristic energy scale E_0 depends on the WIMP mass m_χ and the target nucleus mass M_A. In a Maxwell–Boltzmann velocity distribution, this form is modified by the high-velocity cutoff: WIMPs exceeding the local galactic escape velocity $v_{\rm esc}$ are absent, producing a sharp drop in the recoil spectrum at higher E_r.

Heavier WIMPs tend to generate higher-energy recoils, while lighter WIMPs produce softer spectra. These kinematic effects influence both the optimal choice of target material and the mass range to which a given experiment is most sensitive.

2.1.3.2 Annual modulation

Because the Earth orbits the Sun at $\sim 30\,\mathrm{km/s}$ while the Sun moves through the Galactic halo at $\sim$ 220–250 km/s, the relative velocity of WIMPs in the laboratory frame varies over the year [47]. This leads to a small annual modulation in the event rate:

$$\frac{dR}{dE_r}(t) \;=\; \frac{dR}{dE_r}(0)\,\left[1 + R_m\,\cos\!\big(\omega\,(t - t_0)\big)\right], \tag{2.18}$$

where $\omega = 2\pi/T$, with $T \simeq 1\,\mathrm{year}$, and t_0 is the phase offset (typically in late spring). The modulation amplitude R_m is expected at the percent level. This signal is actively searched for by experiments like DAMA/LIBRA [51], and, if confirmed, would provide a distinctive though not conclusive signature of dark matter.

2.1.3.3 Angular dependence and directional detection

An even more striking signature arises from the anisotropy of the recoil directions. As the Sun (and Earth) move through the Galaxy, WIMPs are expected to arrive predominantly from the direction of the constellation Cygnus [52]. Consequently, nuclear recoils should exhibit a dipole distribution, peaking opposite to the average WIMP wind. At any fixed instant in time, the angular dependence of the recoil rate can be expressed as

$$\frac{1}{R_0}\frac{d^2R}{dE_r\,d\cos\phi} \;\propto\; \left[\,v_E\,\cos\phi \;-\; v_{\min}(E_r)\right]^2\,\exp\!\left[-\frac{\big(v_E\,\cos\phi - v_{\min}(E_r)\big)^2}{2\,E_0\,r\,v_0^2}\right], \tag{2.19}$$

where v_E is the Earth's velocity relative to the dark matter halo at that moment, $v_{\min}(E_r)$ is the minimum speed required to produce a recoil of energy E_r, v_0 is the characteristic WIMP velocity dispersion, and ϕ is the angle between the incoming WIMP and the recoil direction.

This directional anisotropy represents a substantially stronger signal than the annual modulation effect. While the seasonal variation in the total rate amounts to only $\sim 3\%$ over the course of a year [47], the angular distribution exhibits a forward-backward asymmetry of order unity: recoils are expected to be several times more frequent along the direction of the WIMP wind than in the opposite direction. This makes directional detection a particularly powerful discriminant, albeit technically more demanding.

A measurement of recoil tracks or directions enables a strong discrimination between a true WIMP signal, which should cluster from the incoming wind direction, and isotropic backgrounds like those induced by environmental radioactivity or solar neutrinos. Prototypes of directional dark matter detectors (e.g. low-pressure TPCs, nuclear emulsion chambers, etc.) aim to exploit this anisotropy as a "smoking gun" signature of galactic dark matter. Although technically challenging, directional detection is regarded as one of the most robust methods to confirm a dark matter origin of nuclear recoils.

In addition to the annual modulation, directional detectors can exploit a daily modulation of the recoil direction caused by Earth's rotation. As the Earth rotates with a period of one sidereal day ($\sim$ 23.93 hours), the direction of the incoming WIMP wind in the laboratory frame changes continuously [52]. At any given location on Earth, the apparent direction from which WIMPs arrive sweeps through the sky over the course of a day. This daily rotation of the preferred recoil axis provides a distinctive time-varying signature that is extremely difficult for isotropic backgrounds to mimic, making it a powerful discriminant for WIMP signals in directional detectors.

2.2 Experimental challenges and detection techniques

Direct searches for particle Dark Matter (DM) pose a double challenge. On the one hand, the expected scattering rate of a WIMP on ordinary matter is extraordinarily small, as shown in Eq. (2.3); on the other, the hoped-for recoil signal releases at most a few-keV of energy, barely above the detection threshold of even the most sensitive instruments. Consequently, collaborations must accumulate exposures of $\gtrsim 10^2$ t yr while guaranteeing that any other interaction able to mimic the nuclear recoil (NR) signature is suppressed to an almost vanishing level. The present section surveys the origin and phenomenology of *background sources* that limit the discovery reach and introduces basic mitigation strategies. Directional detectors, which can reconstruct the track of a WIMP-induced NR, receive special attention because they exploit the angular anisotropy of the WIMP signal to discriminate against isotropic backgrounds (see Sect. 2.1.3.3). A comparative review of the available detector technologies is postponed to Sect. 2.3.

A nuclear recoil (NR) generated by the scattering of a WIMP can be faked by two broad classes of background events, both of which must be suppressed or rejected to maximise sensitivity:

- **Electromagnetic backgrounds.** These are electron recoils (ERs) or ER-like signals produced by low-energy electrons in the sensitive volume. The primary sources are (i) direct interactions of cosmic radiation (especially penetrating muons), (ii) electrons from β decays of radioactive impurities, and (iii) γ and X-rays from radioactive impurities interacting via Compton scattering or photoelectric effect with atomic electrons of the target medium. Passive shields can attenuate much of this flux. However, a fraction of the background can be generated by internal materials as well (although very pure materials are usually used). The surviving events can be statistically distinguished from NRs through particle-ID observables such as scintillation timing or charge–light ratios. Unfortunately, these analytical techniques lose efficiency as the deposited energy approaches the sub-keV regime, making the rejection of ERs increasingly challenging.

- **Neutral backgrounds.** Neutral particles that scatter elastically off nuclei give rise to NRs that are practically indistinguishable from a WIMP interaction. The most relevant contributors are radiogenic or cosmogenic *neutrons* and *neutrinos* (via coherent elastic ν–nucleus scattering). In addition, α particles (and, more generally, any moving heavy ion) can mimic a NR if the energy they deposit in the active medium falls within the same low-energy window expected for a WIMP signal. A particularly relevant source of α-induced backgrounds is the radioactive contamination of internal detector materials, where α decays from natural radioactive chains (e.g. ^{238}U, ^{232}Th, and ^{210}Po) occurring on or near the surfaces of detector components can produce low-energy nuclear recoils that are difficult to distinguish from a genuine WIMP signal.

These two background categories are the macroscopic consequence of how photons, electrons, neutrons, neutrinos, and charged hadrons interact in a detector. The following paragraphs review the underlying microscopic processes that ultimately generate ER- or NR-like events in dark-matter experiments.

2.2.1 Interaction of particles with matter

Understanding the interaction mechanisms (photon absorption and scattering, neutron elastic and inelastic processes, neutrino scattering, and charged particle energy loss with quenching) is essential for designing effective shielding, identifying signal and background channels, and correctly interpreting the energy spectra observed in dark-matter detectors.

A clear picture of how the most common particles deposit energy in bulk matter is essential when designing the shielding and analysis strategy of any dark-matter experiment. In the following subsections, only a few topics particularly relevant in this discussion are outlined.

2.2.1.1 Photon interactions

Photons interact with matter through three main processes that dominate in different energy ranges. Below roughly 100 keV, the photoelectric effect dominates, in which a photon is completely absorbed by an atom and a bound electron is ejected with kinetic energy $E_e = E_\gamma - E_B$, where E_B is the binding energy. The cross-section scales strongly with atomic number as $\sigma_{\mathrm{pe}} \propto Z^5/E_\gamma^{3.5}$ [53, 54], making high-Z materials effective for photon shielding.

Between approximately 100 keV and 2 MeV, Compton scattering becomes the dominant mechanism. In this process, a photon scatters inelastically from a quasi-free electron, transferring part of its energy according to the Klein-Nishina formula [55]. The scattered photon energy is given by

$$E_{\gamma'} = \frac{E_\gamma}{1 + (E_\gamma/m_e c^2)(1 - \cos\theta)}, \tag{2.20}$$

where θ is the scattering angle. The Compton cross-section scales linearly with atomic number, $\sigma_{\mathrm{C}} \propto Z$, and depends on electron density.

Above a threshold of $2m_e c^2 = 1.022$ MeV, pair production becomes energetically possible and dominates at higher energies. In the Coulomb field of a nucleus, the photon converts into an electron-positron pair. The cross-section increases approximately as $\sigma_{\mathrm{pp}} \propto Z^2 \ln(E_\gamma)$ [53, 56]. The subsequent positron annihilation produces two 511 keV photons, contributing to the electromagnetic cascade.

Each of these mechanisms ultimately produces electron recoils (ER) through ionization and excitation of the medium. The resulting scintillation time profile and charge-to-light ratio exhibit characteristic signatures that enable discrimination from nuclear recoils in dual-phase time projection chambers [57, 58].

2.2.1.2 Neutron interactions

Neutrons, being electrically neutral, do not suffer electromagnetic interactions and can traverse substantial thicknesses of material, making them particularly challenging backgrounds in dark-matter searches. Their interaction mechanisms depend critically on kinetic energy.

At thermal and epithermal energies ($E_n < 0.5$ eV), radiative neutron capture (n, γ) reactions dominate. In these processes, a neutron is absorbed by a nucleus, forming a compound nucleus in an excited state which subsequently de-excites by emitting one or more gamma rays [59]. The cross-section follows the $1/v$ law, $\sigma_{(n,\gamma)} \propto 1/\sqrt{E_n}$, and can be extremely large for certain isotopes (e.g., ^{10}B, ^{113}Cd, ^{157}Gd). The emitted photons, often in the MeV range, then interact via the mechanisms described above, ultimately producing electron recoils. Materials with high thermal neutron capture cross-sections are therefore used in neutron shielding (e.g., borated polyethylene) but must be carefully positioned to avoid generating photon backgrounds near the detector [60].

In the intermediate energy range from a few eV to several MeV, elastic scattering off nuclei becomes the primary interaction channel. In these collisions, described by (n, n) kinematics, momentum and energy conservation require:

$$E_R = E_n \frac{4A \cos^2 \theta_{cm}}{(1 + A)^2}, \tag{2.21}$$

where E_R is the nuclear recoil energy, A is the target mass number, and θ_{cm} is the center-of-mass scattering angle [61]. For isotropic scattering in the center-of-mass frame, the average recoil energy is $\langle E_R \rangle = E_n A/(1 + A)^2$. Lighter nuclei therefore provide more efficient neutron moderation. The elastic scattering cross-section exhibits resonance structure at certain energies, particularly for medium and heavy nuclei, and generally decreases with increasing neutron energy above the MeV range [62].

Crucially, nuclear recoils from elastic neutron scattering are practically indistinguishable from WIMP-induced recoils based solely on recoil energy, making neutron backgrounds the most pernicious for dark-matter experiments. Discrimination strategies rely on multiple-scatter identification (neutrons can scatter multiple times, WIMPs typically scatter once) [63], vetoing systems, and statistical analysis of spatial and temporal distributions.

Above approximately 1 MeV, inelastic scattering $(n, n'\gamma)$ becomes increasingly probable. In this process, the neutron excites the target nucleus to a discrete energy level, which subsequently decays via gamma emission. The threshold energy depends on the excitation energy of nuclear levels and the target mass. For example, the first excited state of ^{12}C at 4.44 MeV can be populated by neutrons with $E_n > 4.8$ MeV [64]. The emitted photons contribute to the electromagnetic background.

At still higher energies (typically above 5−10 MeV), other reaction channels open, including $(n, 2n)$, (n, p), (n, α), and for fissile isotopes such as ^{235}U and ^{238}U, neutron-induced fission [62]. Fission reactions can release large amounts of energy ($\sim$ 200 MeV) in the form of fission fragments, neutrons, beta particles, and gamma rays, all of which contribute to backgrounds.

Fast neutron spectra and interaction cross-sections used in Monte Carlo simulations of dark-matter detectors are typically taken from evaluated nuclear data libraries such as ENDF/B-VIII.0 [62] or JENDL-4.0 [65], which compile experimental measurements and theoretical calculations for all relevant isotopes and energy ranges.

2.2.1.3 Neutrino interactions

Neutrinos interact only via the weak force, with extremely small cross-sections, typically below 10^{-44} cm^2 at MeV energies. However, in tonne-scale detectors operating for years, even these rare interactions become relevant.

Neutrinos can interact through elastic scattering on atomic electrons ($\nu e^- \to \nu e^-$) [66], producing electron recoils with energies up to $E_{e,\max} \approx 2E_\nu^2/(m_e c^2 + 2E_\nu)$ for $E_\nu \gg m_e c^2$. Solar neutrinos from *pp* fusion ($E_\nu < 420$ keV) and ^{8}B decay ($E_\nu < 15$ MeV) produce a continuous electron-recoil spectrum [67].

More importantly for sub-keV threshold detectors, coherent elastic neutrino-nucleus scattering (CEνNS) was predicted by Freedman [68] and first observed by the COHERENT collaboration in 2017 [69]. In this process, the neutrino scatters off the entire nucleus coherently, with a cross-section that scales as $\sigma_{\mathrm{CE}\nu\mathrm{NS}} \propto N^2$ where N is the neutron number. The differential cross-section is given by:

$$\frac{d\sigma}{dE_R} = \frac{G_F^2 M}{4\pi} \left(N - (1 - 4\sin^2\theta_W)Z\right)^2 F^2(E_R) \left(1 - \frac{ME_R}{2E_\nu^2}\right), \tag{2.22}$$

where G_F is the Fermi constant, M is the nuclear mass, θ_W is the weak mixing angle, and $F(E_R)$ is the nuclear form factor [70].

Solar (pp, ^{7}Be, ^{8}B), atmospheric ($E_\nu \sim$ GeV), and diffuse supernova neutrinos generate an irreducible nuclear-recoil spectrum in dark-matter detectors [71]. This "neutrino floor" represents a fundamental sensitivity limit for non-directional WIMP searches, occurring at cross-sections near 10^{-48} cm^2 for WIMP masses around 6 GeV/c^2 in xenon targets and somewhat higher for lighter or heavier WIMPs [72]. Directional detection strategies could in principle discriminate WIMP-induced recoils from the largely isotropic neutrino background [73].

2.2.1.4 Charged particle interactions and quenching

Charged particles such as electrons, muons, protons, alpha particles, and heavier ions lose energy primarily through ionization and atomic excitation as they traverse matter. The mean energy loss per unit path length is described by the Bethe-Bloch formula [74, 75]:

$$-\left\langle \frac{dE}{dx} \right\rangle = \frac{4\pi e^4 z^2 n}{m_e v^2} \left[\ln\left(\frac{2m_e v^2}{I}\right) - \ln(1-\beta^2) - \beta^2 \right], \tag{2.23}$$

where z is the projectile charge, v its velocity, n the electron density, and I the mean excitation energy of the medium. For electrons, radiative losses (bremsstrahlung) become important at high energies, with the critical energy (where ionization and radiation losses are equal) given approximately by $E_c \approx 610$ MeV$/Z$ [76].

For nuclear recoils and slow heavy ions, however, the energy deposition process is fundamentally different. A large fraction of the kinetic energy is dissipated through elastic collisions with nuclei in the lattice, producing phonons (lattice vibrations) that do not contribute to ionization or scintillation signals. Only the fraction of energy deposited in electronic excitation and ionization is detectable.

The **quenching factor** (QF), also called the relative scintillation efficiency or ionization efficiency depending on the measured quantity, quantifies this effect:

$$\mathrm{QF}(E_R) = \frac{L_{\mathrm{NR}}(E_R)}{L_{\mathrm{ER}}(E_R)}, \tag{2.24}$$

where L_{NR} and L_{ER} are the light or charge yields for nuclear and electron recoils of the same energy, respectively [77]. Typical values range from 0.1 to 0.3 for liquid noble gases, meaning that a 10 keV nuclear recoil produces the same signal as a 1–3 keV electron recoil.

The physical origin of quenching was first described by Lindhard and colleagues [78], who partitioned the recoil energy into electronic stopping (ν) and nuclear stopping ($1-\nu$):

$$\nu(E_R) = \frac{kg(\epsilon)}{1 + kg(\epsilon)}, \tag{2.25}$$

where $k \approx 0.133Z^{2/3}A^{-1/2}$ is a material-dependent parameter, $\epsilon = 11.5E_R Z^{-7/3}A^{-1}$ is a reduced energy, and $g(\epsilon) = 3\epsilon^{0.15} + 0.7\epsilon^{0.6} + \epsilon$ is the Lindhard function [78]. This model, originally developed for crystalline semiconductors, provides a semi-empirical framework that has been extended to liquid and gaseous targets.

In liquid noble gases (argon, xenon), the quenching factor has been measured experimentally using mono-energetic neutron beams and nuclear recoil sources [79–81]. The QF exhibits energy dependence, generally decreasing at lower recoil energies, and depends on the collection field strength due to electron-ion recombination effects [82, 83].

For gaseous detectors, quenching is generally less severe than in liquids. In gas-phase noble gases, Hitachi and colleagues [77] showed that the scintillation quenching factor depends on gas density, electric field, and recoil energy. For low-pressure gas TPCs like CYGNO, the longer mean free paths and different recombination dynamics lead to QF values closer to unity, potentially improving sensitivity to low-mass WIMPs [84].

The accurate measurement and modeling of quenching factors remains an active area of research, as uncertainties in QF directly propagate to uncertainties in reconstructed WIMP masses and interaction cross-sections [85]. Modern dark-matter experiments invest significant effort in calibrating their nuclear recoil response using neutron sources (e.g., AmBe, ^{252}Cf, D-D generators) and comparing results across different target materials and detector configurations [81, 86].

2.2.2 Cosmic rays

One of the most significant and unavoidable sources of background in underground dark matter searches originates from cosmic radiation. Primary cosmic rays, composed predominantly of protons (about 90%) and α particles (helium nuclei, about 9%), continuously impinge on the Earth's atmosphere with energies ranging from a few MeV up to and beyond 10^{20} eV. When these high-energy particles collide with nuclei in the upper atmosphere, they initiate a cascade of secondary particles, forming extensive air showers composed primarily of mesons (pions and kaons), photons, electrons, and muons, as well as atmospheric neutrinos generated from meson decay.

The hadronic component of these showers, comprising mainly charged pions and kaons, is efficiently absorbed within the first few metres of rock or dense material due to their strong interaction cross section. In contrast, muons, being minimum ionizing particles with a relatively long lifetime ($\tau_\mu \sim 2.2$ μs), can penetrate several kilometres underground, even through dense shielding. For this reason, muons represent a significant source of background in deep underground laboratories, as illustrated by the strong dependence of the muon flux on depth shown in Fig. 2.1.

Once underground, cosmic-ray muons can contribute to the background through several mechanisms. First, they produce secondary neutrons via inelastic scattering, spallation, and photo-nuclear interactions with the detector materials or surrounding rock. These neutrons, if not properly moderated and tagged, can mimic nuclear recoil signals and thus be indistinguishable from potential dark matter interactions. Second, muons can activate detector components through nuclear reactions, leading to the formation of long-lived radioactive isotopes such as ^{68}Ge and ^{49}V. These isotopes decay via β or β^+ emission, potentially producing background events in the energy region of interest.

To mitigate these effects, modern experiments employ active veto systems such as water Cherenkov detectors or liquid scintillator panels, instrumented with photomultiplier tubes (PMTs). These systems are capable of tagging more than 99.5% of through-going

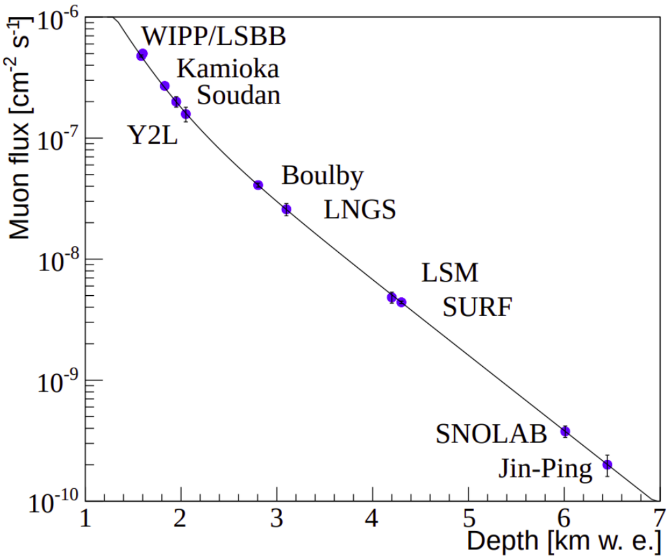

Figure 2.1: Muon flux as a function of depth, expressed in kilometers of water equivalent (km w.e.), for several underground laboratories hosting dark-matter experiments [87].

muons. However, muon-induced neutrons may be produced at significant distances from the detector, or be delayed with respect to the parent muon, making them difficult to associate with a specific muon tag. For this reason, passive shielding (often composed of hydrogen-rich materials like polyethylene) is employed in conjunction with veto systems, and timing cuts are implemented in the analysis to reject delayed coincidences.

2.2.3 External backgrounds

External backgrounds originate outside the detector assembly, in the laboratory environment that hosts the experiment. Even at great depth, where overburden rock suppresses the cosmic-ray flux by several orders of magnitude, the natural radioactivity of the surrounding cavern remains a major source of photons and neutrons that can mimic WIMP signals.

Natural γ rays come mainly from the decay chains of ^{232}Th, ^{238}U and ^{235}U, together with the long-lived isotope ^{40}K. Smaller contributions arise from anthropogenic or cosmogenic radionuclides such as ^{85}Kr, ^{137}Cs, ^{39}Ar, ^{110}Ag$^{\mathrm{m}}$ and ^{60}Co, which are often present in laboratory equipment and create a diffuse, almost isotropic flux capable of inducing electron-recoil backgrounds in the active volume [88]. Beta particles from these decays travel only a few millimetres in solids or liquids and are mostly absorbed on the spot, whereas the accompanying γ rays can escape and penetrate the detector.

Radiogenic neutrons are produced when α particles from the same decay chains trigger (α, n) reactions in light nuclei, yielding neutrons with energies up to about 10 MeV. Spontaneous fission of ^{238}U (and, to a lesser extent, ^{235}U) provides an additional source. Because neutrons interact chiefly through elastic scattering, they can traverse shielding materials and generate nuclear recoils that are practically indistinguishable from a WIMP signal.

Another concern is radon. ^{222}Rn, a noble gas in the ^{238}U series with a mean lifetime of 3.8 d, diffuses out of rocks, accumulates in cavern air and can enter the detector. Its charged progeny (^{218}Po, ^{214}Pb, and others) plate out on detector surfaces and add localised

α, β and γ activity unless rigorous mitigation measures (air recirculation, charcoal traps, nitrogen or argon purges) are in place [89].

Several techniques are used to suppress these backgrounds. First, passive γ shields of high-Z material (typically lead outside and ultra-clean copper inside) attenuate external photons; archaeological lead, recovered from ancient shipwrecks, is sometimes chosen to minimise the ^{210}Pb content thanks to its 22.3-yr half-life [90]. Second, hydrogen-rich neutron moderators such as water or polyethylene slow down fast neutrons via elastic scattering. The mean fractional energy loss per collision,

$$\frac{\Delta E}{E} = \frac{4A}{(1+A)^2}, \qquad A = \frac{M_{\text{target}}}{M_n},$$

is maximal for hydrogen ($A = 1$). About 13 cm of polyethylene reduce the radiogenic neutron flux by an order of magnitude [91]; adding boron or gadolinium enhances capture of the thermalised neutrons. Finally, active vetoes (water-Cherenkov tanks or liquid-scintillator panels instrumented with PMTs) surround the detector and tag muons with efficiencies above 99.5 %. The same systems detect neutron captures on Gd or B, providing a powerful handle to reject single-scatter nuclear-recoil candidates.

Sustained ventilation, inert-gas purges and cooled adsorption traps complete the strategy by keeping radon concentrations in the experimental hall and inside the detector at the lowest practical level.

2.2.4 Internal backgrounds

Internal backgrounds originate inside the experiment itself and are mainly due to the intrinsic radioactivity of detector materials, the target medium and the surrounding shielding. Unlike external radiation, many of the decays involved have very short ranges: an α emitted near or inside the active volume can deposit all its energy where it is produced, mimicking a nuclear recoil if only a fraction is observed.

Screening of construction materials. The first line of defence is a careful selection of radiopure components. Four complementary techniques are widely used to assay trace contaminants:

- *Neutron activation analysis* (NAA) is a non-destructive method applicable to solids and liquids. A sample is irradiated with neutrons and the subsequent γ emission is measured to infer primordial isotopes such as ^{238}U, ^{232}Th and ^{40}K. Sensitivities reach $10^{-2}\,\mu\mathrm{Bq\,kg^{-1}}$ with tens of grams of material and run times of a few weeks .

- *Inductively-coupled plasma mass spectrometry* (ICP-MS) is destructive: the solid is dissolved or a liquid sample is nebulised and fully ionised in a high-temperature argon plasma. The ion beam is analysed by mass, yielding isotope concentrations with sub-$\mu\mathrm{Bq\,kg^{-1}}$ sensitivity on milligram quantities in a matter of days [90].

- *Alpha spectrometry* measures the discrete α energies of surface contaminants. Because the α range is only a few tens of micrometres, the technique probes the outer layer of the sample; typical sensitivities are at the $\mathrm{mBq\,kg^{-1}}$ level with exposures of a few months.

- *Gamma spectrometry* with high-purity germanium (HPGe) detectors identifies characteristic γ lines from most long-lived radionuclides. It is non-destructive and suited to bulk solids but requires large samples and measuring times of weeks to months; activities down to 10–100 $\mu\mathrm{Bq\,kg^{-1}}$ can be reached underground . Although HPGe gamma spectrometry may have lower absolute sensitivity compared to some of the techniques listed above, it provides unique information on the composition of radioactive decay chains, including the ability to identify possible departures from secular equilibrium among daughter isotopes, which is essential for a complete characterisation of the radioactive content of detector materials.

Material purification. Where no sufficiently clean commercial alternative exists, raw materials are further treated. Metal parts are de-contaminated by chemical etching or electropolishing, which remove the outer layer where most surface impurities reside. High-purity crystals are obtained by zone refining or zone melting, in which a narrow molten region sweeps through the ingot and drags impurities to one end that is later discarded. For noble gases such as xenon and argon, cryogenic distillation columns separate chemically similar isotopes, reducing krypton (and the β emitter ^{85}Kr) or the cosmogenic isotope ^{39}Ar to the part-per-trillion level. To prevent cosmogenic activation, sensitive components are stored and machined underground whenever possible and their exposure to surface cosmic rays is minimised during transport.

Detector-level mitigation. After construction, a fiducial volume cut eliminates events occurring close to the vessel walls where most residual activity remains; this requires at least a two-dimensional, and ideally a full three-dimensional, position reconstruction. Residual electron-recoil events are statistically rejected by comparing the relative amounts of ionisation, scintillation and (where measured) phonon production, which differ for electrons and nuclei. The only nuclear-recoil background that cannot be shielded is due to neutrinos producing coherent elastic neutrino–nucleus scatters; this ultimate limitation is discussed in Section 2.2.5.

2.2.5 Neutrino background and the neutrino fog

As direct detection experiments push toward ever-lower cross sections and higher exposures, neutrinos become an increasingly relevant and ultimately irreducible background. This arises because neutrinos, though weakly interacting, can scatter coherently off atomic nuclei via the process of coherent elastic neutrino–nucleus scattering (CEνNS) [68]. In this regime, the wavelength of the incident neutrino is larger than the size of the nucleus, and the scattering amplitude adds coherently across all nucleons, enhancing the cross section with an approximate N^2 dependence. The resulting nuclear recoils are indistinguishable from those produced by WIMP interactions on an event-by-event basis, thus posing a significant challenge for future direct detection experiments.

Several astrophysical neutrino sources contribute to this background. The most prominent are solar neutrinos, particularly those from the *pp* chain and ^{8}B decays, which dominate at low energies and generate recoil spectra that overlap with the signal expected from light WIMPs. At higher energies, atmospheric neutrinos (produced in cosmic-ray interactions with the atmosphere) become relevant and can mimic the signatures of heavier WIMPs. A subdominant but non-negligible contribution comes from the diffuse supernova neutrino background (DSNB), the integrated flux from all past core-collapse supernovae. These sources together span a broad energy range and result in a continuous, direction-dependent recoil spectrum that current detectors are only beginning to probe.

The presence of this irreducible background leads to what is often called the "neutrino floor", a term introduced to indicate the sensitivity limit below which a potential WIMP signal becomes statistically degenerate with fluctuations in the neutrino-induced recoil spectrum [71]. However, this limit is not absolute: it depends on detector target, exposure, energy threshold, and systematic uncertainties in the neutrino flux and recoil modeling. A more accurate characterization of this limit has led to the concept of a "neutrino fog" [92], which refers to a statistical region where discovery is still possible but becomes progressively more difficult due to overlapping signal and background likelihoods.

From an experimental standpoint, the neutrino background is particularly challenging because it cannot be eliminated through passive shielding, as neutrinos penetrate the Earth with minimal interaction. This makes them fundamentally different from other backgrounds such as gammas, neutrons, or radon progeny, which can be suppressed with shielding materials, cleanliness protocols, or veto systems. Instead, new detection strategies must be developed to maintain discovery potential in the presence of the neutrino fog.

Several mitigation approaches are under study. The most promising is the use of directional detectors, which aim to reconstruct the recoil direction of the scattered nucleus. Since solar neutrinos arrive from a known direction (the Sun) while the WIMP "wind" is expected to come from the direction of the Cygnus constellation, a sufficiently precise angular reconstruction could allow separation of signal and background. This would require detectors with sub-millimeter spatial resolution and low-energy thresholds, which remains technically demanding but feasible in gaseous TPCs or nuclear emulsion-based detectors.

Other approaches rely on target complementarity: since different nuclear targets have different neutrino response functions, combining data from multiple detectors (e.g., xenon, argon, fluorine) could help disentangle a WIMP signal. In addition, improving the accuracy of solar and atmospheric neutrino flux models, or measuring them independently, would reduce systematic uncertainties and sharpen the statistical contrast between WIMP and neutrino-induced events.

2.3 Direct dark matter searches

Direct detection experiments aim to observe the scattering of dark matter particles, particularly WIMPs, off nuclei in terrestrial detectors. The fundamental principle underlying these searches is the elastic scattering process between a WIMP and a target nucleus, which produces a nuclear recoil that can be measured through various detection channels. The expected signal is extremely rare, making these experiments some of the most challenging endeavors in modern physics.

The search for direct evidence of dark matter has evolved significantly over the past decades, with increasingly sophisticated detector technologies pushing the sensitivity to ever-lower cross-sections. These experiments must contend with numerous backgrounds while searching for a signal that manifests as nuclear recoils with energies typically in the keV range. The current generation of experiments has achieved remarkable sensitivity, excluding large regions of the parameter space defined by WIMP mass and cross-section.

2.3.1 Current limits

The current landscape of direct detection experiments provides stringent constraints on the properties of WIMPs, particularly for spin-independent (SI) and spin-dependent (SD) interactions. Figure 2.2 shows the current status of SI limits on the WIMP-nucleon cross-section as a function of WIMP mass, based on the Standard Halo Model assumption and nuclear recoil searches.

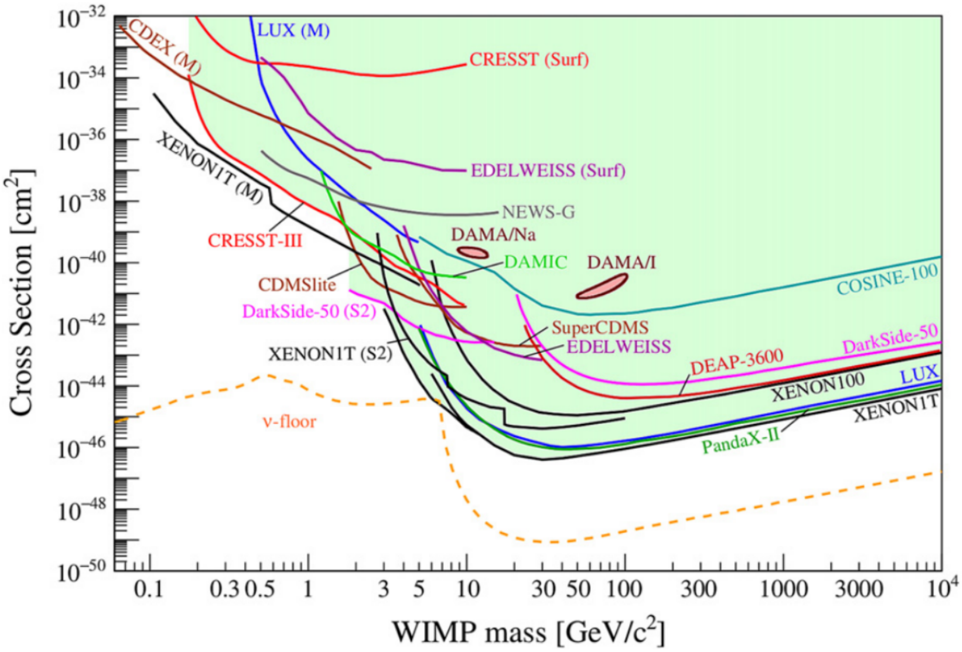

Figure 2.2: Current status of the SI limits on the cross section WIMP mass parameter space based on SHM assumption and nuclear recoils searches. The figure shows results from various experiments including XENON1T, LUX, PandaX, CRESST-III, SuperCDMS, and others. The shaded regions indicate excluded parameter space [87].

For spin-independent interactions, the most stringent constraints come from liquid xenon time projection chambers, particularly the XENON1T and LUX-ZEPLIN experiments. The best current limit reaches approximately 3×10^{-47} cm^2 at WIMP masses around 100 GeV [93]. This remarkable sensitivity results from the combination of large target masses, excellent background rejection capabilities, and long exposure times achieved by these experiments. The shape of the exclusion curves reflects the kinematics of WIMP-nucleus scattering: the limits are strongest when the WIMP mass is comparable to the target nucleus mass, where the energy transfer in collisions is most efficient.

At higher WIMP masses, the limits rise due to the decreasing number density of WIMPs for a fixed local dark matter density, which goes as $1/m_\chi$. At lower masses, the limits rise more steeply because the nuclear recoils become softer and eventually fall below the energy threshold of the detectors. This threshold dependence explains why different detector technologies dominate different mass ranges: liquid noble gas detectors excel at masses above a few GeV, while cryogenic bolometers with their ultra-low thresholds extend sensitivity down to sub-GeV masses.

An interesting tension exists in the field due to the DAMA/LIBRA experiment, which has reported an annual modulation signal consistent with WIMP interactions over many years of data taking, with a total exposure of 2.86 ton×years and a significance of 13.7σ in the 2-6 keV energy range [94]. However, this result appears inconsistent with the null results from other experiments that have already explored regions with lower cross-sections. Several experiments using the same NaI(Tl) target material, including ANAIS-112 [95], COSINE-100 [96], SABRE [97], and COSINUS [98], are attempting to verify or refute the

DAMA claim. Recent 90% confidence level upper limits from COSINE-100 and ANAIS-112 already exclude the parameter space favored by DAMA under standard assumptions, deepening this puzzle.

For masses above approximately 3 GeV, the field is dominated by dual-phase liquid noble gas TPCs, primarily xenon-based detectors. These experiments benefit from the high density of the target, excellent scintillation properties, and the ability to scale to multi-ton masses relatively efficiently. The combination of primary scintillation and ionization signals in these detectors provides powerful discrimination between nuclear recoils and electron recoils, which is crucial for background rejection.

At lower masses, around $\mathcal{O}(1)$ GeV and below, cryogenic bolometers achieve the best sensitivity due to their exceptionally low energy thresholds, reaching down to $\mathcal{O}(10)$ eV in some cases. Experiments like CRESST-III [99] and SuperCDMS [100] utilize light target nuclei, which are better matched to low-mass WIMPs for kinematic reasons. Future directional detectors like CYGNO aim to probe the region around $\mathcal{O}(1)$ GeV and potentially down to $\sim$0.3 GeV with hydrogen-enriched targets.

The spin-dependent sector shows weaker constraints, typically about five orders of magnitude less sensitive than the SI case, as illustrated in Fig. 2.3. This reduced sensitivity arises from two main factors: the limited availability of nuclei with unpaired spins, and the absence of the coherent enhancement factor A^2 (where A is the atomic mass number) that amplifies SI cross-sections for heavy nuclei. For SD WIMP-proton interactions, the PICO collaboration [101] provides the leading constraints thanks to their large exposures with dense superheated liquids in bubble chambers and high SD sensitivity due to the high fluorine content in their target. For SD WIMP-neutron interactions, the LUX experiment [102] sets the best limits, benefiting from xenon's natural isotope ^{129}Xe, which has a large SD coupling to neutrons, and the high density that enables large exposures.

Several recent experiments have reported low-energy excesses that initially generated significant interest as potential dark matter signals. These include anomalous events observed by XENON1T [103], DAMIC [104], SuperCDMS [100], CRESST-III [99], and EDELWEISS [105]. However, with increased exposure, improved analyses, and better understanding of backgrounds, all of these excesses have been subsequently excluded as dark matter signals and attributed to previously unaccounted background sources. This progression underscores the importance of patience and thorough background characterization in direct detection experiments.

2.3.2 Directional dark matter search

Directional detection represents a qualitatively different approach to searching for dark matter, one that promises to overcome the neutrino floor and provide definitive evidence for a galactic dark matter signal. The key insight is that WIMP-induced recoils should exhibit a strong directional bias in galactic coordinates, pointing predominantly away from the direction of the Solar System's motion through the dark matter halo. This angular anisotropy provides a smoking-gun signature that cannot be mimicked by any known background, including neutrinos.

2.3.2.1 Fundamental principles

The directional dependence of WIMP scattering arises from the motion of our Solar System through the Galactic dark matter halo. As discussed in Section 2.1.1, the Earth orbits

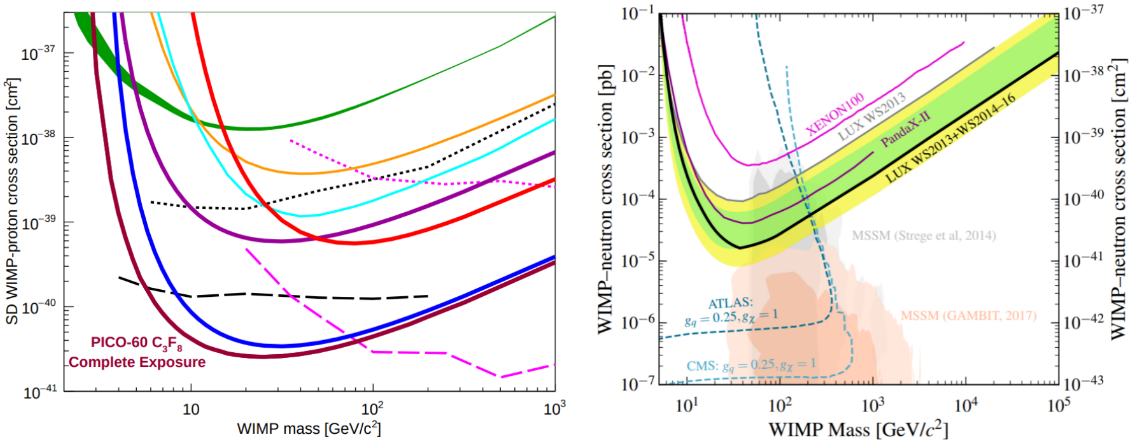

Figure 2.3: Summary of the current status of spin-dependent (SD) limits in the WIMP mass–cross section parameter space from nuclear-recoil searches. Left: SD WIMP–proton cross section limits from PICO-60 (blue), PICO-2L (purple), PICASSO (green), SIMPLE (orange), and PandaX (cyan) [101]. Right: SD WIMP–neutron cross section limits from nuclear-recoil experiments [106].

the Sun at approximately 30 km/s, while the Solar System moves through the Galaxy at roughly 220 km/s, resulting in an apparent "WIMP wind" from the direction of the constellation Cygnus. In galactic coordinates (where l denotes the galactic longitude and b the galactic latitude), this direction corresponds approximately to $(l, b) \sim (90°, 0°)$, i.e., toward the galactic plane in the direction of galactic rotation.

When a WIMP elastically scatters off a target nucleus, the recoil direction is strongly correlated with the WIMP's velocity vector. For a WIMP traveling with velocity $\vec{v}$ relative to the detector and scattering off a nucleus of mass m_A, the relationship between the recoil angle θ_r and the recoil energy E_r is given by:

$$\cos\theta_r = \frac{v_{\min}}{v} = \sqrt{\frac{m_A E_r}{2\mu^2 v^2}} \tag{2.26}$$

where the WIMP-nucleus reduced mass is:

$$\mu = \frac{m_\chi m_A}{m_\chi + m_A} \tag{2.27}$$

and the minimum WIMP velocity required to produce a recoil of energy E_r is:

$$v_{\min} = \sqrt{\frac{m_A E_r}{2\mu^2}} \tag{2.28}$$

This equation shows that the recoil angle is restricted to the range 0° to 90° with respect to the WIMP velocity direction.

The angular distribution of WIMP-induced recoils exhibits a dipole-like pattern in galactic coordinates, with most recoils pointing away from Cygnus. At higher recoil energies, this dipole becomes stronger (with θ_r closer to 0°), though the event rate decreases. At lower energies and for certain combinations of WIMP mass, target mass, and reduced mass, the distribution can develop a ring-like feature when $m_A E_r/(2\mu^2 v^2) \to 0$, causing $\theta_r \to 90°$. This produces a maximum rate in a ring around the WIMP arrival direction. While this ring feature is more challenging to detect than a dipole, it can serve as a secondary WIMP signature.

The daily motion of the Earth causes the WIMP velocity vector in the laboratory frame to vary throughout the day, and the annual motion around the Sun causes it to vary throughout the year. This leads to an aberration pattern in the angular distribution between the minimum and maximum of the velocity distribution. However, detecting this aberration requires accumulating a large number of events and is therefore challenging.

Figure 2.4 illustrates the stark contrast between the directional distributions expected from WIMPs and from solar neutrinos in galactic coordinates. The WIMP signal shows a strong peak toward Cygnus, while the neutrino background traces the path of the ecliptic throughout the year, with essentially no overlap between the two distributions.

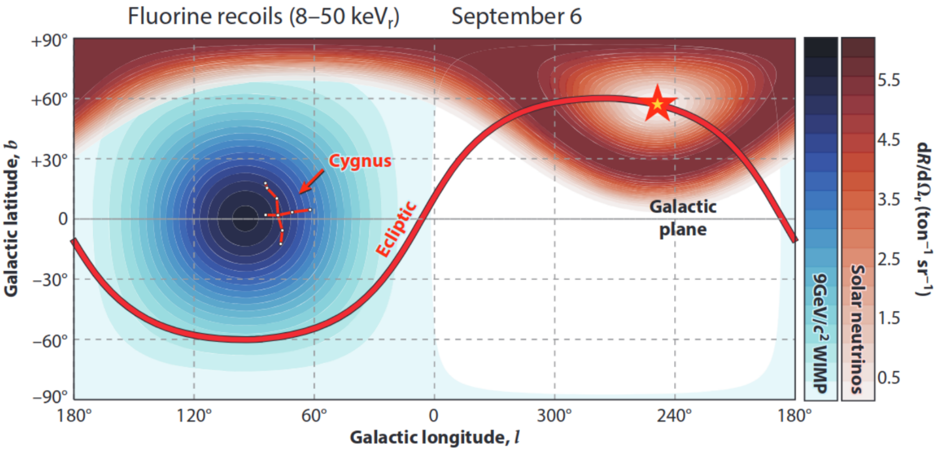

Figure 2.4: Directional event rates from a 9 GeV WIMP (blue) and solar neutrinos (red) displayed in galactic coordinates (l, b). The red line indicates the path of the ecliptic, showing the very low superposition expected between the two distributions throughout the year. The WIMP signal peaks strongly toward the Cygnus constellation, while the solar neutrino background follows the Sun's apparent motion [107].

2.3.2.2 Advantages of directional detection

The directional approach offers several compelling advantages over conventional non-directional searches. First and foremost, directional information provides much stronger background discrimination. Internal and external backgrounds in a terrestrial detector have angular distributions that are approximately isotropic when viewed in galactic coordinates, thanks to the Earth's rotation and axial tilt, which average out local anisotropies. Crucially, no known background can mimic the WIMP signal's strong directionality toward Cygnus.

This powerful discrimination capability means that directional detectors can set more stringent exclusion limits than non-directional detectors with the same exposure. Moreover, even with a relatively small number of events and reasonable background contamination, directional detectors can claim a positive discovery if they observe the characteristic angular anisotropy, provided they achieve directional capabilities at the level of approximately 30° resolution.

The only significant directional background comes from coherent elastic neutrino-nucleus scattering (CEνNS) from solar neutrinos, which point back toward the Sun. However, this background is easily distinguished from WIMPs because the direction to the Sun and the direction to Cygnus never overlap throughout the year. By excluding events from the solar direction, directional detectors can effectively eliminate this background on an event-by-event basis, something that is impossible for non-directional experiments which must rely on improved knowledge of neutrino fluxes, multiple target materials, and large statistics.

To fully exploit these advantages and overcome the neutrino floor, directional detectors must meet certain technical requirements [73, 108, 109]. These include: temporal resolution better than a few hours (to track the Sun's position), energy resolution better than 20%, head-tail recognition efficiency greater than 75%, and angular resolution better than 30°. Meeting these requirements ensures that directional detectors maintain steep discovery slopes similar to background-free scenarios even at very large exposures where conventional detectors are limited by neutrino backgrounds.

The number of events required for a discovery depends on several factors including the target material, angular resolution, head-tail recognition capability, effective WIMP mass, and most crucially, the energy threshold. Background levels are less critical for directional detectors due to their powerful ability to discriminate isotropic events. Head-tail recognition, the ability to distinguish not just the axis but also the sense of the recoil direction, has a major impact on discovery potential. Without full vectorial information, the dipole feature is mirrored across hemispheres, significantly reducing the discrimination power against a flat background.

Simulations for detectors with excellent characteristics (perfect head-tail recognition, 3D readout, 5 keV threshold, zero background) show that only 5 WIMP events would be needed for a 3σ discovery at 5 GeV mass, increasing to about 30 events at 1000 GeV mass [110]. The number of required events increases with background level but remains relatively independent of the background's energy distribution if direction and sense are well reconstructed. This fundamental difference, the ability to positively identify a dark matter signal and establish its galactic origin, makes directional detection uniquely powerful and justifies the technical challenges involved.

Beyond discovery, directional detection offers unparalleled capabilities for characterizing dark matter properties. The free parameters in WIMP models that can be constrained include both particle properties (WIMP mass and nucleon interaction cross-section) and astrophysical properties (velocity distribution and halo structure). The Standard Halo Model is a simplification of the real dark matter halo, and simulations with different assumptions about baryonic and non-baryonic matter content show various density profiles as a function of galactic radius, directly influencing the velocity distribution [39, 41].

Directional detectors can measure the velocity structure of dark matter through the angular distribution of recoils. The three-dimensional nature of directional information provides theoretical access to the complete velocity distribution function, which is impossible for detectors measuring only energy spectra, since the recoil spectrum depends only on the speed distribution, not the full velocity vector [52, 111]. This means directional measurements can constrain properties of the Galactic dark matter halo without assuming knowledge of the dark matter particle properties. Once the velocity distribution is better characterized through complementary astrophysical measurements and dark matter detections, directional measurements can then determine particle physics parameters with greater accuracy. Although the performance of any real detector will be imperfect and experimental conditions may not be ideal, the discriminating power of directional information is so compelling that it justifies the significant experimental challenges involved. Quantitative simulations suggest that even with realistic detector assumptions, directional measurements can substantially improve constraints on both astrophysical and particle physics parameters compared to non-directional approaches [110, 112, 113].

2.3.2.3 Directional detection technologies

Achieving directional sensitivity presents significant technical challenges that require careful trade-offs between conflicting requirements: low energy thresholds, good angular resolution, and high exposures. The key challenge is that nuclear recoil tracks at low energies are extremely short (sub-micron in solids and liquids, but $\mathcal{O}(1)$ mm in gases). This fundamental difference explains why gaseous targets dominate directional dark matter searches despite their much lower density.

The primary trade-off is between density and track length. Dense targets (liquids and solids) enable large masses and exposures more easily, but their short recoil tracks make precise directional measurements extremely difficult. Gaseous targets have much lower density, reducing the exposed mass for a given volume, but their longer tracks enable much better direction and sense reconstruction. Operating at lower pressure improves directional capabilities further but reduces the target mass even more, creating a challenging optimization problem.

Nuclear emulsions Nuclear emulsions represent an approach to directional detection in a dense medium. These consist of silver halide crystals dispersed in a gelatin binder, with sub-micron grain sizes enabling detection of very short nuclear recoil tracks. When a charged particle traverses the emulsion, it creates electron-hole pairs in the crystals. Chemical development renders these grains visible as aligned silver grains along the particle track, which can be reconstructed using optical microscopy to determine position, inclination, and grain density patterns.

The NEWSdm experiment [114] employs nuclear emulsion films with silver halide crystals in a polymer matrix. The target composition includes light elements (H 1.6%, C 10.1%, N 2.7%, O 7.4%, S 0.3%) and heavy elements (Br 32.0%, Ag 44.0%, I 1.9%) with an overall density of 3.2 g/cm^3. This composition provides good sensitivity to both light and heavy WIMP masses [115]. The sensitive volume is surrounded by shielding to reduce external backgrounds.

NEWSdm utilizes Nano Imaging Tracker (NIT) technology [116], which employs nanometric grains with diameters around $\mathcal{O}(10)$ nm, approximately ten times smaller than conventional emulsions. Nuclear recoils generate clusters of nanometric silver grains, and 3D tracks are reconstructed using optical microscopy with automated scanning systems. The primary scanning with optical microscopes proceeds at approximately 200 cm^2/hour, identifying nuclear recoil candidates. The intrinsic spatial resolution is about 200 nm, and discrimination is achieved through track ellipticity: single grains from thermal excitation appear spherical, while real tracks show elliptical shapes.

Further analysis employs light polarizers exploiting plasmon resonance [117], which modifies the intensity and wavelength of light reflected from metallic materials depending on polarization and illumination angles. Rotating the polarization provides information about track substructures beyond optical resolution, discriminating single grains (noise) from multiple grains (signal). This technique achieves an effective spatial resolution of approximately 5 nm [118].

The experimental setup is mounted on an equatorial telescope to compensate for Earth's rotation, necessary because emulsions are not time-sensitive and must maintain fixed orientation relative to the apparent WIMP flux. The current setup uses a 10 g target at

LNGS (underground) with fixed support, aimed at testing production, calibration, analysis techniques, and measuring ambient backgrounds. Passive shielding includes 10 cm of lead for ambient gammas and 40 cm of polyethylene for neutrons. Geant4 simulations indicate negligible contributions from external backgrounds.

The projected sensitivity, assuming 100 background events, reaches approximately 10^{-42} cm^2 at 100 GeV WIMP mass with 100 kg×year exposure, assuming a 30 nm detection threshold with 10 nm resolution. Reaching the neutrino floor would require an exposure of 10 ton×years in a zero-background scenario [118].

Gaseous time projection chambers Time projection chambers (TPCs) filled with low-pressure gas remain the most developed and promising technology for directional dark matter detection. The fundamental advantages of gaseous targets (longer recoil tracks enabling better topological identification) have driven the development of numerous TPC-based experiments worldwide.

A TPC consists of a chamber filled with the target gas, with a uniform electric field established between an anode and cathode at opposite ends. A field cage, typically consisting of a series of conducting rings or strips connected by a resistor chain, ensures field uniformity throughout the drift region [119–121]. When a charged particle ionizes the gas, the electric field prevents primary ionization electrons from recombining and drifts them toward the anodic plane while ions drift toward the cathode. A charge amplification stage multiplies the produced charges, and signals are read out either from the charge directly or from secondary scintillation light.

The low energy required to produce an electron-ion pair (a few tens of eV) combined with high charge gains available from modern amplification structures (approaching $\mathcal{O}(10^6)$) enables very low energy thresholds. Track reconstruction can be one-, two-, or three-dimensional depending on the readout method. Full 3D reconstruction typically projects the 2D electron cloud onto a pixelated readout plane, with temporal sampling recovering the 3D track shape. Resolution in x-y depends on readout segmentation, while resolution along the drift direction (z) depends on sampling frequency. Alternatively, 2D readout can be combined with other technologies (CCD/CMOS for x-y projection, PMTs for timing) to recover the z projection and achieve 3D tracking.

These tracking capabilities enable powerful particle identification through measurement of the stopping power (dE/dx) directly from energy deposition along the track. The stopping power changes with decreasing energy along the particle's path, creating an asymmetric energy deposition pattern. This produces the "head-tail" effect: low-energy nuclear recoils deposit more energy at the beginning of their tracks, while electron recoils deposit more at the end. Measuring this head-tail asymmetry identifies not just the axis but the sense (full directional vector) of the track.

With 3D capabilities and highly granular readout (much finer than track lengths), TPCs can achieve excellent angular resolution and high head-tail recognition efficiency. Combined with low thresholds, good background rejection, and the inherent directionality, TPCs are optimal candidates for directional dark matter detection.

Negative ion drift A significant limitation of conventional TPCs is the diffusion of primary electrons during drift, which degrades spatial resolution. The negative ion drift (NID) technique [122, 123] solves this problem by using anions as charge carriers instead of electrons. A small quantity of an electronegative dopant is added to the gas mixture.

Atoms or molecules of the dopant capture primary ionization electrons near the interaction point (within $\mathcal{O}(100)$ μm), and the resulting anions transport the charge toward the anode. In the high field region near the anode, the excess electrons are stripped off, allowing normal electronic amplification.

NID offers two major advantages. First, it dramatically reduces diffusion. Electrons, being very light, have their direction randomized in collisions with minimal energy loss, so energy from the drift field dominates over thermal energy. Anions, having mass similar to gas atoms, lose a large fraction of their energy in each collision, preventing momentum randomization and causing efficient thermalization. Since the diffusion coefficient scales as $\sqrt{E_{\text{particle}}}$, anions diffuse much less than electrons, significantly reducing track shape degradation after long drift distances.

Second, NID enables absolute z-position measurement. The electron attachment process forms multiple negative ion species with different masses [124]. One species carries the majority of the charge (major carrier), while others constitute minority carriers. Since ionic mobility depends on mass, measuring the arrival time difference between species determines the absolute z position with precision around $\mathcal{O}(1)$ mm:

$$z = \frac{v_m v_M}{v_m + v_M} \Delta T \tag{2.29}$$

where v_m and v_M are the velocities of minority and major carriers respectively, and ΔT is their arrival time difference. An alternative method exploits the dependence of diffusion on drift distance: analyzing track shapes allows recovery of the third coordinate with resolution of a few cm. This complete 3D reconstruction capability enables fiducialization of the sensitive volume, an important background reduction strategy.

Gas choice and scalability The flexibility in gas choice is another advantage of TPC technology. A wide range of options exists for light and heavy elements, and spin-odd nuclei are available, providing enhanced sensitivity for both SI and SD couplings over a broad mass range. The scalability of TPC designs to very large volumes, with only one side requiring instrumentation (amplification and readout), offers favorable cost-to-volume ratios. This helps overcome the inherent limitation of low target density in gaseous detectors.

Major TPC experiments Several major experiments have pioneered directional detection with gaseous TPCs. The DRIFT experiment [125] operated dual 1 m^3 TPCs at Boulby Underground Laboratory using Multi-Wire Proportional Counters (MWPC) for amplification and readout. With a CS_2:CF_4:O_2 gas mixture at 30:10:1 Torr, DRIFT demonstrated head-tail measurements for nuclear recoils down to 38 keV$_{nr}$[1] using a ^{252}Cf neutron source [126]. Operating in NID mode with CS_2^- ions as charge carriers reduced diffusion and improved tracking performance, while O_2 introduced minority carriers enabling z-position measurement [127]. With a 0.803 m^3 fiducial volume, plastic shielding for neutron moderation, and an alpha-tagging system to reject radon backgrounds, DRIFT-IId achieved essentially background-free operation and set the best SD WIMP-proton limit from directional detectors: 0.28 pb at 100 GeV [128].

---

[1] Throughout this chapter, keV$_{nr}$ denotes the nuclear-recoil equivalent energy, i.e. the kinetic energy of a recoiling nucleus, while keV$_{ee}$ denotes the electron-equivalent energy, i.e. the energy that would produce the same detector signal if deposited by an electron. The two scales are related through the energy-dependent quenching factor.

The MIMAC experiment [129] employs dual TPCs with pixelated Micromegas at Modane Underground Laboratory. Using CF_4 + 28% CHF_3 + 2% C_4H_{10} at 50 mbar, MIMAC achieves a competitive 2 keV_{ee} threshold with 200 μm pixel width. The 50 MHz strip readout with 424 μm effective pitch provides x-y coordinates as a function of time, converted to a third spatial coordinate using known drift velocity [130]. With a dynamic range up to 62 keV_{ee}, MIMAC demonstrated excellent ER/NR discrimination with rejection power of 10^5 and NR efficiency of $86.49 \pm 0.17\%$ above 2 keV_{ee} using a Boosted Decision Tree algorithm [131]. The experiment has measured radon progeny nuclear recoils [132] and achieved 10°–20° angular resolution in ion beam measurements [133]. Cathode signal analysis enables z-position determination through correlation of anode-cathode timing differences with event distance from the grid [134], allowing volume fiducialization. The COMIMAC facility at LPSC Grenoble [135] provides desktop ion and electron beams for calibrating energy and measuring quenching factors for various gas mixtures [28, 136–138], including preliminary measurements for CYGNO gas mixtures.

The NEWAGE experiment [139] operates micro-TPCs filled with CF_4 at 100 mbar at Kamioka Underground Laboratory. The detector uses Gas Electron Multipliers (GEMs) and low-radioactivity μ-PIC readout planes with additional amplification. The μ-PIC, developed specifically to reduce surface radioactive contamination using materials with 100 times lower U/Th concentrations [140], performs identically to standard μ-PIC [141]. With 768×768 pixels at 400 μm pitch and orthogonally installed anode and cathode strips, signals are recorded with 100 MHz flash-ADC to measure x-y plane charge. Time-over-threshold for each strip enables 3D track reconstruction [142]. The detector achieves ER/NR discrimination, axial direction determination, head-tail recognition, and total energy measurement through integrated charge. With a 50 keV_{ee} threshold, 40° angular resolution [143], gamma rejection of $1.3^{+3.0}_{-1.1} \times 10^{-6}$ (50-60 keV range), and 20% NR efficiency [144], NEWAGE set a 90% CL SD WIMP-proton limit of 25.7 pb at 150 GeV mass from 318 live-days using forward-backward asymmetry in galactic coordinates [145].

The DMTPC experiment [146] developed TPCs with external optical readout (CCD, PMT) and charge readout using CF_4 at 30-100 Torr. Closely-spaced ground mesh and anode planes (0.6-1 mm) with high applied fields create proportional multiplication of primary electrons and secondary scintillation light emission. Light sensors (CCD + PMT) installed on the opposite side from the amplification region minimize target gas contamination. Total light measures event energy, while pixelated light sensors provide 2D track shapes. PMT timing and charge readout enable attempted 3D reconstruction [147]. Integrated charge on ground/anode planes provides independent energy measurement [148]. Initial prototypes operated at MIT, then underground at WIPP, with a 10-liter detector setting initial SD WIMP-proton cross-section limits [149]. DMTPC made the first measurements of recoil directionality with approximately 75% head-tail efficiency at 200 keV [150], though the collaboration has ceased operations.

The D3 experiment [151] focused on highly segmented charge readout for small volume TPCs using ATLAS FE-I3 to FE-I4b chips [152, 153] with 50×400 μm and 50×250 μm pixels. Each pixel incorporates an integrating amplifier, discriminator, shaper, and digital control. Double-GEM stacks provide gains around 10^4 with low intrinsic electronic noise, enabling stable operation with nearly 100% single-electron efficiency. A 4.5 cm drift prototype with He:CO_2 or Ar:CO_2 at atmospheric pressure achieved single-point resolutions of $\sigma_x = (197 \pm 11)$ μm and $\sigma_y = (142 \pm 9)$ μm [152] with approximately 1° angular resolution for alpha tracks. A 15 cm drift prototype demonstrated 1-2 cm accuracy for absolute position measurement along drift direction by studying diffusion profiles with a ^{210}Po source at various positions [153]. Development continues toward CYGNUS-HD, a approximately 40-liter detector with a 50 cm drift back-to-back configuration with shared cathode and 20×20 cm^2 readout planes using CERN Micromegas with strip charge readout, aiming toward meter-cube scale experiments [73, 109].

The CYGNO experiment [154] represents the next generation of directional detectors, employing He:CF$_4$ 60:40 at atmospheric pressure with triple-GEM amplification and optical readout combining sCMOS and PMT signals for 3D track reconstruction. Chapter 3 provides a detailed description of the CYGNO experiment and its future prospects.

The CYGNUS proto-collaboration Recognizing the power of directional detection, the international community has formed the CYGNUS proto-collaboration [107] to unite worldwide efforts in directional dark matter research for optimal operation of large-scale gaseous TPCs. CYGNUS proposes a multi-site directional dark matter and neutrino observatory at ton-scale [73]. Current R&D among CYGNUS collaborators focuses on: achieving approximately $\mathcal{O}(1)$ keV$_{ee}$ thresholds with directionality, complete background rejection, expanding sensitive volumes to 1000 m^3, optimizing Micro-Pattern Gaseous Detector (MPGD) amplification technology, optimizing readout technology (charge with MWPCs or optical with PMTs/CCDs/CMOS), and optimizing gas mixtures through electronic and negative ionic drift studies. A feasibility study [73] simulated CYGNUS performance assuming negative ion operation with SF$_6$ and charge readout. The current proposal uses He + SF$_6$ mixtures in atmospheric pressure TPCs. Construction objectives include: first, a approximately $\mathcal{O}(100)$ m^3 detector competitive on SD WIMP-proton cross-sections and capable of solar neutrino studies; and ultimately, approximately $\mathcal{O}(10^5)$ m^3 for dark matter astronomy and geoneutrino measurements [109]. The directional detection approach represents a paradigm shift in dark matter searches, offering the potential to definitively establish the galactic origin of any detected signal and characterize both particle and astrophysical properties with unprecedented precision. The technical challenges are substantial, but the physics rewards (including the ability to overcome the neutrino floor and achieve positive discovery rather than mere exclusion) make this one of the most exciting frontiers in experimental dark matter research. An overview of the projected sensitivity of directional detectors is presented in Chapter 3.

Chapter 3

The CYGNO project

The CYGNO experiment [154] aims at developing a gaseous Time Projection Chamber (TPC) [155, 156] with an optical readout for rare events searches. The CYGNO detector uses a mixture of helium and carbon tetrafluoride at atmospheric pressure as the working gas, while charge amplification is achieved with Gas Electron Multipliers (GEMs) [157]. Over the years, several prototypes of increasing size have been constructed and tested to evaluate the detector's performance and refine the technique. The ultimate goal is the construction of a large-scale detector, with an active volume of tens of cubic meters, to be installed underground. Such an apparatus would allow directional DM searches and solar neutrino spectroscopy.

The CYGNO Collaboration currently includes around 60 researchers from Italy, Portugal, Brazil, and the United Kingdom. In addition, CYGNO takes part in the CYGNUS proto-collaboration, a global initiative uniting several research groups. CYGNUS aims at designing and operating a distributed observatory for directional recoil measurements, capable of investigating the dark matter hypothesis beyond the neutrino fog and detecting neutrinos from the Sun and supernovae at the ton scale [73].

The next sections provide an overview of the design and working principles of CYGNO detectors, focusing on their main components: charge amplification, optical readout, and gas mixture. The development of successive prototypes and the experiment's long-term outlook are also discussed.

3.1 Experimental approach

The CYGNO detection method relies on a gaseous TPC filled with a He:CF_4 mixture in a 60:40 ratio, operating at atmospheric pressure and room temperature. A three-GEM stack is employed to achieve both charge amplification and photon production. The optical readout system combines scientific CMOS cameras and photomultiplier tubes (PMTs) for event detection.

The TPC is a well-established detector concept in particle physics, used across a wide range of energy scales to reconstruct charged particle tracks with high precision. Its operating principle is illustrated in Figure 3.1, which shows the schematic of a CYGNO-type detector. A TPC consists of a volume filled with a gas or liquid medium where, as a charged particle traverses, it ionizes the medium, producing electron–ion pairs.

When an ionizing particle crosses the active volume, electrons and ions are produced and drift in opposite directions under the influence of the electric field established between the cathode and anode. Electrons move toward the anode, where they undergo acceleration

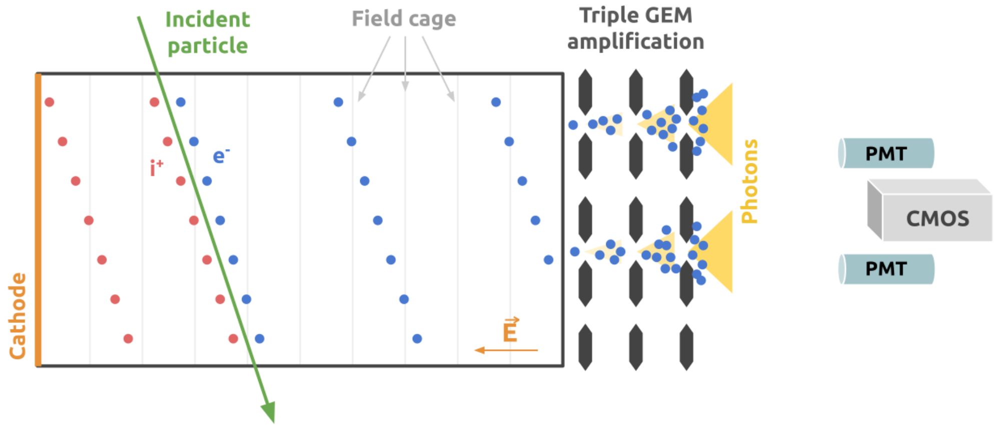

Figure 3.1: Schematic representation of the working principle of a gaseous Time Projection Chamber. Following an ionizing event, the freed electrons drift under an electric field toward the amplification region, where they are multiplied and finally detected. In the CYGNO setup, this process takes place through a stack of GEMs, while the resulting signals are read by CMOS cameras and PMTs [158].

and trigger an avalanche process that amplifies the initial signal. This amplification can be realized through different micro-structured devices collectively known as micro-pattern gas detectors (MPGDs). These detectors feature sub-millimeter amplification structures capable of providing high spatial resolution and rate capability. Among the main MPGD technologies are GEMs, micro-strips, and MicroMegas [61, 159]. In CYGNO, the electron multiplication stage is achieved using a triple-GEM configuration [160].

Depending on the detection strategy, both the electrical charge and the light generated in the amplification stage can be recorded. In CYGNO, the He:CF_4 mixture emits scintillation photons during the avalanche process. These photons are simultaneously captured by CMOS cameras, providing fine-grained images of the event, and by PMTs, which deliver precise timing information. The combination of these two complementary signals allows reconstruction of the three-dimensional topology of the ionization track. From this, it is possible to identify the type of particle, determine its incoming direction, and effectively suppress background events.

The CYGNO technique thus shares the core principles of conventional gaseous TPCs used in dark matter experiments but introduces several innovative aspects, such as the use of optical readout and the optimization of the gas mixture for directional detection.

1. **Gas mixture and operation at atmospheric pressure.** The chosen He:CF_4 (60:40) gas mixture allows simultaneous sensitivity to both spin-independent (SI) and spin-dependent (SD) dark matter interactions. The SD channel is accessible thanks to the high fluorine content and the presence of an unpaired proton in the fluorine nucleus. Helium, on the other hand, enhances sensitivity to low-mass WIMPs (of order $\mathcal{O}(\text{GeV})$) due to its favorable kinematics, while CF_4 contributes to visible scintillation light emission, enabling the use of high-resolution CMOS cameras. Operating the TPC with this mixture at atmospheric pressure significantly increases the ratio of active volume to target mass compared to conventional directional dark matter gaseous TPCs, thus improving sensitivity to rare interactions. The selected pressure and gas ratio result in a density close to that of air, which, unlike in liquid-

phase detectors, allows particles to travel over much longer paths. This feature provides accurate tracking and directional reconstruction capabilities even for events at the keV energy scale. Maintaining the TPC at atmospheric pressure simplifies the mechanical design, increases the active-to-mass ratio, and enhances the sensitivity to low-energy signals. The gas density (similar to that of air) enables the observation of extended tracks, a key factor for reconstructing directionality down to a few keV.

2. **GEM-based charge multiplication.** Charge amplification in CYGNO is achieved using a stack of three Gas Electron Multipliers (GEMs). These devices can provide large and stable gains, reaching up to $\mathcal{O}(10^6)$ when combined in cascade [159, 161]. Moreover, GEMs have a fine granularity (around $\mathcal{O}(10^2)$ μm) which matches perfectly with the spatial resolution of CMOS sensors. Their large-area scalability and self-supporting geometry, which does not require a separate electron collection plane, also make them ideal for optical readout, since photons emitted at the GEM surface can freely reach the sensors.

3. **Optical readout system.** CYGNO employs a hybrid optical detection system consisting of CMOS sensors and photomultiplier tubes (PMTs). The CMOS cameras provide detailed two-dimensional images with a spatial resolution of about $\mathcal{O}(150)$ μm, enabling the extraction of topological and directional information from the projected ionization tracks. PMTs, on the other hand, record the scintillation light with excellent time resolution, providing information on the longitudinal position of the event along the drift axis. Combining the spatial data from CMOS sensors (XY) with the temporal profile from PMTs (ΔZ) allows for full 3D event reconstruction [162]. Since the two systems operate independently, dual and cross-checked energy measurements are possible, potentially improving the overall energy resolution.

4. **Track topology and particle identification.** Different particle types produce distinct track shapes: α-particles and nuclear recoils create short, straight, and dense tracks, whereas electron recoils generate longer, more diffuse paths ranging from a few millimeters for keV-scale events to several centimeters above 100 keV. By analyzing these morphological differences, CYGNO can distinguish between nuclear and electron recoils, effectively identifying signal events.

    - *Directionality.* The distribution of charge along the ionization path encodes information about the particle's trajectory. Both CMOS and PMT data reveal characteristic asymmetries in the energy deposition profile: alpha particles exhibit a pronounced Bragg peak at the end of their range, while nuclear recoils show enhanced ionization at the beginning of the trajectory, where the recoiling nucleus is slowest and most ionizing. This asymmetry, known as the head–tail effect, allows determination of the sense of motion along the track direction.
    - *Fiducialization.* The excellent spatial resolution of the sCMOS cameras provides precise reconstruction of the interaction position in the x-y plane, corresponding to the GEM amplification plane. The position along the drift direction (z) can be inferred by analyzing the diffusion of the ionization cloud: tracks originating farther from the GEM plane undergo longer drift times and therefore exhibit greater transverse spreading due to electron diffusion in the gas. By comparing the measured track width with the expected diffusion parameters, one can estimate the drift distance and thus localize the interaction point within

the TPC volume. This three-dimensional reconstruction effectively enables the rejection of background events originating near the detector walls, defining a clean fiducial volume for physics analyses.

5. **Operational advantages.** Operating the detector at room temperature and atmospheric pressure offers several practical benefits. It eliminates the need for complex vacuum vessels or high-pressure systems and avoids the technical challenges associated with cryogenics. These conditions simplify prototype development, facilitate detector scaling, and reduce costs compared to cryogenic dark matter detectors. Furthermore, working under such flexible conditions allows the experimenters to easily modify the gas mixture or adjust the ratio of its components to optimize performance for specific physics goals.

Following the general introduction to the CYGNO experimental approach, the next sections of this chapter focus on a detailed discussion of its key components: the gas mixture, the triple-GEM amplification system, and the optical readout based on CMOS sensors and PMTs. The evolution of CYGNO prototypes is then summarized, with particular emphasis on the LIME detector.

3.1.1 The gas mixture

Choosing the right target gas is a critical step for optimizing detector performance and maximizing the sensitivity to possible DM interactions with Standard Model particles. In CYGNO, the selected gas mixture consists of 60% helium (He) and 40% tetrafluoromethane (CF_4).

CF_4 is well known for its scintillation properties, especially when mixed with noble gases [163–166]. It exhibits two main emission peaks, one in the visible and another in the UV region. Figure 3.2 shows the normalized emission spectrum of the He:CF_4 (60/40) mixture, together with the quantum efficiency curves of the sCMOS camera and PMT used in CYGNO detectors, highlighting their strong spectral compatibility.

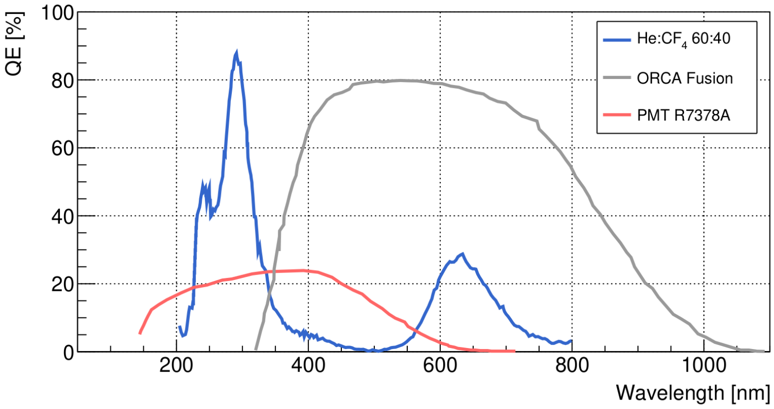

Figure 3.2: He:CF_4 (60/40) emission spectrum superimposed with the quantum efficiency of the ORCA-Fusion camera and the R7378 PMT [163].

In the UV range, two pronounced peaks appear around 240 nm and 290 nm, originating from multiple excited ionic species [164] produced via dissociative ionization of CF_4, which has a threshold energy of 15.9 eV. The visible emission, instead, comes from the de-excitation of the neutral fragment CF_3^* in a Rydberg state, formed at a lower threshold of about 12.5 eV. The use of CF_4-based mixtures also results in remarkably low diffusion during electron drift [159], thanks to the large scattering cross-sections in electron-CF_4 interactions, an essential feature for maintaining the integrity of the track structure.

In the context of direct dark matter searches, both the WIMP-to-target mass ratio and the detector's energy threshold determine the minimum detectable DM mass. Using a light target ($A < 10$) together with an energy threshold around $\mathcal{O}(1)$ keV allows sensitivity to WIMP masses below 10 GeV, a region still largely unexplored. The presence of helium ($A = 4$) in the CYGNO gas mixture maximizes sensitivity to WIMPs of a few GeV for spin-independent (SI) interactions. Owing to helium's small atomic mass, nuclear recoils generate longer tracks, which are easier to reconstruct for directionality and head–tail discrimination. At the same time, the fluorine atoms in CF_4 contribute sensitivity to spin-dependent (SD) interactions even at low WIMP masses, thanks to fluorine's unpaired proton and relatively low atomic mass. This combined He:CF_4 configuration makes CYGNO one of the few experiments capable of probing both SI and SD interactions for WIMP masses below 10 GeV.

Throughout the CYGNO R&D program, several gas proportions were studied in order to balance light yield, stability, and performance. As reported in [167], an optimal compromise was found with a 60% He and 40% CF_4 mixture. The corresponding longitudinal and transverse diffusion coefficients, along with the drift velocity as a function of the electric field, were simulated with Garfield [168, 169] and are shown in Figure 3.3.

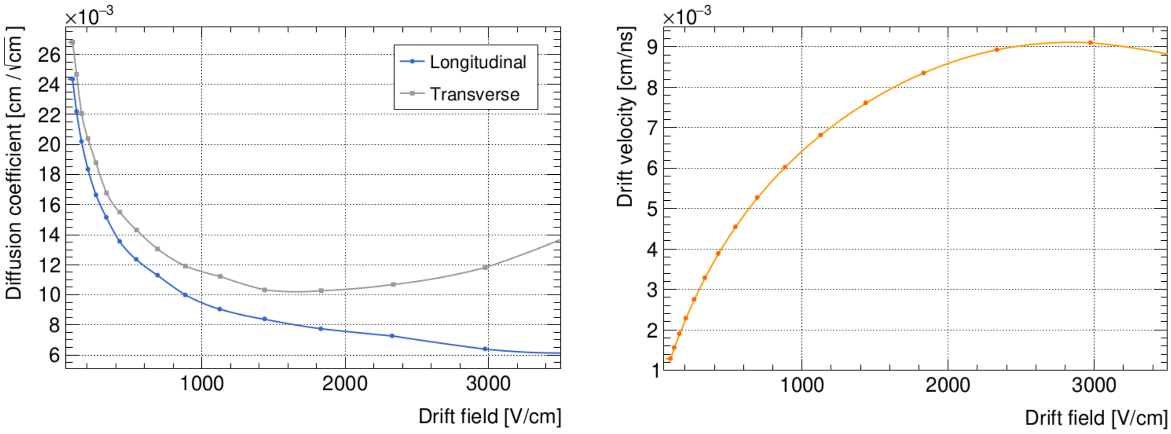

(a) **(b)**

Figure 3.3: Longitudinal and transverse diffusion coefficients (left) and drift velocity (right) as functions of the electric drift field, obtained with Garfield simulations for the CYGNO gas mixture [167].

The simulated transverse diffusion coefficient for the He:CF_4 (60/40) mixture is about 130 $\mu\mathrm{m}\sqrt{\mathrm{cm}}$ at a drift field of 500 V/cm. This low diffusion value, crucial for preserving track shape, has also been experimentally confirmed using minimum ionizing particles (MIPs) [170]. The mean energy required to produce an electron–ion pair, commonly referred to as the W value, is 35 eV [171], although different experimental techniques report slightly varying numbers [172, 173].

The three-dimensional ranges of electrons and ions in the gas were simulated using Geant4 [174] and SRIM [175], respectively. Figure 3.4 shows that helium ions, which represent nuclear recoils (NRs), have sub-millimeter ranges up to energies of 100 keV. Consequently, they appear as compact bright spots whose apparent size is mainly governed by gas diffusion. Electrons, corresponding to electron recoils (ERs), display much longer paths, already exceeding 1 mm at 10 keV and extending to several centimeters at 100 keV.

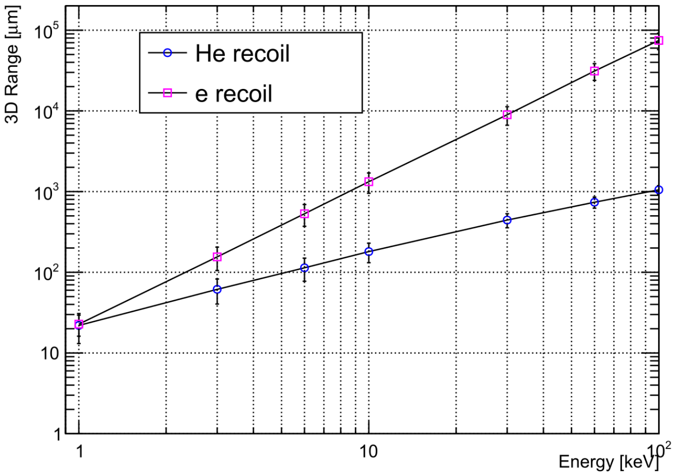

Figure 3.4: Simulated 3D range of electrons and He ions in He:CF_4 (60/40) [154].

At energies below 10 keV, ERs also tend to appear as small clusters or spot-like structures, since their intrinsic track size becomes comparable to the diffusion spread in the gas. In this low-energy regime, distinguishing between ERs and NRs becomes increasingly difficult, as both exhibit similar morphologies. Discrimination is then primarily based on the density of the ionization cloud, defined as the total light yield divided by the projected spot area. The distinct energy loss behavior along the track (dE/dx) of electrons and nuclei can be exploited for classification, using the fine spatial information from the sCMOS camera in combination with the timing and intensity data from the PMTs.

3.1.2 Charge amplification

Optically readout TPCs require substantial charge amplification, since only a small fraction of the scintillation photons are detected due to the limited solid angle of optical collection. To achieve the necessary gain, CYGNO employs Gas Electron Multipliers (GEMs), which can reach very high amplification factors, as illustrated in Fig. 3.5. These devices maintain excellent spatial granularity, minimizing the distortion of the original ionization track.

GEMs belong to the Micro Pattern Gas Detector (MPGD) family, introduced by F. Sauli in 1997 [157]. They were developed to enhance the spatial resolution and rate capability of traditional wire chambers operating in high particle flux environments [61, 159]. A GEM is composed of a thin insulating foil (typically Kapton or fiberglass) metalized on both sides and perforated with a dense pattern of microscopic holes. Applying a potential difference of a few hundred volts between the two conductive layers generates electric fields on the order of $\mathcal{O}(10)$ kV/cm within the holes, initiating electron avalanches. The positive ions produced inside the holes are largely trapped by the top electrode, which significantly reduces ion backflow into the drift region and ensures stable operation even at high rates [176].

The fabrication materials and dimensions of GEMs can vary. Thin foils, around 50 μm thick, usually feature hole diameters of approximately 70 μm and pitches of about 140 μm. Smaller holes do not necessarily improve the effective gain due to charge saturation inside the channels [159]. The micro-holes are generally produced by chemical etching, creating a double-conical shape narrower at the center. For larger geometries (diameters above 300 μm), mechanical drilling is used instead, yielding cylindrical holes.

The electrons multiplied in one GEM layer can be collected on an anode or transferred to subsequent GEMs for further amplification. By stacking multiple GEMs, total gains from 10^4 up to 10^6 can be achieved [159, 161]. In CYGNO, the amplification stage employs a triple-GEM configuration, using three foils each 50 μm thick, ensuring both high gain and stable operation.

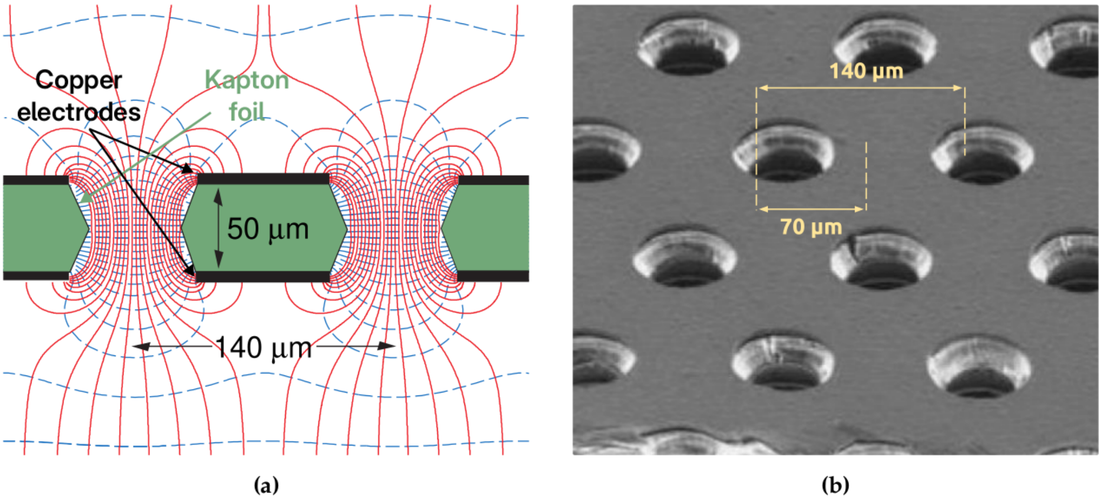

(a) (b)

Figure 3.5: Structure of a thin GEM: (a) cross-sectional view with electric field lines generated by a potential difference across the electrodes [61]; (b) electron microscopy image showing the hole pattern and pitch of a GEM foil [159].

3.1.3 The optical readout

When a charged particle traverses the target medium, it not only ionizes atoms and molecules but can also excite them. During the subsequent de-excitation processes, photons are emitted, and the resulting light spectrum and intensity depend on the properties of the gas and, in some cases, on the applied electric field. Scintillating gases such as Ar, Xe, CF_4, He:CF_4, and Ar:CF_4 typically produce between 10^{-2} and 10^{-1} photons per secondary electron, depending on the gas pressure and charge amplification regime [163, 164, 177, 178]. The idea of exploiting the scintillation light generated during electron multiplication was proposed more than thirty years ago [179], but has gained renewed importance thanks to recent advances in optical sensor technology, which now allow this effect to be fully utilized.

Modern optical sensors, such as the CMOS devices developed for consumer electronics, are rapidly improving in terms of sensitivity, resolution, and noise performance. This technological progress, largely driven by commercial applications, has also had a major impact on scientific research, enabling the use of compact, high-performance cameras in experimental setups. In detectors like CYGNO, these cameras can be conveniently positioned outside the sensitive volume, thus avoiding potential issues related to high voltage operation or gas contamination. Although this configuration reduces the amount of light reaching the sensor due to the limited solid angle coverage, the loss can be compensated by increasing the charge gain, which in CYGNO is achieved with the triple-GEM amplification system [167]. A major advantage of the optical readout technique is the ability to image large active areas (on the order of $\mathcal{O}(1)$ m^2) with a single sensor while maintaining an effective spatial resolution of $\mathcal{O}(100)$ μm through the use of appropriately chosen lenses.

In CYGNO, the scintillation light is read out using a hybrid system consisting of sCMOS cameras and PMTs. The cameras provide high-resolution images of the track projected onto the (x, y) plane, while the PMTs measure the time structure of the light signal along the drift direction (z axis). Together, these measurements allow for full three-dimensional reconstruction and energy estimation of the ionizing events.

3.1.3.1 Optics

As discussed above, focusing lenses are employed to project large sensitive areas onto a single sCMOS sensor. All CYGNO detectors use a Schneider Xenon lens characterized by a focal length $f = 25.6$ mm, an aperture ratio (f-number) $N = 0.95$, and an optical transmission of about 85%. With the typical active area of Hamamatsu sCMOS sensors (see Table 3.1), it is possible to image surfaces of $\mathcal{O}(1000)$ cm^2 by placing the camera roughly $\mathcal{O}(50)$ cm from the GEM plane. A schematic illustration of the optical system under the Gaussian approximation is shown in Figure 3.6.

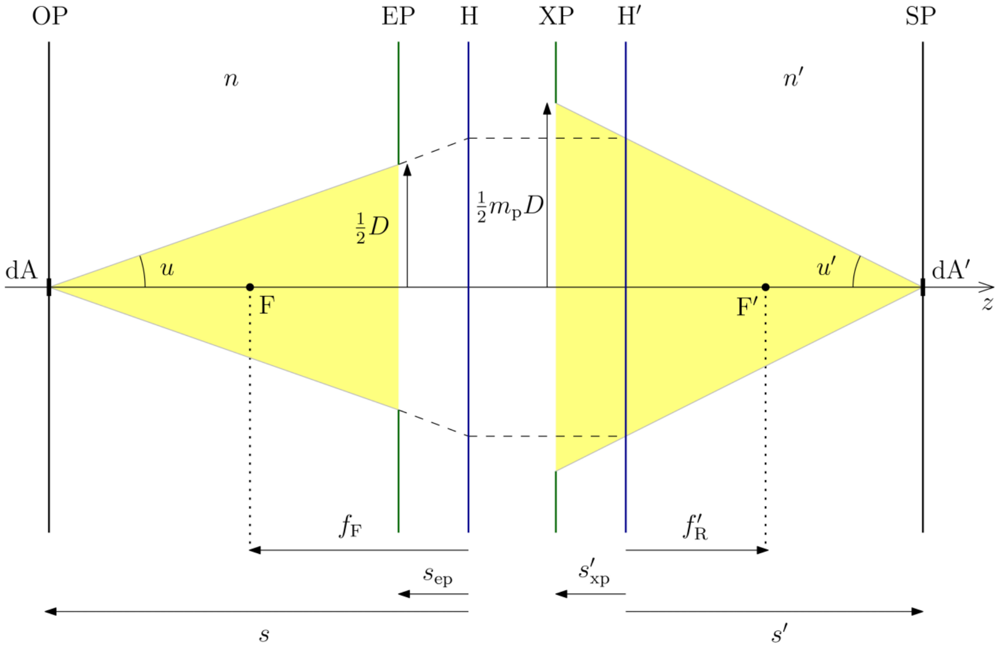

Figure 3.6: Schematic of a lens under the Gaussian approximation, showing the solid angle of emission from the object plane (OP) focused onto the sensor plane (SP) [180].

The diagram is represented on a plane defined by the optical axis (the line passing through the lens center and connecting the object to the sensor) and an orthogonal axis, which can be any direction in the case of a circular lens. The object plane (OP) corresponds to the location of the source being imaged, while the sensor plane (SP) denotes the position of the photosensitive detector. EP and XP indicate the entrance and exit planes of the lens, through which photons enter and leave the optical system. The points H and H′ mark the hyperfocal planes, representing the equivalent positions of a thin lens with the same optical properties as the real thick lens [180]. The parameter D denotes the lens aperture radius, determining the effective area that collects photons. This parameter can be adjusted mechanically by varying the diaphragm opening, which controls the light admitted through the lens.

In the schematic, dA represents the infinitesimal emitting area on the object plane, u is the tangent of the acceptance angle, s and s' denote the distances from the hyperfocal planes H and H′ to the object and sensor, respectively. The focal length is indicated as f_F, with focal points F and F′ typically assumed to coincide ($F = F'$ and $f_F = f'_F = f$). The figure illustrates how light emitted from the region highlighted in yellow on the left side of EP is collected and focused onto the sensor surface, providing a simplified representation of how a thick lens forms an image in the Gaussian approximation.

When the planes OP, EP, XP, and SP are parallel, the photon flux Φ emitted from a small area element dA on the object plane and reaching the lens can be expressed as [180]:

$$\Phi = \pi L dA u^2 \tag{3.1}$$

where L denotes the source luminosity. The fraction of the total solid angle Ω_f subtended by the lens can then be derived by normalizing to the total emission over 4π steradians:

$$\Omega_f = \frac{\Phi}{LdA}\frac{1}{4\pi} = \frac{\pi u^2}{4\pi} = \frac{(D/2)^2}{4s^2} \tag{3.2}$$

The last expression arises directly from geometric considerations. For CYGNO, where $s \gg s_{ep}$, the relationship between the magnification I and the distances s and s' follows the standard thin-lens approximation, hence:

$$\frac{1}{f} = \frac{1}{s} + \frac{1}{s'} \tag{3.3}$$

and

$$I = \frac{y'}{y} = \frac{s'}{s} \tag{3.4}$$

with y and y' representing the object and image dimensions, respectively. Combining the above relations yields:

$$\Omega_f = \frac{1}{\left[4N^2\left(\frac{1}{I}+1\right)\right]^2} \tag{3.5}$$

where $N = D/f$ is the f-number or aperture ratio.

As the camera is placed farther from the source (increasing s), the solid angle fraction Ω_f (and therefore the number of photons reaching the sensor) decreases rapidly. At the same time, the projected area being imaged grows. This trade-off results in a small light collection efficiency, explaining why CYGNO employs relatively high charge gains using a triple-GEM configuration. The benefit, however, is a considerable reduction in the number of required optical sensors per unit area, which simplifies both the overall system design and the cost.

The expression above assumes a point-like light source positioned on the optical axis. For an extended source, regions located away from the axis emit photons under an angle ϕ with respect to the optical axis. In these conditions, the illuminance on the sensor decreases with increasing ϕ, since only a fraction of the emitted photons reach the lens. The photon flux from an off-axis source element becomes:

$$\Phi = \pi L dA u^2 \cos^4\phi \tag{3.6}$$

Thus, the larger the deviation from the optical axis, the smaller the flux collected, an effect known as *vignetting*. In the context of CYGNO, vignetting causes a non-uniform light yield across the image plane: the edges of the frame appear dimmer than the center for the same intrinsic luminosity. This spatial non-uniformity must be corrected during data analysis.

3.1.3.2 sCMOS cameras

Recent technological advances have led to major improvements in the performance and affordability of optical sensors, driven primarily not by scientific needs but by industrial and consumer market demand. High-resolution, pixelated light sensors are now extensively used in particle physics, including imaging applications in TPCs with scintillating gas mixtures [181–183]. The two main technologies for digital imaging are *charged-coupled devices* (CCDs) and *active pixel sensors* (APS), the latter commonly implemented on *complementary metal-oxide-semiconductor* (CMOS) chips. Both types convert incident light into electrical charge and process the resulting signal electronically.

In CCDs, each pixel acts as a metal–oxide–semiconductor (MOS) capacitor biased in the depletion region, where photons generate electrons. These capacitors form an array connected by a transmission layer acting as a shift register. After the exposure, charge packets are transferred sequentially from one pixel to the next until the final capacitor delivers its charge to an amplifier, which converts it to a voltage signal. This analog voltage can then be digitized or read continuously. Because the entire pixel area is photosensitive, CCDs provide high uniformity and excellent image quality, key features in scientific imaging.

CMOS sensors, by contrast, perform charge-to-voltage conversion directly within each pixel using a pinned photodiode. Each pixel may include its own amplifier, noise-correction circuit, and analog-to-digital converter, allowing the chip to output digital data directly. Although this architecture leads to slightly lower pixel-to-pixel uniformity, it enables massively parallel readout and therefore much higher frame rates (see Figure 3.7). CMOS sensors also offer lower power consumption and reduced production costs compared to CCDs, making them particularly attractive for large-scale detector applications like CYGNO.

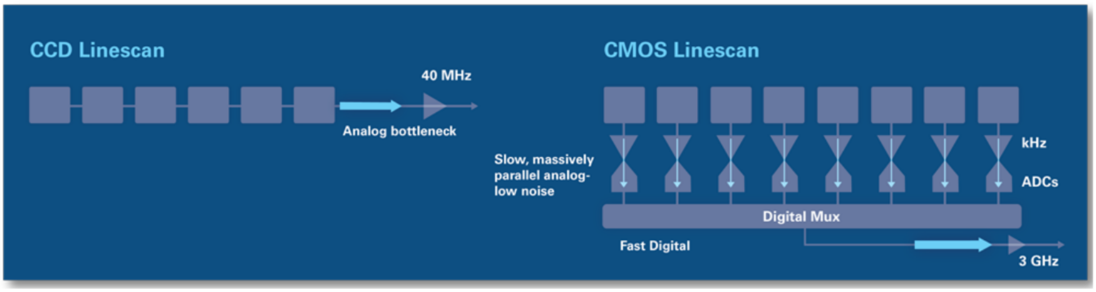

Figure 3.7: Comparison of CCD (left) and CMOS (right) sensor readout schemes. In CCDs, pixels are read sequentially in rows: the charge accumulated in each pixel is transferred through a shift register to a common amplification stage. In CMOS sensors, each pixel includes its own amplifier and digitization electronics, allowing for independent parallel readout [184].

For many years, CCDs were considered superior to CMOS sensors in terms of noise performance. However, continuous technological progress has allowed CMOS devices to not only catch up but in several aspects surpass CCDs [185–187]. Their rapid development is strongly supported by widespread use in commercial applications (such as smartphone cameras) which drives constant improvement and cost reduction. This makes CMOS technology extremely promising for scientific detectors of the next generation.

High-end CMOS sensors featuring very low noise, fast frame rates, large dynamic range, high quantum efficiency, and fine spatial resolution are generally referred to as *scientific CMOS* (sCMOS). Because of their combination of low readout noise, high pixel granularity, and strong potential for future upgrades, CYGNO employs sCMOS cameras for its optical readout system.

As part of the CYGNO R&D program, several Hamamatsu sCMOS models were tested, and their main characteristics are summarized in Table 3.1. From the older ORCA-Flash model to the latest ORCA-Quest, the number of pixels has steadily increased while the individual pixel size has decreased. At the same time, the RMS noise level improved by about a factor of five, reaching 0.27 e^- in the ORCA-Quest, low enough to allow photon counting with sub-photon uncertainty. The electronic Gaussian noise of the sensor adds to the intrinsic Poisson fluctuations of the photon signal, slightly broadening the distribution of detected counts. A readout noise of 0.3 e^- RMS or less ensures a 90% probability of correctly identifying the number of photoelectrons, thereby enabling *photon-number-resolving* capability, as illustrated in Figure 3.8 [188]. For this reason, these next-generation sensors are often called *quantitative CMOS* (qCMOS).

Table 3.1: Key characteristics of the three Hamamatsu CMOS cameras evaluated within the CYGNO experiment. The chronological order (top to bottom) highlights the evolution of the technology over time, particularly in pixel resolution, sensor size, and RMS noise reduction [188].

Model	**Resolution** [# pixels]	**Pixel** size [µm]	**Sensor** size [mm^2]	**Noise** RMS [e^-]	**Frame** rate [Hz]
ORCA Flash	2048 × 2048	6.5 × 6.5	13.312 × 13.312	1.4	30
ORCA Fusion	2304 × 2304	6.5 × 6.5	14.976 × 14.976	0.7	5.4
ORCA Quest	4096 × 2304	4.6 × 4.6	18.841 × 10.598	0.27	5

All sCMOS cameras tested by CYGNO show excellent quantum efficiency (QE) between 80% and 90% in the visible region, particularly around 500–600 nm (see Figure 3.2). This range matches well with the emission spectrum of the He:CF$_4$ gas mixture. The current camera employed in the LIME detector is the ORCA-Fusion C14440-20UP, which demonstrated the best compromise between resolution, sensitivity, and stability among all tested models [189]. The ORCA-Quest, although offering superior noise performance, began testing within the CYGNO Collaboration only after LIME's commissioning and is therefore not included in the operational setup. It will be exploited for the demonstrator CYGNO_04 currently under installation at LNGS.

Thanks to their fine spatial resolution and low noise, sCMOS cameras allow precise measurement of the (x, y) projection of the events in the gas, along with a quantitative estimate of the total light yield. This capability enables the determination of both the energy and the two-dimensional topology of ionization tracks, facilitating particle identification and 2D directional analysis. When combined with the time information provided by PMTs, these measurements allow for full three-dimensional reconstruction of the ionization tracks within the detector.

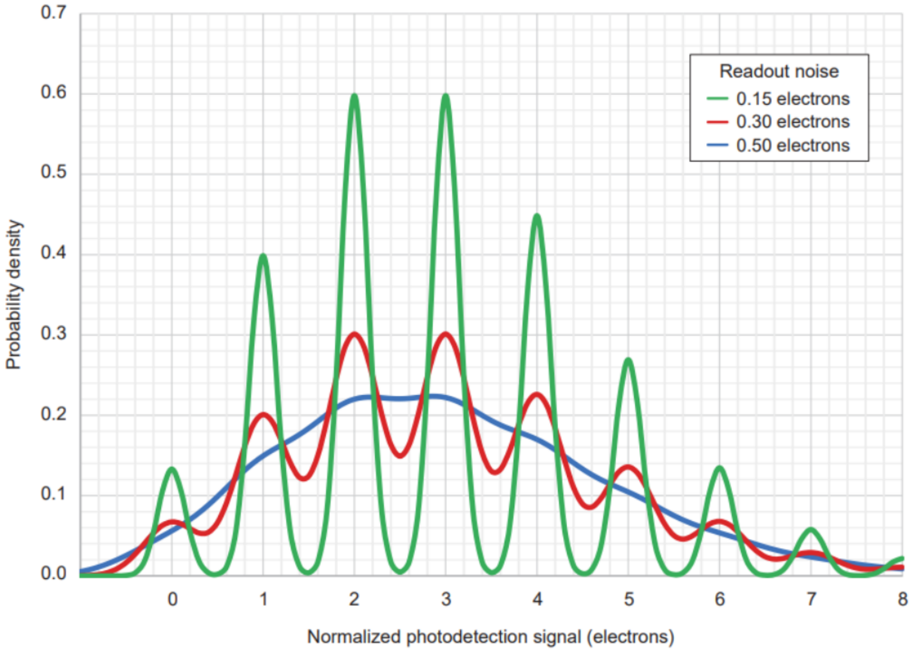

Figure 3.8: Probability distribution of the observed photoelectron counts for a Poisson mean $N = 3$, shown for different readout noise levels [188].

3.1.3.3 Photomultiplier Tubes (PMTs)

Photomultiplier Tubes (PMTs) are widely used devices for detecting fast and faint light signals, based on the conversion of photons into electrons via the photoelectric effect. As illustrated in Figure 3.9, a PMT consists of a vacuum glass tube that houses a photocathode on one end and an anode on the other. Between them lies a series of electrodes known as dynodes, which act as electron multipliers. The amplified charge is finally collected at the anode, where the output signal can be read.

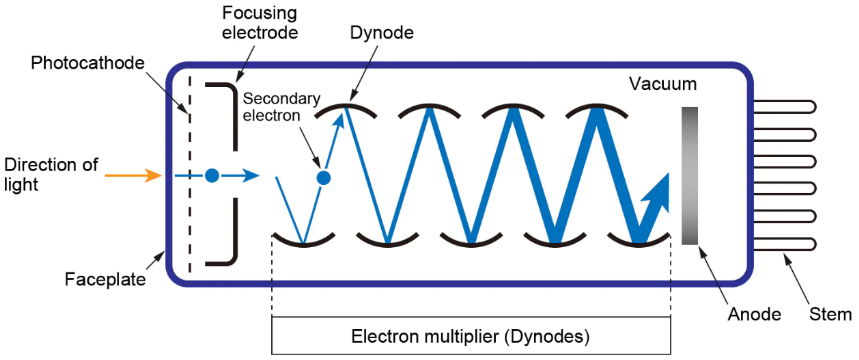

Figure 3.9: Schematic representation of a photomultiplier tube (PMT) and its internal structure [190].

The photocathode consists of a very thin semiconductor layer deposited on the inner surface of a transparent window. When photons strike the photocathode, electrons are emitted through the photoelectric effect. The conversion efficiency is not perfect, and the ratio of emitted electrons to incident photons is referred to as the quantum efficiency (QE). These photoelectrons are accelerated and directed toward a sequence of dynodes, each maintained at progressively higher potentials. The dynodes, typically made of materials such as BeO or Mg–O–Cs with high secondary-electron emission coefficients (g), multiply the number of electrons at each stage. For electron energies between 100 and 200 eV (typical for inter-dynode acceleration), the secondary emission factor g is around 3–5 [191]. The photocathode is kept at a negative potential, while the anode is generally grounded. The total potential difference between them, of the order of $\mathcal{O}(10^3)$ V, is distributed through a resistor chain across the dynodes. The overall gain of the PMT depends on the number of dynodes n and the emission coefficient g, and is typically $g^n \approx 10^7$ for $g \approx 4$ and $n \approx 12$ [190].

The most commonly used photocathodes in scintillation-based detection are *bialkali* compounds, such as Sb–K–Cs, which offer sensitivity from the ultraviolet to the visible range, with a QE around 25% at 400 nm. More advanced GaAs or GaInAsP photocathodes can achieve QEs up to 50% and extend sensitivity into the infrared, though they are less commonly used due to higher cost and operational constraints [190]. Multialkali photocathodes (e.g., Na–K–Sb–Cs) offer broader spectral coverage from UV to IR but exhibit higher intrinsic noise. For its purposes, CYGNO employs bialkali PMTs, which provide an optimal balance between sensitivity and stability for visible light detection.

The electrons collected at the anode generate a current that, when passed through a resistor, yields a voltage signal with nanosecond-scale timing resolution. The PMT output waveform reflects the arrival time distribution of photons at the photocathode, which in turn encodes the relative position of the ionization electrons along the drift direction. This time profile provides information about the z-coordinate of each event, complementing the (x, y) projection recorded by the sCMOS camera. Together, these data allow for a complete three-dimensional reconstruction of the ionization tracks. Moreover, the integral of the PMT signal is proportional to the total emitted light and thus provides an independent energy measurement that can be cross-calibrated with the optical signal recorded by the camera.

3.2 The CYGNO timeline

The CYGNO project has been progressing through successive prototype stages of increasing scale. The development roadmap is organized into three main phases, as summarized in Figure 3.10. CYGNO is currently nearing completion of PHASE_0, the R&D stage, during which multiple prototypes have been constructed to test and optimize the detection technique. This phase culminated in the installation and run of the LIME detector underground. The next stage, PHASE_1, will demonstrate the scalability of the technology by deploying a 0.4 m^3 prototype, named CYGNO_04, featuring a modular optical readout and serving as a platform for radiopurity assessment. The final stage, PHASE_2, foresees the construction of a large-scale detector with an active volume of several tens of cubic meters, marking the transition to the full CYGNO experiment, aimed at dark matter detection and neutrino spectroscopy.

It should be noted that, at present, the project has been approved only up to PHASE_1, which is now entering its initial implementation phase.

3.2.1 PHASE_0: R&D and prototypes

During PHASE_0, three main prototypes were developed to refine and validate the experimental technique. The first prototype, named ORANGE (Optically Readout GEM), was

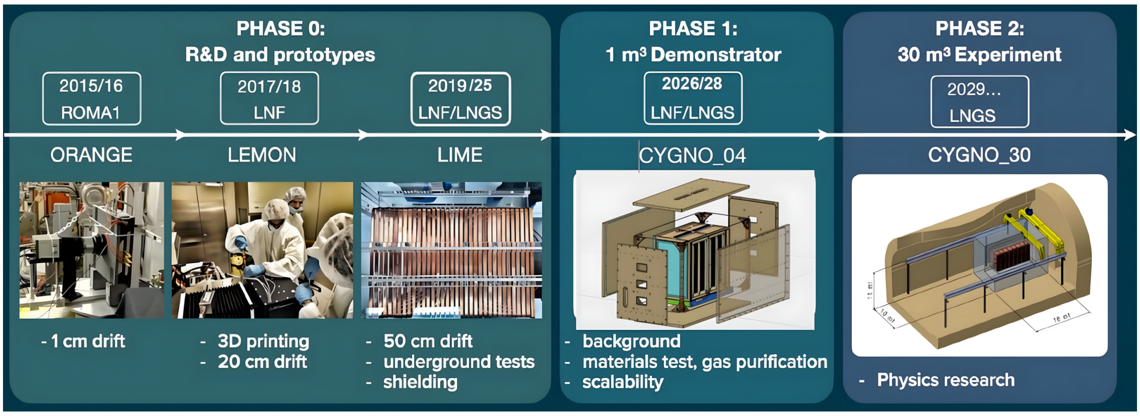

Figure 3.10: Timeline of the CYGNO project. PHASE_0 corresponds to the R&D stage, during which several prototypes were built and tested. PHASE_1 will focus on demonstrating the scalability of the approach and verifying radiopurity, paving the way for PHASE_2, the construction of the full-scale CYGNO_30 detector for dark matter and neutrino studies.

designed to explore the optical readout capabilities of GEMs for three-dimensional event reconstruction. It served as a proof of concept demonstrating that GEM-based optical readout could effectively capture 3D track information.

ORANGE employed a triple stack of 10×10 cm^2 GEMs, separated by 2 mm spacers and coupled to a 1 cm drift gap, for a total sensitive volume of about 100 cm^3. Light was collected by a Hamamatsu ORCA-Flash 4.0 camera positioned 20 cm from the final GEM, with a geometrical acceptance of 3.46×10^{-2}. A schematic view of the ORANGE setup is presented in Figure 3.11. The prototype successfully demonstrated track imaging through optical readout [167], provided early measurements of light yield [182], and achieved the first 3D track reconstruction using PMTs within the CYGNO framework [162].

Following the success of ORANGE, the next step aimed to assess the feasibility of using TPC technology for directional dark matter detection and to test the CYGNO approach with an extended drift region. To this end, the LEMOn (Long Elliptical Module) detector was developed. LEMOn (shown in Figure 3.12) features a 7-liter active volume, a 20 cm drift length, and a 24×20 cm^2 readout plane. The detector is enclosed in a gas-tight acrylic chamber operating in continuous gas flow mode.

Inside the vessel, an ellipsoidal field cage made of silver wires, supported by 3D - printed plastic rings with a 1 cm pitch, ensures a uniform electric field across the 20 cm drift gap. The cathode consists of a fine metallic mesh with 30 μm wire diameter and 50 μm spacing. The charge amplification is provided by three 24×20 cm^2 GEM foils, each separated by 2 mm. The optical readout is achieved with a Hamamatsu ORCA-Flash 4.0 sCMOS camera, coupled to the detector through a transparent TEDLAR window and a flexible optical bellow. The camera response was calibrated at 0.9 counts per photon [182]. On the opposite side, behind the transparent cathode, an HZC Photonics XP3392 PMT is installed to record the time structure of the light signals.

LEMOn validated the CYGNO detector concept on a medium scale, providing key performance benchmarks such as energy resolution [167], stability [167], and the first estimation of the absolute event position along the drift direction [192]. It also enabled preliminary studies on particle identification and topological discrimination [192, 193]. Tests performed with 5.9 keV electron recoils demonstrated a 100% detection efficiency for drift fields above 300 V/cm and drift distances up to 20 cm, achieving an energy res-

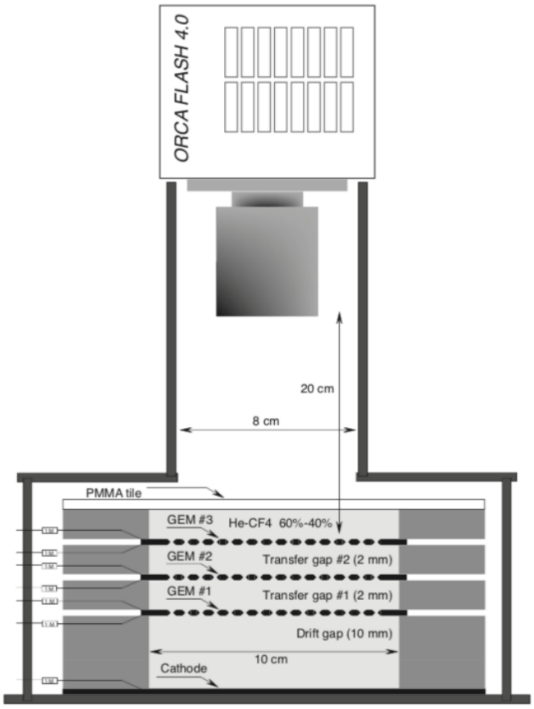

Figure 3.11: Schematic illustration of the ORANGE (Optically Readout GEM) detector, the first prototype developed within the CYGNO project. The system employed three thin GEM foils for charge amplification and a 1 cm drift gap, resulting in a total active volume of 100 cm^3 [167].

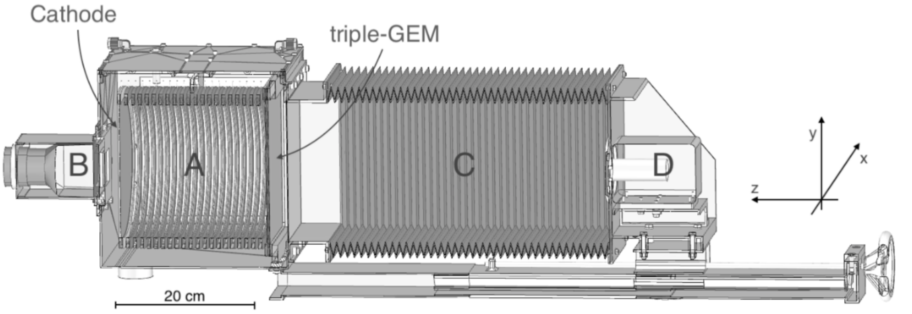

Figure 3.12: The LEMOn prototype showing (B) the PMT holder, (A) the elliptical field cage rings, (C) the optical bellow, and (D) the sCMOS camera support [170].

olution of approximately 12% [167]. Additionally, data collected using an AmBe neutron source allowed the first validation of the background rejection capability of the CYGNO technique [193]. By applying simple selection criteria to remove cosmic ray events and identify nuclear recoils from neutron elastic scattering (based on their high track density), LEMOn achieved an electron-recoil rejection efficiency of 96.5% at 5.9 keV while retaining 50% of nuclear recoil events [193]. Further details regarding the LEMOn design and its experimental performance are provided in [170, 192, 194].

The third and largest prototype of PHASE_0 is LIME, representing the most advanced stage of CYGNO's R&D effort. LIME has a sensitive volume of approximately 50 liters and was initially operated at the INFN Frascati National Laboratories (LNF) for surface characterization tests. In February 2022, the detector was relocated at the underground INFN Gran Sasso National Laboratory (LNGS), where it has been continuously operated for more than two years under different shielding configurations. These campaigns were dedicated to studying and characterizing various background sources. LIME serves as the reference prototype for the current phase of the project and will be described in detail in the next chapter, including its construction, operating conditions, and the extensive underground data acquisition campaign that forms the core of this thesis.

3.2.2 PHASE_1: CYGNO_04, the CYGNO demonstrator

CYGNO_04 marks the beginning of PHASE_1 of the CYGNO project and involves the realization of a 0.4 m^3 detector that will act as the first large-scale demonstrator for the experiment. The main objectives of CYGNO_04 are the minimization of background contributions from detector materials, the validation of the modular optical readout and of the data acquisition (DAQ) systems.

The CYGNO_04 concept adopts a *back-to-back* configuration consisting of two symmetric TPCs sharing a central cathode. This layout, frequently used in large detectors, effectively doubles the active volume while minimizing the overall amount of structural material. Such a configuration also reduces the maximum drift length by half, which provides two major benefits: (1) it lowers the high voltage required to establish the desired drift field, and (2) it mitigates electron diffusion effects during drift, thereby improving 3D tracking precision and directional reconstruction capabilities.

A 3D exploded rendering of the current CYGNO_04 design is presented in Figure 3.13. The inner PMMA vessel, which contains the He:CF_4 gas mixture, is shown in light blue. Building on the experience and results discussed in this thesis, a double-sealed vessel design is foreseen for CYGNO_04: an inner PMMA chamber enclosed by a secondary ultra-pure copper vessel, which minimizes the diffusion of ambient radon and ensures gas containment. This copper layer also provides passive background shielding and is illustrated in green and brown, representing standard and ultra-pure copper, respectively.

The detector's central cathode is made from a 50 μm Kapton foil coated with 5 μm copper on both sides, similar in structure to a GEM foil. Each of the two TPCs will be instrumented with three Hamamatsu ORCA-Quest cameras evenly distributed across the imaging plane. These cameras, coupled to 50×80 cm^2 GEMs that provide charge amplification and light emission, represent a significant technological advancement over previous models, offering higher resolution, smaller pixels, and lower electronic noise. On each side of the detector, eight PMTs will be positioned around the cameras, facing the GEMs, in a configuration reminiscent of the LIME setup. The chosen number and arrangement of sensors balance spatial granularity, cost efficiency, and geometric constraints. For the final CYGNO_04 geometry, the effective pixel granularity corresponds to 125×125 μm^2, approximately a 25% improvement in spatial resolution compared to LIME.

The design strategy for background reduction in CYGNO_04 is based on detailed simulations and experimental studies performed with the LIME prototype. These analyses identified the dominant internal background sources as the copper components in the drift field cage and cathode, ceramic resistors, GEM foils, and optical elements such as camera lenses. Among these, contamination from the ^{238}U decay chain was found to be the most significant, given its natural occurrence in many detector materials. Mitigation of these contributions will be a central aspect of the CYGNO_04 construction and testing campaign.

As part of the strategy to further minimize potential background contributions, several design enhancements have been introduced in the development of CYGNO_04 compared

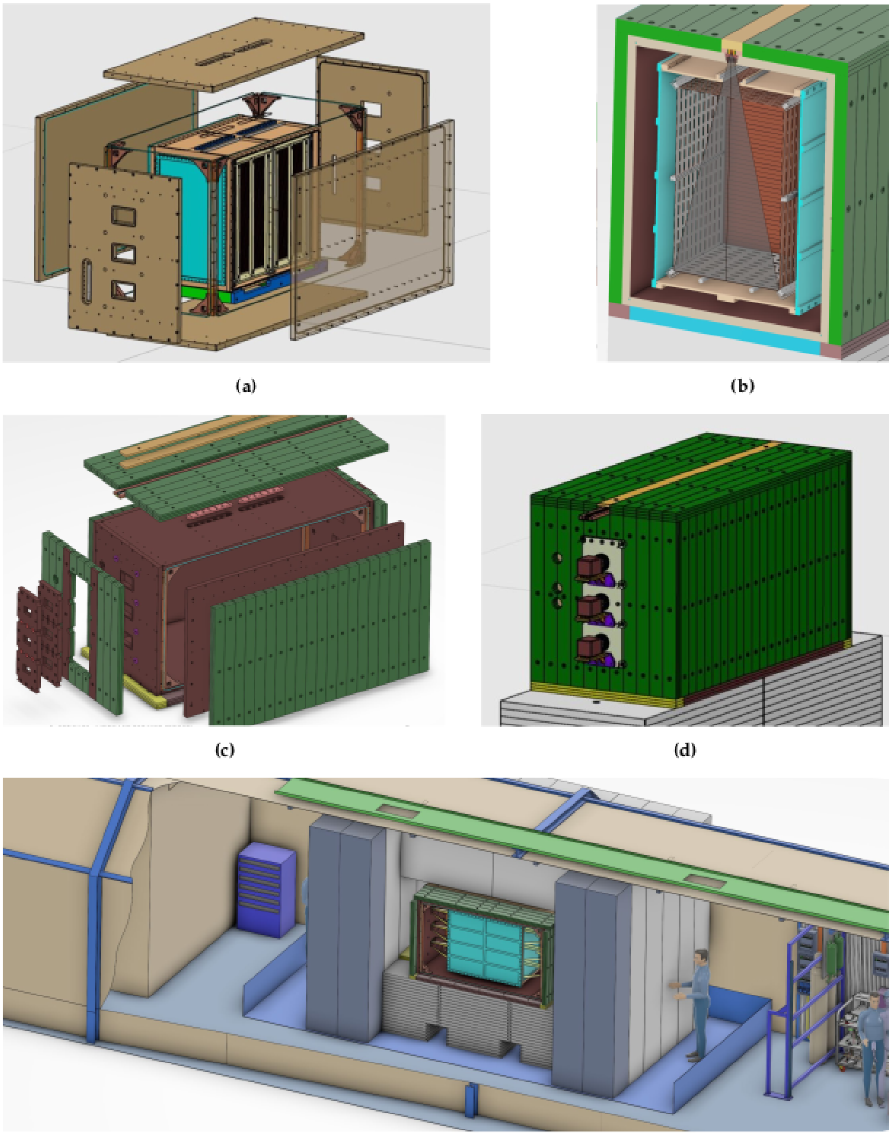

(a) (b) (c) (d) (e)

Figure 3.13: Technical designs of the CYGNO_04 detector: (a) exploded view of the internal structure, showing the PMMA gas vessel (blue) and copper shielding (brown); (b) cross-sectional view highlighting the internal field cage; (c) external exploded view showing standard (green) and ultra-pure (brown) copper layers; (d) closed configuration with three CMOS cameras and eight PMTs per side; (e) location of the detector at the underground LNGS facility, surrounded by water columns for additional shielding [195].

to the previous LIME prototype. One of the most significant upgrades is the use of a custom optical lens fabricated from ultra-pure silica (SUPRASIL), developed in collaboration with industrial partners. This improvement is expected to suppress radioactive background from the lens material by up to four orders of magnitude (10^4). The GEM foils will undergo a thorough cleaning process using high-pressure deionized water baths (a technique successfully adopted in other low-background experiments such as T-REX [196]) to further reduce surface contamination. The drift field cage will be constructed from thin Kapton foil embedded with copper strips interconnected by surface-mounted (SMD) resistors, forming a cylindrical structure around the active region. This configuration significantly reduces the amount of copper and ceramic material exposed to the gas, thereby limiting internal background sources. Moreover, every remaining component of CYGNO_04 will be fabricated from certified low-radioactivity materials, whose activities will be individually measured and validated. For external shielding, the detector will be surrounded by 10 cm of copper and an additional 100 cm of water, expected to reduce external background by roughly a factor of 20 relative to the internal component.

CYGNO_04 will also test the scalability of the CYGNO concept across multiple aspects, including mechanical design, stability, and auxiliary systems. Ongoing studies focus on issues such as structural deformation, uniform power distribution, and GEM tensioning. An important innovation will also be implemented in the data acquisition (DAQ) system. In contrast to previous setups, where the finite exposure time of optical sensors introduced acquisition deadtime, CYGNO_04 will employ continuous-readout CMOS operation. In this mode, each pixel row is read immediately after exposure, allowing for uninterrupted image collection. If a particle track crosses a row during readout, it may appear across two consecutive frames; the combination of these frames then enables full track reconstruction. However, as the number of optical and PMT channels increases, synchronization between readout systems becomes crucial. To meet this requirement, the collaboration is developing a prototype of an advanced DAQ architecture that will be integrated into CYGNO_04.

Overall, CYGNO_04 will serve as a proof of concept demonstrating that the CYGNO collaboration possesses the technological maturity to construct a large, optically readout TPC with a volume of $\mathcal{O}(30\text{–}100)$ m^3, capable of high-granularity imaging and competitive dark matter sensitivity. By employing low-radioactivity materials and extensive shielding, CYGNO_04 will provide key insight into the achievable background levels and the true physics reach of future large-scale CYGNO detectors. The underground infrastructure for CYGNO_04, located in LNGS Hall F, was completed in March 2025, with detector installation scheduled for the first trimester of 2026 and commissioning planned for spring 2026.

3.2.3 PHASE_2: CYGNO_30, the CYGNO experiment

The goal of CYGNO_04 will be to validate the technique on a realistic scale. If the outcomes are convincing, a substantially larger instrument, hereafter CYGNO_30, with a total active volume of order tens of cubic meters, would become an interesting proposal for such a detector. The baseline concept is modular: several $\mathcal{O}(1)$ m^3 units (akin to CYGNO_04 or a slightly enlarged version) will be tiled side by side to form a wall-like apparatus. A representative layout is shown in Figure 3.14: an 8×4 array of 1 m^3 modules reaches an active volume close to 30 m^3. This strategy favors reproducibility, simplifies integration of services and readout, and streamlines scaling. The detector could be hosted at LNGS and protected with passive shielding (copper close to the vessel, water outside) to suppress external backgrounds.

To project the sensitivity for such a detector, a Bayesian inference framework is employed. The analysis treats data as mixtures of background and possible WIMP-induced events. Mock datasets are generated across multiple background scenarios by drawing Poisson-distributed counts with different means. Each event is assigned a direction: backgrounds are taken to be isotropic in galactic coordinates (local anisotropies are effectively smeared by Earth's rotation), while WIMP recoils follow the anisotropic distribution expected in the Standard Halo Model. The ideal distributions are then smeared with a Gaussian kernel to encode finite angular resolution.

For each scenario, a *binned* likelihood fit to the angular distribution is performed, profiling the contribution from a putative DM component. From the posterior, a 90% credible interval (C.I.) on the DM event count is derived. The expected number of WIMP interactions connects this count to the spin–independent (SI) and spin–dependent (SD) WIMP–nucleon cross sections via the recoil rate, which depends on detector inputs (gas composition and elemental fractions, active mass, exposure, threshold) and on astrophysical assumptions (local density and velocity distribution). Equating the 90% C.I. upper bound with the predicted DM yield then maps to an exclusion contour in the (m_χ, σ) plane [197].

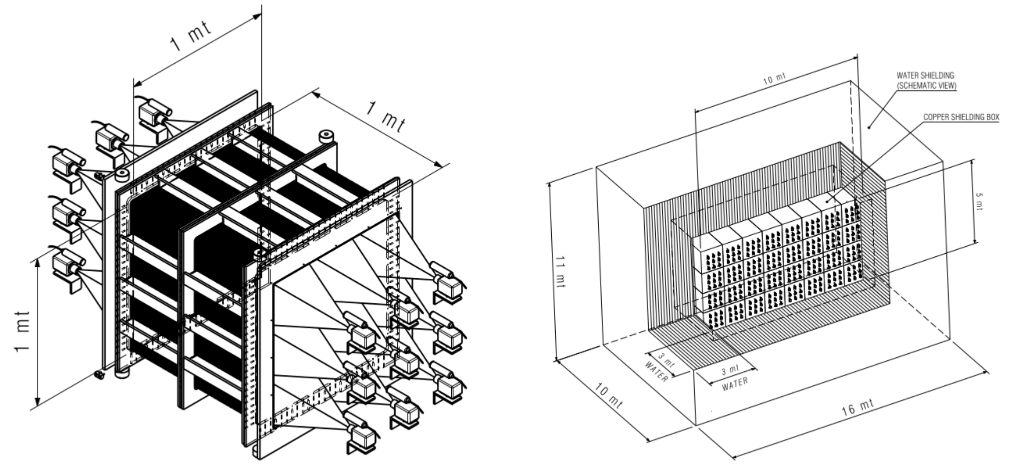

(a) (b)

Figure 3.14: Preliminary technical design of a possible CYGNO Phase 2 detector, illustrating (a) modular 1 m^3 units forming (b) a large, wall-like configuration.

Figure 3.15 summarizes the projected limits for a 30 m^3 detector operated for three years with a 1 keV$_{ee}$ threshold [197]. The study assumes 30° angular resolution with full 3D reconstruction and 100% head–tail efficiency. The adopted resolution is supported by NEWAGE measurements in the 50–400 keV$_{nr}$ range and by recent CYGNUS simulations; it should be conservative at higher E_{nr} for CYGNO-like optics, whereas a constant 100% head–tail efficiency below ~10 keV$_{nr}$ is optimistic and serves as a performance benchmark. Sensitivity is shown for background levels between 10^2 and 10^4 events and for two thresholds, 1.0 and 0.5 keV$_{ee}$.

In the *SI* channel, CYGNO_30 is expected to probe regions of parameter space that remain unexplored. It will be competitive with low-mass programs such as CRESST and CDMSLite [198, 199]. If the threshold can be lowered to 0.5 keV$_{ee}$, the reach extends to $m_\chi \sim 0.7$ GeV/c^2; adding a small hydrogen-bearing fraction improves kinematic matching and can push sensitivity toward ~0.5 GeV/c^2. In this context, mixtures with isobutane (iC_4H_{10}) have been studied [200, 201], and R&D on methane admixtures has identified configurations that retain the same light yield up to 5% CH_4 content. For the *SD* case, the projected reach is competitive with PICO [81] at 1 keV$_{ee}$ and can surpass it in low-background conditions when operating at 0.5 keV$_{ee}$. Unlike threshold-only detectors, directionality provides CYGNO with a powerful discriminant to check the *galactic* origin of any candidate signal.

In summary, a large-scale CYGNO detector will combine low energy thresholds, detailed imaging, and full 3D directionality in a single apparatus. The modular design eases scaling, the LNGS location and shielding suppress external backgrounds, and directionality provides a decisive test to verify the galactic origin of any candidate dark matter signal.

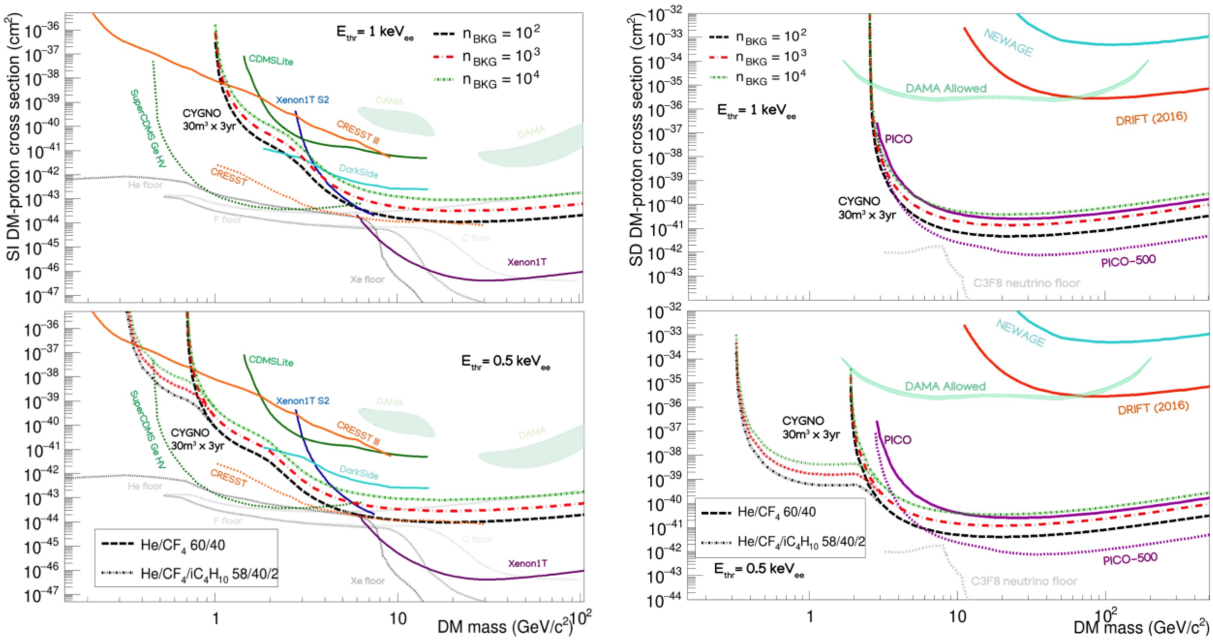

(a) (b)

Figure 3.15: Spin-independent (a) and spin-dependent (b) 90% credible-interval exclusion limits for CYGNO_30, assuming 3 years of exposure under different background scenarios and thresholds of 1 keV$_{ee}$ (top) and 0.5 keV$_{ee}$ (bottom). Dashed curves: He:CF$_4$ (60:40) with 100 (black), 1000 (red), and 10,000 (dark green) background events. Dotted curves: He:CF$_4$:isobutane (58:40:2). Solid lines: current bounds; dotted lines: projected future limits [197].

Chapter 4

LIME: the largest prototype

4.1 Design and components

LIME (Long Imaging ModulE) constitutes the final prototype within the CYGNO development program and serves as the ultimate validation detector prior to the construction of the larger-scale demonstrator. This gaseous Time Projection Chamber features optical readout capabilities and operates at atmospheric pressure and ambient temperature, with a 50-liter active volume.

4.1.1 Mechanical and electrical design

The vessel of the detector is fabricated from transparent polymethyl methacrylate (PMMA) featuring 10 mm thick walls (Figure 4.1). This acrylic container is maintained at a slight overpressure of approximately 3 mbar with respect to the external environment. Along the drift direction, the active detection region spans 50 cm and is bounded at one extremity by a copper cathode and at the opposite end by a Gas Electron Multiplier (GEM) assembly with dimensions of 33×33 cm^2 in a triple-foil stack.

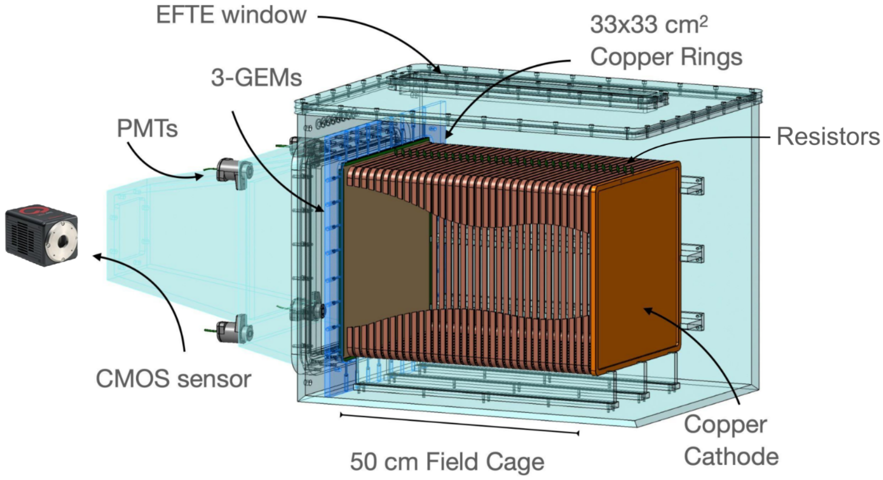

Figure 4.1: View of the LIME prototype illustrating the main components: the 50 cm drift region with copper field-shaping rings, the cathode plate, the triple-GEM amplification structure, and the positioning of the photomultiplier tubes and sCMOS camera for light collection.

Uniformity of the drift field is obtained through a field cage comprised of 34 copper rings. Each ring measures 10 mm in width with 4 mm gaps between successive elements. These rings are linked via 100 MΩ resistors, forming a voltage divider that produces a uniform gradient extending from the cathode to the amplification region. The cathode is a copper plate of 0.5 mm thickness with dimensions that match the field cage cross-section. This arrangement ensures that electric field lines maintain perpendicularity to the cathode surface across the entire drift volume.

Inside the GEM microstructures, intense electric fields initiate electron avalanches, which generate secondary electrons and ions. Scintillation photons are produced through the interaction between these secondary electrons and the gas molecules. The GEM technology provides controlled amplification while preserving the spatial information of the original ionization pattern.

The vessel wall that faces the GEM structure is manufactured with a reduced thickness of 1 mm to enhance optical transparency. This PMMA interface, however, generates reflection artifacts that are especially noticeable for alpha particle trajectories. Figure 4.2 illustrates this phenomenon: the bright track corresponds to the actual particle path, whereas a dimmer mirrored image emerges due to reflection at the PMMA-air interface.

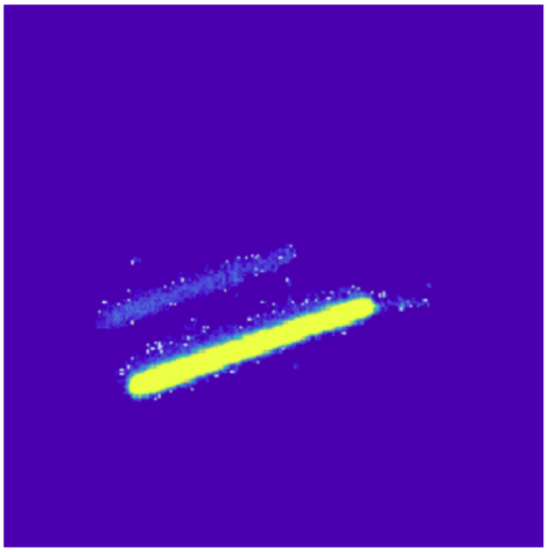

Figure 4.2: sCMOS camera image showing an alpha particle track and its reflection artifact. The brighter track corresponds to the primary ionization event, while the dimmer shadow results from optical reflection at the detector window.

A 3 mm thick aluminum Faraday cage encloses the complete detector assembly, offering electromagnetic interference shielding and light isolation. The required voltages are delivered by two independent power supply systems: an ISEG HPn 500 unit supplies the cathode with voltages up to 50 kV and voltage ripple below 0.2%, while a CAEN A1515TG module delivers up to 1 kV to the GEM electrodes with 20 mV precision.

Radiopurity screening was performed on all major detector components using high-purity germanium spectrometry at the LNGS underground facility. This screening encompasses the cathode, copper shielding elements, field-shaping rings, resistor chain, GEM foils, acrylic vessel, and camera components (lens and housing). Although LIME was assembled using commercially available materials not specifically optimized for low-background applications, these measurements represent an essential input for Monte Carlo background simulations. For the future 1 m^3 CYGNO demonstrator, radiopure alternatives have been identified that preserve detector performance while substantially reducing intrinsic radioactivity contributions.

4.1.2 Optical readout and calibration

Two complementary technologies are combined in the light detection system: a high-resolution scientific CMOS camera and fast photomultiplier tubes.

The primary imaging device is an Orca-Fusion sCMOS sensor, which features a 2304×2304 pixel array. Each pixel possesses an active area of 6.5×6.5 μm^2. A Schneider optical system (25 mm focal length, f/0.95 aperture) equips the camera and it is positioned 623 mm from the amplification plane. This configuration yields a field of view spanning 34.9×34.9 cm^2, where each pixel maps to a 152×152 μm^2 area in the detection plane.

Positioned symmetrically around the camera are four Hamamatsu R7378 photomultiplier tubes. Each PMT is equipped with a 22 mm diameter bialkali photocathode that is optimized for rapid photon detection, which enables precise timing measurements of track development.

Integrated into the upper surface of the vessel is a specialized calibration window measuring 5 cm in width and 50 cm in length. This opening is sealed with a 150 μm thick ethylene-tetrafluoroethylene (ETFE) membrane, which is transparent to low-energy photons while maintaining gas containment (Figure 4.3). Along rails positioned 18 cm above the active volume, a motorized positioning system travels while carrying radioactive sources. These sources can be positioned at distances ranging from 5 to 45 cm from the amplification plane. For beam definition, the trolley incorporates a 5 mm diameter collimator.

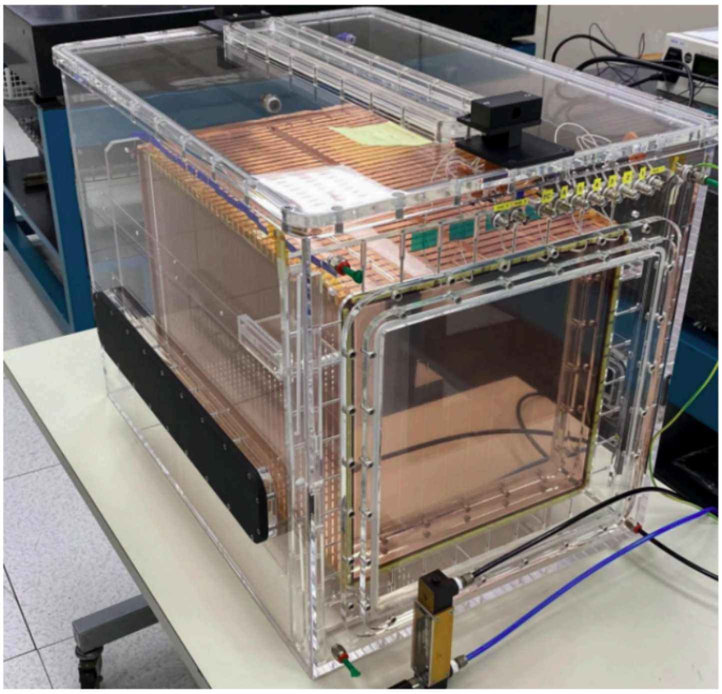

Figure 4.3: View of the LIME detector showing the acrylic vessel construction and the ETFE calibration window on the top surface.

4.2 Overground studies at LNF

Before its underground deployment, the LIME prototype underwent an extensive testing campaign at the Laboratori Nazionali di Frascati (LNF), where it operated in an overground environment for several months. This characterization phase served multiple objectives: demonstrating long-term operational stability, collecting substantial datasets for physics analysis, developing and optimizing image reconstruction algorithms, and measuring the detector's energy response across relevant energy ranges. These results have been thoroughly documented in the literature and already published [202].

The data acquisition infrastructure was based on a C++ framework integrated within the MIDAS[1] software environment. Discriminator and logic modules processed the PMT signals to produce trigger signals based on coincidence requirements, namely, simultaneous above-threshold signals from at least two of the four photomultipliers. A He:CF_4 gas mixture in a 60:40 ratio was maintained at approximately 3 mbar overpressure relative to atmospheric pressure, with continuous flow through the vessel at 200 cc/min to guarantee stable operating conditions and gas purity. The drift field was set at 0.8 kV/cm, while each GEM foil was operated at a fixed voltage of 440 V.

My contribution to this phase included extensive calibration shifts (over 50 hours of data taking with various radioactive sources), development and optimization of image analysis algorithms, and systematic studies of detector performance parameters. For the analyses presented in the following sections, the sCMOS camera operated with a 50 ms exposure time to reduce pile-up probability in the high-rate environment at surface level.

4.2.1 Sensor noise characteristics

The sCMOS sensor exhibits two main sources of baseline fluctuations: readout noise from the electronic amplification circuitry (less than 0.7 electrons RMS) and dark current from thermally-induced leakage (approximately 0.5 electrons per pixel per second)[2]. To characterize these contributions, dedicated pedestal runs were performed periodically by reducing GEM voltages to 220 V, below the amplification threshold, thus preventing any scintillation light from reaching the camera.

Each pedestal run comprised 100 consecutive images. For every pixel, the mean response ($\mathrm{pix}_{\mathrm{ped}}$) and standard deviation ($\mathrm{pix}_{\mathrm{rms}}$) were determined. Figure 4.4 shows the distribution of $\mathrm{pix}_{\mathrm{rms}}$ values, displaying a well-defined peak corresponding to typical noise levels and an extended tail from noisier boundary pixels. A fiducial volume cut excludes these edge pixels from physics analysis.

Monitoring throughout the operational period confirmed excellent stability of both pedestal baseline and noise level, which is crucial for reliable physics measurements and ensures that observed variations in energy spectra reflect genuine detector conditions rather than sensor drift.

4.2.2 Light yield and calibration

Accurate energy calibration requires a reliable method for converting camera counts into physical energy. A ^{55}Fe radioactive source provides the primary reference standard (Figure 4.5). This isotope emits characteristic X-rays at 5.9 keV (Mn K_α line) through electron

---

[1] https://daq00.triumf.ca/MidasWiki/index.php/Main_Page

[2] https://www.hamamatsu.com/jp/en/product/cameras/cmos-cameras/C14440-20UP.html

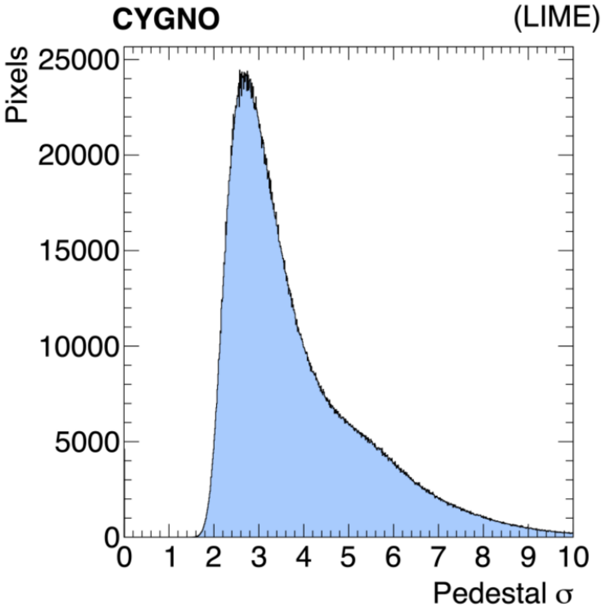

Figure 4.4: Distribution of pixel-level RMS noise (pix_{rms}) measured during a typical pedestal run. The main peak represents nominal sensor performance, while the tail corresponds to noisier boundary pixels [202].

capture decay. These monoenergetic X-rays interact with the gas via photoelectric effect, generating compact, quasi-circular spots covering approximately 20 mm^2 in the camera images.

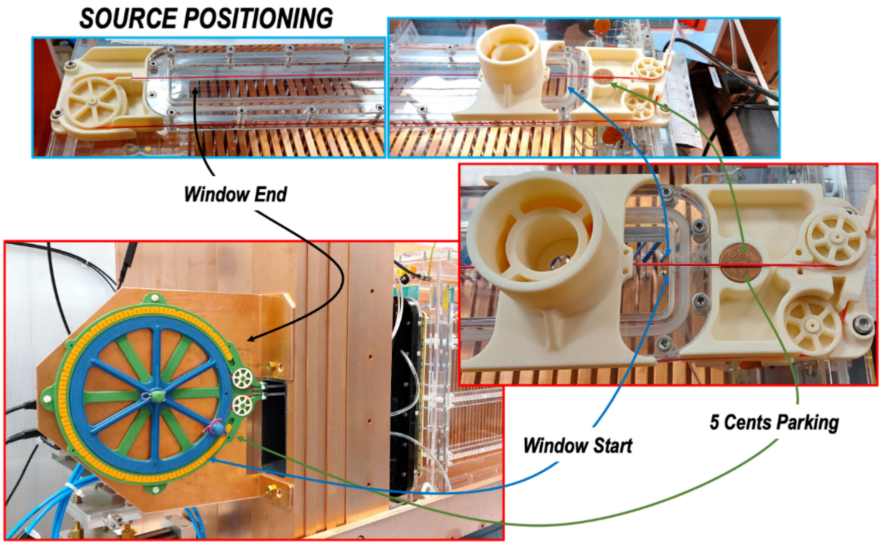

Figure 4.5: Automated system for moving the ^{55}Fe source along the detector window. The motorized wheel drives the trolley through pulleys, allowing precise positioning during calibration measurements.

Reconstruction analysis extracts individual tracks and their physical properties. For this configuration, the light yield typically ranges around 10^3 counts per keV, though it varies with environmental factors such as atmospheric pressure, temperature, and gas composition. Systematic calibration using the ^{55}Fe reference maintains accurate energy measurements throughout operations.

4.2.3 Gain saturation effect

The electron avalanche process in GEM structures produces substantial charge accumulation that can alter local electric fields, particularly in the final amplification stage. This space-charge effect reduces the multiplication factor, a phenomenon termed gain saturation. The magnitude depends on total charge and its spatial density, which correlates with the particle's specific energy loss ($\mathrm{d}E/\mathrm{d}x$).

Figure 4.6 shows systematic measurements using a ^{55}Fe source at various distances from the GEM plane. The saturation effect becomes more pronounced as the source approaches the amplification region. Diffusion plays a key role: as electrons drift through the 50 cm field region, transverse diffusion spreads the charge over a larger area. When ionization occurs far from the GEMs, the more diffuse electron cloud reaching the amplification region experiences less space-charge buildup and consequently less gain suppression.

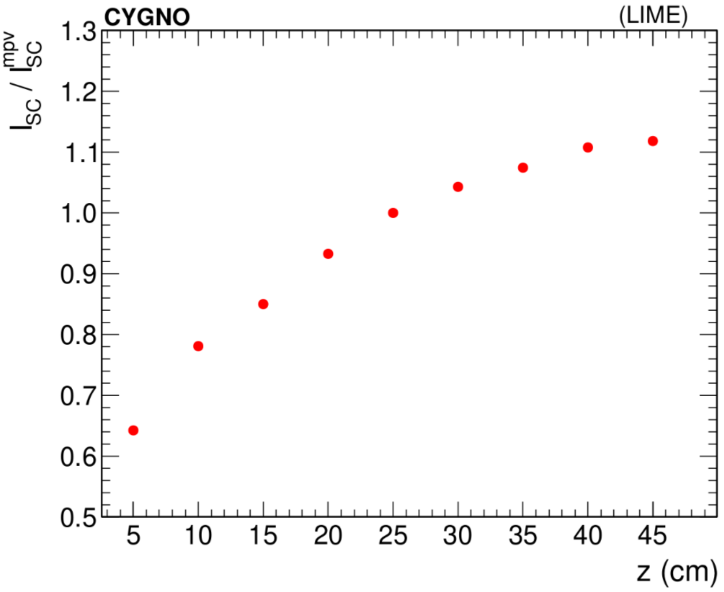

Figure 4.6: Average light integral for ^{55}Fe clusters as a function of distance from the GEM plane. The increasing light yield with distance reflects reduced gain saturation where diffusion has spread the charge over larger areas [202].

This saturation effect is extensively studied in the following chapters, where its impact on energy reconstruction and particle discrimination is analyzed in detail for both electron and nuclear recoils.

4.2.4 Energy response

Multiple radioactive sources spanning photon energies from 3.7 keV to 37 keV were employed to characterize the detector's energy response across the low-energy range relevant for dark matter searches. A multi-target source based on alpha particles from ^{241}Am impinging on different materials (Cu, Rb, Mo, Ag, Ba) provided X-rays in the 8–36 keV range. Figure 4.7 shows the configuration where alpha particles with approximately 5 MeV energy strike metallic targets mounted on a motorized rotating wheel.

The alpha particles ionize inner shells of target materials, creating vacancies subsequently filled by outer-shell electrons. This produces monochromatic K_α and K_β X-rays that enter the detector and interact via photoelectric effect. For lower energies, the ^{55}Fe

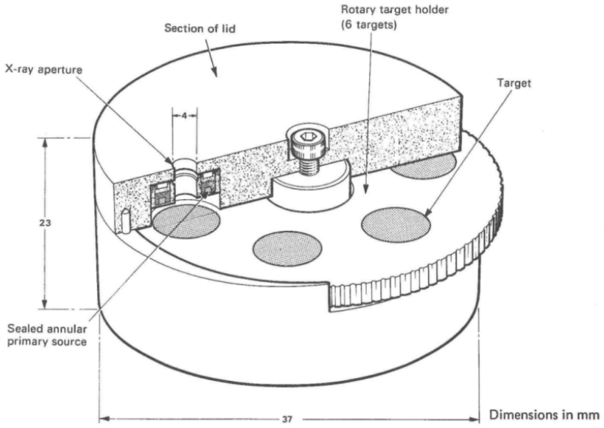

Figure 4.7: Schematic of the multi-target X-ray source system. Alpha particles from ^{241}Am strike different metallic targets, inducing characteristic X-ray emission directed into the detector volume [202].

source excited calcium (Ca) and titanium (Ti) targets through fluorescence, yielding lines around 3.7 keV and 4.5 keV. Table 4.1 summarizes all X-ray lines used.

Source	$\mathbf{E_{K_\alpha}}$ [keV]	$\mathbf{E_{K_\beta}}$ [keV]	**Distance from GEM** [cm]
Ca*	3.69	4.01	25
Ti*	4.51	4.93	25
Fe	5.9	6.5	5–45
Cu†	8.04	8.91	25
Rb†	13.37	14.97	25
Mo†	17.44	19.63	25
Ag†	22.10	24.99	25
Ba†	32.06	36.55	25

Table 4.1: X-ray lines used for energy response characterization. † Multi-target sources (Cu, Rb, Mo, Ag, Ba) based on ^{241}Am. $*$ Lines induced by ^{55}Fe fluorescence (Ca, Ti). Iron lines (Fe) come directly from the ^{55}Fe source in a lead container. Most sources at 25 cm from GEM; Fe also operated at 5, 35, and 45 cm.

Figure 4.8 shows camera images of electron recoils at different energies. Tracks appear as compact spots at lower energies (around 8 keV), where electron range is smaller than the diffused ionization cloud. Above approximately 15 keV, tracks exhibit visible extension with distinguishable trajectories.

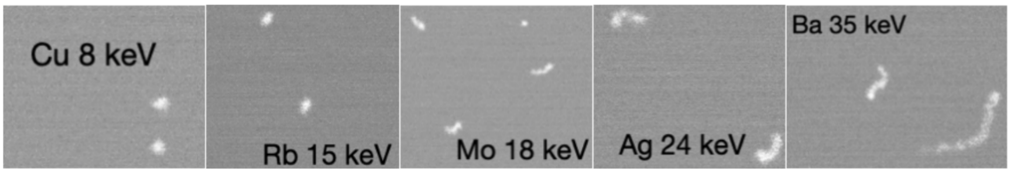

Figure 4.8: sCMOS images of electron recoils at different energies. Morphology transitions from compact spots at lower energies to extended tracks as electron range increases [202].

The reconstruction algorithm identifies individual light clusters corresponding to deposited energy. For each source dataset, the total energy distribution was analyzed, showing distinct peaks from monoenergetic X-rays superimposed on an exponential background from natural radioactivity. Each spectrum was fitted with two Cruijff functions (for K_α and K_β lines) plus an exponential background.

Figure 4.9 presents calibrated energy spectra from sources at $z = 25$ cm. Detector linearity is demonstrated in Figure 4.10, plotting estimated energy response versus expected values from atomic physics. Both K_α (black points) and K_β (orange squares) follow a linear relationship from 3.7 keV to 37 keV. The close agreement with the ideal response (dotted line) demonstrates excellent linearity and validates the detector's capability for accurate energy reconstruction across the energy range of interest for low-mass dark matter searches. A slight deviation from perfect linearity can be observed at the highest energies, where the increasing spatial extension of electron tracks may affect the detector response and the reconstruction performance, leading to a less ideal energy estimate.

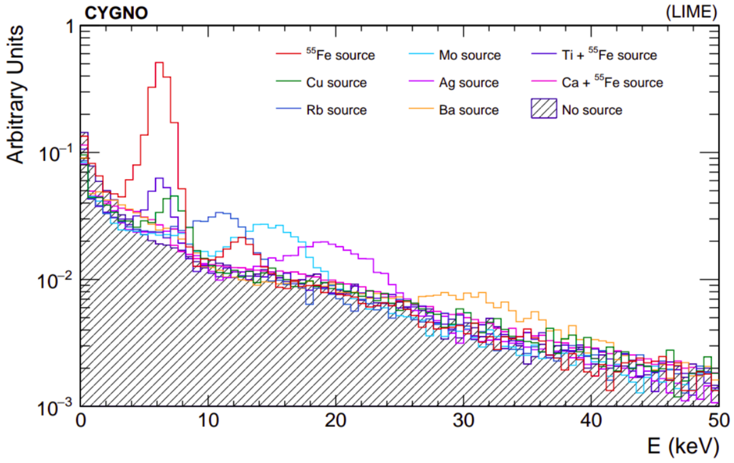

Figure 4.9: Calibrated energy spectra with sources at $z = 25$ cm. Each spectrum shows K_α and K_β peaks on the background continuum [202].

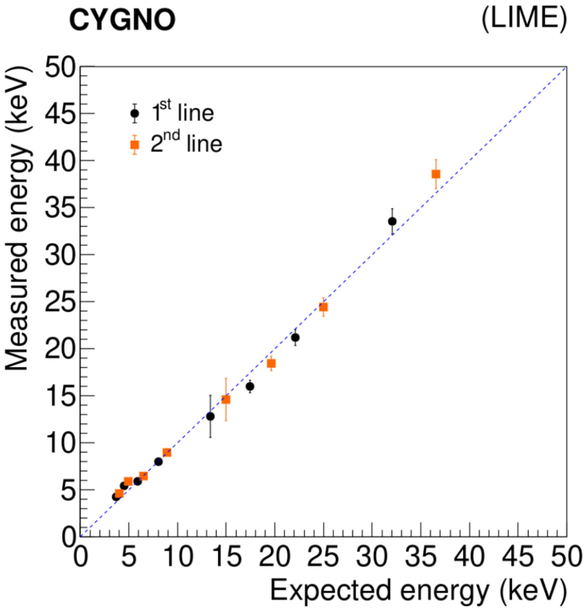

Figure 4.10: Energy response versus expected values for K_α (black circles) and K_β (orange squares) lines. Dotted line represents perfect linearity. Excellent agreement from 3.7 to 37 keV [202].

4.2.5 Energy threshold

Noise fluctuations not eliminated by zero-suppression are occasionally mis-identified as real spots by the image reconstruction algorithm. Analysis of pedestal runs (where no genuine tracks are expected) quantified this contribution. False-positive clusters become negligible above approximately 400 camera counts, corresponding to roughly 0.5 keV deposited energy.

The effective energy threshold was established at approximately 1 keV by requiring false-positive rates below 10 events per year, negligible contamination for the physics program. For a gaseous detector at atmospheric pressure, this threshold represents excellent performance and enables sensitivity to low-energy recoils relevant for dark matter and neutrino physics.

4.2.6 Longitudinal position reconstruction

Thanks to the effect of transverse diffusion of the ionization cloud during drift, the z - coordinate (distance from the GEM plane) can be inferred from the light pattern morphology. The charge distribution spreads laterally during drift, with spreading proportional to the square root of drift distance.

Using the ^{55}Fe source at known distances, a morphological parameter ζ was defined as the product of the Gaussian width of the transverse intensity profile (σ_T) and the standard deviation of pixel intensities (I_{rms}). Figure 4.11 shows ζ distributions versus source distance, confirming that spot morphology encodes drift distance information.

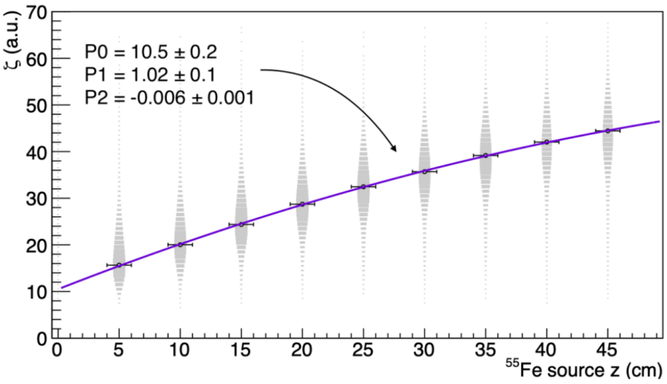

Figure 4.11: Morphological parameter ζ for ^{55}Fe spots at different distances from the GEM plane, demonstrating feasibility of longitudinal position reconstruction [202].

Event-by-event fluctuations limit the z-resolution to approximately 4–8 cm depending on drift distance. While insufficient for precise 3D tracking, this provides useful information for background rejection and correcting diffusion and saturation effects.

4.3 Underground installation at LNGS

In February 2022, the LIME detector was transported to the underground LNGS facility, with operations beginning in June 2022 following successful commissioning. The detector setup was located in a dedicated structure within the TIR gallery between Hall A and Hall B and occupies two levels. LIME and its shielding configurations are contained on the lower level, while the upper level houses the control room, data acquisition servers, electronic modules, and voltage–supply systems. Adjacent to the structure is a specialized gas system developed through collaboration between the CYGNO experiment and Air Liquide.

The data taken in these periods are used in the next chapters to validate the simulation and to support the analyses presented thereafter.

4.3.1 Gas system

Four essential functions are performed by the gas delivery system: supplying a He:CF_4 mixture in 60:40% proportions, chemically purifying contaminants, recirculating the gas mixture, and recovering it for disposal. A cart and four cylinders arranged in a bank configuration comprise the system: two supply cylinders containing He and CF_4, and two recovery cylinders with a maximum operating pressure of 40 bar. The gas mixture is fully recovered from the system, preventing any atmospheric discharge. This enables both purification and recirculation within the detector, along with proper recovery for greenhouse gas disposal.

Starting in July 2023, recirculation capabilities were added. Prior to this upgrade, gas from supply bottles flowed through LIME and was collected directly into recovery bottles. With the recirculation configuration, a pump at the LIME chamber output increases gas pressure to 1-2 bar above atmospheric in a buffer volume. The gas is driven through a flowmeter into a purification system with commercial filters by this overpressure. Before returning to the LIME volume, fresh gas from supply bottles at levels of $\mathcal{O}(20\%)$ or below is mixed with the recirculated gas. Pressure progressively builds in the recirculation buffer volume as fresh gas is introduced and is then periodically transferred via pressure booster into recovery bottles.

Commercial oxygen traps constitute the current purification filters, though plans exist to replace them with 5A molecular sieves for radon contamination removal. Custom, low-radioactivity molecular sieves are being developed by Sheffield University (UK) collaborators [203, 204] for evaluation in subsequent phases of the CYGNO experiment.

4.3.2 Data acquisition system (DAQ)

Data collection and processing of acquired signals are managed by the DAQ system. PMT signals in LIME are transmitted to both a digitizer and a discriminator. A logic module receives these outputs and generates the trigger for image acquisition when coincidence of at least two out of four PMTs occurs.

An sCMOS ORCA-Fusion camera with a rolling shutter for pixel exposure is employed by LIME. Each line is exposed sequentially by the sensor with a time delay, ensuring uniform exposure duration across all rows while varying the exposure timing. When operating in external trigger mode, sensor exposure begins via software command. This differs from the PMT trigger, which initiates image collection only when tracks are present, thereby avoiding unnecessary image acquisition.

The selected scan mode, which varies with electronic noise levels, determines row activation speed. When operating in the lowest noise mode, LIME requires 80 μs per row activation, totaling 184 ms for the complete sensor. Sequential activation from top to bottom occurs for the rows, which remain open for a preset exposure duration of 300 ms before readout. To maintain low track occupancy per image even under high background conditions, this exposure time was chosen, minimizing event pile-up while maximizing exposure duration.

A total of 484 ms (184+300 ms) represents the period during which the sensor remains partially or fully open. Images are saved and stored only when a PMT trigger occurred during this window; otherwise they are discarded. The external software trigger is sent to the camera to restart row exposure following image readout (or direct discard). Dead time is introduced into the acquisition process by this operational mode.

4.3.3 LIME underground data taking program

The operation of LIME at LNGS is motivated by several key goals, including the validation of the detector technology in a deep-underground environment, the demonstration of long-term stability for the detector and its auxiliary systems, the measurement of effective background from intrinsic radioactivity and external sources, and the assessment of passive-shielding performance. To support these studies, a detailed Monte Carlo (MC) simulation of the LIME setup and of the dominant expected background contributions was developed. This simulation represents a central and original component of the work presented in this thesis.

A primary goal of underground data taking is validating the MC simulation, which enables proper optimization of PHASE_2 experiment design and materials while demonstrating full understanding of the experimental approach. MC simulation results formed the basis for optimizing the data taking campaign program for LIME underground. To extensively study and identify different background sources while achieving LIME's objectives, a staged approach with progressively increasing shielding thickness was established, as summarized in Table 4.2.

Table 4.2: Summary of the LIME underground data-taking campaign, including the dates, number of runs, and types of shielding used. Each recorded run consists of 400 pictures, each containing at least one triggered signal observed by the PMTs.

Phase	Dates	# runs recorded	Shielding
Run 1	08/11/2022 – 06/12/2022	3744	None
Run 2	15/02/2023 – 09/03/2023	3487	4 cm Cu
Run 3	05/05/2023 – 16/11/2023	22276	10 cm Cu
Run 4	30/11/2023 – 22/04/2024	16099	10 cm Cu + 40 cm H_2O
Run 5	17/05/2024 – 31/12/2024	>25000	10 cm Cu

- **Run 1:** The first data acquisition phase following commissioning studied and fully characterized external backgrounds. LIME remained in its original configuration within the aluminum Faraday cage used during overground tests at LNF, with no additional shielding added for this run. The natural gamma flux in the laboratory was the dominant background source. Completion of this phase occurred in autumn 2022, with data collection spanning from 08/11/2022 to 06/12/2022 and recording 3744 runs without additional shielding.

- **Run 2:** Around LIME on all sides, a 4 cm thick copper shield was installed, suppressing external gammas by approximately a factor of 50. Both event rate in the detector and track occupancy in images were significantly reduced. Internal background contributions became more significant in this phase, although external sources remained dominant. Winter 2023 saw the completion of this phase. The run period extended from 15/02/2023 to 09/03/2023, collecting 3487 runs with 4 cm Cu shielding.

- **Run 3:** Total shielding thickness around LIME was increased to 10 cm through the addition of copper bars. External background sources were suppressed to levels comparable with internal detector material radioactivity contributions. Starting in summer 2023 and concluding in early November 2023, this phase marked the first extended data-taking period lasting several months without interruption. Gas system recirculation parameters and filters were optimized during this run, causing significant changes in light yield and alpha background rates. These tests, while determining detector response stability and data quality, proved critical for developing an optimized and stable gas system configuration by the run's end. Subsequent runs employed this configuration successfully, ensuring high-quality data for physics analysis. An AmBe neutron source was also used during Run 3 for measurements aimed at optimizing signal identification and background rejection with a clean NR sample. The run spanned from 05/05/2023 to 16/11/2023, recording 22276 runs with 10 cm Cu shielding.

- **Run 4:** In this configuration, water tanks were mounted around LIME, providing a 40 cm thick hydrogen-rich layer to moderate environmental neutrons and minimize external source-induced NR background. External neutron flux contribution is reduced to approximately 2 NR/year by this setup, allowing more accurate characterization of internal neutron recoil background. December 2023 saw the installation of the water shielding. During Run 4, data collection focused on introducing gas filters to minimize impurities, which had the additional benefit of reducing alpha background by lowering radon emanation inside LIME. From 30/11/2023 to 22/04/2024, the run period collected 16099 runs with 10 cm Cu + 40 cm H_2O shielding.

- **Run 5:** Performing spectral and directional measurements of environmental LNGS neutron flux constitutes the main objective of Run 5, achievable only without water shielding, as part of the "Zero Radioactivity for Future Experiments" project (PRIN Prot. 2017T5J9J9). A quasi-background-free dataset at energies above 2 keV is expected based on current CYGNO background predictions, owing to the achieved ER-NR discrimination capabilities [205]. Over 6 months, preliminary simulations suggest approximately 250 external neutron recoil events are expected, significantly exceeding the roughly 19 events originating from internal background in one year (after data cuts) [206]. This provides an opportunity to improve current understanding of underground neutron flux at LNGS [207–209], particularly at low energies (< 1 MeV), and to conduct in-depth study of CYGNO's capabilities in 3D-reconstruction, directionality, and energy resolution for NR events, which represent the expected signal from WIMP in CYGNO. Starting on 17/05/2024, the run was ongoing at the time of writing, with more than 25000 runs recorded with 10 cm Cu shielding.

LIME has been successfully operated underground for over two years, during which substantial data has been collected. Analysis of Run 2 and Run 3 revealed discrepancies between observed data and MC simulations, prompting more in-depth study of gas purity and light-related backgrounds. Data from Run 4, which provided high statistics and stable gas and light yield conditions, is primarily used in the analysis presented in this thesis, resulting in particularly clean datasets.

4.4 Track reconstruction

An image–analysis chain has been developed to extract tracks from sCMOS frames, while the full exploitation of PMT waveforms is still being refined. The workflow is Python-based and centers on DBSCAN (Density-Based Spatial Clustering of Applications with Noise) [210]; its intensity-weighted variant, *iDBSCAN* [211], improves robustness to sparse or inhomogeneous deposits by treating pixel intensity as a photon–count proxy. Diverse ionization patterns are generated by interactions in gas, with tortuous and gradually brightening paths for $\mathcal{O}(10)$ keV electrons and short, dense segments for nuclear recoils (NRs). This requires the algorithm to identify tracks and disentangle their overlaps, which are common in surface data due to cosmic rays and ambient radioactivity.

Preprocessing and clustering

A 2304×2304 array of raw ADC counts I_{ij} constitutes each sCMOS frame. Pedestal runs (low GEM voltage, no amplification) provide per-pixel noise maps: the mean μ_{ij} and standard deviation σ_{ij} are stored and used to form pedestal-subtracted images $I_{ij}^{\mathrm{sub}} = I_{ij} - \mu_{ij}$. Zero suppression is then applied,

$$I_{ij}^{\mathrm{ZS}} = \begin{cases} 0, & I_{ij}^{\mathrm{sub}} < n_\sigma \, \sigma_{ij} \\ I_{ij}^{\mathrm{sub}}, & \text{otherwise,} \end{cases}$$

with n_σ tuned per run by adjusting its value until the number of reconstructed tracks matches the PMT count, while visually verifying that the reconstruction properly captures individual tracks without cutting or merging them.

Optical non-uniformities in the camera response are corrected using a *vignetting map*, which is derived from flat-field images acquired by illuminating a uniform surface. To minimize any directional bias introduced by the optical system, the camera is physically rotated during the acquisition of these calibration images. The resulting map provides a pixel-by-pixel correction factor, normalizing each pixel's response to that of the central region. This 2D correction is applied *after* noise suppression rather than before, since applying it to raw data would amplify statistical fluctuations in the noisy regions.

Once the image has been processed through pedestal subtraction, zero suppression, and vignetting correction, all remaining non-zero pixels are grouped into physically meaningful clusters using a custom algorithm called *iDBSCAN* [211]. This is a modified version of the well-known DBSCAN clustering algorithm [210], adapted specifically for optical readout of particle tracks. The key difference is that instead of simply counting neighboring pixels within a search radius ε, iDBSCAN weighs them by their *light intensity*, making it sensitive to the actual energy deposited. Two parameters control the balance between fragmenting a single track and incorrectly merging separate ones: the search radius ε and the minimum support threshold $N_{\min}$, which are tuned for each data set (typical values are $\varepsilon \in [1, 10]$ pixels and $N_{\min} \in [4, 30]$).

The clustering proceeds in multiple passes to handle different track types. The first pass targets dense, bright deposits such as nuclear recoils and alpha particles, which appear as compact spots. Subsequent passes use relaxed thresholds to recover fainter structures like electron recoils and dim track tails. This multi-pass strategy improves the separation of overlapping events, and seed clusters belonging to the same physical track are then merged together through *superclustering*.

To refine track boundaries, a region-based segmentation algorithm [212] partitions the image by comparing average intensities rather than relying on sharp edges. This approach works well for both sharp and blurred features, substantially improving reconstruction quality for all track types.

For long, nearly straight tracks (most commonly produced by cosmic-ray muons), a specialized directional clustering step is applied using *iDDBSCAN* [213]. This method identifies line-like structures and fits them with piecewise polynomials (up to third order), iteratively growing the track by including nearby pixels that fall within a narrow band around the fitted curve.

Finally, a tight-radius scan recovers any small, isolated deposits missed in previous passes, while an isolation veto suppresses spurious clusters near large cosmic tracks.

Feature extraction and data format

A compact set of observables tailored to classification and calibration is computed once tracks are defined, and stored (together with run/event metadata) in a ROOT `TTree` [214] for efficient selections, plotting, and multivariate analyses. The reconstruction output contains both event-level information (run number, event number, pedestal run used for subtraction) and cluster-specific quantities stored in array branches indexed by the number of reconstructed clusters (`nSc`).

For each identified cluster (or supercluster, `sc`), the following key features are extracted:

- **Cluster size and pixel content.** The variable `sc_size` records the total number of pixels in the cluster before zero suppression, while `sc_nhits` gives the number of pixels above the zero-suppression threshold. Individual pixel information is stored in separate branches (`redpix_ix`, `redpix_iy`, `redpix_iz`), where the z component represents the pedestal-subtracted counts for each pixel.

- **Light yield and energy.** The uncalibrated integral of all pixel counts in the cluster is stored as `sc_integral`.

- **Geometric properties from PCA.** Principal component analysis yields `sc_length` (major axis) and `sc_width` (minor axis), describing the projected footprint. The polar angle of the major axis is given by `sc_theta`. The barycenter position is recorded as (`sc_xmean`, `sc_ymean`), while the spatial extent is defined by the extreme coordinates (`sc_xmin`, `sc_xmax`, `sc_ymin`, `sc_ymax`).

- **Statistical moments and profile characteristics.** The RMS of pixel intensities across the cluster is stored as `sc_rms`. Truncated RMS values along the major and minor axes (`sc_longrms`, `sc_latrms`) and full RMS values (`sc_lfullrms`, `sc_tfullrms`) characterize the intensity distribution.

- **Gaussian profile fits.** Longitudinal and transverse intensity profiles are fitted with Gaussian functions. For the longitudinal direction, the stored parameters include amplitude (`sc_lgaussamp`), mean position (`sc_lgaussmean`), standard deviation (`sc_lgausssigma`), chi-squared (`sc_lchi2`), and fit status (`sc_lstatus`). Analogous quantities exist for the transverse profile (`sc_tgaussamp`, `sc_tgaussmean`, `sc_tgausssigma`, `sc_tchi2`, `sc_tstatus`).

- **Peak characteristics.** The longitudinal profile's main peak is characterized by its amplitude (`sc_lp0amplitude`), prominence relative to the local baseline (`sc_lp0prominence`), full width at half maximum (`sc_lp0fwhm`), and mean position from the cluster start (`sc_lp0mean`). The transverse profile's main peak FWHM is stored as `sc_tp0fwhm`.
- **Additional morphological descriptors.** The curved path length obtained via skeletonization is recorded as `sc_pathlength`. The Pearson correlation coefficient (`sc_pearson`) provides a measure of linear correlation in the spatial distribution of the cluster.

Chapter 5

Simulation of the detector response

The simulation of sCMOS images and PMT waveforms from particle interactions is crucial for optimizing detector performance and achieving a comprehensive understanding of its response characteristics. Within the CYGNO collaboration, a dedicated effort has been carried out to develop a sophisticated simulation framework capable of generating realistic sCMOS-like images and PMT signals for both electron and nuclear recoil tracks. The author of this work has played a central role in the implementation of the image simulation, including the modeling of optical signal formation, digitization effects, and detector response. This simulation chain, shown in Fig. 5.1, accounts for all relevant detector effects and accurately reproduces the readout behavior of the detection system.

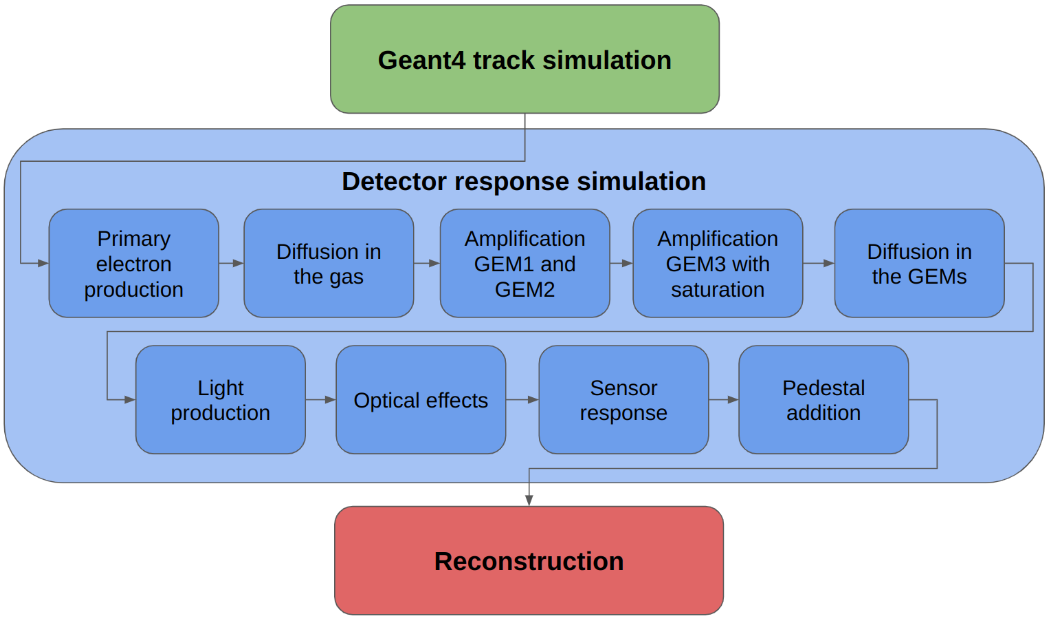

Figure 5.1: Overview of the simulation workflow: Geant4 generates the particle tracks, the detector response is simulated as detailed in Section 5.2, and the resulting images are reconstructed with the same analysis tools used for data, allowing the extraction of relevant features.

The simulation workflow begins with the generation of primary particle tracks using Geant4 to simulate their interaction with the gas mixture. Once the primary tracks are generated, a series of detector effects are sequentially applied to reproduce the physical processes occurring in the real detector.

The primary electrons produced through ionization in the gas undergo drift toward the amplification region, experiencing diffusion during this process. At the amplification stage, the electrons are multiplied in the GEM planes, where additional diffusion, gain fluctuations, and saturation effects significantly influence the final signal. Light production occurs during the amplification process, and this optical signal is subsequently recorded by the sCMOS camera after accounting for fluctuations in photon yield and optical effects introduced by the lens system. Simultaneously, the light is also detected by the PMT system, which provides complementary timing and energy information.

The simulation parameters have been extensively tuned through continuous comparison with experimental data acquired using the LIME prototype detector. This iterative optimization process resulted in excellent agreement between simulated and measured tracks, both in terms of detector response and topological shape variables. In the absence of low-energy electron sources with well-defined direction, these validated simulated tracks serve as an essential tool for assessing the angular resolution performance for low-energy electron recoils.

The overall workflow of the simulation chain is illustrated in Fig. 5.1, which shows the sequential application of all detector effects from the initial particle interaction to the final digitized images and waveforms.

5.1 Primary track simulation

The first step in the simulation chain involves generating the primary particle tracks that represent the initial interaction of particles with the detector medium. The simulation approach is nearly identical for both electron recoils (ERs) and nuclear recoils (NRs), with the key difference being the application of the quenching factor for nuclear recoils to account for the reduced ionization efficiency of recoiling nuclei compared to electrons.

Particle interactions with the CYGNO gas mixture are simulated using the Geant4 software toolkit [215, 216]. Geant4, which stands for GEometry ANd Tracking, is a comprehensive platform designed for simulating particle passage through matter using Monte Carlo methods. The toolkit provides a flexible framework where particles are generated from a defined source point, and their trajectory through a specified material is determined by modeling the relevant physics processes.

In Geant4, each physics process is implemented as a C++ class that computes the interaction probability (characterized by the mean free path) and generates the final state of the particle after the interaction. Different theoretical models can be employed to describe each process, and a single particle may undergo multiple processes during its propagation. For electrons in gas, these processes include ionization (which produces the primary electrons that form the track), bremsstrahlung radiation (leading to photon emission), and delta ray production (generating energetic secondary electrons). Each secondary particle produced follows the same computational framework, creating a cascade of interactions until all particles either come to rest or exit the simulation volume.

For the LIME detector simulation, tracks are produced in a gas mixture consisting of He:CF_4 in a 60:40 volume ratio at atmospheric pressure. The total gas density is calculated as the percentage-weighted average of the densities of the individual gas components. Throughout the simulation, various physical quantities such as energy, position, energy deposit, and traversed volumes are accessible and can be extracted or modified as needed.

5.1.1 Quenching factor application for nuclear recoils

For nuclear recoils, the simulation framework is identical to that used for electron recoils, but an additional correction is applied to account for the reduced ionization yield of recoiling nuclei. This correction is implemented through a quenching factor (QF), which modifies the energy deposited at each simulation step to reflect the actual observable ionization signal.

The quenching factor is defined as $\mathrm{QF}(E) = f(E)/(1+f(E))$, where $f(E) = k(E+aE^b)$ is an empirical function that depends on the kinetic energy E of the recoiling nucleus. The parameters k, a, and b are ion-specific and have been determined through SRIM simulations [175, 217]. For the three main recoiling nuclei in the $\mathrm{CF_4}$:He mixture, the quenching parameters are:

- Helium (^{4}He): $k = 0.1406$, $a = 3.388$, $b = 0.2901$
- Carbon (^{12}C): $k = 0.02162$, $a = 13.89$, $b = 0.28$
- Fluorine (^{19}F): $k = 0.008739$, $a = 27.29$, $b = 0.2785$

It should be noted that the quenching parameters listed above were not obtained through a direct experimental measurement within this thesis work, but were derived from SRIM-based calculations as reported in [217]. In the Geant4 code, the quenching correction is applied step-by-step during the particle tracking. After each energy deposition event, the code checks the particle type: if the particle is identified as a nucleus (helium, carbon, or fluorine), the deposited energy is multiplied by the corresponding factor evaluated at the current kinetic energy of the particle.

The correction applied to each energy deposition step is not simply $\mathrm{QF}(E)$, but rather the derivative of the quenched energy with respect to the initial energy:

$$\frac{dR}{dE} = \mathrm{QF}(E) + E \cdot \frac{d\mathrm{QF}(E)}{dE} = \frac{f(E)}{1+f(E)} + E \cdot \frac{f'(E)}{(1+f(E))^2} \tag{5.1}$$

where $f'(E) = k(1+abE^{b-1})$ is the derivative of $f(E)$. This approach ensures that the total quenched energy deposited along the track correctly integrates to $E \cdot \mathrm{QF}(E)$.

5.1.2 Step size optimization for low-energy tracks

A critical aspect of achieving accurate low-energy electron track simulation is the proper configuration of the step function parameters that control energy loss calculations. Geant4 operates using the finite element method (FEM), which means that particle interactions with matter are processed through discrete steps rather than continuously. For processes involving continuous energy loss, such as ionization, it is essential to use sufficiently small steps to accurately account for the energy dependence of the interaction cross-section. If the step size is too large, the assumption of constant cross-section during the step becomes invalid, leading to inaccurate results. Conversely, using excessively small steps throughout the entire track development becomes computationally prohibitive.

To address this challenge, Geant4 employs a smooth step function that dynamically regulates the maximum step size based on the particle range at its current energy. This function is controlled by two key parameters and is given by the following equation:

$$\Delta S_{\mathrm{lim}} = \alpha_R R + \rho_R(1-\alpha_R)\left(2 - \frac{\rho_R}{R}\right) \tag{5.2}$$

where α_R is the `dRoverRange` parameter, ρ_R is the `finalRange` parameter, and R represents the particle range at the energy of the current step. From this equation, it can be seen that α_R represents the limiting ratio of ΔS_{lim} to R at high energies, while ρ_R represents the range value at which $\Delta S_{\text{lim}} \sim R$.

Since Geant4 was primarily developed for high-energy physics applications, these parameters require careful adjustment for low-energy studies. For the simulation of low-energy electron recoils in CYGNO, very small steps are necessary to ensure sufficient density of energy deposits for accurate track formation and precise calculation of interaction processes. Initial simulations using default Geant4 parameters produced tracks that, after digitization, exhibited discontinuities because consecutive energy deposits were spaced too far apart. To resolve this issue, the step function parameters were optimized to $\alpha_R = 0.01$ and $\rho_R = 0.001$ mm.

For each simulated particle, the simulation stores comprehensive information about the track, including the three-dimensional coordinates of each energy deposit point (x, y, z) and the energy released at each location, ΔE. This detailed track information serves as input for the subsequent stages of the simulation chain.

5.2 Track digitization

Once the primary particle tracks have been generated using Geant4, the next crucial step is to transform these Monte Carlo energy deposits into realistic detector signals through a comprehensive digitization algorithm. This algorithm sequentially applies all the physical processes that occur in the real detector, from the initial gas ionization to the final light detection. The digitization procedure must accurately model each stage of signal formation to ensure that the simulated tracks reproduce as closely as possible the characteristics observed in experimental data.

The digitization algorithm processes the three-dimensional energy deposit information $(x, y, z, \Delta E)$ from the primary track simulation and applies the following sequence of physical effects:

- **Primary electrons production:** The energy deposited at each point along the track creates primary electrons through ionization of the gas molecules. In reality, the ionization process is highly complex, involving primary and secondary ionization, cluster formation, and non-uniform charge distribution along the particle trajectory [120]. For computational efficiency, the simulation employs a simplified approach using average values: the number of electrons produced at each step is sampled from a Poissonian distribution based on the deposited energy and the effective ionization potential of the gas mixture.

- **Drift and diffusion in the gas:** The primary electrons drift toward the amplification region under the influence of the applied electric field. During this drift process, the electron cloud undergoes diffusion, causing the initially localized charge to spread both transversely and longitudinally. The diffusion coefficients depend on the electric field strength and the gas properties.

- **Amplification in the GEM planes:** Upon reaching the GEM foils, the electrons undergo avalanche multiplication. This amplification process is characterized by several important effects:

  - Additional diffusion occurs as electrons pass through the GEM holes, further broadening the charge distribution
  - The GEM gain exhibits statistical fluctuations, leading to variations in the number of electrons produced even for identical input charges
  - Saturation effects become significant at high charge densities, reducing the effective gain

- **Light production:** The amplification process generates scintillation photons through excitation and de-excitation of gas molecules. The number of photons produced is subject to statistical fluctuations and depends on the properties of the gas mixture, particularly of the CF_4 component which is responsible for most of the light emission.

- **Optical effects:** The photons emitted in the amplification region propagate through the detector volume and a fraction of them reaches the optical sensors. During this propagation, several optical effects modify the spatial and intensity distribution of the light:
  - The lens system introduces geometric distortions and vignetting effects, which reduce the light collection efficiency at the edges of the field of view
  - Light absorption and scattering in the gas and on detector surfaces attenuate the signal

- **Sensor response and pedestal addition:** Finally, the photons are converted into electronic signals by the sCMOS camera and PMT detectors. For the sCMOS sensor, the simulation incorporates electronic noise by adding a baseline level (pedestal) characteristic of the detector readout. For the PMTs, the quantum efficiency of the photocathode is applied to determine the probability of photon detection.

Each of these steps is carefully modeled using parameters that have been measured experimentally or tuned through comparison with data. The sequential application of all these effects transforms the idealized Monte Carlo track into a realistic detector image that includes all the complexities present in actual measurements. This comprehensive approach is essential for accurate performance studies and for developing analysis algorithms that can be reliably applied to both simulated and real data.

The following subsections will provide detailed descriptions of the most important stages of this digitization process, with particular emphasis on those aspects that are crucial for reproducing the observed track characteristics.

5.2.1 Primary electron production and absorption

Each primary energy deposit from the Geant4 track simulation is characterized by a three-dimensional position (x, y, z) and the energy released at that point, ΔE. The digitization process begins by converting these energy deposits into primary ionization electrons, which represent the initial charge signal that will eventually be detected.

The average number of ionization electrons produced, $\bar{N}_e$, is directly proportional to the deposited energy and is given by:

$$\bar{N}_e = \frac{\Delta E}{W_i} \tag{5.3}$$

where W_i is the w-value of the gas mixture, representing the mean energy required to create a single electron-ion pair through ionization.

For the CYGNO gas mixture of He:CF$_4$ in a 60:40 volume ratio, the effective w-value must account for the contributions from both gas components. The individual w-values for helium and CF$_4$ have been measured to be $W_i^{\text{He}} = 41.3$ eV/pair [218] and $W_i^{\text{CF}_4} = 34$ eV/pair [172, 219], respectively. A value of $W_i(\text{He:CF}_4, 60:40) = 35$ eV/pair was assumed, as obtained by taking the weighted mean [220] of the individual contributions.

In the simulation, the number of primary electrons produced, N_e^{pr}, is sampled from a Poisson distribution with mean value $\bar{N}_e$. As discussed previously, this represents a simplified statistical model that captures the average ionization yield while neglecting the detailed cluster structure and non-Poissonian fluctuations of the actual ionization process [120]. This approximation provides a reasonable representation of the charge variance that contributes to the detector energy resolution.

During the drift from the ionization point to the GEM amplification plane, primary electrons move through the gas under the applied electric field. Over drift distances of several centimeters, a fraction of electrons can be lost through attachment to electronegative molecules in the gas. This effect must be properly modeled in the simulation to reproduce the charge collection efficiency observed in data.

Electron attachment occurs when free electrons are captured by impurities in the gas mixture. Even in nominally pure systems, some contamination is unavoidable due to outgassing, permeation through seals, and residual impurities in the gas supply. The attachment rate depends on both the concentration and electron affinity of the contaminants.

In the simulation, this loss is modeled as an exponential attenuation with characteristic length λ, representing the mean drift distance before capture. The number of electrons reaching the amplification plane, N_e, is thus reduced compared to the initial number N_e^{pr} according to:

$$N_e = N_e^{pr} \cdot e^{-\frac{z}{\lambda}} \tag{5.4}$$

where z is the drift distance. This simple model effectively describes the cumulative losses during drift.

The attenuation length λ strongly depends on gas purity. For highly pure mixtures, electron absorption rates as low as 3%/m have been reported [119], corresponding to $\lambda > 30$ m, where attachment becomes negligible. In practice, however, maintaining such purity is challenging, and oxygen (O$_2$) contamination, even at ppm levels, can significantly increase attachment rates [221], reducing λ to values in the range of a few meters or less. For the CYGNO simulation, the attenuation length was treated as a free parameter to be determined empirically. An initial value of $\lambda \approx 1$ m was adopted as a starting point based on conservative estimates of achievable gas purity in the experimental setup. This parameter was subsequently refined by fitting simulated detector response to experimental data from the LIME prototype, as discussed in Chapter 6. The optimized value accounts for the actual contamination levels and attachment rates present in the operational detector. Electron attachment introduces a spatial dependence in detector response: since the loss probability increases with drift distance, events near the cathode experience greater charge loss than those close to the GEM plane.

5.2.2 Electron amplification and GEM gain

After drifting through the gas volume, the ionization electrons N_e that successfully arrive at the GEM amplification system undergo a crucial multiplication process. Achieving sufficient signal strength for the optical readout system requires this amplification to be substantial. The CYGNO detector implements a triple-GEM configuration in which electrons traverse three GEM foils sequentially, with each foil contributing to the total signal amplification.

5.2.2.1 GEM gain and amplification mechanism

When the ionization electrons N_e reach the GEMs, they experience subsequent amplification. The electric field within the GEM holes becomes extremely intense, with values reaching approximately 50 kV/cm [222].

These strong fields provide electrons with sufficient acceleration to acquire enough kinetic energy for ionizing gas molecules along their path. When an ionization event occurs, it liberates additional free electrons that are subsequently accelerated by the same field, producing further ionizations. This cascading process, referred to as a Townsend avalanche mechanism, leads to an exponential growth in the electron population as it moves through the GEM hole. The gain G of the GEM quantifies this amplification and is defined as the ratio between electrons exiting (n_{out}) and entering (n_{in}) a GEM hole:

$$G = \frac{n_{\text{out}}}{n_{\text{in}}} \tag{5.5}$$

For the TPC's electric field configuration, the single GEM gain has been parameterized as a function of the applied GEM voltage, as documented in [167]:

$$G = 0.034 \cdot e^{0.021 \cdot \Delta V} \tag{5.6}$$

This expression captures the exponential voltage dependence characteristic of the process. The parameterization incorporates the collection efficiency, which represents the probability that an electron arriving at a GEM foil successfully enters a GEM channel.

5.2.2.2 Gain fluctuations and extraction efficiency

During amplification, several physical mechanisms introduce fluctuations in the GEM gain. Electron absorption processes and manufacturing imperfections in the GEM foils can modify the effective field distribution, consequently affecting the gain. Research documented in [223] demonstrates that the effective GEM gain follows an exponential distribution, with the mean value corresponding to the average gain shown in Eq. 5.6.

The importance of these fluctuations varies across amplification stages. In the first stage, where primary electron numbers are relatively small (typically ranging from a few to several tens of electrons), gain fluctuations play a significant role. Following this initial multiplication, the electron count grows by approximately $\mathcal{O}(300)$ (corresponding to a single GEM operating at 440 V). With such large electron populations, gain fluctuations have negligible effects since statistical variations average out. Therefore, to reduce computational demands without sacrificing physical accuracy, these fluctuations are not simulated in detail for subsequent amplification stages.

The amplification process exhibits another important characteristic: not every electron generated during avalanche multiplication successfully exits the GEM hole. Some electrons undergo absorption at the GEM surface. The extraction efficiency ϵ_{extr} quantifies this effect and depends on the applied GEM voltage. For the TPC's field configuration, this efficiency can be expressed as [224, 225]:

$$\epsilon_{\text{extr}} = 0.87 \cdot e^{-0.002 \cdot \Delta V} \tag{5.7}$$

This relationship demonstrates that extraction efficiency decreases slightly with increasing voltage.

5.2.2.3 Implementation in the simulation

The simulation implements the amplification process by treating each track point containing N_e primary ionization electrons individually. For the first GEM, the number of amplified electrons $N_e^{G_1}$ is computed as:

$$N_e^{G_1} = \sum_{k=1}^{N_e} \left(G_k^{G_1} \cdot \epsilon_{\text{extr}}^{G_1} \right) \tag{5.8}$$

Here, $G_k^{G_1}$ represents the actual gain experienced by each electron, which is randomly sampled from an exponential distribution with mean G^{G_1} (given by Eq. 5.6). The parameter $\epsilon_{\text{extr}}^{G_1}$ gives the probability that an electron successfully exits the GEM channel.

For the second amplification stage, gain fluctuations are no longer considered, yielding:

$$N_e^{G_2} = N_e^{G_1} \cdot \left(G^{G_2} \cdot \epsilon_{\text{extr}}^{G_2} \right) \tag{5.9}$$

Saturation effects become important in the third and final amplification stage, and their detailed treatment is provided in Section 5.2.4.

5.2.3 Electrons diffusion

As primary electrons drift through the gas, they experience spatial diffusion. The transverse component $\sigma_{x,y}$ combines two contributions: diffusion occurring as electrons travel through the gas volume (σ_T), and a fixed contribution arising from the GEM amplification process (σ_{T0}). The longitudinal diffusion σ_z is treated similarly, following the approach described in [119]:

$$\sigma_{x,y} = \sqrt{\sigma_T^2 \cdot z + \sigma_{T0}^2} \qquad \sigma_z = \sqrt{\sigma_L^2 \cdot z + \sigma_{L0}^2} \tag{5.10}$$

The coefficients σ_T and σ_L have been determined through Garfield++ simulations and vary with the applied drift field as reported in [167]. Meanwhile, σ_{T0} and σ_{L0} were extracted from experimental data in [226] and [227], respectively.

Within the simulation framework, diffusion is applied by smearing the spatial coordinates (x, y, z) of each electron from the $N_e^{G_2}$ population around every interaction point along the track. A Gaussian function with standard deviation $\sigma_{x,y}$ is applied to the transverse coordinates (x-y), while σ_z is used for the longitudinal coordinate (z). The resulting positions are stored in a three-dimensional histogram using voxels of size V_x, V_y, and V_z. Transverse voxel dimensions (V_x and V_y) are selected to match the physical area corresponding to each optical sensor pixel. The longitudinal voxel size V_z is chosen to be comparable to the GEM thickness.

In actual TPC operation, diffusion during drift occurs prior to electrons entering the GEMs, with additional spreading introduced at each amplification stage. The simulation simplifies this by implementing diffusion after the first two amplification stages in an uncorrelated manner. Since diffusion parameters were determined from experimental measurements performed downstream of the amplification region, where total diffusion is observed, this simplified approach successfully reproduces the diffusion behavior.

5.2.4 GEM gain saturation

Previous studies demonstrated that the standard exponential relationship between GEM gain and applied voltage breaks down when electron cloud density exceeds certain thresholds [202, 226]. In LIME, this phenomenon becomes particularly relevant at the third GEM stage, where charge density can reach levels at which the electric charge itself partially screens the electric field within the hole, thereby reducing field strength.

A charge-density-dependent modification of the GEM gain has been incorporated into the simulation to capture this behavior.

5.2.4.1 Saturation model

The saturation model accounts for the screening effect that occurs when the space charge of electrons within a GEM channel reduces the effective electric field driving the avalanche multiplication. A complete derivation of the model, starting from the modified Townsend equation with field screening, is provided in [226].

According to this model, the total number of electrons exiting a GEM channel can be expressed as:

$$n_{\text{out}} = \frac{n_{\text{in}}\, e^{\tilde{\alpha}\,(\Delta V - V_0)}}{1 + \beta\, n_{\text{in}} \big(e^{\tilde{\alpha}\,(\Delta V - V_0)} - 1\big)} \tag{5.11}$$

where n_{in} represents the number of electrons entering the channel, ΔV is the voltage drop across the GEM foil, and $\tilde{\alpha}$ and V_0 are constants characterizing the linear parametrization of the Townsend coefficient.

By defining the unsaturated gain as $g = e^{\tilde{\alpha}\,(\Delta V - V_0)}$, Eq. 5.11 can be rewritten in terms of the effective gain $G(n_{\text{in}})$:

$$G(n_{\text{in}}) = \frac{n_{\text{out}}}{n_{\text{in}}} = A \cdot g \left[1 + \beta\, n_{\text{in}}\, (g - 1) \right]^{-1} \tag{5.12}$$

where A is a normalization factor of order unity.

The parameter β in Eq. 5.12 plays a crucial role in determining the onset of saturation effects. From a physical perspective, β can be interpreted as the inverse of an equivalent charge number n_{eq} that would completely screen the internal field:

$$\beta \simeq \frac{1}{n_{\text{eq}}} \tag{5.13}$$

This parameter determines the critical electron population at which amplification becomes significantly reduced. When n_{in} reaches $1/\beta = n_{\text{eq}}$, the gain approaches unity and amplification is effectively lost. Measurements have established that β is of order 10^{-5} [226], corresponding to a critical charge density of approximately 10^5 electrons where screening effects dominate.

The behavior of Eq. 5.12 can be understood by examining limiting cases. In the regime where $\beta\, n_{\text{in}} \ll 1$ (negligible screening), the denominator approaches unity and the gain reduces to the standard unsaturated form $G \simeq A \cdot g$. Conversely, when $\beta\, n_{\text{in}} \simeq 1$ (complete saturation), the denominator grows large and multiplication becomes strongly suppressed, with $G \simeq 1$.

5.2.4.2 Implementation in the simulation

This saturation correction is applied exclusively at the third amplification stage, where electron populations can approach 10^5. Each voxel within the 3D electron cloud is scaled by $G(n_{\text{in}})$ according to Eq. 5.12, where n_{in} corresponds to the number of electrons in that specific voxel. To determine the total electron count N_e^{out} exiting the third GEM at each x-y position, the 3D cloud is projected along the z-axis onto the x-y plane.

The practical implications of this saturation model on detector response for different energies and drift distances are discussed in the following subsection.

5.2.4.3 Energy and position dependence of saturation effects

To better understand the behavior of the saturation model described above, it is useful to analyze how this effect depends on the deposited energy and the position of the track within the detector volume.

A systematic study was performed using simulated data to investigate this dependence. For each simulated event, the ratio between the total charge integral obtained under saturated conditions (i.e., close to the GEM plane where charge density is highest) and the corresponding integral expected under ideal, non-saturating conditions (i.e., far from the GEM plane) was computed. This ratio quantifies the charge produced after the third GEM amplification stage.

Figure 5.2 shows this ratio as a function of both deposited energy and drift distance.

The analysis reveals two particularly important characteristics of the detector response. At low energies, saturation effects become significant even at 1 keV for high z positions, far from the GEM plane. This indicates that the operational limits of the GEM system are reached at unexpectedly low energy thresholds.

At higher energies, the behavior changes significantly. Saturation is reduced and the increasing track length allows the charge integral to continue growing with energy. In this regime, saturation does not affect the longitudinal development of the track, and the overall response becomes dominated by the geometrical extension of the ionization rather than by local charge density effects.

5.2.5 Light production and sCMOS sensor response

The scintillating nature of the He:CF$_4$ gas mixture ensures that the avalanche process naturally produces secondary photons in addition to avalanche electrons. Photon production scales proportionally with the number of electrons participating in the avalanche.

Since the electron population following the first two amplification stages remains substantially smaller than that produced after the third GEM, and considering that the third GEM effectively shields optical sensors from light produced in earlier stages, we can reasonably assume that detected photons originate predominantly from electrons exiting the third GEM, N_e^{out}.

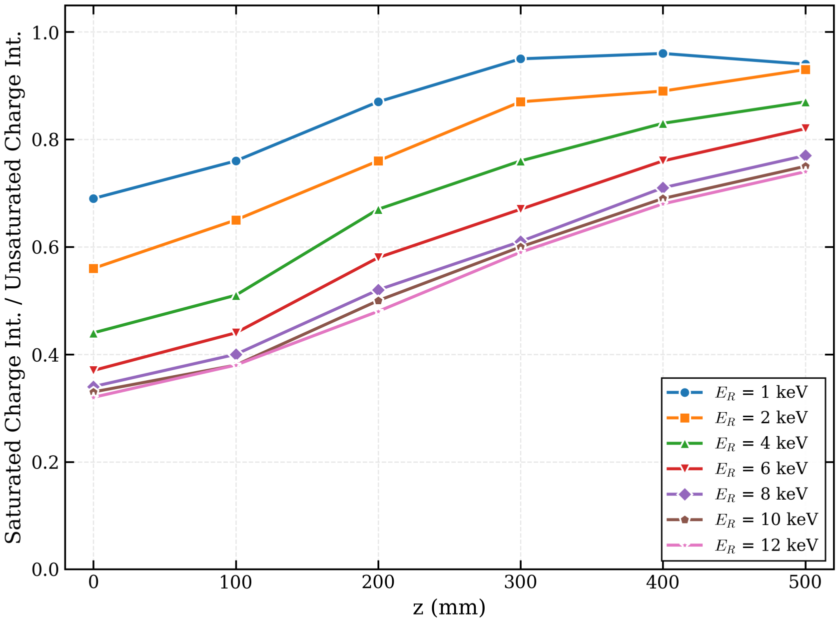

Figure 5.2: Ratio between saturated and unsaturated charge integral as a function of source position from the GEM for different electron recoil energies ($E_R = 1$–12 keV). The simulation indicates significant saturation effects even at 1 keV for high drift distances. The curves reach a plateau around 400 mm, where diffusion has spread the charge cloud sufficiently that further increasing the drift distance no longer significantly reduces the local charge density at the GEM. At higher energies, the saturation trends converge due to the increasing track length.

In the simulation code, these electrons are converted into scintillation photons, which the camera ultimately detects as ADC counts. The mean photon yield $\overline{N_\gamma}$ is given by:

$$\overline{N_\gamma} = \mathrm{LY} \cdot N_e^{\mathrm{out}} \tag{5.14}$$

where LY $= 0.07$ ph/e$^-$ represents the light yield of the gas mixture at atmospheric pressure [163, 182, 228]. Since photon production results from gas molecule dissociation, it follows Poisson statistics. The actual photon count N_γ^{tot} is therefore randomly sampled from a Poisson distribution with mean $\overline{N_\gamma}$.

Each bin in the 2D projection maps directly to the physical area of a single camera pixel, creating a one-to-one correspondence between simulation voxels and detector pixels.

Only a fraction of the produced photons reach the lens due to geometric constraints of the optical system. The solid angle Ω quantifies this collection efficiency, giving $N_\gamma^{\mathrm{pix}} = N_\gamma^{\mathrm{tot}} \cdot \Omega$. This solid angle is expressed as:

$$\Omega = \frac{1}{\left(4\,N\left(\frac{1}{I}+1\right)\right)^2} \tag{5.15}$$

where N denotes the focal number and I represents the magnification [154].

To achieve more accurate reproduction of real images, we must account for the vignetting effect. This optical phenomenon causes brightness reduction near image edges relative to the center, typically approximated by $\cos^4(\phi)$, where ϕ represents the angle between the optical axis and incoming rays [229]. Natural vignetting in a single-lens setup can reduce intensity at image borders by approximately 20%. Additionally, gain non-uniformities across the GEM surface introduce spatial variations in light production. To address both effects, each pixel's photon count is multiplied by a response map incorporating both lens vignetting and GEM response variations.

Construction of this map involved collecting and summing one thousand images with 2 s exposure time while the detector recorded events from internal and external radioactivity, including cosmic rays. Prior to summation, each image underwent correction through subtraction of pedestal images to eliminate fixed-pattern noise and other systematic effects unrelated to physical signals. Pedestal images are recorded in dedicated runs with no external light present, where camera pixel counts arise solely from the optical sensor's intrinsic electronic noise (including both readout noise and dark current). For these pedestal acquisitions, the GEM voltage was set to 200 V, sufficiently low to prevent signal generation in the gas while remaining close enough to standard data acquisition voltages for accurate sensor baseline characterization. Finally, each pixel in the 2D map was normalized to the brightest pixel's intensity.

The resulting map, displayed in Figure 5.3, naturally incorporates both lens vignetting and potential GEM response non-uniformities, facilitating more accurate data-simulation comparisons. Vertical line features visible in the map, spaced approximately 200 pixels apart, result from actual discontinuities in the GEM lower electrode that were introduced to enhance detector stability.

To validate the reliability of this map for reproducing gain non-uniformities, an alternative first-principles method was tested. Earlier studies [230] reported that for a 3-GEM stack of 10 × 10 cm^2, gain variations are approximately 8.8% within 1.5 × 1.5 cm^2 regions. As a cross-check, a per-track gain fluctuation was introduced in the simulation, with its magnitude optimized by comparing simulated energy resolution to experimental data. The optimization identified 15% as the optimal gain fluctuation value, consistent with measurements in [230]. The agreement between results using per-track gain fluctuations and those using the 2D map confirms the reliability of the map-based method, which is the approach actually implemented in our simulation framework.

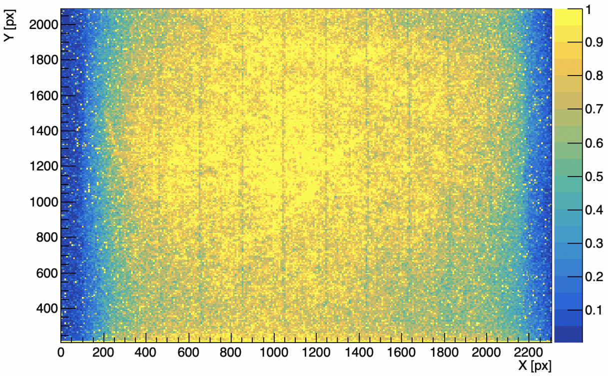

Figure 5.3: Example of the 2D response map constructed as described in the text. This map reproduces effects from gas-gain non-uniformities, vignetting, and drift-field non-uniformity.

In the simulation's final stage, sensor response is modeled explicitly. The camera converts incident photon counts per pixel into ADC counts using a proportionality factor $C_{\text{conv}} = 4$ specified by the manufacturer. The track image is obtained through:

$$\text{ADC} = C_{\text{conv}} \cdot N_{\gamma}^{\text{pix}} \tag{5.16}$$

Subsequently, the digitized track is superimposed onto a real sCMOS pedestal to generate the final simulated image. Figure 5.4 (bottom panel) shows an example of an electron recoil track generated in Geant4, processed through digitization, and combined with pedestal.

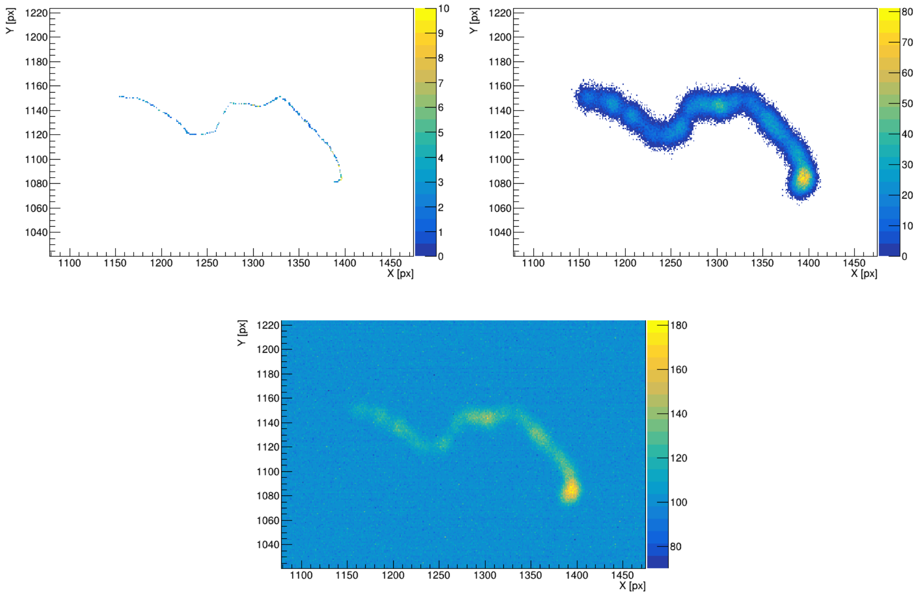

Figure 5.4: Detail of an image from a 60 keV ER simulation: (upper left) without considering diffusion effects in gas and GEM stack; (upper right) with diffusion effects included; (lower) incorporating sensor electronic noise in the final result.

5.3 Computational optimization for high-energy event processing

The implementation of the comprehensive detector simulation framework described in the previous section revealed significant computational challenges when processing high-energy events, particularly those corresponding to extended particle tracks with energies exceeding 50 keV. This Section details the optimization strategies developed to address these challenges and enable the simulation of realistic background events that are crucial for the CYGNO experiment's sensitivity studies. It should be noted that, although the framework was optimised to handle the computational demands of higher-energy events, the experimental validation of the simulation discussed in this thesis was performed only in the low-energy regime, below approximately 45 keV (see Chapter 6).

5.3.1 Computational bottlenecks in long track digitization

The digitization process for extended particle tracks presented substantial memory management challenges that threatened the feasibility of simulating realistic detector backgrounds. The primary computational bottleneck emerged from the need to model saturation effects in the Gas Electron Multiplier (GEM) amplification process.

The saturation modeling necessitates the use of three-dimensional histograms where each voxel represents a specific GEM channel at a discrete time interval. For each voxel, the number of primary electrons must be computed to accurately apply the corrected gain, which accounts for space-charge effects that reduce the effective amplification when electron densities become sufficiently high. This approach ensures physical accuracy but creates substantial memory requirements that scale with both the spatial extent and energy deposition of the simulated events. In fact, the positions of all individual electrons must be stored in memory.

For low-energy events such as the ^{55}Fe calibration sources discussed in previous chapters, the memory usage remains manageable due to the localized nature of the energy deposition. However, high-energy events produce extended tracks that can span significant portions of the detector volume, requiring histogram arrays with dimensions that can exceed available system memory. Background events, which are essential for understanding the experiment's sensitivity to dark matter interactions, often involve even more complex energy deposition patterns that exacerbate these computational demands.

The original implementation required approximately 30 GB of RAM for processing 100 keV tracks, making it impossible to execute such simulations on standard computing infrastructure. This limitation effectively prevented the generation of realistic background datasets.

5.3.2 Layered saturation processing algorithm

To address the memory limitations while preserving the physical accuracy of the saturation modeling, a novel layered processing algorithm was developed. This approach decomposes the saturation volume into a series of more manageable smaller layers that can be processed sequentially rather than simultaneously.

The optimization introduces a configurable parameter V_{max} representing the maximum allowed volume of the three-dimensional histograms, expressed as the maximum number of voxels that can be allocated in memory. This parameter serves as a computational constraint that determines how the track processing is subdivided into manageable segments.

The algorithm begins by analyzing the spatial extent of the particle track to determine the minimum cuboid volume that completely encompasses all energy deposition points. The number of processing layers N is then calculated by dividing this total volume by the maximum allowable volume V_{max}:

$$N = \left\lceil \frac{V_{\text{track}}}{V_{\text{max}}} \right\rceil \tag{5.17}$$

where V_{track} represents the volume of the smallest cuboid containing the complete particle track.

The track is then subdivided into N layers oriented perpendicular to the z-axis, with each layer containing approximately equal volumes of the original track. For each layer, the algorithm performs the following sequence:

1. **Layer isolation:** extract the subset of primary electron positions and energies contained within the current layer boundaries.

2. **Histogram construction:** build the three-dimensional histogram for the isolated layer, ensuring that the total number of voxels does not exceed V_{max}.

3. **Saturation modeling:** apply the saturated gain model to each voxel within the layer, accounting for local electron density effects on the GEM amplification process.

4. **Intermediate storage:** store the processed results for the current layer in a format suitable for subsequent combination with other layers.

After all layers have been processed independently, the results are combined through summation along the z-axis to reconstruct the complete track response. This summation preserves the physical accuracy of the saturation modeling while avoiding the memory limitations of the original approach. As described in Section 4.2.3, the saturated gain depends on the electron density within each individual channel of the GEM amplification region. Since the diffusion process has been applied prior to the saturation calculation, the spatial distribution of electrons is already established. The saturation effect can therefore be computed independently for each channel based solely on its local electron population, making the order of summation irrelevant: calculating the saturated gain for each channel and then combining the layers yields identical results to processing the entire track simultaneously.

5.3.3 Performance analysis and validation

The layered processing optimization delivers substantial improvements in computational efficiency across a wide range of event energies. For events below 50 keV, the optimization introduces minimal overhead, with memory usage and processing times remaining essentially unchanged compared to the original implementation. This behavior confirms that the algorithm correctly reduces to the original approach when memory constraints are not limiting factors. A comparison in the performances between the original and the optimized algorithm is reported in Table 5.1.

For moderate-energy events in the range 50–200 keV, the optimization achieves dramatic memory reduction from approximately 32 GB to 8 GB while maintaining processing times around 1 minute. This improvement enables routine simulation of events that were previously computationally challenging, expanding the accessible energy range for detector studies.

The most significant benefits emerge for high-energy events approaching 1000 keV, where the original implementation was computationally intractable. The optimized algorithm reduces memory requirements to approximately 32 GB with processing times of 2 minutes, making such simulations feasible on standard computing infrastructure for the first time.

Table 5.1: Performance comparison between the original and the optimized digitization.

Energy	**Mem. Orig.**	**Mem. Opt.**	**Time Orig.**	**Time Opt.**
$<$ 50 keV	$\sim$ no change	$\sim$ no change	$\sim$ 1 min	$\sim$ 1 min
50–200 keV	$\sim$ 32 GB	$\sim$ 8 GB	$\sim$ 1 min	$\sim$ 1 min
$\sim$ 1000 keV	Not feasible	$\sim$ 32 GB	Not feasible	$\sim$ 2 min

Most importantly, the optimization preserves the physical accuracy of the simulation results. Comparative analysis of simulated detector images before and after optimization shows identical characteristics, including energy linearity relationships between light integral and deposited energy. This validation confirms that the computational optimizations do not compromise the accuracy of the simulation framework.

5.3.4 Implementation and optimization strategies

The optimized algorithm was successfully deployed on the computing cluster infrastructure at the Laboratori Nazionali del Gran Sasso (LNGS), where it enables routine production of background event datasets that were previously computationally prohibitive. The implementation demonstrates excellent potential for scaling on multi-core systems, as the layered processing naturally lends itself to parallelization strategies.

To further optimize computational performance and memory efficiency, the simulation framework has been migrated from Python to C++. While Python was initially chosen to accelerate prototyping, the project's current maturity makes a C++ implementation more appropriate. This transition overcomes the intrinsic performance limits of interpreted languages and enables low-level memory management essential for detector simulations. C++ offers several decisive advantages: static compilation removes interpretation overhead, strong typing enables advanced compiler optimizations, and explicit memory control allows the design of cache-friendly data structures and custom memory pools that minimize fragmentation. These features are particularly beneficial in three-dimensional histogram processing for the saturation algorithm, where precise memory layout reduces cache misses and improves throughput. The migration has yielded performance gains of up to a factor 10 across the entire pipeline, enabling routine simulation of complex background events and extended particle tracks.

Several additional optimization strategies have been identified for future implementation, ordered by increasing complexity and development effort required:

Parallel processing of saturation layers. The current implementation processes layers sequentially, but the independence of each layer makes parallelization straightforward. Implementing multi-threading or multi-processing for the saturation loop could provide significant speedup, particularly for high-energy events requiring many layers. Each layer could be processed independently on separate CPU cores, providing nearly linear speedup for systems with sufficient memory bandwidth to support concurrent operations.

Adaptive spatial resolution. For oblique tracks that extend primarily in the x–y plane rather than the z direction, the current uniform layer subdivision may not be optimal. Introducing an adaptive spatial resolution that reduces the x–y dimensions of individual layers based on track geometry could yield additional memory savings for specific track topologies.

Sparse matrix implementation. The current approach employs dense arrays that allocate memory for all voxels, including those without energy deposition. Replacing them with sparse data structures that store only non-zero elements could substantially reduce memory requirements, especially for low-density tracks with large empty regions.

Optimized data types. At present, standard floating-point arithmetic is used throughout the calculation chain. For many applications, reduced precision with 16-bit integers or specialized fixed-point arithmetic could provide memory savings without compromising physical accuracy.

5.4 Integration of the PMT simulation branch

The digitization framework described in the previous sections produces a comprehensive three-dimensional distribution of scintillation photons at the exit of the third GEM stage, $N_\gamma(x, y, z)$, which serves as the foundation for both the sCMOS optical readout and the PMT-based time-resolved readout. While the sCMOS branch integrates this distribution along the drift coordinate to produce two-dimensional images, the PMT simulation branch preserves the temporal information by explicitly converting the spatial coordinate z into arrival times at the photosensors.

Although the author of this thesis did not directly contribute to the development of the PMT simulation algorithms (since the studies reported in the following chapters rely exclusively on sCMOS data analysis), significant effort was invested within the CYGNO collaboration to ensure seamless integration between the two simulation branches. On the other hand, the author actively participated in establishing the common interface between the sCMOS and PMT simulation pipelines, ensuring consistency in the upstream digitization chain and facilitating the parallel development of both readout systems.

5.4.0.1 Common foundation and branch point

Both simulation branches share an identical upstream processing chain:

1. **Geant4 energy deposits:** The Monte Carlo simulation provides a sequence of energy deposits $(x, y, z, \Delta E)$ for each particle track in the active gas volume.
2. **Primary ionization and drift:** Each deposit is converted into primary electrons according to the gas w-value, which then drift toward the GEM stack, undergoing attachment losses and diffusion as described in Section 5.2.1.
3. **GEM amplification:** The triple-GEM system multiplies the electron population through successive amplification stages, including extraction efficiency, gain fluctuations in the first stage, and saturation effects in the third stage, as detailed in Section 5.2.2 and Section 5.2.4.
4. **Photon generation:** The amplified electron distribution $N_e(x, y, z)$ is converted into scintillation photons using the light yield factor LY, producing the common three-dimensional photon field:

$$N_\gamma(x, y, z) = \mathrm{LY} \cdot N_e(x, y, z) \tag{5.18}$$

At this point, the simulation branches in the two independent optical readout pathways, each processing the same underlying photon field with the different detection strategies.

5.4.0.2 Divergence between sCMOS and PMT branches

The fundamental difference between the two branches lies in how they handle the temporal dimension of the scintillation light distribution:

- **sCMOS branch (spatial integration):** As described in the previous sections, the sCMOS simulation projects the three-dimensional photon distribution onto the (x, y) plane by integrating along the drift coordinate z:

$$N_\gamma(x, y) = \sum_z N'_\gamma(x, y, z) \tag{5.19}$$

  where $N'_\gamma(x, y, z)$ includes corrections for optical acceptance Ω, vignetting effects, and GEM response non-uniformities. This integration effectively collapses the temporal evolution of the light signal into a single integrated image, where each pixel records the total number of photons collected during the entire event exposure.

- **PMT branch (temporal resolution):** In contrast, the PMT simulation explicitly converts the spatial coordinate z into time using the electron drift velocity v_d (Sec. 3.1.1) [167]:

  $$t = t_0 + \frac{z}{v_d} \tag{5.20}$$

  This transformation yields a time-dependent photon distribution $N_\gamma(x, y, t)$, where the arrival time of photons at the PMTs directly reflects the original depth z of the ionization event in the active volume. The (x, y, t) space is then discretized into voxels, and for each voxel the photons are propagated to the four PMTs according to geometric acceptance, optical path losses, and PMT quantum efficiency. This produces time-resolved photoelectron counts $N_{\text{pe}}^{(m)}(t)$ for each PMT indexed by m.

5.4.0.3 Implementation of the common interface

The integration between the two branches was achieved by using the three-dimensional data structure described in Sec. 5.2.4. Specifically, after the third GEM amplification stage, the electron distribution $N_e(x, y, z)$ is stored in a three-dimensional histogram.

The photon conversion factor LY is applied uniformly to this histogram, producing $N_\gamma(x, y, z)$, which serves as the input for both branches:

- The sCMOS simulation reads this histogram, applies the spatial response corrections described in Section 5.4, integrates along z, and produces the final two-dimensional image.
- The PMT simulation reads the same histogram, converts each z-bin into a corresponding time bin using the drift velocity, and constructs time-resolved waveforms by propagating photons from each voxel to the PMT positions. For each detected photon, a single-photoelectron template is placed at the appropriate time in the waveform, and the contributions from all voxels are summed to produce the analog PMT signals.

This architecture ensures that both readout systems are sensitive to the same underlying physical processes (diffusion, attachment, GEM amplification, and saturation), thereby maintaining full consistency between the sCMOS images and PMT waveforms for any given simulated event.

5.4.1 Overview of the PMT simulation

Although the PMT data analysis is not utilized in the studies presented in this thesis, the availability of a unified simulation framework opens the possibility for future joint analyses that exploit the complementary strengths of both readout systems: the high spatial resolution of the sCMOS cameras and the precise timing information provided by the PMTs.

In this section, a brief overview of the PMT simulation methodology will be provided to complete the description of the CYGNO detector simulation framework.

The CYGNO experiment employs four Hamamatsu R7378A PMTs [231] positioned at specific locations within the detector volume (Figure 5.5), operating at different supply voltages to optimize light collection efficiency across the active area. The PMT simulation workflow begins immediately after the common three-dimensional photon distribution $N_\gamma(x, y, z)$ is generated at the GEM exit plane, as described in Section 5.4.

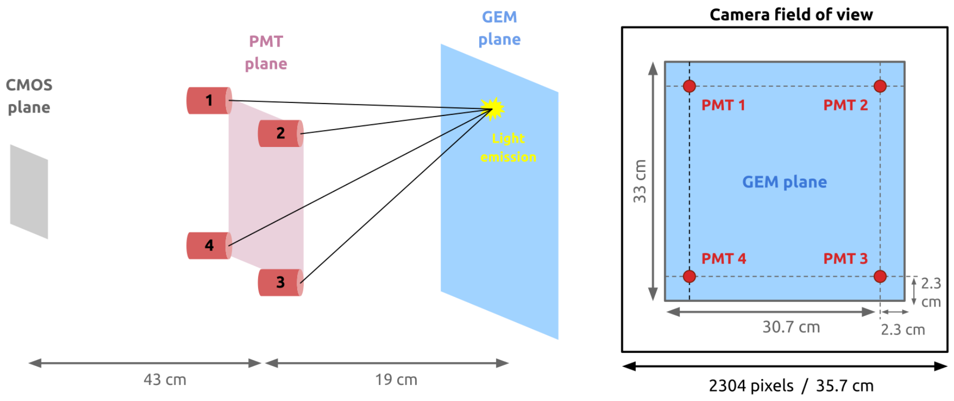

(a) Side view

(b) Front view

Figure 5.5: Representation of the fields of view of the CMOS and PMT sensors, seen from **(a)** the side and **(b)** the front [158].

5.4.1.1 Photon propagation and temporal modeling

The simulation converts the spatial z-coordinate of each photon into an arrival time using the drift velocity, producing a time-dependent distribution $N_\gamma(x, y, t)$. For each photon emission point on the GEM plane, the geometric acceptance of each PMT is computed based on the solid angle subtended by the photosensor. The light collection efficiency depends on the distance R_i between the emission point and PMT i, following approximately an inverse power law relationship $1/R^\alpha$, where α is an empirical parameter accounting for optical losses and scattering effects [232].

5.4.1.2 Spectral response and detection efficiency

The detection efficiency depends on the interplay between the scintillation spectrum of the He:CF$_4$ gas mixture, the transmission properties of detector materials (primarily plexiglass components), and the PMT quantum efficiency [167]. The gas mixture produces photons in two spectral regions: a dominant UV component (200–350 nm) and a secondary visible component (550–800 nm). However, the UV photons are largely absorbed by plexiglass, while the visible photons experience reduced quantum efficiency in the R7378A PMT. The combined effect of these factors results in a relatively low overall detection probability, as detailed in [158, 231].

5.4.1.3 Single photoelectron response

The foundation of the PMT signal simulation relies on the accurate modeling of single photoelectron (SPE) waveforms. Each SPE pulse is parametrized using an Exponentially Modified Gaussian (EMG) distribution [233], a functional form that captures the asymmetric pulse shape arising from the combination of Gaussian diffusion processes and exponential decay tails observed in experimental data.

The SPE waveform amplitude is determined by the PMT gain, which follows a power law dependence on the supply voltage typical of photomultiplier tubes [234]. Calibration measurements were performed at multiple voltage settings (typically in the range 772–800 V) using ^{55}Fe sources to extract both the temporal parameters and the voltage-dependent gain factors required for accurate signal reconstruction.

5.4.1.4 Electronic noise and digitization

Electronic noise from the data acquisition system is incorporated into the simulation using noise characteristics measured directly from the CAEN digitizers (V1742 for fast signals and V1720 for slow signals) [235, 236]. Power Spectral Density analysis of real pedestal data provides the frequency-dependent noise properties, which are then used to generate synthetic noise waveforms that preserve the statistical characteristics of the experimental setup.

The final PMT waveform is constructed by superposing individual SPE contributions at their respective arrival times, as determined by the photon propagation model, and adding the characterized electronic noise. The resulting analog signal is then digitized with 12-bit resolution to match the actual digitizer specifications, completing the simulation chain.

5.4.2 Validation of the PMT simulation

The integrated simulation framework has been validated by comparing both sCMOS and PMT outputs with experimental data from the LIME prototype. Preliminary comparisons of PMT waveforms with data have confirmed that the time-resolved features, such as pulse rise times and total pulse charge, are reproduced with reasonable accuracy by the simulation.

To demonstrate the simulation capabilities, several representative scenarios were examined using ^{55}Fe calibration sources, which produce characteristic 6 keV energy deposits appearing as circular spots in the detector images. These events are particularly suitable for validation purposes due to their well-defined energy and spatial characteristics, corresponding to electron recoil events in the detector.

The simulation demonstrates the expected geometrical dependencies described in Figure 5.5. When the ^{55}Fe source is positioned at the center of the detector (equidistant from all PMTs), the simulated signals exhibit similar amplitudes across all four channels, reflecting the symmetric light collection geometry (Figure 5.6 and 5.7). Conversely, when the source is positioned directly above one PMT, the proximity effects become apparent, with the closest PMT receiving the largest signal, adjacent PMTs showing intermediate responses, and the opposite PMT detecting the weakest signal (Figure 5.8 and 5.9).

The temporal evolution of the simulated waveforms reflects the diffusion processes modeled in the detector simulation. Events occurring at larger z distances from the GEM plane (Figure 5.7 and 5.9) exhibit broader temporal distributions due to increased electron cloud diffusion during drift.

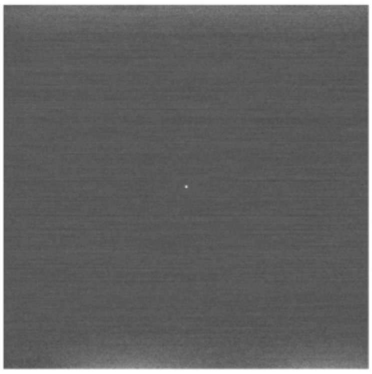

(a) Simulated image.

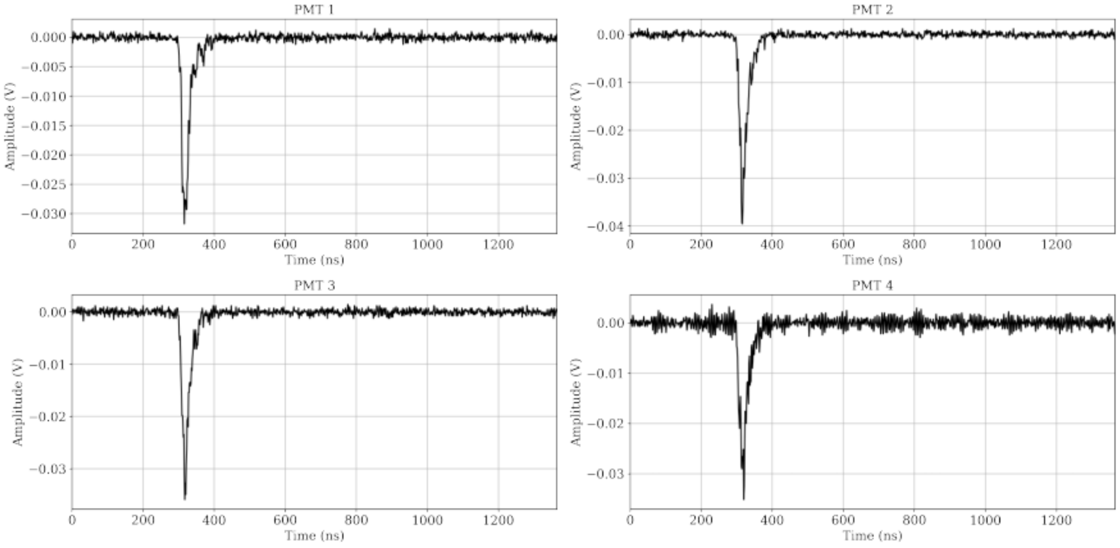

(b) Simulated waveforms of the Fast Digitizer.

Figure 5.6: Simulation example showing a centered ^{55}Fe event at z = 50 mm: (a) simulated detector image and (b) corresponding Fast Digitizer waveforms demonstrating symmetric response from all four PMTs.

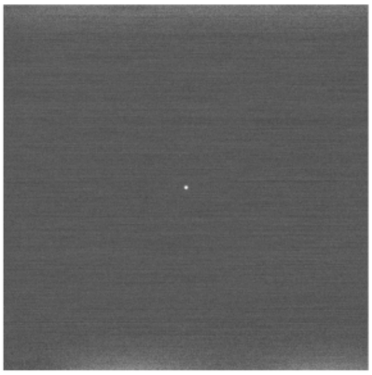

(a) Simulated image.

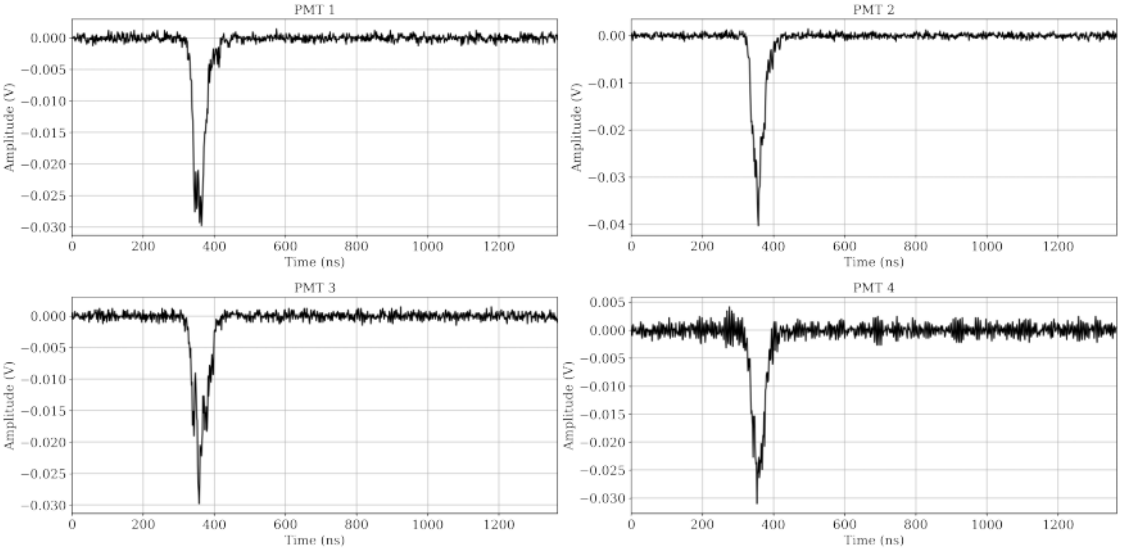

(b) Simulated waveforms of the Fast Digitizer.

Figure 5.7: Simulation example for a centered ^{55}Fe event at z = 466 mm: (a) simulated detector image and (b) corresponding Fast Digitizer waveforms, showing increased signal width due to enhanced electron diffusion at larger z distances compared to the previous example.

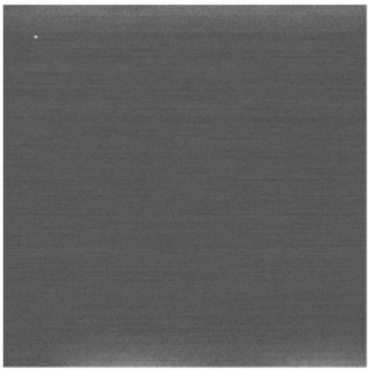

(a) Simulated image.

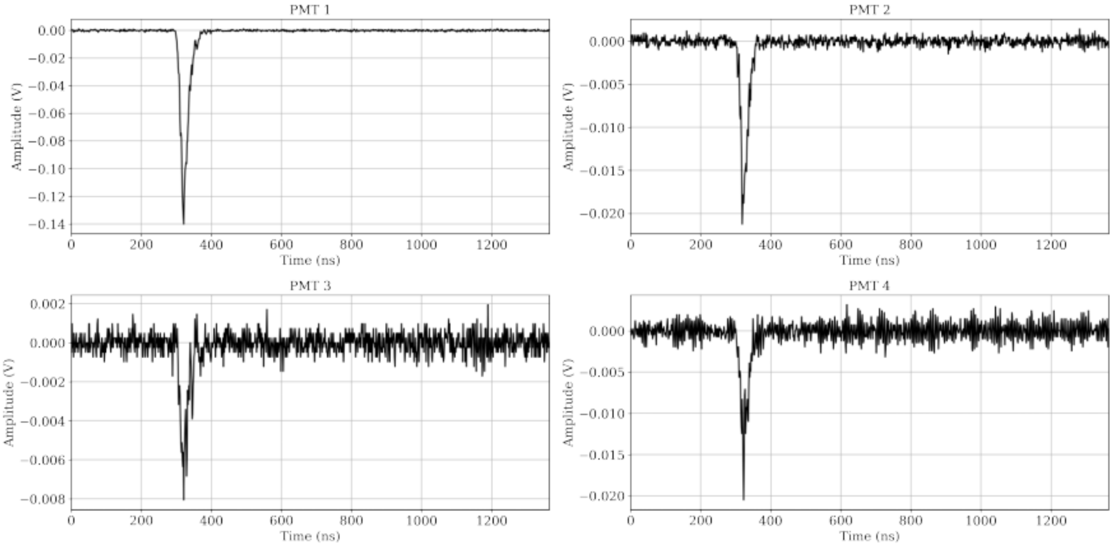

(b) Simulated waveforms of the Fast Digitizer.

Figure 5.8: Asymmetric PMT response for a ^{55}Fe event positioned directly above PMT 1 at z = 50 mm: (a) simulated detector image and (b) corresponding Fast Digitizer waveforms, demonstrating the geometrical acceptance effects and $1/R^{\alpha}$ distance dependence implemented in the simulation.

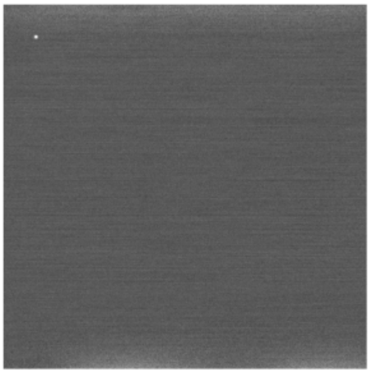

(a) Simulated image.

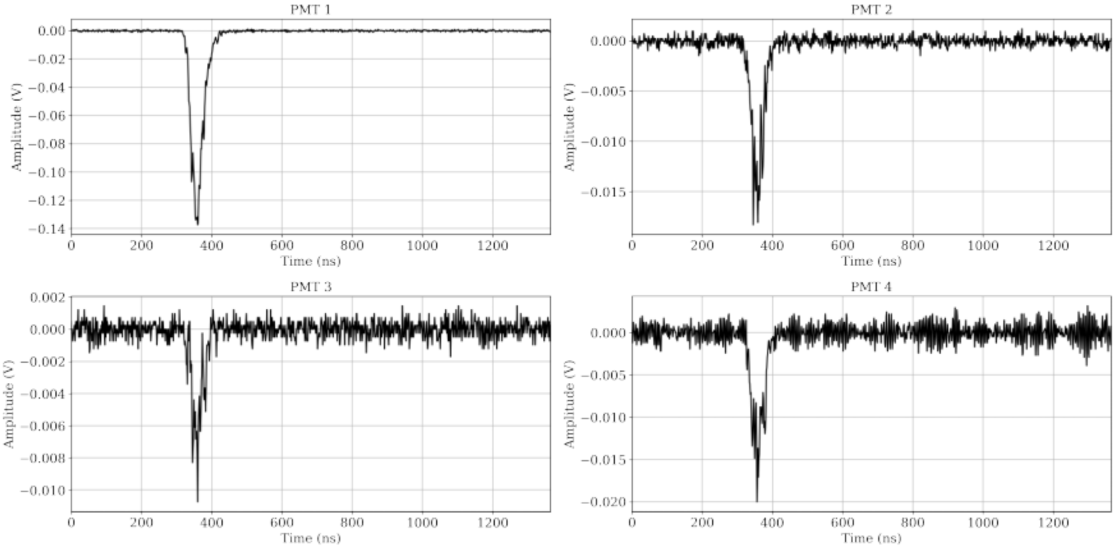

(b) Simulated waveforms of the Fast Digitizer.

Figure 5.9: Similar asymmetric configuration at z = 466 mm: (a) simulated detector image and (b) corresponding Fast Digitizer waveforms, showing how increased diffusion affects the relative signal amplitudes while maintaining the geometrical pattern.

5.4.2.1 Quantitative validation against experimental data

Preliminary studies within the CYGNO collaboration indicate that the PMT simulation framework closely reproduces data distributions also from a quantitative perspective. A systematic comparison between simulated and experimental data was conducted using ^{55}Fe calibration runs acquired across multiple detector positions, spanning the full range of source-to-PMT distances relevant for physics analyses. The analysis examined key observables including peak amplitude, total charge, RMS noise, signal-to-noise ratio, and temporal width parameters (FWHM and Full Width at Baseline), all analyzed as functions of the distance between the source position and each PMT. As shown in Figures 5.10 and 5.11, the simulation shows strong agreement with experimental data for amplitude-related parameters and noise characteristics across the entire range of distances investigated. This level of agreement validates the core components of the simulation framework, including SPE signal characterization, gain calibration, and electronic noise modeling, demonstrating that the underlying physical processes are correctly implemented. However, temporal width measurements reveal systematic discrepancies, particularly at smaller z distances corresponding to shorter drift times, suggesting that the current temporal dispersion model may require refinement to fully capture photon propagation effects and near-field optical phenomena that become more relevant when the interaction point is closer to the amplification plane. These preliminary results, while promising for the overall simulation performance and sufficient for the purposes of this thesis, highlight specific areas for future development in the temporal modeling components of the PMT simulation chain.

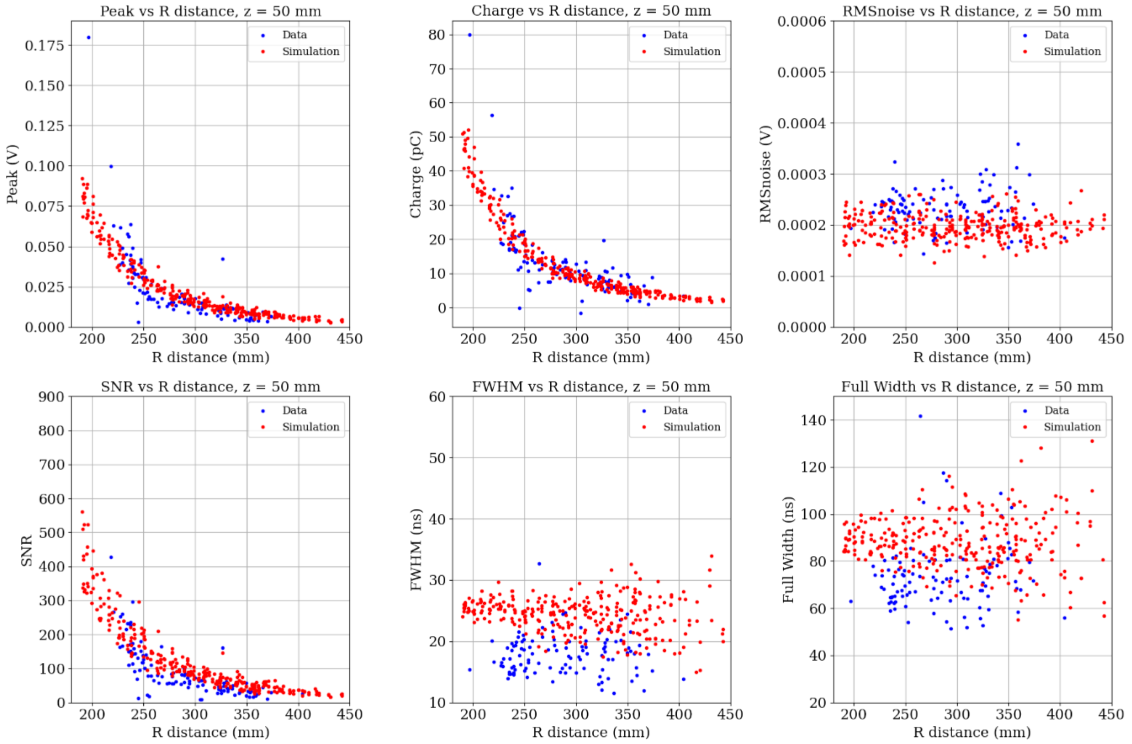

Figure 5.10: Comprehensive comparison between simulated (blue) and experimental (red) data for ^{55}Fe events, showing agreement in amplitude-related parameters and systematic discrepancy in temporal-width observables. Figure adapted from L. G. M. de Carvalho [237].

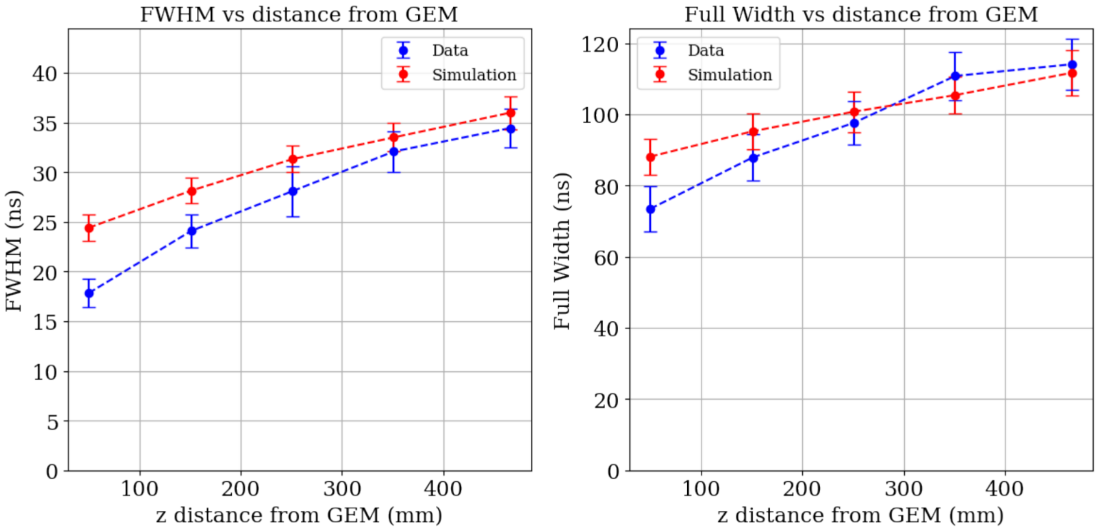

Figure 5.11: FWHM and Full Width at Baseline as functions of z distance from the GEM, illustrating the systematic difference in temporal-width measurements between simulation and experimental data. Figure adapted from L. G. M. de Carvalho [237].

5.5 Validation of the sCMOS ER simulation with LIME overground data

The validation of the electron recoil (ER) sCMOS simulation was initially performed using experimental data collected with the LIME detector during a dedicated above-ground data-taking campaign at the Laboratori Nazionali di Frascati (LNF).

The validation campaign focused on three critical aspects of the detector response: track topology, energy resolution, and light integral reconstruction. A systematic approach was adopted, fixing the detector gain through the high voltage of the GEMs (440 V), and subsequently exposing the detector to various X-ray sources spanning different energies in the range of interest (3-45 keV).

5.5.1 Experimental setup and methodology

The LIME detector was operated in stable conditions with optimized GEM voltages to ensure uniform gain. Its performance, linearity, and energy resolution were tested with a wide set of X-ray sources. A multi-target ^{241}Am source provided characteristic X-ray lines from 8 to 36 keV (Cu, Rb, Mo, Ag, Ba), while a ^{55}Fe source produced 5.9 and 6.5 keV lines and, through fluorescence on Ca and Ti targets, additional lines at 3.7 and 4.5 keV.

The sources were placed 25 cm from the GEM stack. The ^{55}Fe deposit, housed in a lead collimator, ensured a controlled spread of events, concentrated mostly in the upper detector region due to gas absorption.

Data were processed with the standard CYGNO reconstruction pipeline, applying identical procedures to both experimental and simulated datasets for a consistent comparison.

5.5.2 Detector response and resolution

The energy resolution, defined as the ratio between the standard deviation of the Gaussian fit to the reconstructed energy peak and its mean value, was systematically measured for different energies. The comparison between experimental data and simulation results demonstrated excellent agreement across the entire energy range studied, as shown in Figure 5.12.

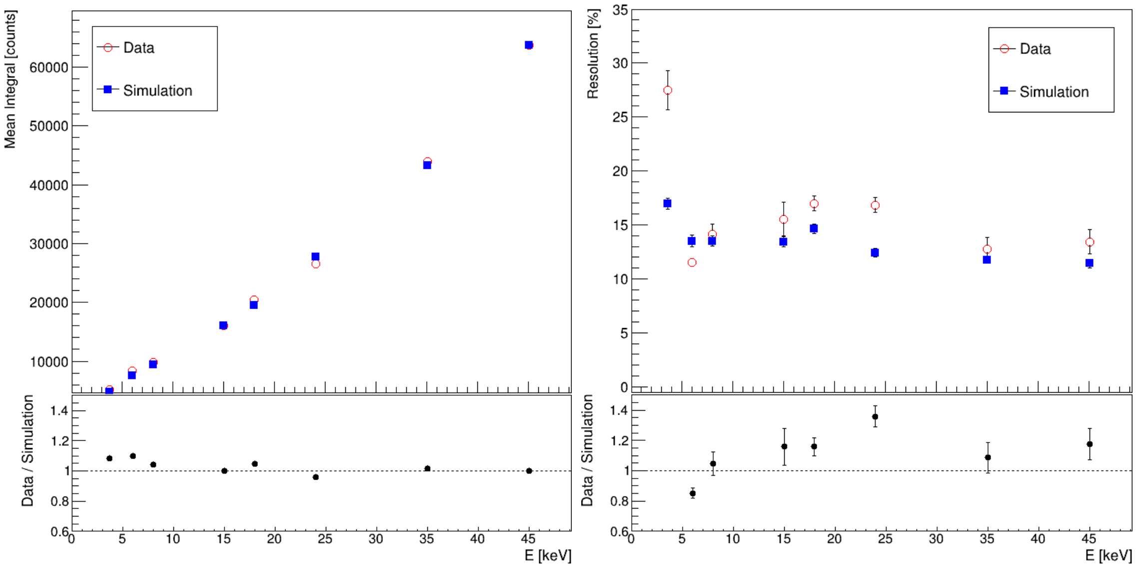

Figure 5.12: Comparison between data and simulation for the detector response (left panel) and energy resolution (right panel) as a function of energy. The mean light integral (I_{SC}) and the resolution (σ/I_{SC}) are extracted from Gaussian fits to the light integral distributions, with statistical uncertainties shown by the error bars. Data were collected using X-rays from ^{241}Am on different targets (Cu, Rb, Mo, Ag, Ba, Tb) at 8, 15, 18, 24, 35, and 47 keV, from a ^{55}Fe source at 5.9 keV, and from ^{55}Fe on a Ca target at 3.7 keV. A noticeable discrepancy is observed for the calcium point in the right panel, where the measured energy resolution deviates from the simulation prediction. This may be attributed to the larger relative background level at this low energy, to the difficulty of fitting a broad peak partially overlapping with adjacent spectral features, or to systematic effects not yet fully accounted for in the simulation framework at the lowest energies. Adapted from [238].

The mean reconstructed light integral values were reproduced within a few percent accuracy, highlighting the robustness of the simulation model in capturing the fundamental detector response (Figure 5.12, left panel). The energy resolution showed the expected dependence on both the incident photon energy and the drift distance, with systematic improvements observed at higher energies due to increased signal-to-noise ratios.

Minor discrepancies were observed at the lowest energies, particularly for certain source configurations, which may indicate the presence of additional systematic effects not fully captured in the current simulation framework. These deviations point to potential areas for future refinement, such as improved modeling of low-energy backgrounds

The light integral response was validated across the full energy range, demonstrating excellent linearity between the incident photon energy and the total light yield collected by the sCMOS camera system (Figure 5.12).

5.5.3 Topological shape variables comparison

A comprehensive comparison of track-shape variables between data and simulation was performed to validate the features of electron recoil reconstruction. Nine key topological observables, formally defined in the track reconstruction procedure described in Section 4.4, were selected for this analysis: Light Integral, Transverse Gauss Sigma (σ_T), Transverse

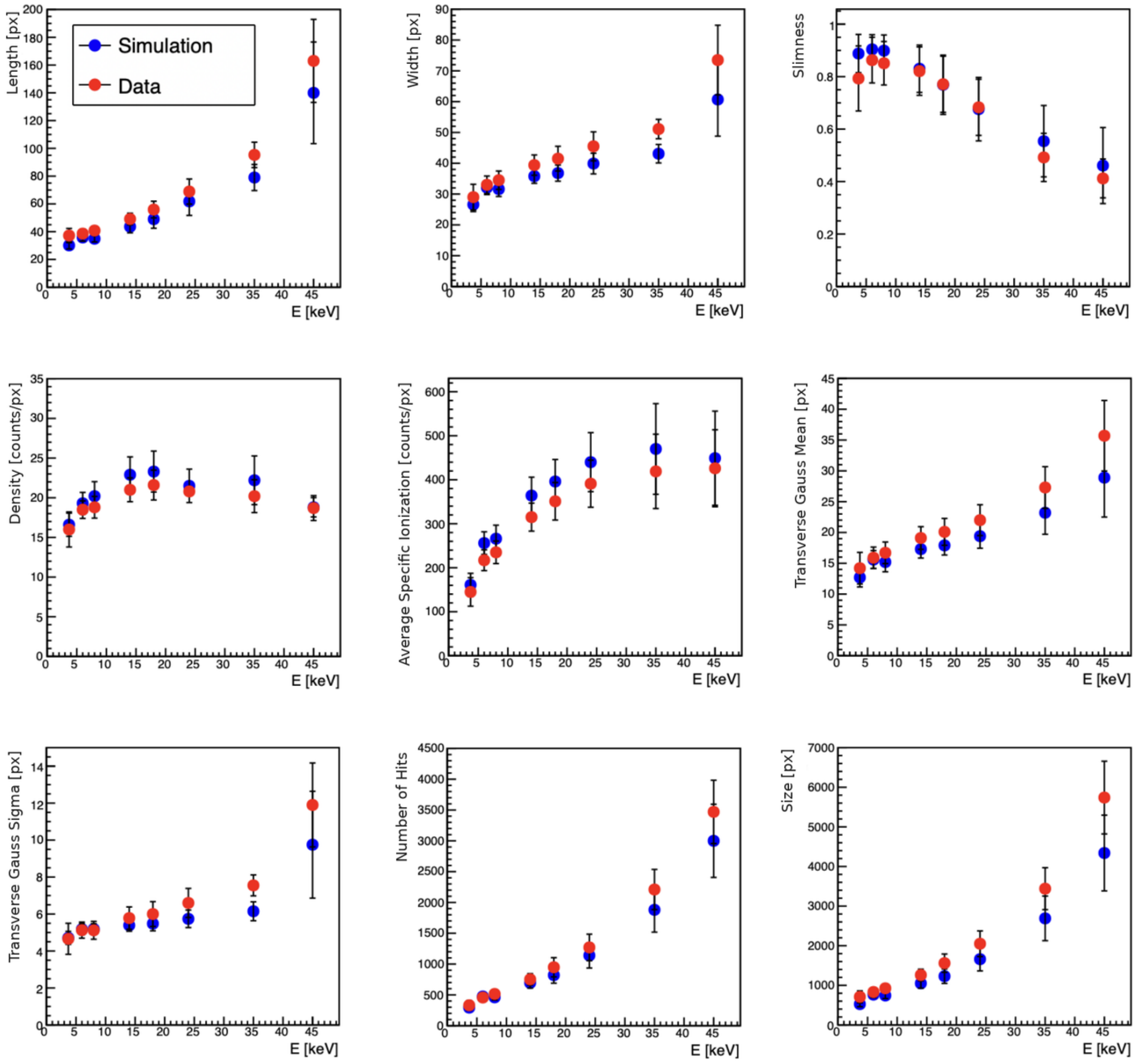

Figure 5.13: Mean values of the track-shape variables used in the data–simulation comparison, shown as a function of energy: Length, Width, Slimness (top row); Density, Average Specific Ionisation, Transverse Gauss Mean (middle row); Transverse Gauss Sigma (σ_T), Number of Hits, Size (bottom row). Blue markers correspond to simulated events, while red markers represent experimental data. The variable definitions are given in Section 4.4. Figure adapted from [239].

Gauss Amplitude, Number of Hits, Size, Length, Width, Slimness, Density, and Average Specific Ionisation.

To address the challenge of background subtraction in the experimental data, the ${}_s\mathcal{P}lot$ statistical technique [239] was employed. This method enabled the extraction of pure signal distributions from data containing both signal and background components, using the light integral as a control variable with known probability density function.

The comparison revealed generally good agreement between data and simulation for most shape variables, as illustrated in Figure 5.13. Track length showed excellent reproduction, being primarily governed by the underlying physics of electron energy loss.

Particularly noteworthy was the performance in reproducing track density and dE/dx, which are crucial for electron recoil identification and discrimination against nuclear recoils.

Overall, these results demonstrate that the simulation framework reproduces the essential features of the detector response with reasonable accuracy. Beyond this initial validation, a comprehensive set of additional studies has been performed using data acquired underground at LNGS under different and controlled experimental conditions, further consolidating the reliability of the simulation framework as discussed in the following Chapter.

Chapter 6

Electron recoil simulation studies with LNGS underground data

In order to further optimize the simulation framework, it is essential to understand the variability of the detector response over time and along the drift direction. This chapter, therefore, combines experimental and computational studies to bridge real detector behavior and its simulated model. Section 6.1 establishes a phenomenological description of light-yield attenuation and its temporal evolution, providing the reference conditions for tuning. In Sec. 5.3 and 6.2, the simulation and digitization models are refined using underground calibration data, introducing computational optimizations to enable high-energy event processing, and validating the goodness of the simulation tailored to overground measurements.

6.1 Stability Analysis of Daily ^{55}Fe Calibrations

The long-term stability of detector response represents a critical aspect of the CYGNO experiment's operational reliability and data quality assurance. While the simulation framework described Chapter 5 shows excellent agreement with experimental data under controlled conditions, systematic deviations have been observed when comparing simulation predictions with underground LIME data collected over extended periods. These discrepancies manifest primarily as time-dependent variations in light detection along the drift direction.

This section presents a comprehensive analysis of the detector stability using daily ^{55}Fe calibration data collected during RUN 3 and RUN 4. The investigation reveals systematic temporal variations in light yield and attenuation length, examines their correlations with environmental parameters, and introduces a real-time monitoring system.

6.1.1 Motivation and experimental approach

The daily calibration procedure described in Chapter 4 provides an ideal opportunity for studying detector stability over extended periods. Each calibration sequence involves systematic z-scanning with the ^{55}Fe source across five discrete positions (steps 1–5), generating consistent datasets that can be compared across different operational periods while maintaining identical conditions and source characteristics.

Initial comparisons between simulation predictions and experimental data revealed persistent mismatches in the light collection profile along the drift direction. As illustrated in

Figure 6.1, these discrepancies exhibit clear temporal evolution: calibration data from different periods show progressively different light yield profiles at large drift distances. This behavior cannot be explained by static detector properties or calibration uncertainties, suggesting the presence of time-dependent effects in the detector response.

The systematic nature of these discrepancies suggested the presence of time-dependent physical mechanisms affecting the primary electrons transport towards the GEM plane. Potential contributions include contamination and changes in gas composition affecting scintillation or transmission properties.

To isolate and quantify these temporal effects, a comprehensive reanalysis of the daily calibration database was undertaken.

6.1.2 Data selection and normalization

A critical aspect of the temporal stability analysis involves controlling for systematic effects that could introduce artificial variations in the measured parameters. The most significant potential bias arises from saturation effects in the GEM amplification system, which can vary between different calibration runs due to environmental conditions.

To mitigate these effects, a careful data selection protocol was implemented. For each comparison between different days, only datasets exhibiting similar light integral at step 1, i.e. the first source position at 50 mm from the GEM plane in the calibration procedure described in Section 4.2.2, were included in the analysis. This selection criterion ensures that all compared datasets operate in similar saturation regimes, minimizing the influence of non-linear amplification effects on the measured light yield profiles.

By equalizing the step 1 integrals across different days, the analysis effectively normalizes out global gain variations while preserving the relative changes in attenuation along the z.

Figure 6.1 demonstrates the effectiveness of this approach and reveals the underlying temporal variations. Despite a comparable value at step 1, the light yield decreases at larger z for later calibration runs, indicating progressive increases in attenuation strength over the operational period. This systematic pattern provides strong evidence for time-dependent degradation of the gas mixture of the detector.

6.1.3 Phenomenological model development

The observed temporal variations in the light collection profiles arise because the simulation framework does not account for changes in the detector operating parameters over time. While saturation and attenuation effects are individually well reproduced under fixed conditions, the actual detector performance evolves due to environmental factors and gas quality degradation. To parametrize these residual dependencies in a data-driven manner, a phenomenological model was developed to describe the light collection profile as a function of drift distance.

The functional form selected for this analysis combines exponential rise and decay components:

$$LY(z) = p_0 \left(1 - e^{-(z-p_3)/p_1}\right) e^{-z/p_2} \tag{6.1}$$

where z represents the source position (drift distance of the primary electrons), and the four parameters have distinct physical interpretations:

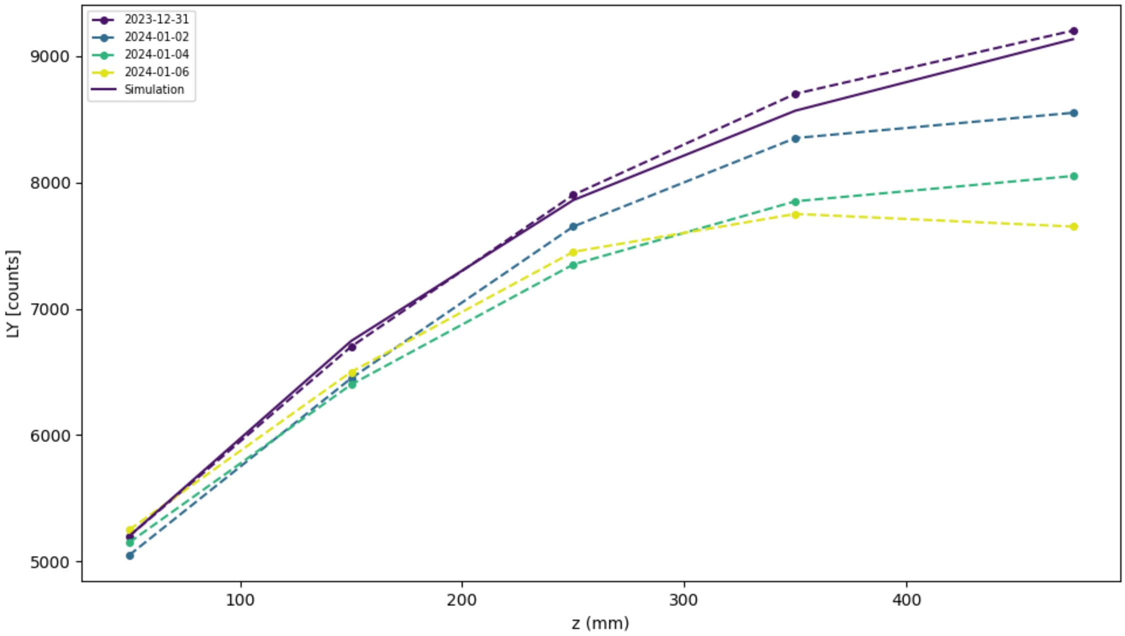

Figure 6.1: Temporal evolution of the light collection profiles from RUN3 daily calibrations after step-1 integral normalization. Dashed curves represent data taken at different times, while the solid line shows the simulation tuned to the earliest dataset. The increasing deviation between data and simulation at large z highlights a progressive mismatch developing with time.

- p_0: plateau light yield representing the maximum achievable signal in the absence of attenuation effects and is highly correlated to the GEM gain

- p_1: saturation scale parameter controlling the rise to plateau behavior at short drift distances

- p_2: attenuation length parameter encoding the exponential decay at large drift distances, due to the reabsorption of primary electrons during the drift

- p_3: offset parameter locating the transition region between rise and decay behaviors

The robustness of the parametrization was validated through extensive fitting studies (Figure 6.2) using calibration data spanning the complete operational period. The model consistently achieves excellent agreement with experimental profiles, with reduced chi-squared values typically below 1.2, indicating that the functional form captures the essential physics without over-parametrization.

Figure 6.3 shows the correlation matrix obtained from fitting multiple calibration datasets, revealing the expected strong correlation between p_0 and p_1. This behavior arises because saturation strongly depends on the gain (the light yield at the plateau): the higher the produced light, the stronger the saturation effect described by p_1, as discussed in Chapter 5.

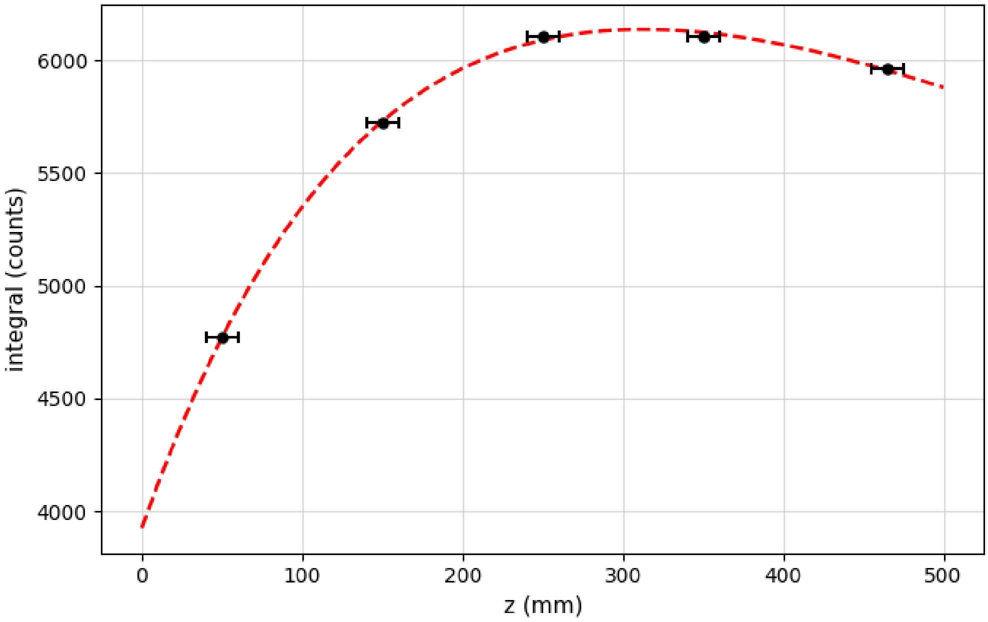

Figure 6.2: Representative fit of the phenomenological model to experimental calibration data, demonstrating the model's ability to capture both the initial rise to plateau and subsequent exponential attenuation. The excellent agreement validates the physical assumptions underlying the parametrization.

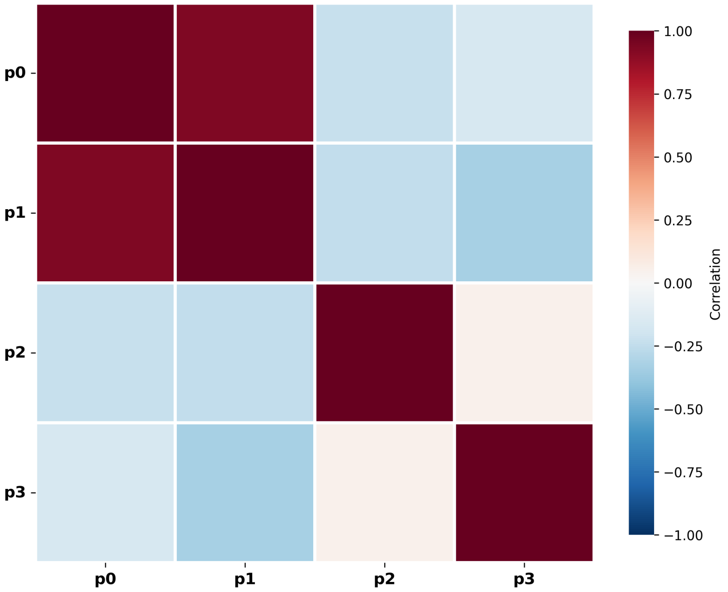

Figure 6.3: Correlation matrix for the phenomenological model parameters across multiple calibration fits. The correlation structure reflects the physical relationships between p_0 and p_1.

6.1.4 Dependence of the plateau parameter on environmental correlations

Application of the phenomenological model to the complete database of daily calibrations for RUN 3 and RUN 4 generates time series for the four fit parameters, enabling systematic investigation of the temporal trends and of the correlation with environmental or operational variables.

The plateau parameter p_0 represents the plateau light yield, i.e. the maximum achievable signal in the absence of attenuation effects, and is strongly correlated with the GEM gain. Environmental factors that could influence p_0 include humidity variations affecting optical transmission and temperature fluctuations modifying gas properties and scintillation efficiency. Additionally, variations in the gas system operating conditions, such as pressure regulation and gas mixture stability, could impact the overall light yield.

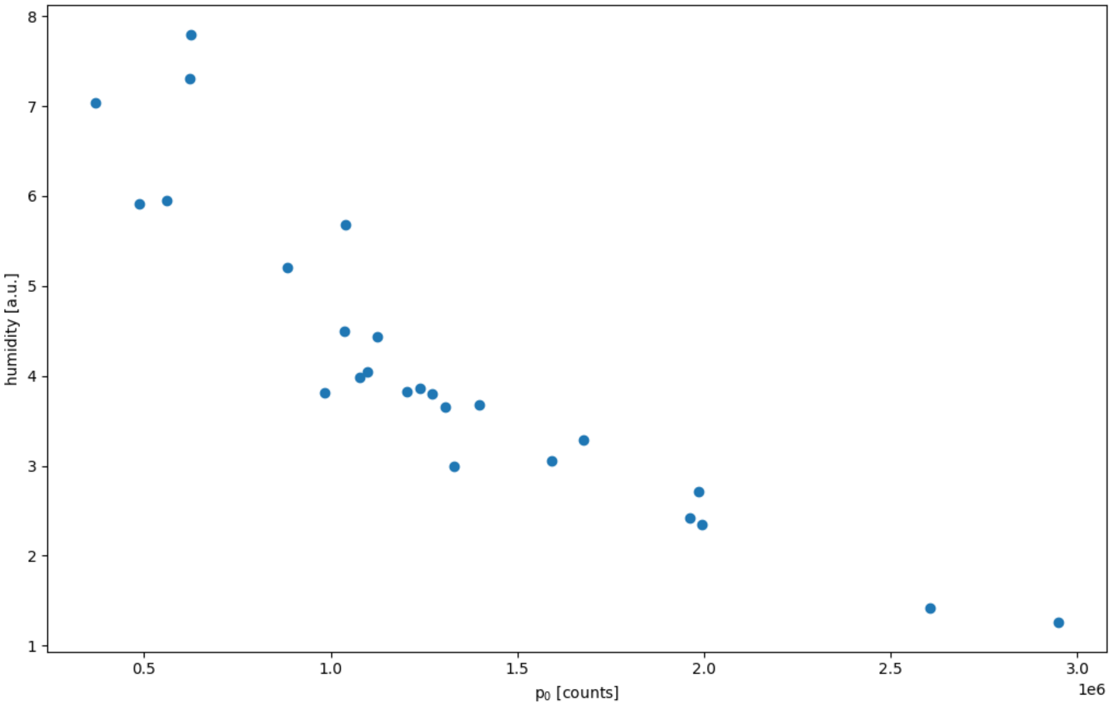

Figure 6.4: Correlation between environmental humidity and plateau light yield parameter p_0. The negative correlation confirms the expected sensitivity of optical transmission to water vapor content, providing validation of the physical interpretation of the model parameters.

Figure 6.4 demonstrates a clear correlation between environmental humidity and the plateau parameter p_0. In days with a higher humidity level, reduced plateau values are measured, consistent with the expected impact of water vapor on optical transmission properties. Water molecules can act as quenching centers for excited states in the gas mixture, reducing the overall scintillation efficiency. Additionally, humidity can affect the transmission properties of optical elements through condensation or surface contamination effects.

This correlation provides important validation of the physical interpretation of the model parameters and demonstrates the detector's sensitivity to environmental conditions.

6.1.5 Attenuation parameter and gas contamination

The attenuation parameter p_2 encapsulates the effective reabsorption length for primary scintillation photons during propagation through the detector volume. Unlike the plateau parameter, which reflects overall light production capacity, p_2 specifically characterizes the optical quality of the detector medium.

Figure 6.5 shows a clear temporal evolution of the attenuation parameter, characterized by a gradual degradation occurring over timescales of months. This systematic trend

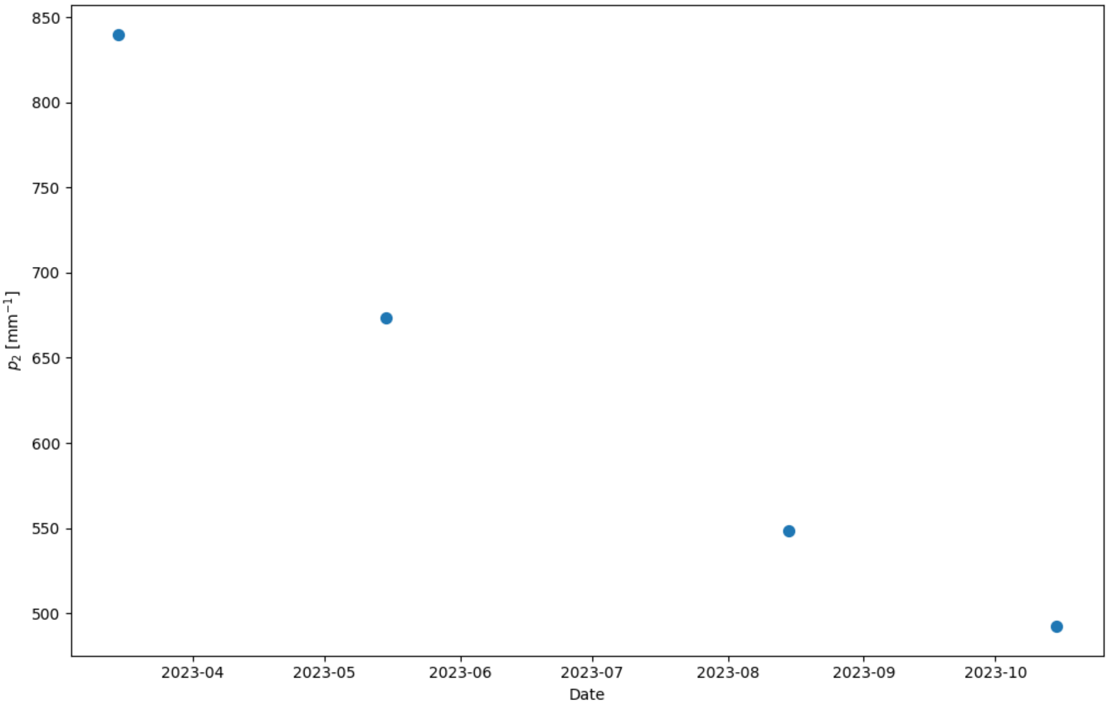

Figure 6.5: Temporal evolution of the attenuation parameter p_2. Each data point corresponds to the monthly average of the values extracted from individual runs.

suggests the presence of cumulative contamination effects affecting the optical properties of the gas mixture. A possible explanation for this behavior is the progressive accumulation of impurities in the gas volume. Studies conducted within the CYGNO collaboration have indeed demonstrated the presence of radon, which could degrade the optical transparency of the scintillating gas over time [158].

The parameters p_1 and p_3 were not investigated independently due to their limited physical significance. As shown in Figure 6.3, p_1 exhibits a strong correlation with p_0, reflecting the fact that the saturation effect depends directly on the light yield: higher gain produces more photons, which in turn leads to stronger saturation. The offset parameter p_3 serves primarily as a mathematical adjustment to locate the transition region between the rising and decaying components of the light profile, without a direct physical interpretation.

6.1.6 Operational mitigation strategies

The systematic characterization of temporal variations and their correlations with environmental and operational parameters enables the development of effective mitigation strategies. The most successful intervention identified through this analysis involves increasing the gas flow rate during periods of degraded optical performance.

Enhanced gas flow serves multiple functions in maintaining optical quality. Fresh gas continuously dilutes accumulated contaminants, preventing the buildup of species that could absorb or scatter scintillation light. Additionally, increased flow maintains positive pressure within the detector volume, reducing the infiltration of external contaminants such as water vapor or atmospheric pollutants.

Temperature and humidity control also contribute to detector stability, though these parameters are largely determined by the underground environment and offer limited operational flexibility.

The phenomenological model described in Equation 6.1 has been integrated into the experiment's real-time monitoring infrastructure (Figure 6.6). This integration enables continuous tracking of the fit parameters (p_0, p_1) providing immediate feedback on detector stability and performance trends.

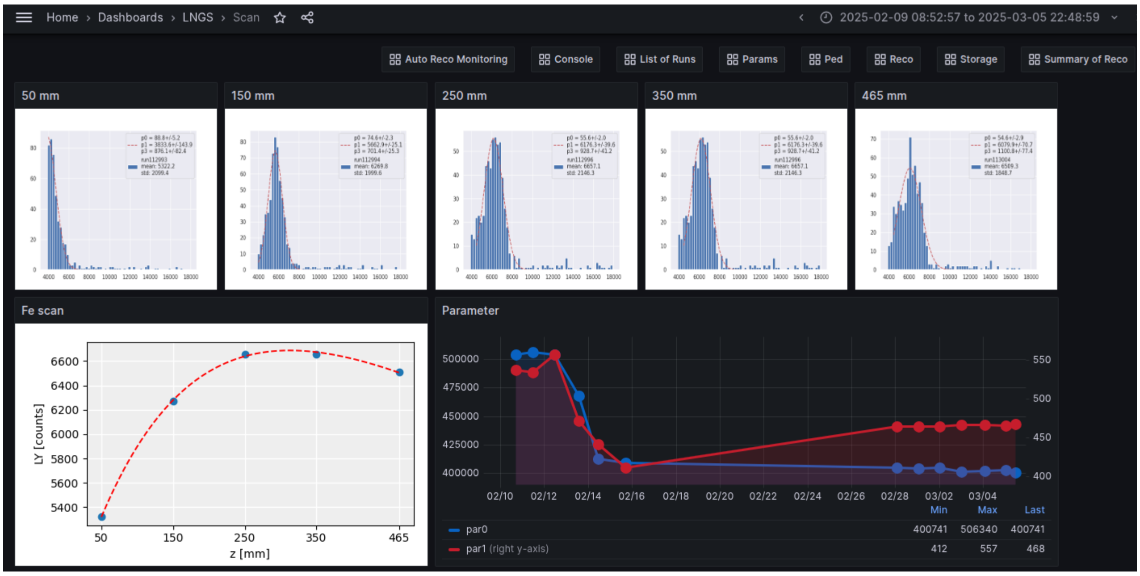

	Min	Max	Last
par0	400741	506340	400741
par1 (right y-axis)	412	557	468

Figure 6.6: Monitoring system implemented within the Grafana framework for live monitoring of the ^{55}Fe scan. The top five panels show Gaussian fits to the ^{55}Fe peak. The bottom-left panel displays the fit using the function described in Eq. 6.1, while the bottom-right panel shows the time evolution of the parameters p_0 and p_1.

6.2 Characterization of the saturation model with LIME underground data

This section presents a comprehensive study of detector simulation and digitization parameter optimization achieved through systematic comparisons between experimental data of LIME collected underground at LNGS and Monte Carlo simulations. It should be noted that the saturation model is constrained using low-energy X-ray calibration data from ^{55}Fe sources, and that this procedure does not by itself constitute a full validation of the model for electron-recoil events at higher energies. However, within the scope of this thesis and the targeted CYGNO applications discussed here, the most relevant energy regime is the low-energy domain, from a few keV to a few tens of keV.

The simulation framework has been introduced in Chapter 5, while the analysis procedure is presented in Chapter 4. The ^{55}Fe calibration dataset employed here consists of dedicated measurements acquired at multiple GEM voltages and source positions, ensuring sensitivity to both amplification and drift-related effects. These ^{55}Fe runs enable a robust parameter determination across diverse operating points, thereby ensuring reproducibility and reliability of the simulation-to-data comparison, expanding and complementing the optimization in Chapter 5 and the studies in Section 6.1.

6.2.1 Experimental setup and data collection

The experimental data used for parameter optimization were collected during Run 4 at the Laboratori Nazionali del Gran Sasso (LNGS) on December 15, 2023. The experimental approach consisted of systematic scans that varied both the GEM1 voltage and the ^{55}Fe source position along the drift direction (z-axis), enabling comprehensive characterization of detector response under different amplification conditions and drift distances. This dual-parameter approach was crucial for disentangling the effects of gain saturation from those of electron reabsorption, described in Chapter 5.

The experimental parameter space was chosen to cover a GEM1 voltage range from 260 V to 440 V, spanning from low amplification conditions where saturation effects are expected to be minimal to higher amplifications where the non-linear behavior of the gain emerges. Source positions were systematically varied at $z = 5, 10, 15, 25, 35,$ and 46.5 cm from the GEM stack, providing sensitivity to electron absorption and diffusion effects during the drift process. In each experimental configuration, 500 ^{55}Fe interaction events were recorded, ensuring adequate statistical precision for reliable parameter extraction while maintaining a reasonably short data collection time to ensure the stability of the environmental parameters.

Data quality was ensured through the application of comprehensive selection criteria designed to isolate genuine single-electron tracks while removing spurious events and backgrounds. The selection cuts were carefully optimized on Monte Carlo studies and included:

- Constraints on track length to remove cosmic ray events:

$$\texttt{sc\_length} < 7.5 \text{ cm} \tag{6.2}$$

- Average energy density requirements to avoid high density tracks:

$$\frac{\texttt{sc\_integral}}{\texttt{sc\_nhits}} < 100 \text{ counts/pixel} \tag{6.3}$$

- Track width-to-length ratio constraints to select spot-like tracks:

$$0.5 < \frac{\texttt{sc\_width}}{\texttt{sc\_length}} < 1.0 \tag{6.4}$$

- Fiducial volume requirements with track barycenters inside a central circular region of radius 750 pixels (11.25 cm) to remove sensor noise on the border and exclude other possible background events.

6.2.2 Parameter optimization strategy

The primary objective of this analysis is to determine the digitization parameters λ and α, which characterize the detector response as discussed in Chapter 5. In this context, α denotes the inverse characteristic voltage scale (measured in V^{-1}) governing the exponential dependence of the avalanche multiplication on the applied GEM voltage, effectively encapsulating the overall amplification behavior of the detector. The parameter λ instead represents the absorption length associated with electron attachment processes in the gas, and characterizes the exponential loss of primary electrons as a function of the drift distance z. These parameters can be determined by fitting experimental data acquired in unsaturated conditions, where low V_{GEM1} and large z values ensure that the mean reconstructed track integral follows:

$$I \equiv \texttt{sc\_integral} = I_0\, e^{\alpha V_{\mathrm{GEM1}}}\, e^{-z/\lambda}, \tag{6.5}$$

where I_0 encapsulates the initial number of primary electrons, the three-GEM cascade amplification, the photon yield, and the camera detection efficiency.

The fitting procedure exploits the exponential dependencies on both GEM voltage and drift distance to simultaneously extract α and λ from data acquired at multiple (V_{GEM1}, z) configurations. By restricting the analysis to the unsaturated regime, we ensure that these parameters reflect the fundamental detector response.

6.2.3 Low density correction

A critical aspect of accurate parameter extraction is accounting for the systematic underestimation of track light yield that occurs when tracks are faint. Under conditions of reduced GEM voltages and long drift distances, corresponding to low values of `sc_integral`, the ratio between the reconstructed integral and the true integral decreases significantly. This effect arises from noise threshold effects, clustering algorithm limitations, and statistical fluctuations that become more pronounced at low signal-to-noise ratios.

The magnitude of this systematic bias has been quantified through detailed Monte Carlo studies, where the true deposited light was compared to the reconstructed integrals obtained after the full digitization and reconstruction chain described in Chapter 4. Figure 6.7 illustrates this effect by showing the comparison between true Monte Carlo integrals (solid lines) and reconstructed integrals (dashed lines) as a function of drift distance for different GEM voltages. The systematic divergence between these curves at low integral levels clearly demonstrates the underestimation that must be corrected to enable accurate parameter extraction.

To correct this systematic effect, the ratio between reconstructed and true integrals was parameterized as a function of track density, defined as `sc_integral`/`sc_nhits`. This parameterization was chosen because the degree of underestimation correlates strongly with the average light yield per pixel, which reflects both the total signal and its spatial distribution. The correction function was fitted using a sigmoid curve:

$$f(x) = \frac{L}{1 + e^{-k(x - x_0)}}, \tag{6.6}$$

where x = `sc_integral/sc_nhits` represents the track density. As illustrated in Figure 6.8, the fitted parameters are $L = 1.00$, $x_0 = 2.85$, and $k = 2.08$. The sigmoid functional form naturally captures the transition from significant underestimation at low densities to negligible bias at high densities, providing a smooth correction across the full density range. This correction function was applied inversely to both the experimental and simulated data, dividing the measured `sc_integral` by $f(x)$ to recover an unbiased estimate of the true light yield in the low-density regime.

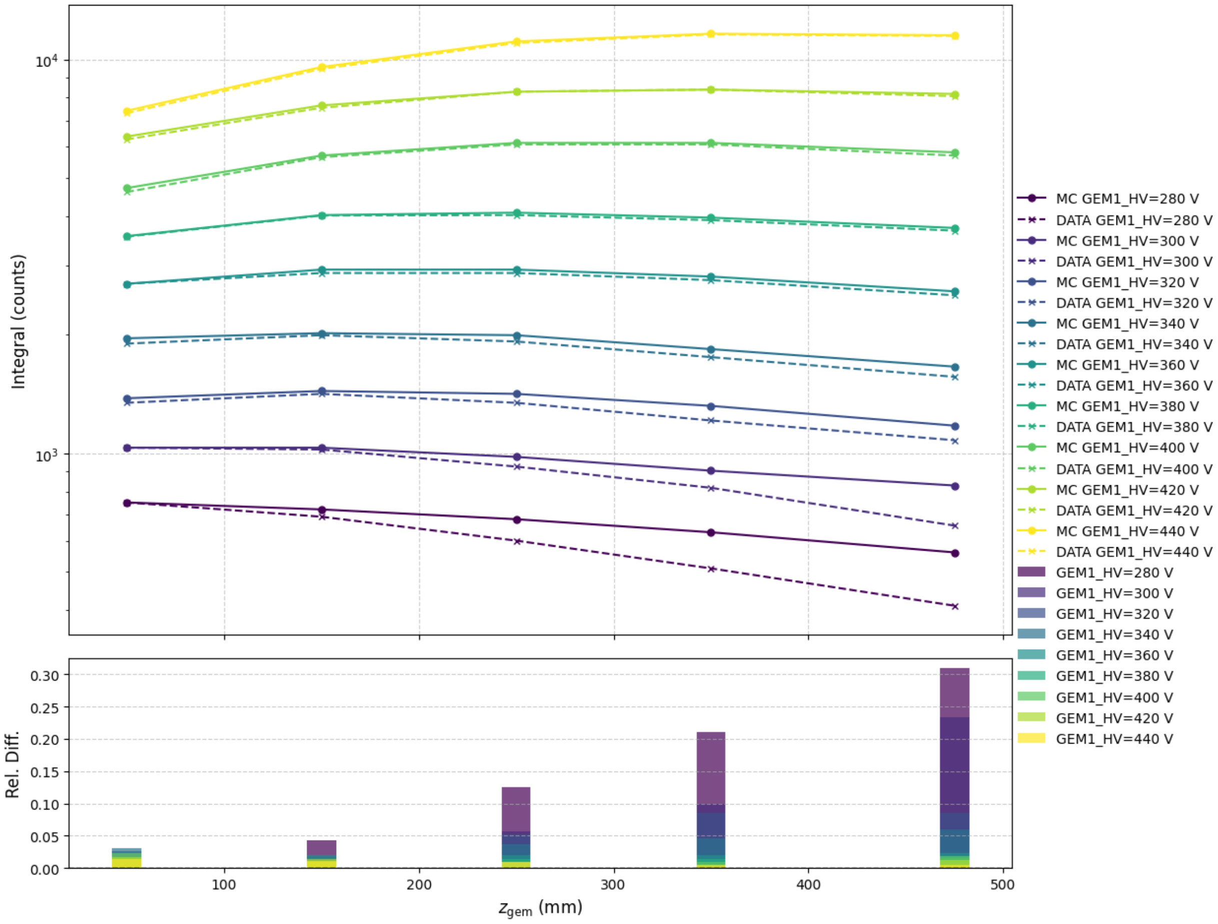

Figure 6.7: Comparison between true Monte Carlo integral (solid lines) and reconstructed integral (dashed lines) as a function of drift distance for different voltages of GEM1. The divergence at low integral values demonstrates the systematic underestimation of track light yield in the low-density regime.

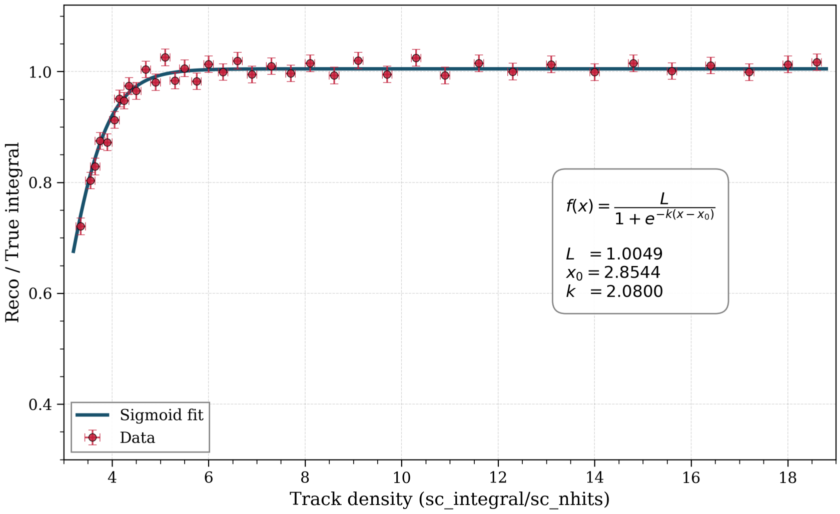

Figure 6.8: Ratio of reconstructed to true integral as a function of track density (defined as `sc_integral`/`sc_nhits`), fitted with a sigmoid curve. This correction function was applied to compensate for systematic underestimation in the low-density regime.

6.2.4 Parameter optimization results

The parameter optimization process employed a fitting procedure applied to the complete experimental dataset, where each data point represents the average `sc_integral` over approximately 500 reconstructed tracks.

To determine the parameters without being affected by saturation effects, the fitting procedure includes only a subset of data points that are considered to be in the unsaturated regime, where the simple exponential model in Eq. 6.5 applies. The choice of which points to include in the fit directly influences the extracted parameter values. Therefore, a systematic scan was performed by progressively varying the number of included points and monitoring the resulting parameter stability, as detailed below.

Figure 6.9 presents the results of this fit, displaying `sc_integral` as a function of both GEM voltage and drift distance. The red data points, each representing the statistical average of 500 individual track measurements, show the characteristic behavior of the detector response across different operating conditions. The green threshold line serves as a critical boundary, indicating the division between saturated and unsaturated regimes used in the fitting procedure. Data points falling above this threshold were excluded.

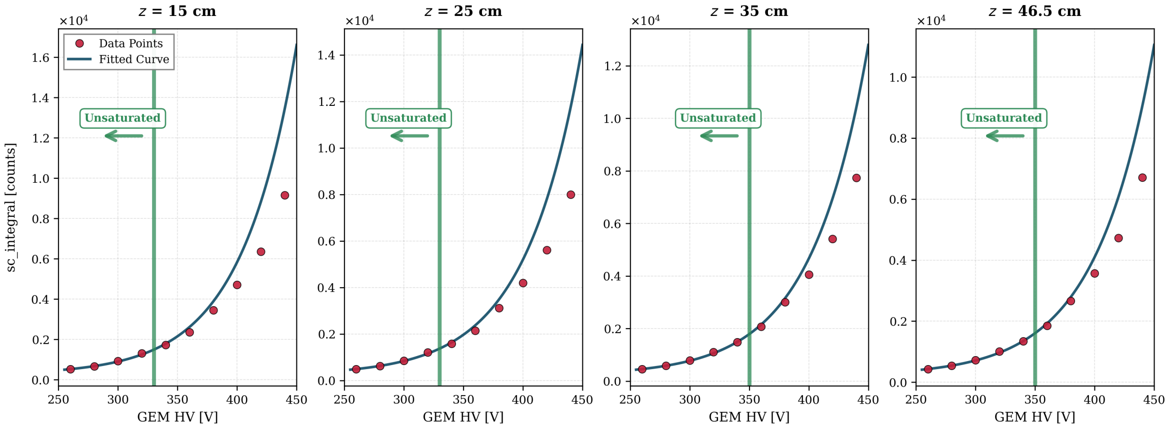

Figure 6.9: Results of simultaneous fit of `sc_integral` as a function of both GEM voltage and drift distance. Each red data point represents the average of 500 tracks. The green threshold line indicates the boundary between "saturated" and "unsaturated" regimes, hence the points actually included in the fit.

The selection of which data points to include in the fit requires careful consideration of the saturation behavior. At fixed voltage, points at higher drift distances (larger z) experience less saturation due to the lower charge density reaching the GEM stack. Conversely, at fixed z, higher voltages lead to stronger saturation effects. Therefore, a uniform selection strategy (e.g., including only the lowest voltage for all z values and then uniformly increasing voltage) would not properly account for the different saturation levels across the parameter space.

The adopted selection strategy proceeds as follows: starting with $N = 1$, we include only the least saturated point in absolute terms, corresponding to the highest drift distance and lowest voltage. For $N = 2$, we add the point with the next highest z at the same lowest voltage. This process continues by progressively decreasing z at fixed voltage until all drift distances at the lowest voltage are included, after which the voltage is increased and the process repeats. This approach ensures that saturation effects are gradually introduced in a controlled manner. It should be noted that alternative selection strategies were explored, such as uniformly increasing the number of points for each z or prioritizing voltage increase over z decrease, and these yielded similar results.

Figure 6.10 illustrates the systematic study performed to determine the optimal threshold position. By varying the number of included data points N according to the selection strategy described above, we observe how the fitted parameters evolve. The four panels show the behavior of the normalization factor I_0, the amplification slope α, the absorption length λ, and the fit quality quantified by χ^2. A key observation from this analysis is the presence of a plateau region where the parameters exhibit minimal variation as N changes. This plateau indicates a regime where the fit is stable and insensitive to the exact choice of threshold, suggesting that the included data points are predominantly from the unsaturated regime.

The final parameter values were extracted from this stable region, where changing the number of fitted points does not significantly alter the results. This methodology provides confidence that the optimized parameters genuinely characterize the unsaturated detector response rather than being artifacts of an arbitrary threshold choice.

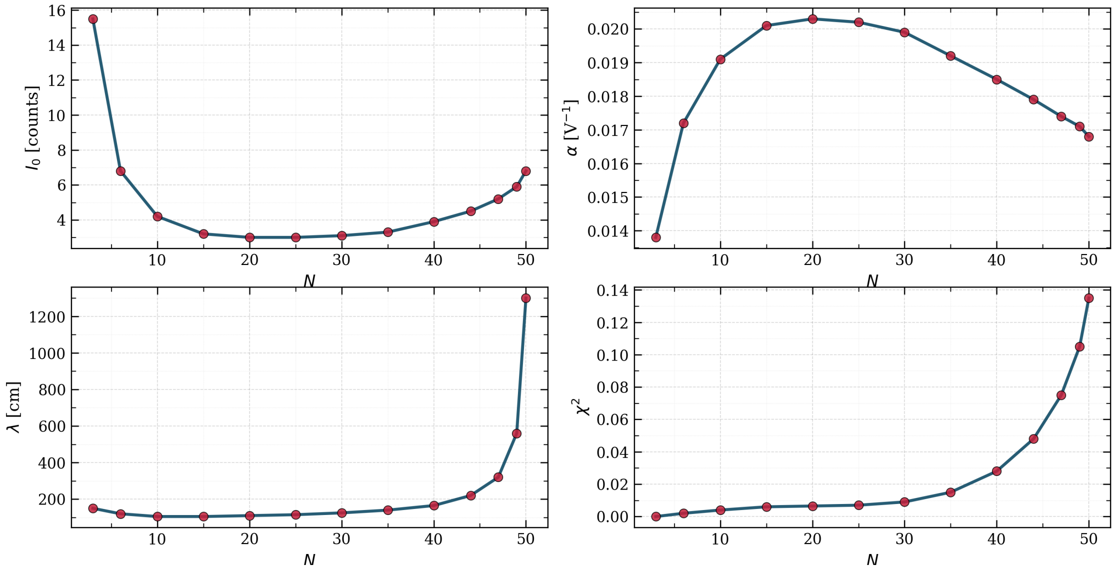

Figure 6.10: Sensitivity analysis of the fitted parameters as a function of the number of included data points N. The four panels show: top left, the fitted normalization I_0; top right, the amplification slope α; bottom left, the absorption length λ; and bottom right, the χ^2 of the fit. The presence of plateau regions indicates parameter stability, guiding the selection of the optimal threshold that separates saturated from unsaturated regimes.

The final optimized digitization parameters obtained from this procedure are

$$\lambda_{\text{abs}} = 1350 \text{ mm}, \tag{6.7}$$

$$\alpha = 0.0209 \text{ V}^{-1}, \tag{6.8}$$

These values summarize the outcome of the LNGS optimization and represent the reference parameter set for LIME underground simulation.

6.2.5 Simulation validation

With the optimized parameters established and fixed, a validation procedure was carried out to assess the accuracy of the simulation framework across multiple characteristics of the ^{55}Fe tracks.

Figure 6.11 demonstrates the remarkable accuracy achieved by the simulation framework, showing the comparison between experimental data points and Monte Carlo simulation predictions for the light integral as a function of both GEM voltage and drift distance. Each experimental data point represents the carefully computed average `sc_integral` over 500 individual tracks, ensuring robust statistical precision. It should be noted that this comparison uses the same dataset that was employed for the parameter optimization procedure described in the previous Section. However, the agreement extends across the entire dataset, spanning the full range of experimental conditions: all drift distances and all GEM voltages, including both the saturated and unsaturated regimes. The simulation achieves agreement within 5% across two full orders of magnitude variation in signal amplitude, spanning from approximately 1,000 counts to over 100,000 counts. This exceptional level of precision, maintained across such a broad range of operating conditions, validates both the underlying physical model and the parameter optimization procedure, providing strong confidence in the simulation framework.

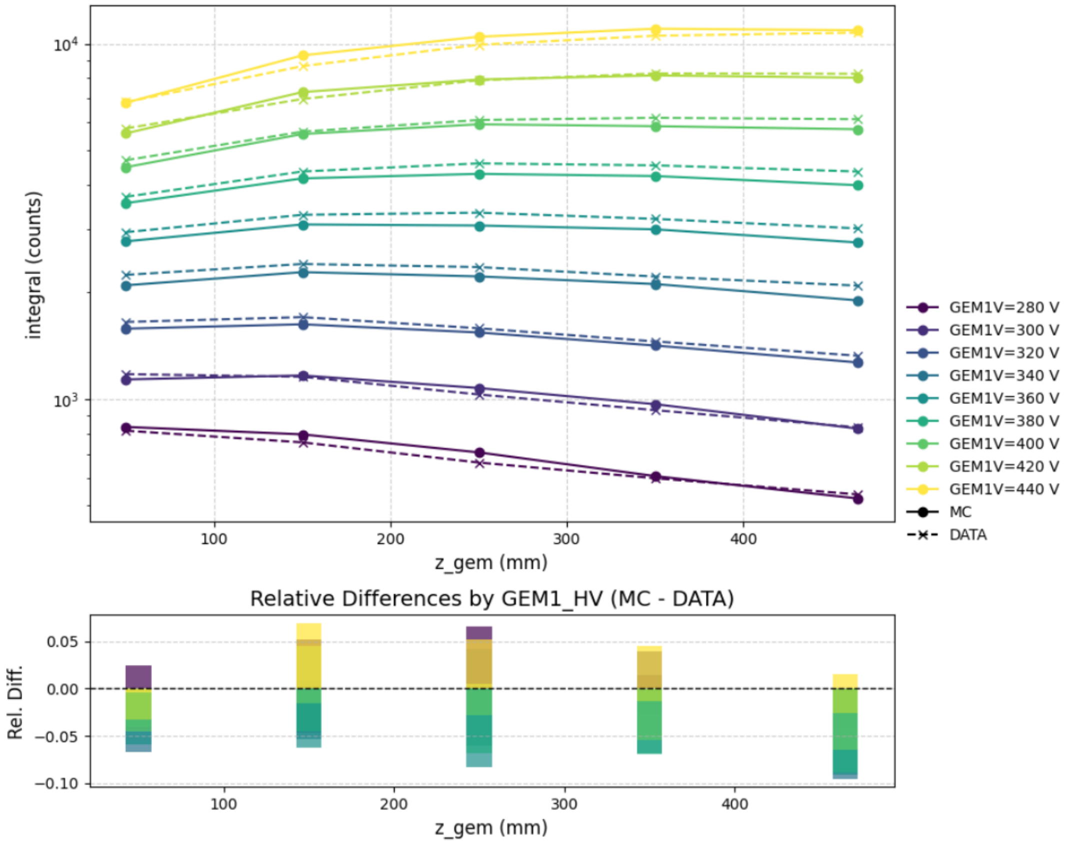

Figure 6.11: Comparison between experimental data (points) and Monte Carlo simulation (lines) for the light integral as a function of both GEM voltage and drift distance. Each data point represents the average `sc_integral` over 500 tracks. The simulation achieves 5% accuracy across two orders of magnitude variation in signal amplitude.

Beyond the light integral, the simulation framework demonstrates its ability to accurately reproduce the Gaussian profile characteristics of the reconstructed tracks. Figure 6.12 presents the comparison of the average Gaussian sigma parameter, defined as $\langle\sigma_{\text{gauss}}\rangle = (\sigma_T + \sigma_L)/2$, where σ_T and σ_L denote the transverse and longitudinal standard deviations of the Gaussian fits to the track intensity profile, respectively (see Section 4.4), between experimental data and simulation as a function of the drift distance. The transverse and longitudinal width parameters show excellent agreement across the full range of experimental conditions, with the variation in sigma reflecting the changing GEM voltage conditions.

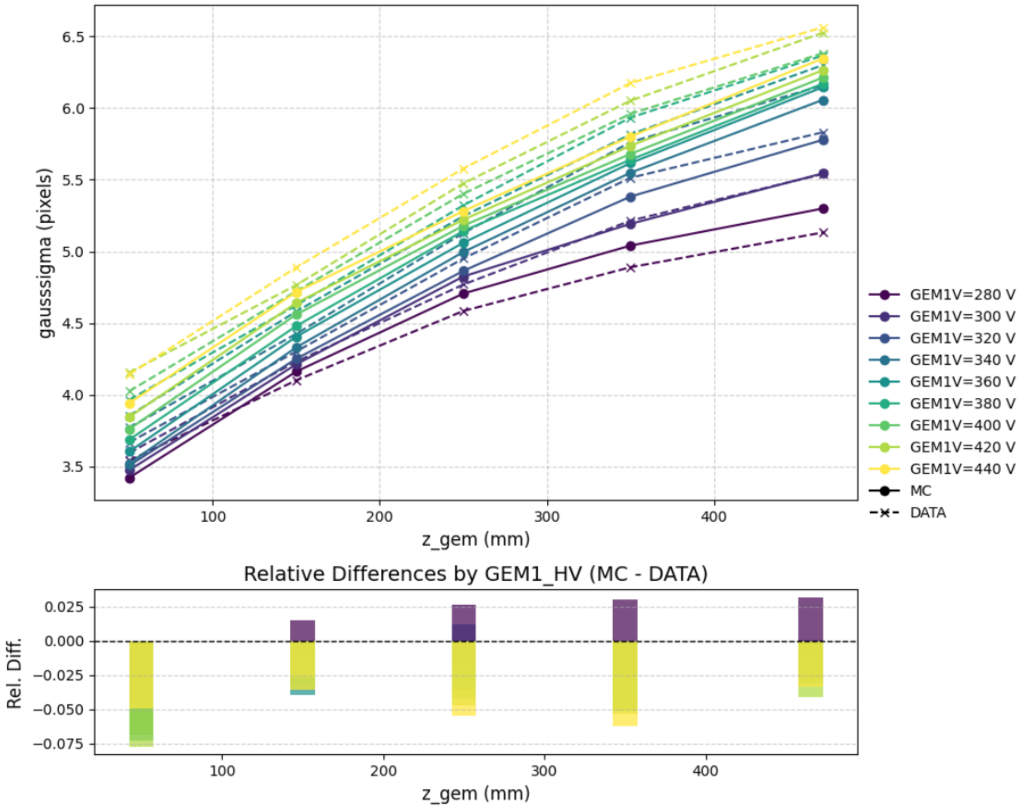

Figure 6.12: Comparison of average Gaussian sigma parameter ($\langle\sigma_{\text{gauss}}\rangle = (\sigma_T + \sigma_L)/2$) between experimental data and simulation as a function of both GEM voltage and drift distance.

The evolution of track width characteristics is further illustrated in Figure 6.13, which shows how the Gaussian sigma parameter varies with the light integral. This relationship provides insight into the effect of changing GEM voltage conditions on track spatial characteristics, with higher voltages generally leading to more compact light distributions due to the increased multiplication efficiency. The upturn observed at very low integral values reflects reconstruction efficiency limitations: at low light yield, a fraction of events falls below the detection or reconstruction threshold, leading to a systematic bias in the reconstructed sample rather than a genuine physical broadening of the tracks.

The validation extends to the amplitude characteristics of the Gaussian fits, as demonstrated in Figure 6.14. This comparison of the average Gaussian amplitude parameter between experimental data and Monte Carlo simulation shows consistent agreement across different experimental conditions. The good agreement in amplitude parameters validates the light production and detection modeling implemented within the digitization framework, confirming that the simulation accurately captures both the total light yield and its spatial distribution.

Additional validation of the spatial modeling accuracy is provided through analysis of cluster size parameters. Figure 6.15 shows the comparison of the total cluster size (`sc_size`) between experimental data and simulation, where this parameter represents the total number of pixels in the reconstructed cluster without application of zero-suppression

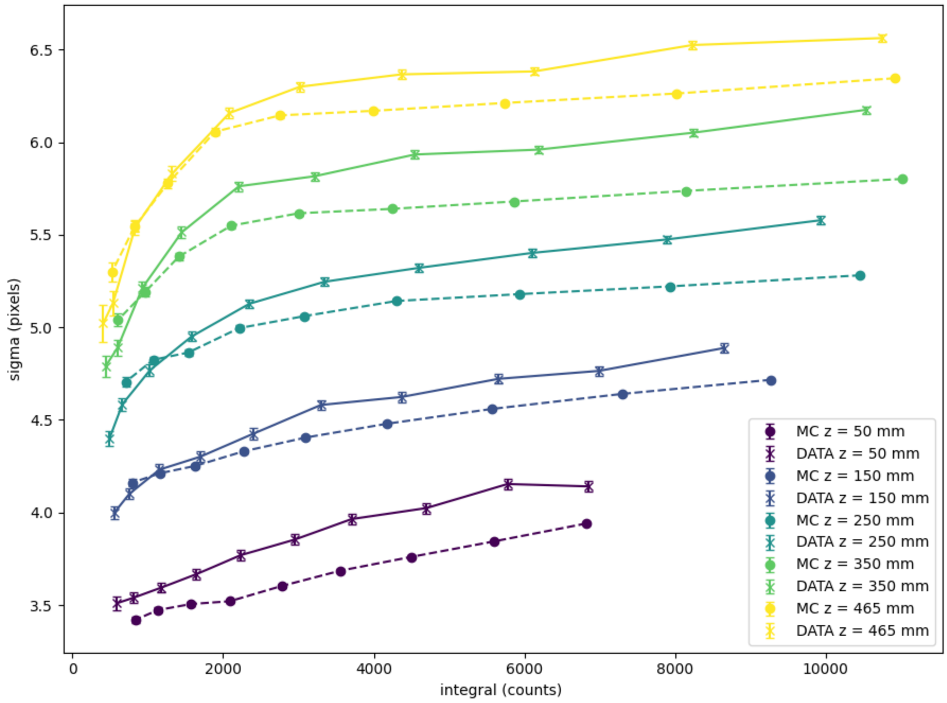

Figure 6.13: Evolution of Gaussian sigma parameter with light integral, showing the effect of changing GEM voltage on track spatial characteristics. The upturn at low integral values reflects reconstruction efficiency limitations rather than physical broadening. A residual discrepancy of approximately 5% is observed at high light-integral values, whose origin is not yet fully understood and deserves further investigation. Nonetheless, the overall agreement remains very good, as the simulation is able to reproduce both the light integral and the spot-width behaviour over roughly two orders of magnitude in integral and across the full drift-distance range considered in the analysis.

thresholds. The excellent agreement across all experimental conditions validates the accuracy of the spatial extent modeling for the light distribution, confirming that the simulation properly captures the physical processes that determine track topology.

Figure 6.16 presents the comparison of the reconstructed variable `sc_nhits`, which represents the number of pixels above the zero-suppression threshold. This parameter provides additional sensitivity to the spatial distribution characteristics.

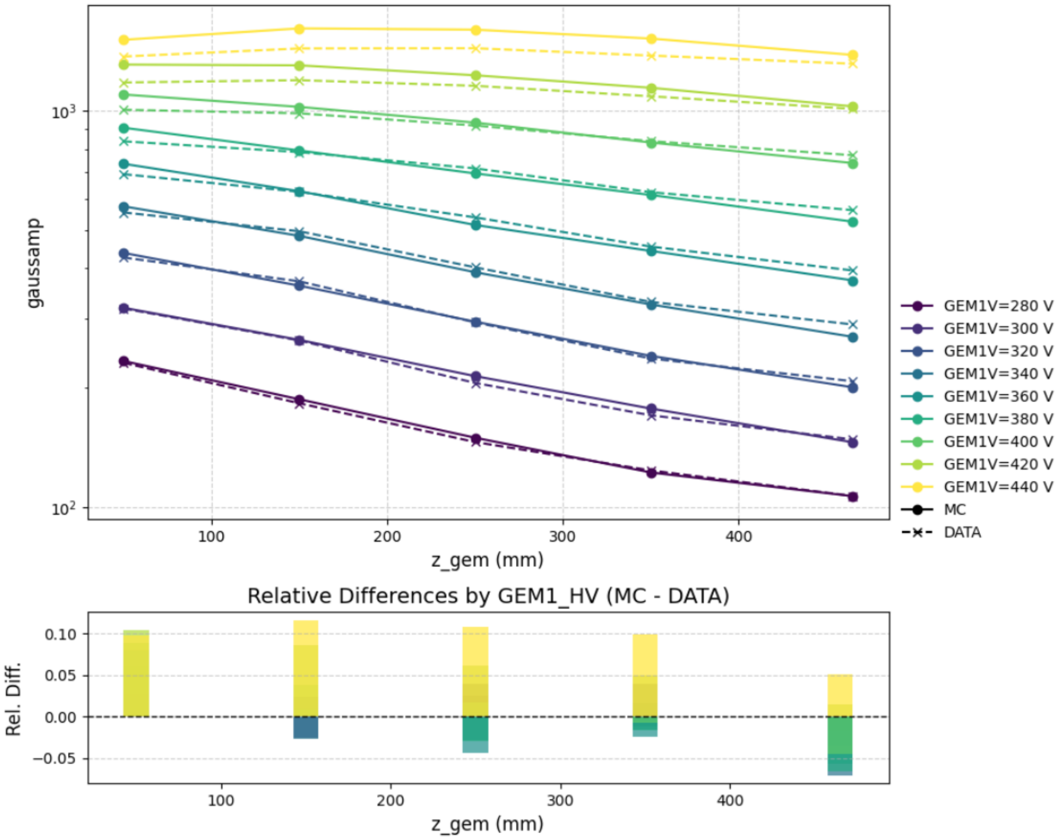

Figure 6.14: Comparison of average Gaussian amplitude parameter ($\langle A_{\text{gauss}} \rangle = (A_T + A_L)/2$) between experimental data and Monte Carlo simulation, demonstrating consistent light production modeling across different experimental conditions.

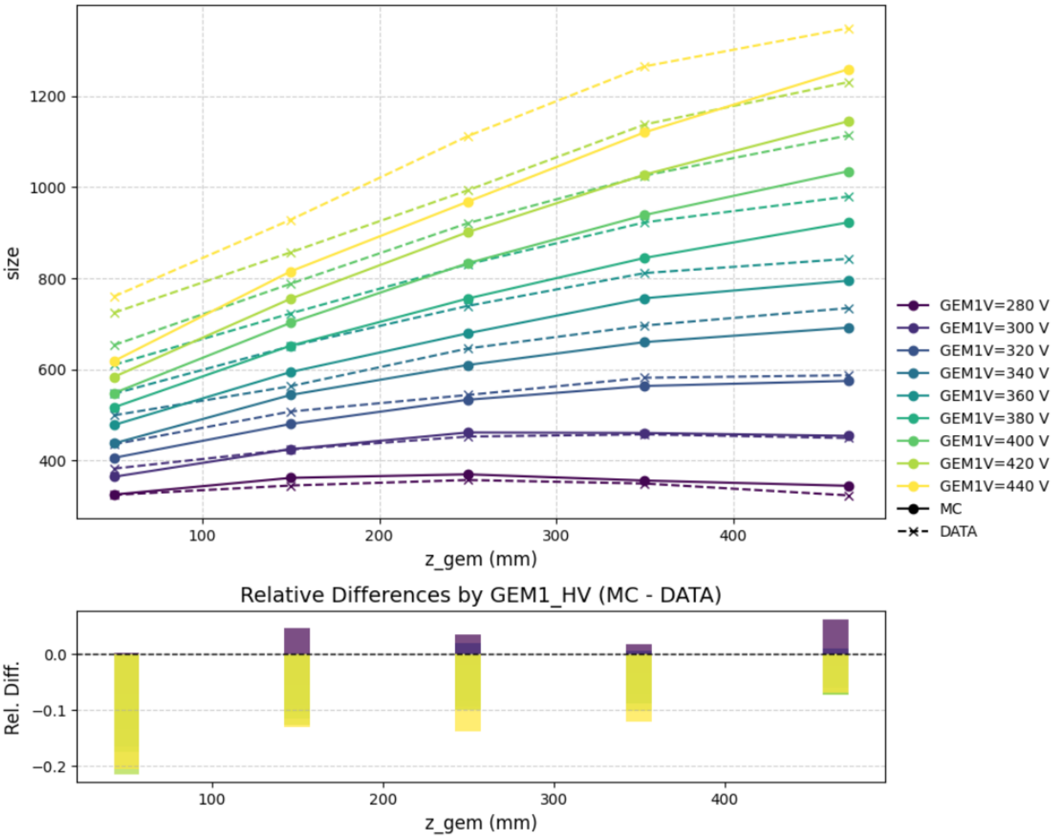

Figure 6.15: Comparison of cluster size (`sc_size`) between experimental data and simulation, representing the total number of pixels in the cluster without zero-suppression. The agreement validates spatial extent modeling of the light distribution.

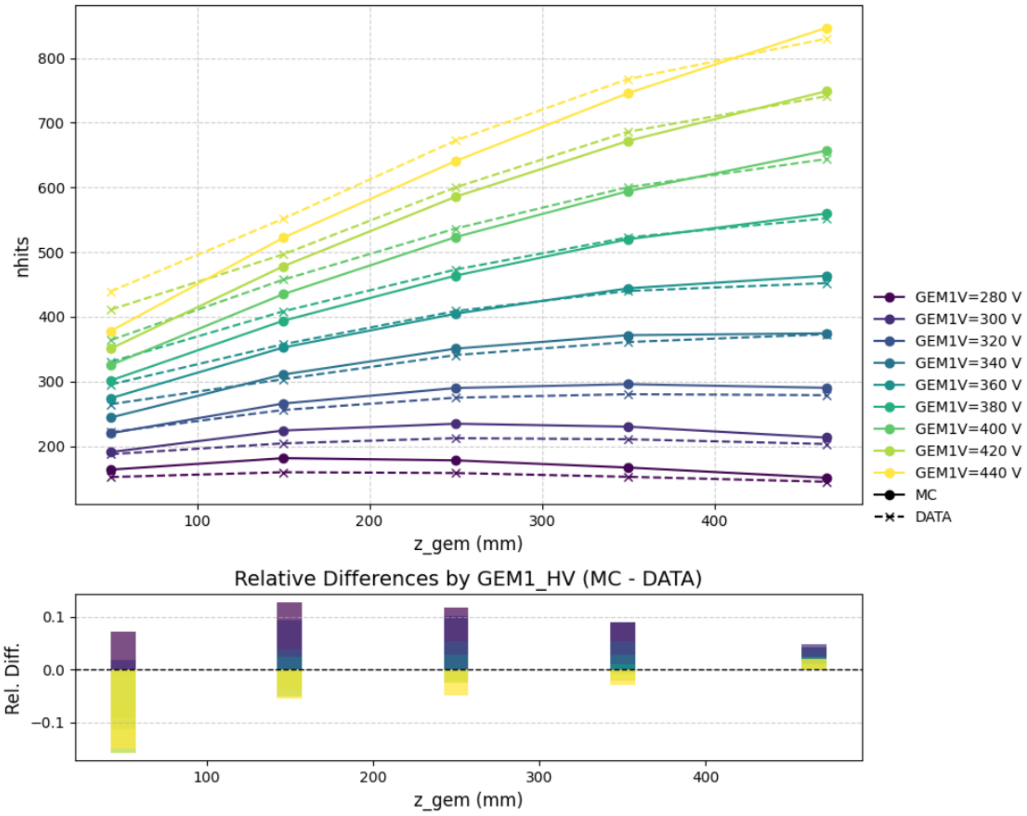

Figure 6.16: Comparison of hit multiplicity (`sc_nhits`) between experimental data and simulation, showing the number of pixels above zero-suppression threshold. This parameter is sensitive to both spatial distribution and threshold settings in the digitization chain.

6.2.6 Concluding remarks and outlook

The parameter optimization framework developed in this study is based on a specific set of experimental runs conducted under particular environmental conditions during a limited time period (December 2023). The applicability of these parameters to different experimental configurations or time periods must be carefully considered.

A dedicated stability study has been carried out (Section 6.1), providing a more quantitative understanding of the variability and its impact on detector response. Gas condition variations, such as changes in gas composition, pressure, and temperature over time scales ranging from hours to months, directly impact detector properties including electron drift velocity, attachment coefficients, and amplification characteristics, potentially requiring periodic re-optimization of parameters. In particular, the absorption length λ_{abs} is most sensitive to these conditions, as it is directly related to the electron attachment process in the gas mixture.

The present optimization is restricted to a GEM voltage range between 260 V and 440 V, chosen to balance detector performance with operational stability. Extending the simulation to higher voltages, where different saturation regimes may emerge, or to lower voltages, where the signal to noise ratio becomes more challenging, would likely require further parameter adjustments and additional validation studies.

Finally, the optimized parameters are primarily tuned for keV-scale electron recoils, specifically the 5.9 keV photopeak from the ^{55}Fe calibration source. Applications to significantly different energy ranges will require dedicated validation and potentially parameter adjustments to account for different detector response characteristics. In this context, the studies presented in Chapter 7 provide additional insights and cross-checks that help to assess the robustness of the parameterization across different energy regimes and track types (electron recoils vs. nuclear recoils).

Chapter 7

Validation of nuclear recoil simulation with AmBe source data

7.1 AmBe Neutron Source Monte Carlo Studies

The accurate simulation of neutron interactions represents a crucial component for understanding backgrounds and calibration signatures in dark matter search experiments. Neutron sources, particularly AmBe (Americium-Beryllium) sources, provide nuclear recoil signatures that are essential for detector calibration and validation of discrimination capabilities between nuclear recoils (signal-like) and electron recoils (background-like). This section presents a comprehensive Monte Carlo study of AmBe neutron interactions, focusing on understanding the fundamental physics of neutron interactions, kinematics, and the implementation of quenching factor corrections necessary for accurate energy reconstruction.

7.1.1 AmBe source characteristics and neutron interactions

AmBe sources represent one of the most commonly used neutron sources for detector calibration due to their relatively simple neutron energy spectrum and manageable radioactive decay properties. The neutrons are produced through the (α, n) reaction when alpha particles from ^{241}Am decay interact with ^{9}Be nuclei, producing neutrons with a characteristic energy spectrum extending from thermal energies up to approximately 11 MeV, with a mean energy around 4-5 MeV.

Figure 7.1 illustrates the energy spectrum of neutrons from the AmBe source as implemented in the Monte Carlo framework. The simulation incorporates realistic neutron production spectra and accounts for the geometric constraints imposed by the experimental setup.

The AmBe source geometry implemented in the Geant4 Monte Carlo simulation consists of a stainless-steel capsule with a diameter of 6.4 mm and a height of 17.6 mm, enclosing an AmBe source cylinder composed of a homogeneous mixture of AmO_2 and Be, with a diameter of 4 mm and a height of 4 mm. This simplified representation captures the essential geometric features while maintaining computational efficiency in the Monte Carlo calculations.

The probability of neutron interactions with different nuclei in the detector gas can be estimated using fundamental nuclear cross-section principles. For low-energy neutrons (below approximately 1 MeV), the interaction probability can be approximated using simple

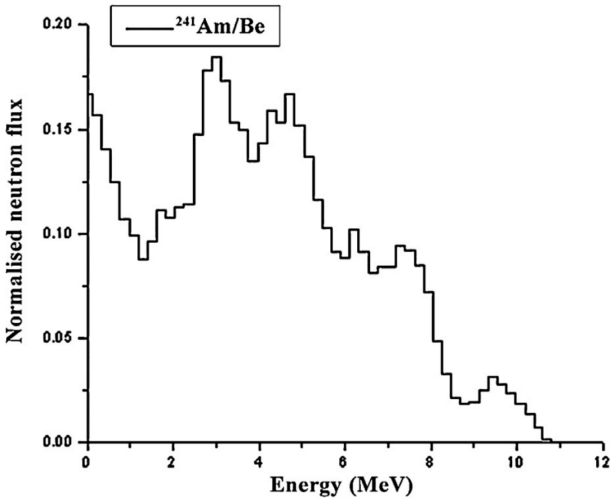

Figure 7.1: AmBe neutron spectrum from [240].

geometric considerations based on nuclear size. The nuclear radius can be written as:

$$R \approx r_0 A^{1/3} \tag{7.1}$$

where $r_0 \approx 1.2$ fm is the nuclear radius constant (representing the characteristic size scale of nuclear matter) and A is the mass number. The interaction cross-section is then proportional to the projected area of the nucleus:

$$\sigma \sim \pi R^2 \sim \pi r_0^2 A^{2/3} \tag{7.2}$$

For the gas mixture components of CYGNO/LIME (He:CF_4 60:40), we can calculate the theoretical relative interaction probabilities. The calculation accounts for three factors: the relative concentration in the gas mixture (0.6 for He and 0.4 for CF_4), the number of atoms of each type per molecule (1 for He, 1 for C, and 4 for F in each CF_4 molecule), and the cross-section scaling $A^{2/3}$. The individual contributions are:

$$\text{He contribution:} \quad 0.6 \times 1 \times 4^{2/3} = 1.51 \tag{7.3}$$

$$\text{C contribution:} \quad 0.4 \times 1 \times 12^{2/3} = 2.10 \tag{7.4}$$

$$\text{F contribution:} \quad 0.4 \times 4 \times 19^{2/3} = 11.40 \tag{7.5}$$

The relative probabilities are then obtained by normalizing to the total $(1.51 + 2.10 + 11.40 = 15.01)$:

- **Helium (He, A=4)**: Probability $\approx 10.08\%$
- **Carbon (C, A=12)**: Probability $\approx 13.98\%$
- **Fluorine (F, A=19)**: Probability $\approx 75.95\%$

Above 1 MeV, the interaction probability becomes significantly more complex and depends strongly on detailed nuclear cross-sections that exhibit resonance structures and energy-dependent behavior. However, this regime is well beyond the energy range relevant for CYGNO operations.

The theoretical predictions are compared to the actual Geant4 simulation results, as demonstrated in Figure 7.2. The dotted lines represent the theoretical predictions while

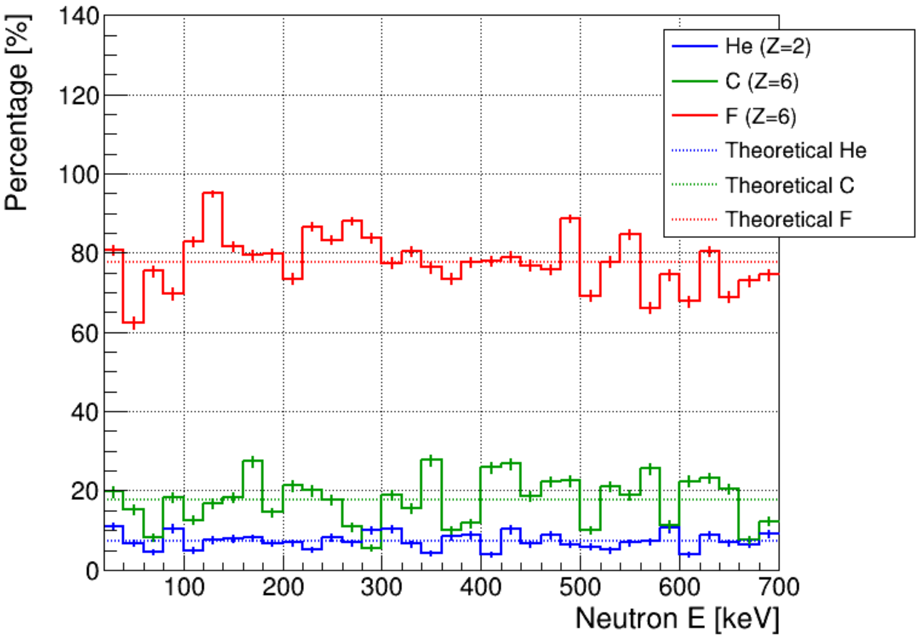

Figure 7.2: Comparison between theoretical predictions (dotted lines) and Geant4 simulation results (solid histograms) for neutron interaction probabilities as a function of neutron energy, showing excellent agreement for all nuclear species.

the solid histograms show the Geant4 simulation results. The simulation shows excellent agreement with theoretical expectations, with fluorine dominating the interaction probability (∼75-85%), followed by carbon (∼13-20%) and helium (∼5-10%). This validation provides confidence in the physical modeling of neutron interactions within the detector medium and confirms that the simplified theoretical approach captures the essential physics governing neutron-nucleus interaction probabilities.

7.1.2 Elastic scattering kinematics from the angular point-of-view

The aim of this section is to provide a derivation of the formulas applied to model the angular behavior of sphere-like particles, assuming elastic scattering, in Monte Carlo simulations.

First, we define the scenario in the center of mass (COM) frame, with graphical reference in Figure 7.3:

- Let our particles be spheres of radii r and R
- Let the two sphere's centers be separated by an "impact parameter" b
- The two particles have masses m and M, respectively
- The two particles are moving towards each other with velocity magnitude v

From simple geometric arguments, we can deduce that the angle γ between the recoil direction and the horizontal axis is related to b, r and R by the equation:

$$\sin\gamma = \frac{b}{r+R} \tag{7.6}$$

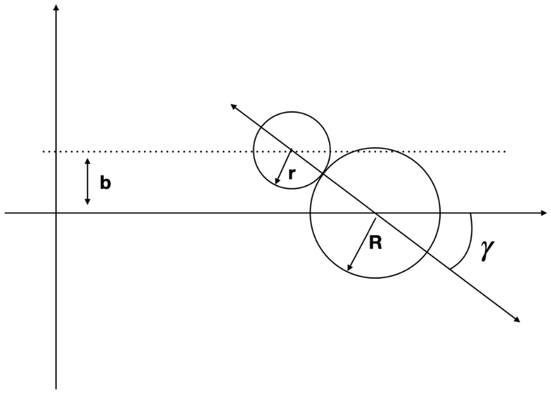

Figure 7.3: Sketch of the elastic scattering in the center of mass reference frame.

From purely classical mechanics reasoning, we can deduce that the COM velocity is $v_c = \frac{mv}{m+M}$, while the two velocities after the scattering are, in magnitude:

$$v_m^* = \frac{M}{m+M}v, \quad v_M^* = \frac{m}{m+M}v \tag{7.7}$$

with the superscript $*$ to represent the COM frame.

If we now move the discussion to the laboratory (LAB) frame, we are in front of the situation depicted in Figure 7.4.

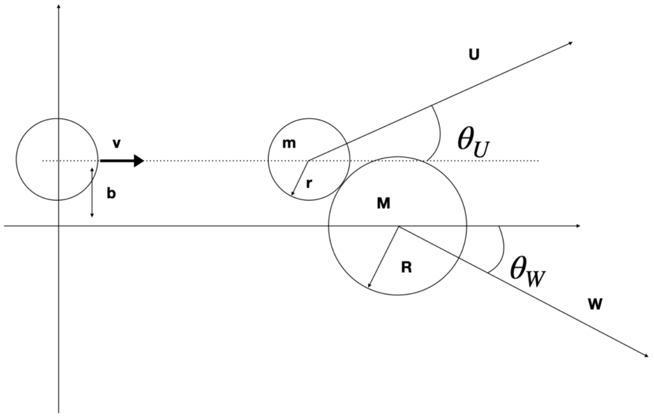

Figure 7.4: Sketch of the elastic scattering in the laboratory reference frame.

In particular:

- The smaller particle is the projectile (the neutron), impinging with velocity v on the bigger particle which is at rest (a nucleus)
- After the scattering, the two particles recoil away with velocities U and W, and angles θ_U and θ_W with respect to the horizontal, respectively

Transforming equations 7.7 with the Galileo transformations, we can obtain the following equations for the velocities in the LAB frame.

In particular we need to sum v_c to the x components of v_m^*, v_M^*, while the y components are unchanged. Note also that the $v_{m,x}^*$ is taken with a minus sign, since the positive direction for the horizontal axis is facing towards the right side of the plot in the figures.

In the end, we obtain:

$$\begin{cases} U_x = \frac{v}{m+M}(m - M\cos\gamma) \\ U_y = \frac{M}{m+M} v \sin\gamma \end{cases}, \quad \begin{cases} W_x = \frac{mv}{m+M}(1+\cos\gamma) \\ W_y = -\frac{mv}{m+M}\sin\gamma \end{cases} \tag{7.8}$$

We can now extract the formulas for the recoiling angles by simply exploiting the fact that $y/x = \tan\theta$ for two vectors x and y separated by an angle θ.

What we obtain is:

$$\theta_U = \arctan\left(\frac{M\sin\gamma}{m - M\cos\gamma}\right), \quad \theta_W = \arctan\left(\frac{-\sin\gamma}{1+\cos\gamma}\right) \tag{7.9}$$

from which we can see that the recoiling nucleus angle is completely independent from the particles masses.

Figure 7.5 shows the distributions of the recoil angles in the laboratory reference frame for different nuclear species (He, C, F). Specifically, θ_W represents the polar angle between the recoil direction and the incident neutron direction (horizontal axis), while ϕ is the azimuthal angle around the neutron beam axis. As evident from the distributions, and in agreement with the theoretical prediction of Equation 7.9, the angular distributions are independent of the nuclear species, confirming that the scattering kinematics depends only on the geometry of the collision and not on the masses of the recoiling nuclei. In particular, the polar angle θ_W of the recoiling target nucleus is completely independent of the mass ratio M/m between the nucleus and the incident neutron, as analytically demonstrated in Equation 7.9.

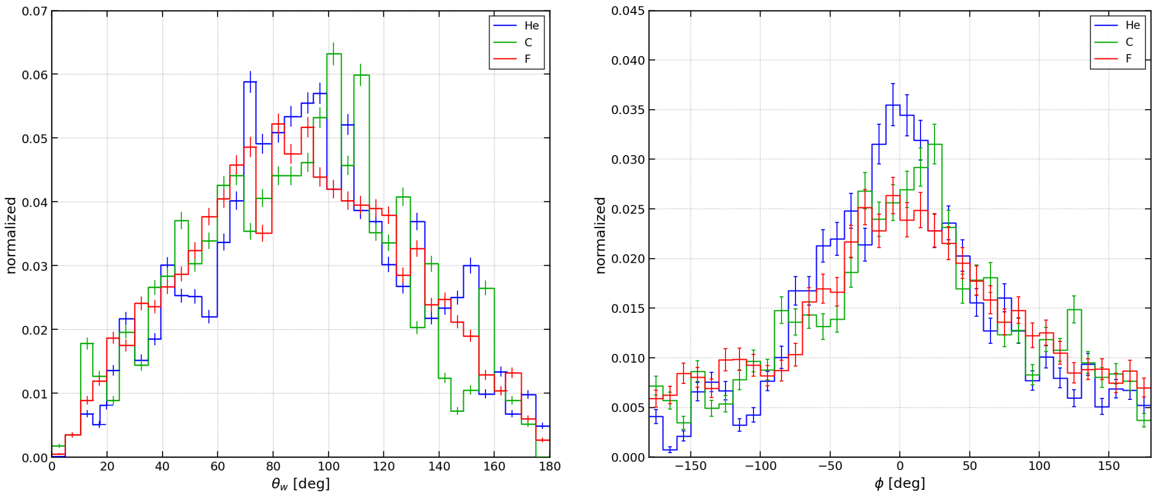

(a) Polar angle θ_W distribution.

(b) Azimuthal angle ϕ distribution.

Figure 7.5: Angular distributions of nuclear recoils in the laboratory reference frame: (a) polar angle θ_W and (b) azimuthal angle ϕ distributions for helium, carbon, and fluorine recoils from neutron elastic scattering. The overlapping distributions confirm the mass-independence of the recoil angles.

7.1.3 Nuclear species and energy dependencies

The simulation reveals important insights into the energy-dependent composition of nuclear recoil events within the detector. Figure 7.6 demonstrates that helium nuclear recoils begin

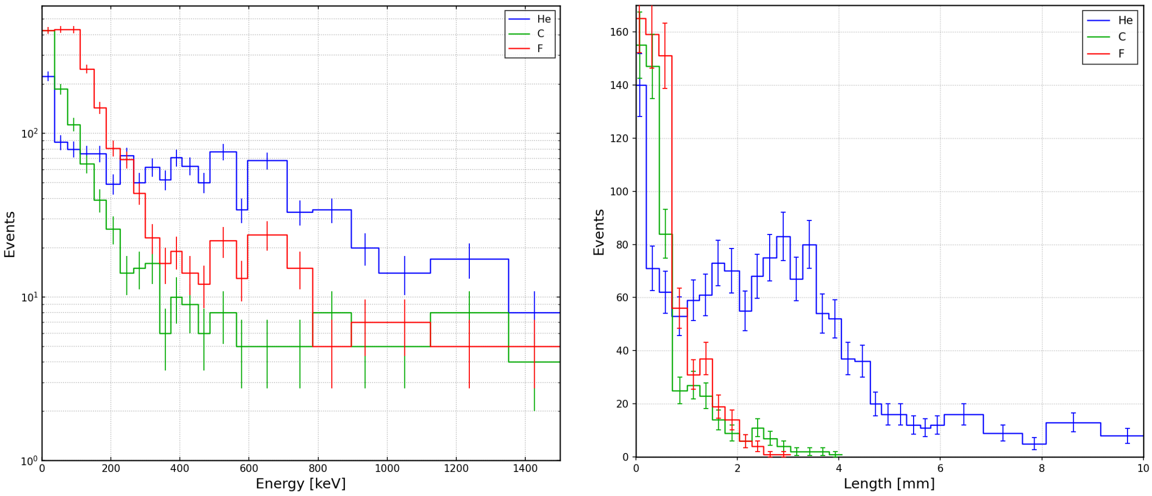

(a) Deposited energy distribution.

(b) Track length distribution.

Figure 7.6: Energy-dependent composition of nuclear recoil species (He, C, F): (a) deposited energy distribution, showing the transition to helium-dominated recoils above 300 keV, and (b) track length distribution, with characteristic track lengths of 2-4 mm for helium nuclei.

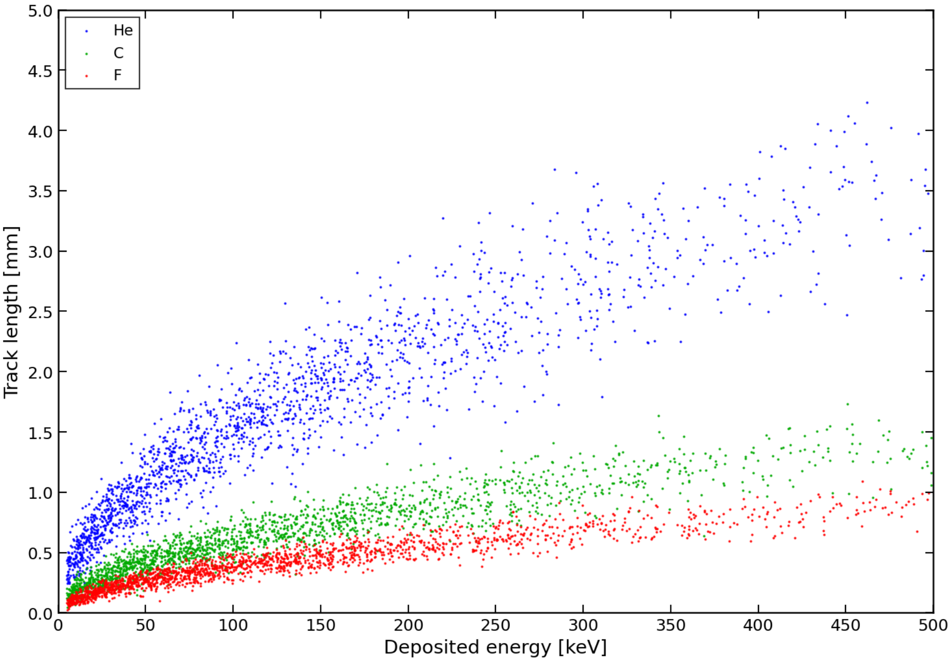

Figure 7.7: Range–energy relationship for nuclear recoils in He, C, and F obtained from Monte Carlo simulations. Points show simulated track lengths as a function of deposited nuclear recoil energy.

to dominate the recoil spectrum above approximately 300 keV, with typical track lengths ranging from 2-4 mm.

The range-energy relationship for nuclear recoils provides crucial information for understanding detector signatures and reconstruction efficiency. As discussed in Section 3.1.1, the three primary recoiling nuclei in the He:CF_4 mixture (helium, carbon, and fluorine) exhibit distinctly different behaviors due to their different masses and stopping powers. Helium recoils, being the lightest, produce the longest tracks for a given energy, extending to several millimeters in the energy range of interest, while carbon and fluorine recoils are characterized by shorter, more compact tracks due to their higher mass and correspondingly higher stopping power. These differences are illustrated in Figure 7.7, which presents the simulated range versus energy relationship for each nuclear species.

Beyond its fundamental importance for understanding event topology, this range becomes particularly valuable when addressing the gain saturation effects described in Section 4.2.3. By measuring the spatial extent of a nuclear recoil and comparing it to the simulated curves in Figure 7.7, one can infer the recoil energy. Establishing whether the detector can reliably measure track lengths and thereby estimate energies in the target range is a critical benchmark for demonstrating its capability to reconstruct nuclear recoils at the energies relevant for low-mass WIMP searches.

7.2 Analysis of AmBe data and pre-processing

Americium-Beryllium (^{241}AmBe, or simply AmBe) is a widely utilized calibration source, particularly valued for its neutron generation capabilities. The source is manufactured by enclosing ^{241}Am radioactive material within a ^{9}Be container. The neutron generation mechanism operates as follows: ^{241}Am decays to Neptunium releasing an alpha particle ($^{241}\text{Am} \rightarrow^{237}\text{Np} + \alpha$), which is then captured by Beryllium atoms, subsequently emitting a neutron ($^{9}\text{Be} + \alpha \rightarrow^{12}\text{C}^{*} + n$). The emitted neutrons possess an extremely broad kinetic energy distribution, spanning from 0 to 11 MeV.

Low-energy neutrons generate low-energy nuclear recoils that mimic WIMP-induced nuclear recoils, providing an excellent means of testing detector performance within the parameter space region of interest. The LNGS-provided source exhibited a neutron activity of $I = 200$ n/s.

Beyond the neutron channel, the AmBe source produces additional relevant emissions: a 4.43 MeV γ ray from $^{12}\text{C}^{*}$ de-excitation (expected to generate Compton electrons within the gas volume) and a 59 keV γ ray from ^{241}Am alpha decay to ^{237}Np with 58% probability (largely absorbed by the copper shielding).

The initial analysis of the RUN 3 AmBe dataset revealed critical issues: the background data suffered from substantial contamination due to a defective filter line, and unstable humidity resulted in non-constant light yield (LY) throughout the data acquisition period. While the initial analysis mitigated these issues, the following presents a more comprehensive multi-step pre-processing methodology.

Alongside the AmBe campaign (consisting of two segments separated by runs utilizing both ^{55}Fe and AmBe sources), this analysis exploits background and stability data acquired during a distinct time period. Relevant details are summarized in Table 7.1. Throughout the following discussion, "AmBe" denotes the combined AmBe_p1 + AmBe_p2 dataset.

Clusters used in the analysis were pre-selected by applying two cuts: (i) `sc_tgausssigma` > 0.5 mm, eliminating fake clusters and sensor interactions [202]; (ii) tracks with (x, y) coordinates sufficiently close to the image borders while simultaneously having `sc_length` < 25 mm were removed, as these are likely generated outside the camera field of view. Tracks exceeding 25 mm in length are retained, as information loss from truncation is considered negligible for such extended events.

Table 7.1: Summary of the datasets used in the analysis. The `Bkg_calibration` effective exposure is not listed, as it corresponds to a single calibration run with the ^{55}Fe source performed during step 3 of the calibration procedure, i.e. the source position farthest from the GEM plane (see Section 4.2.2). All dates correspond to 2023.

Dataset	**Run range**	**Date range**	**Effective Exposure [h]**
Stability	25486–25772	Sept. 26–29	10.5
Bkg_calibration	27512	Oct. 9	–
Bkg	27322–27844	Oct. 7–10	56.6
AmBe_p1	23820–23984	Aug. 2–3	16.9
AmBe_p2	24023–24328	Aug. 3–4	31.0
AmBe + ^{55}Fe	23988–24022	Aug. 3	2.1

7.2.1 Data normalization

Previous analyses normalized data by dividing by the number of acquired images during the considered run range. While this provides a reasonable rate estimate, consistent execution requires normalizing to the actual exposure time, computed by extracting start and stop times of each run from the SQL database logbook. Pedestal and daily calibration runs are excluded from this calculation, yielding the "effective exposure" reported in Table 7.1.

7.2.2 Light yield stability and calibration

The humidity level within the detector decreased slowly throughout the AmBe data acquisition period. Since humidity variations manifest as light yield variations, this pre-processing aims to quantitatively establish the relationship between light yield and humidity to correct `sc_integral` for this effect, while simultaneously enabling proper ADU to keV calibration.

The procedure consists of the following steps. First, the ^{55}Fe peak position is fitted run-by-run in the Stability dataset (Table 7.1) to extract the light yield as a function of humidity. Assuming a linear relationship, the light yield dependence on humidity is modeled with a linear fit. The resulting fit parameters are then used to derive a correction factor for each humidity value, which is applied to equalize the light yield across different runs. Finally, the signal is converted from ADU to keV by scaling it to the known 5.9 keV ^{55}Fe peak energy. Figure 7.8 (left) shows the measured dependence of the light yield on humidity before correction, while Figure 7.8 (right) demonstrates that this dependence is successfully flattened after applying the calibration, as expected.

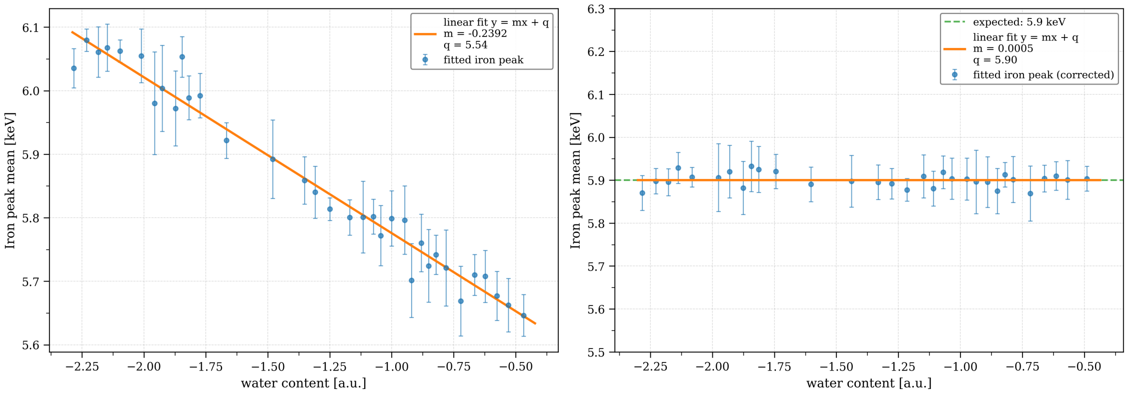

Figure 7.8: Summary of the calibration procedure (left) and calibration verification (right) performed on the Stability dataset.

Figure 7.9 presents the comparison between raw and fully pre-processed energy distributions for AmBe and Bkg datasets, demonstrating the effectiveness of the complete pre-processing pipeline.

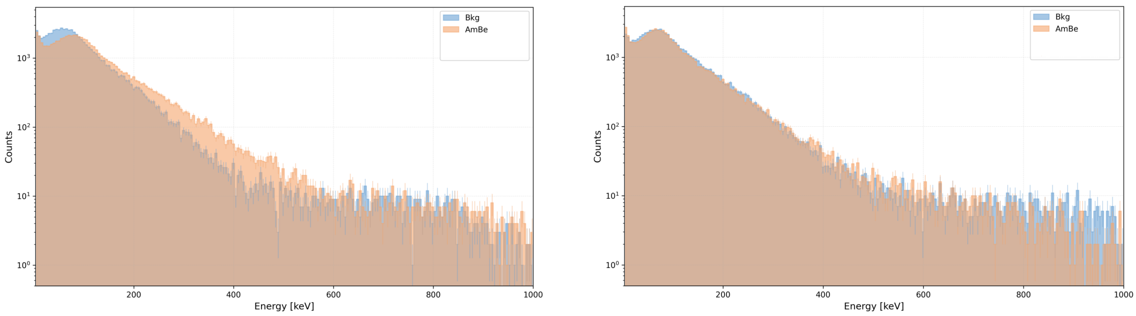

(a) Raw energy spectra for the `Bkg` and `AmBe` datasets.

(b) Energy spectra after full preprocessing for the `Bkg` and `AmBe` datasets.

Figure 7.9: Comparison between energy spectra before and after preprocessing: (a) raw spectra, directly obtained from the detector readout; (b) fully pre-processed spectra, after the application of baseline correction, noise suppression, and event selection.

7.3 Monte Carlo simulation of the AmBe neutron source

This section presents the Monte Carlo simulation framework developed to model the AmBe neutron data taken during RUN 3. The simulation chain integrates Geant4 for particle transport, digitization to reproduce detector response, and reconstruction algorithms identical to those applied to real data. This comprehensive approach enables a detailed understanding of the detector's response to neutron interactions and provides the ideal environment to develop tools for discriminating between electron recoils and nuclear recoils.

7.3.1 Simulation setup and event generation

The Monte Carlo simulation employs Geant4 to model the complete detector geometry and particle interactions. A total of $3.5 \cdot 10^5$ neutrons were generated from the AmBe source, with the neutron energy spectrum following the characteristic distribution spanning from 0 to 11 MeV as previously discussed. The simulation incorporates the quenching factor to account for the reduced ionization yield of nuclear recoils compared to electron recoils of equivalent energy.

The simulation pipeline consists of three main stages. First, the Geant4 simulation generates primary neutrons from the AmBe source and tracks all secondary particles through the detector geometry, including interactions in the gas volume, PMMA vessel, and copper shielding. Second, the digitization step converts Geant4 energy deposits into 2D images (Chapter 5), replicating the RUN 3 data acquisition conditions. Finally, the reconstruction applies the same clustering and track algorithms used for experimental data analysis.

Of the $3.5 \cdot 10^5$ generated neutrons, only approximately 10^4 events produce measurable energy deposits in the gas volume. This low interaction rate reflects both the geometrical acceptance and the cross-section of neutron interactions. A crucial observation from the simulation results is that more than a half of the events generating a signal are actually ERs rather than NRs. These ER events originate from neutrons interacting with the PMMA vessel and copper shielding, producing photons and electrons that subsequently deposit energy in the sensitive volume.

7.3.2 Truth-level matching procedure

Currently, the information about the so-called Monte Carlo truth (i.e. particle type and values of the kinematic variables) is not saved with each cluster by the reconstruction algorithms. In fact, the clustering algorithm could cut tracks or join them, and this makes it more difficult to match the information of reconstructed tracks with the Monte Carlo truth information. Therefore, there is a need for a systematic matching procedure to associate reconstructed clusters with Monte Carlo tracks. The matching algorithm begins by computing the barycenter position in the (x, y) plane for each reconstructed cluster. For the corresponding Geant4 event, all particle hits in the gas volume are extracted and grouped by track ID. For each unique track ID in the Geant4 output, the (x, y) position of the barycenter is calculated using all hits belonging to that track. The reconstructed barycenter is then compared with all Monte Carlo barycenters within the same event, and a match is assigned to the closest MC barycenter if the distance is below a predefined threshold.

To establish an appropriate threshold, we analyzed the distribution of the barycenter distances. Figure 7.10 presents the distribution of differences between Monte Carlo truth and reconstructed positions for both x and y coordinates. The analysis was restricted to events containing a single track at the Geant4 level and a single high-density cluster (density > 20) in the reconstruction, ensuring clean, unambiguous matches.

The distributions are sharply peaked around zero, with standard deviations of approximately 17 mm in x and 13 mm in y. On this basis, a matching threshold of 10 mm was chosen.

After a successful matching, the complete Monte Carlo truth information becomes available for each reconstructed cluster. This includes the particle type, the true energies of both the neutron and the recoiling nucleus, and the interaction vertex position. Such truth-level information enables detailed studies of the reconstruction performance and provides the labels required for training supervised machine learning algorithms to distinguish between ER and NR events.

Reconstructed clusters were classified into four categories based on the interacting particle. Electron recoils, induced by electrons, positrons, or photons, constitute the largest category with 6890 events. Nuclear recoils are subdivided by target nucleus: helium recoils

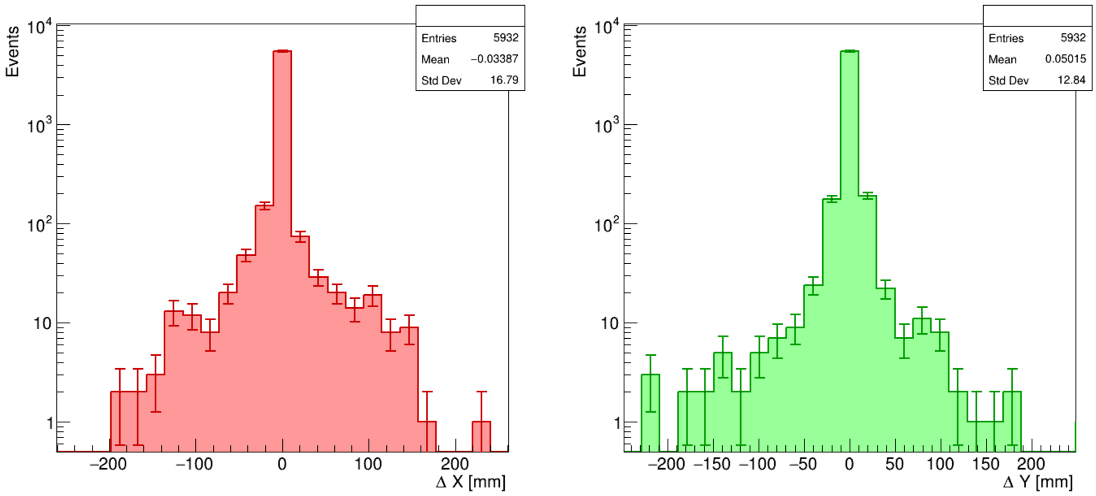

Figure 7.10: Spatial differences between Monte Carlo truth and reconstructed positions. The left panel shows the x-coordinate difference with a mean of -0.03 mm and a standard deviation of 16.79 mm. The right panel shows the y-coordinate difference with a mean of 0.05 mm and a standard deviation of 12.84 mm.

account for 831 events, carbon recoils for 546 events, and fluorine recoils for 3004 events. The prevalence of fluorine recoils reflects the CF_4 gas composition and higher mass of fluorine as discussed in Sec. 3.1.1.

7.3.3 Reconstructed observables by particle type

The distributions of key reconstructed variables for each particle type provide insight into the characteristic signatures that enable discrimination. These observables span energy deposition, spatial extent, and track morphology, collectively forming a multi-dimensional feature space where different particle types occupy distinct regions.

Figure 7.11 presents the distribution of `sc_integral`, which represents the total integrated light collected by the camera and serves as a proxy for deposited energy. Electron recoils dominate at higher `sc_integral` values, with the distribution extending beyond 250000 ADU, while nuclear recoils concentrate at lower values due to the quenching of ionization for heavily ionizing particles.

Beyond the deposited energy, the spatial morphology of tracks provides powerful discrimination between ER and NR events. The slimness parameter, defined as the ratio `sc_length`/`sc_width` and shown in Figure 7.12, quantifies the degree of track elongation in a dimensionless form. Electron recoils typically produce elongated, filament-like tracks, resulting in slimness values that extend to significantly higher ranges. In contrast, nuclear recoils yield predominantly compact, spot-like clusters with slimness values concentrated near unity, reflecting their short range in the gas. The overall distribution thus features a broad tail for ER and a narrow peak around one for NR, making slimness an effective parameter for event-type discrimination.

The track density parameter ρ, defined as `sc_rms`/`sc_nhits` and shown in Figure 7.13, quantifies the compactness of charge deposition along a track. Lower ρ values correspond to more diffuse, discontinuous ionization patterns typical of elongated, low-density tracks, while higher ρ values indicate denser and more localized charge deposition. Electron recoils

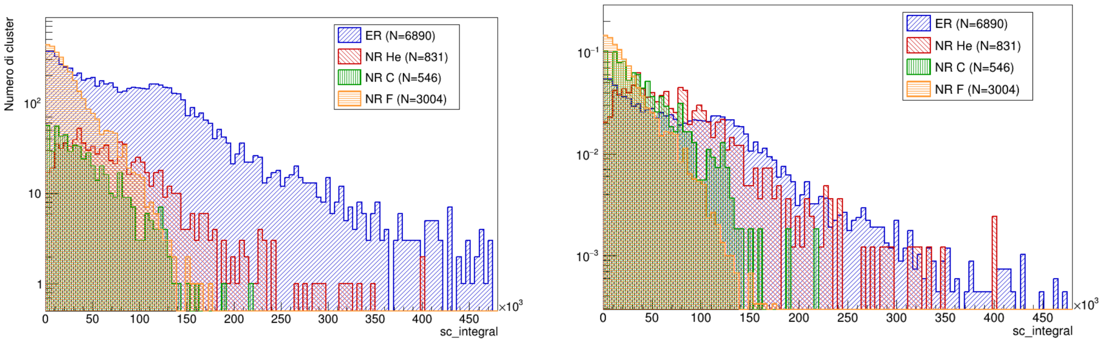

(a)

(b)

Figure 7.11: Distribution of `sc_integral` (total integrated charge) for different particle types. (a) Absolute distributions showing that ER events dominate at higher values, while nuclear recoils concentrate at lower integral values due to quenching effects. (b) Normalized distributions revealing the relative spectral shapes for each particle type.

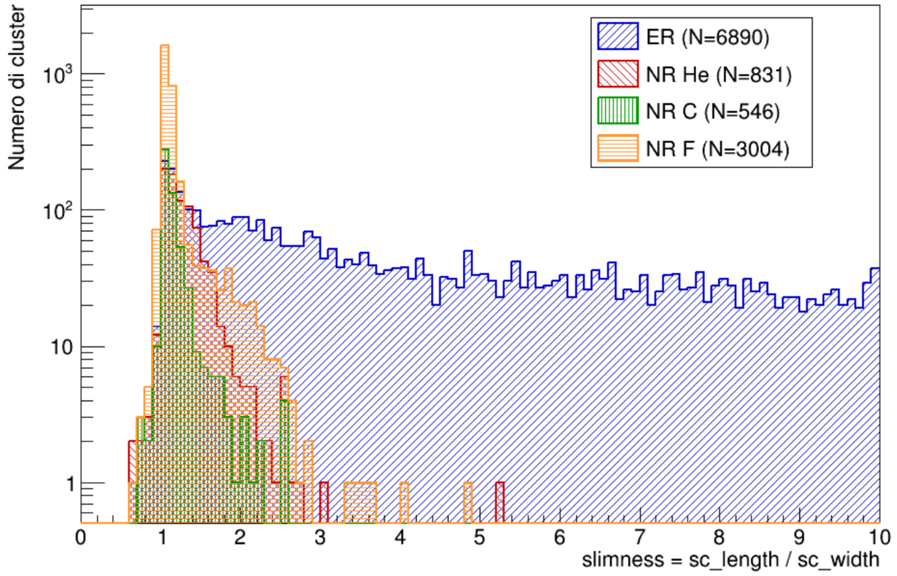

Figure 7.12: Slimness distribution (`sc_length`/`sc_width`) for different particle types. NR events produce predominantly spot-like signatures (slimness ~ 1), while ER events generate elongated tracks with higher slimness values.

populate the lower end of the ρ distribution, generally below 0.01, consistent with their sparse and irregular energy deposition along extended tracks. In contrast, nuclear recoils exhibit higher ρ values, reflecting their dense and continuous ionization over shorter path lengths.

The composite morphology parameter η, defined as sc_width $\times$ sc_length $\times$ ρ combines geometric and density information into a single discriminant variable. This parameter effectively captures the overall "volume" occupied by the ionization track in a generalized sense, providing an integrated measure of track morphology. The resulting distributions for different event types are illustrated in Figure 7.14.

Additional observables provide complementary information about track characteristics. Figure 7.15 shows the distribution of `sc_density`, defined as `sc_integral`/`sc_nhits`, which represents the average charge collected per hit pixel. This quantity differs from ρ in that it directly measures charge deposition rather than spatial spread. While electron

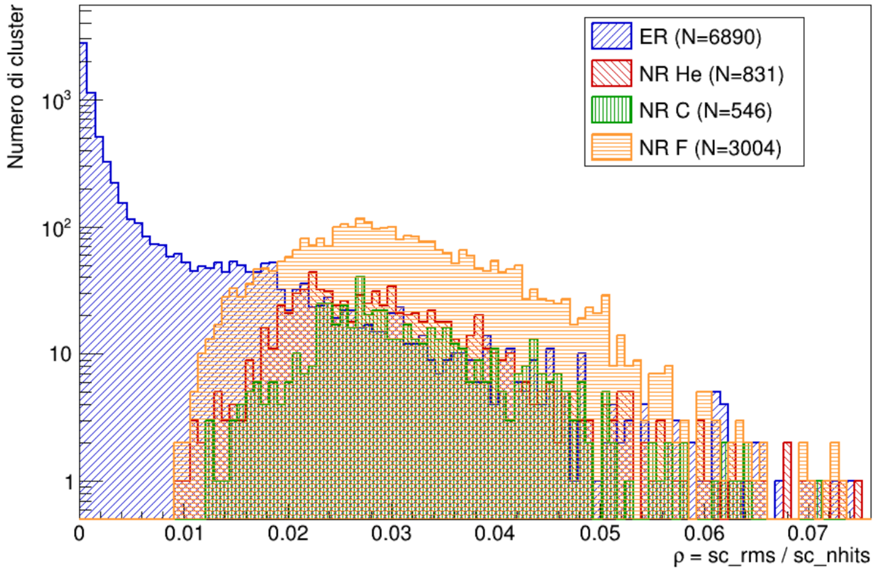

Figure 7.13: Track parameter ρ (`sc_rms`/`sc_nhits`) distributions. NR events cluster at low ρ values (compact spots), while ER events extend to higher ρ values reflecting more distributed ionization.

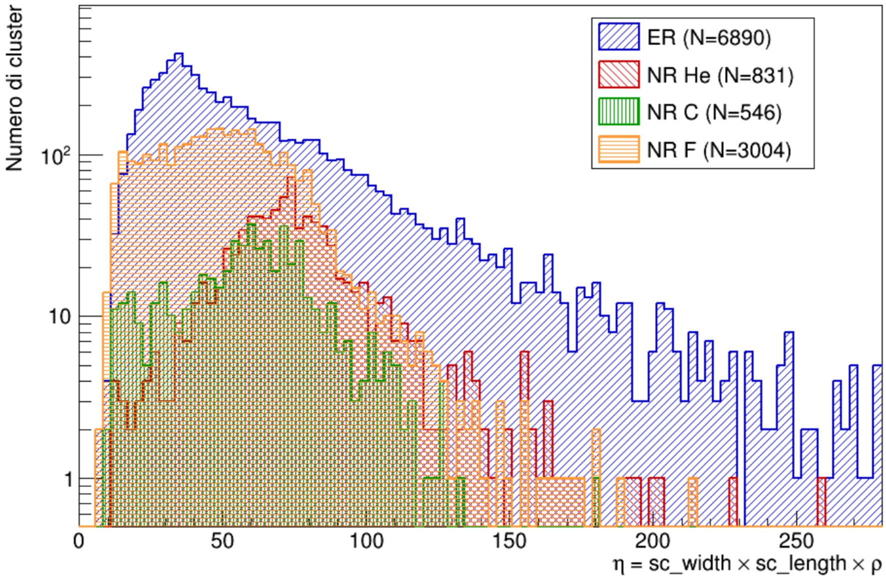

Figure 7.14: Composite morphology parameter η combining width, length, and density.

recoils show a sharp peak at low density values, nuclear recoils exhibit much broader distributions extending to higher densities. This reflects the higher specific ionization (dE/dx) characteristic of slow, heavy particles, which deposit more energy per unit length compared to minimum-ionizing electrons.

Track length, measured in pixels and displayed in Figure 7.16, directly quantifies the maximum extent of the track. This observable is particularly effective at distinguishing particle types because it closely relates to the physical range of the particle in the gas. The distinct length scales for different particle types reflect their characteristic ranges in the CF_4:He gas mixture, mainly determined by their mass.

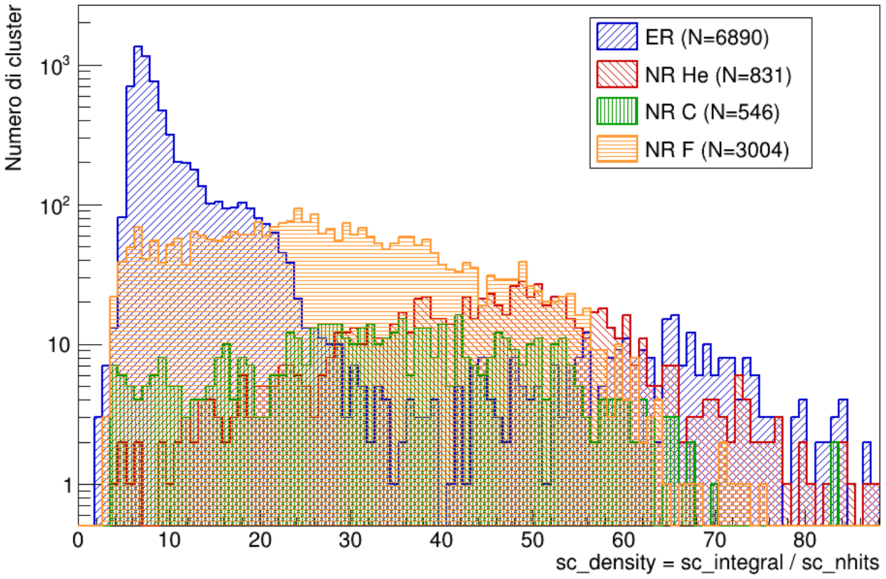

Figure 7.15: Distribution of `sc_density` (`sc_integral`/`sc_nhits`), representing the average light per hit. Nuclear recoils show broader distributions reflecting variable ionization density along the track.

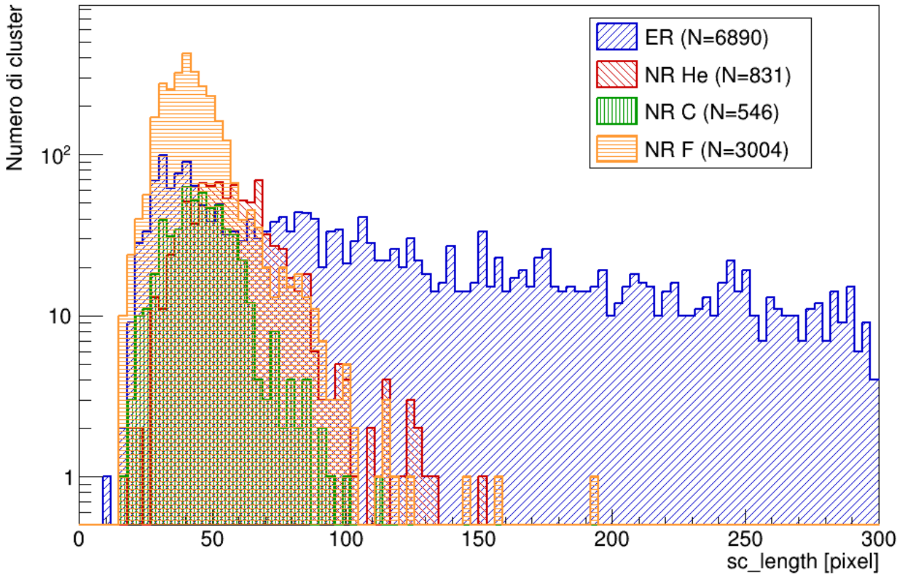

Figure 7.16: Track length distributions measured in pixels. The distinct length scales for different particle types reflect their characteristic ranges in the CF_4:He gas mixture.

7.3.4 Two-dimensional feature space analysis

While one-dimensional distributions reveal important differences between particle types, visualization in two-dimensional feature space provides deeper insight into the structure of the data. Figure 7.17 presents the correlation between `sc_density` and `sc_energy` (integral after ^{55}Fe calibration), with color indicating the true kinetic energy from Monte Carlo truth. This representation reveals how NRs naturally cluster in the joint distribution of these two variables. The region of interest for CYGNO studies, corresponding to nuclear recoil energies of a few tens of keV (blue-green), lies in the low-density regime, typically below about 20 ADU/pixel.

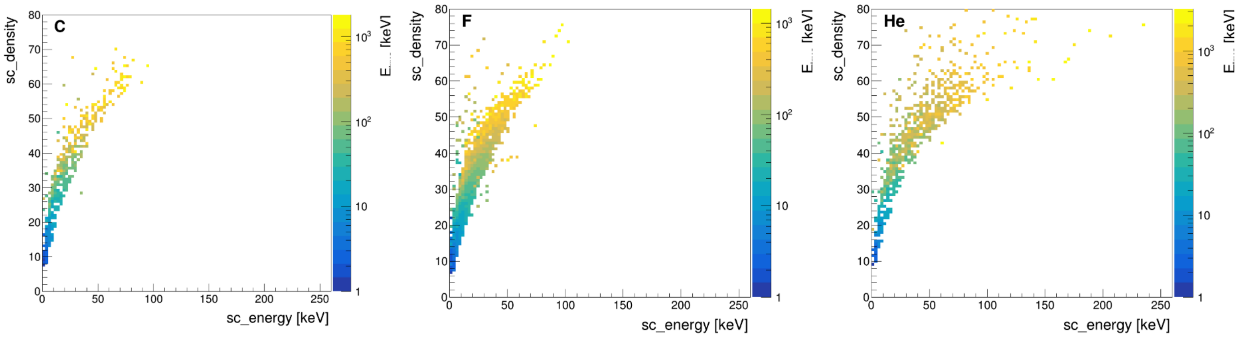

Figure 7.17: Two-dimensional distribution of `sc_density` versus `sc_energy` for NRs, with color indicating the true kinetic energy from Monte Carlo truth. Left panel: carbon recoils; center panel: fluorine recoils; right panel: helium recoils.

7.4 Data and Monte Carlo comparison

A comparison between experimental data and Monte Carlo predictions is essential to validate the simulation's fidelity and assess its predictive power. This section presents a systematic data/MC comparison.

7.4.1 Normalization to experimental exposure

A proper normalization procedure is essential to enable quantitative comparison between Monte Carlo simulation and experimental data. The comparison strategy involves three distinct datasets: experimental data acquired with the AmBe neutron source, experimental background data acquired without the source, and simulated AmBe events. To obtain meaningful results, these three components must be normalized coherently to represent the same exposure conditions.

The approach adopted in this analysis is to fix the exposure time based on the experimental AmBe dataset. The background is normalized by sampling from the experimental background dataset the same number of images as in the corresponding AmBe dataset. This procedure ensures that both the AmBe data and the background data represent identical acquisition periods, naturally accounting for contributions from natural radioactivity, cosmic rays, and detector noise at the same statistical level. The Monte Carlo simulation must then be scaled to reproduce the equivalent neutron exposure for the same time period.

The normalization of the simulated AmBe events is based on the trigger rates measured during RUN 3. Without the AmBe source, the trigger rate was 1.6 Hz, reflecting background activity from natural radioactivity, cosmic rays, and detector noise. With the AmBe source installed, the rate increased to 1.8 Hz. The net excess of 0.2 Hz corresponds to neutron-induced events, as gamma contributions from the AmBe source are negligible compared to the natural background.

The AmBe source emits approximately 200 neutrons/s over the full 4π solid angle. The measured event rate of 0.2 Hz corresponds to a global detection efficiency of 0.1%, which already includes the geometrical acceptance of the detector with respect to the source position. Geant4 simulations indicate an interaction efficiency of 0.3%. The ratio between the measured efficiency and the simulated interaction efficiency yields a DAQ efficiency of about 33%, accounting for trigger-logic inefficiencies and reconstruction failures. This is the only factor we do not account for in the simulation.

Therefore, to simulate one hour of AmBe exposure matching RUN 3 conditions, the required number of generated neutrons is:

$$N_{\text{neutrons}} = 3600\,\text{s} \times 200\,\text{n/s} \times 0.33 = 237600\,\text{neutrons}.$$

This prescription enables straightforward scaling to arbitrary exposure times and ensures that the simulated AmBe events, when combined with the experimental background images, can be directly compared to the experimental AmBe dataset under equivalent exposure conditions.

Figure 7.18 provides a first qualitative validation comparing simulated events with RUN 3 experimental data in the sc_density versus sc_energy plane.

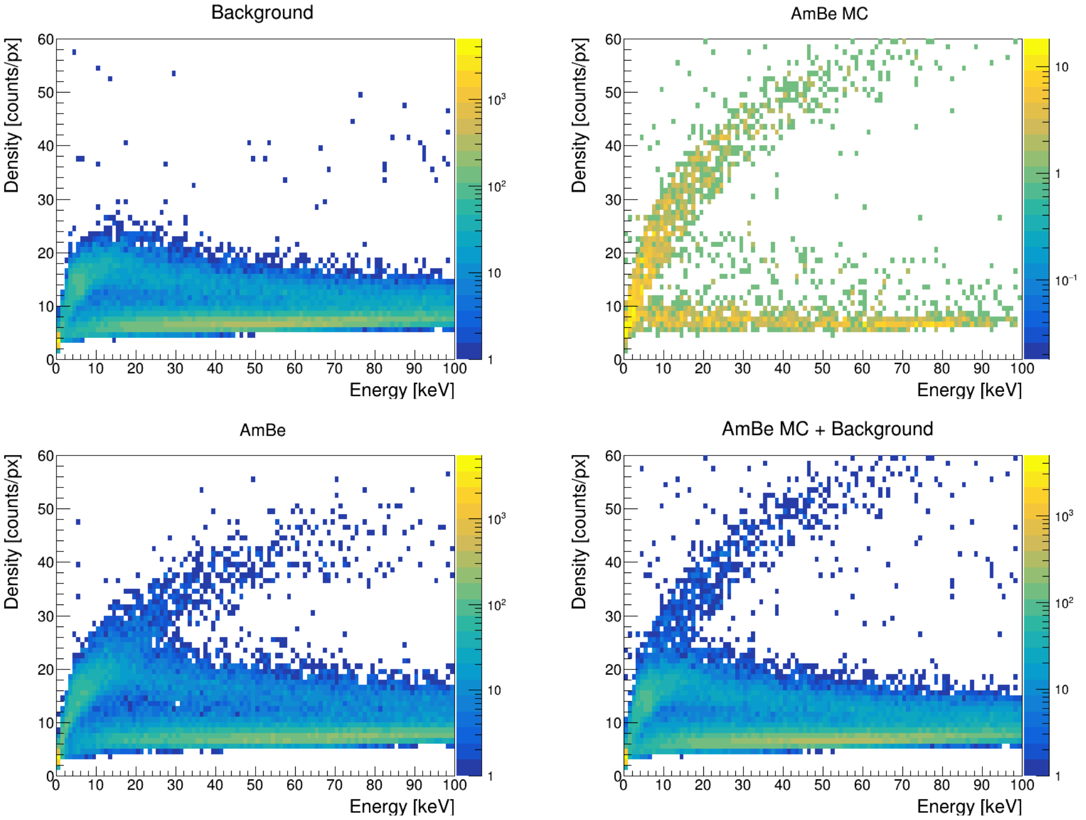

Figure 7.18: Comparison of simulated events with RUN 3 experimental data. Top left: real background data only. Top right: AmBe simulation only. Bottom left: real AmBe data. Bottom right: combined view where the AmBe contribution is taken from simulation and the background contribution is taken from experimental data.

The comparison reveals qualitative agreement between simulation and data, with the bottom panels showing similar features. A key observation emerges from examining the nuclear recoil (NR) region, the characteristic band structure at high density and low energy, already observed in Figure 7.17. This feature is notably absent in the background-only data (top left), while it is clearly populated in both the AmBe experimental data (bottom left) and the combined simulation (bottom right). It should be noted that the shape of this band is slightly different in the two cases, suggesting an imperfect prediction of some track shape variables, as will be detailed in the next sections. The presence of this NR-specific signature in the simulated AmBe events demonstrates that the Monte Carlo framework successfully reproduces the detector response to neutron-induced nuclear recoils. The combined simulation panel appropriately captures the mixing of signal and background contributions when compared with the experimental AmBe dataset.

7.4.2 Selection criteria and analysis regions

Without appropriate selection criteria, the relatively rare NR events would be overwhelmed by the dominant ER background population. Therefore, to enable a meaningful comparison between simulation and data and to evaluate the Monte Carlo performance under different signal conditions, it is necessary to define selection strategies that progressively isolate the NR population while controlling the level of ER contamination.

To assess simulation performance across varying signal (NR) purities, three distinct selection strategies were employed, progressively isolating nuclear recoil populations while accepting different levels of electron recoil contamination. The selection criteria were developed based on the Monte Carlo truth analysis presented in Figures 7.11–7.16.

The **baseline selection** applies minimal requirements to select genuine tracks, based on the track-shape variables defined in Section 7.2: (i) `sc_length` $>$ 25 pixels, to reject very short clusters that are likely noise artifacts rather than particle tracks; (ii) `sc_tgausssigma` $>$ 0.5 mm, to exclude point-like sensor noise that does not exhibit the Gaussian transverse profile expected from a genuine ionisation track; and (iii) radial distance from detector centre $<$ 800 pixels, to reject border tracks affected by optical distortions and incomplete light collection. This represents the most inclusive sample without bias toward specific particle types, providing a complete view of the detector response to both electron and nuclear recoils.

The **NR-enriched selection** introduces additional requirements derived from the feature space analysis in Figures 7.13 and 7.16, which identified regions of enhanced nuclear recoil concentration. Specifically, the requirement $\rho > 0.01$ exploits the observation that nuclear recoils preferentially populate the higher track density region, as evident in the ρ distributions where NR and ER populations show clear separation above this threshold. The `sc_length` $<$ 200 pixels cut removes very long tracks, which the Monte Carlo truth analysis revealed to be predominantly electron recoils, particularly at higher energies. Together, these cuts substantially enhance the nuclear recoil fraction while maintaining reasonable efficiency: approximately 99% of NR events are retained while rejecting 83% of the ER background, targeting the region of feature space where NR dominance begins but ER contamination remains non-negligible.

The **high-purity NR selection** adds a stringent requirement on `sc_density` ($>$ 25), directly motivated by the `sc_density` versus `sc_energy` distributions shown in Figure 7.15. This threshold was chosen based on the observation that above this density value, the Monte Carlo truth population becomes almost exclusively nuclear recoils, with minimal electron recoil overlap even at low energies. This selection successfully rejects more than 99% of ER contamination, achieving excellent purity. However, this comes at the cost of significantly reduced efficiency (approximately 50% of NR events are retained), with particular losses among low-density nuclear recoils that fall below the threshold. Despite the efficiency penalty, this selection provides a clean sample for validation where nuclear recoil identification is most straightforward.

These three selections thus span a range from maximum inclusivity (baseline) to maximum purity (high-purity NR), enabling validation of the simulation under different conditions and assessment of how well the feature space separation observed in Monte Carlo truth translates to real data.

Figure 7.19 demonstrates the impact of these selections on simulated event populations in the `sc_density` versus `sc_energy` plane.

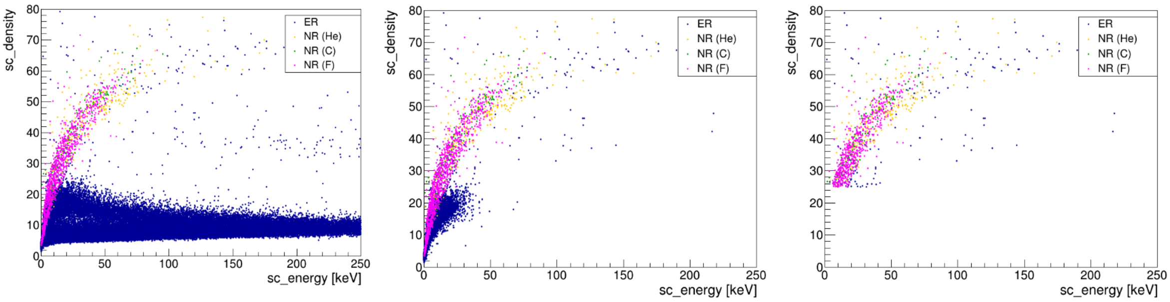

Figure 7.19: Effect of the three selection strategies on Monte Carlo events in `sc_density` versus `sc_energy` space. Left: baseline selection. Center: NR-enriched selection. Right: high-purity NR selection. Color coding indicates particle type from Monte Carlo truth.

7.4.3 Quantitative data/MC comparison across observables

The Monte Carlo prediction consists of simulated AmBe-induced events (both ER and NR) normalized according to the procedure described previously, plus real background data from RUN 3. The experimental AmBe data serves as validation target.

Figure 7.20 presents the calibrated energy distributions for the three selections. Top panels show stacked histograms comparing data (black points) against Monte Carlo (stacked colored regions: electron recoils in blue, nuclear recoils in yellow/green/magenta for helium/carbon/fluorine). Bottom panels display data/MC ratios.

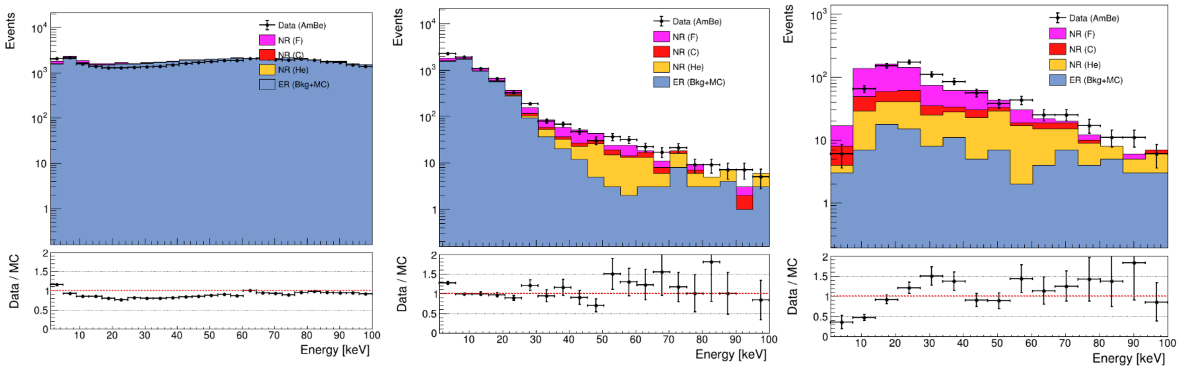

Figure 7.20: Energy spectrum comparison between data and Monte Carlo for the three selections. Left: baseline. Center: NR-enriched. Right: high-purity NR. Top panels show stacked distributions with data overlaid. Bottom panels show data/MC ratios centered at unity (red dashed line).

For the baseline selection, the agreement is quite good from 10 to 100 keV, with data/MC ratios around unity. The Monte Carlo slightly underestimates data below 10 keV, suggesting incomplete modeling of low-energy backgrounds or reconstruction efficiency differences.

The NR-enriched selection reveals larger discrepancies above 20 keV where NRs become more abundant.

The high-purity NR selection shows the most significant discrepancies. The simulation substantially underpredicts observed data below 20 keV while showing better agreement above 50 keV, suggesting underestimation of either production rate or reconstruction efficiency of high-density nuclear recoils.

Figure 7.21 shows the number of hit pixels per cluster.

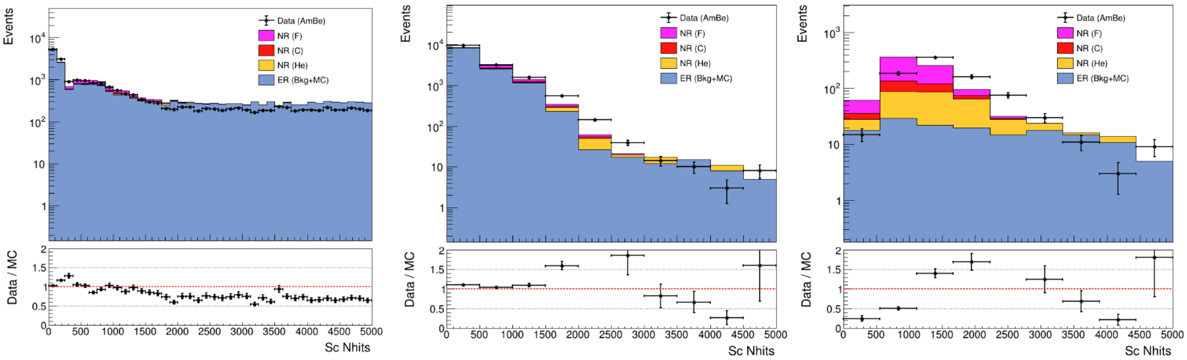

Figure 7.21: Comparison of `sc_nhits` distributions between data and Monte Carlo for the three selections.

For the baseline selection, the data/MC ratio fluctuates around unity in the core but falls below 1.0 at very high nhits, indicating that the simulation overproduces the longest tracks.

The NR-enriched selection shows degraded agreement, with data/MC close to unity only for nhits $<$ 1500. Beyond this threshold, systematic underprediction suggests the selection retains events where simulation performance is less reliable.

For high-purity NR selection, the agreement worsens, although the overall shape remains consistent. The MC distribution appears to be shifted towards slightly lower values, which could also account for the discrepancies already observed in the discussion of Figure 7.18.

Figure 7.22 presents the root-mean-square of pixel values, serving as a proxy for track density.

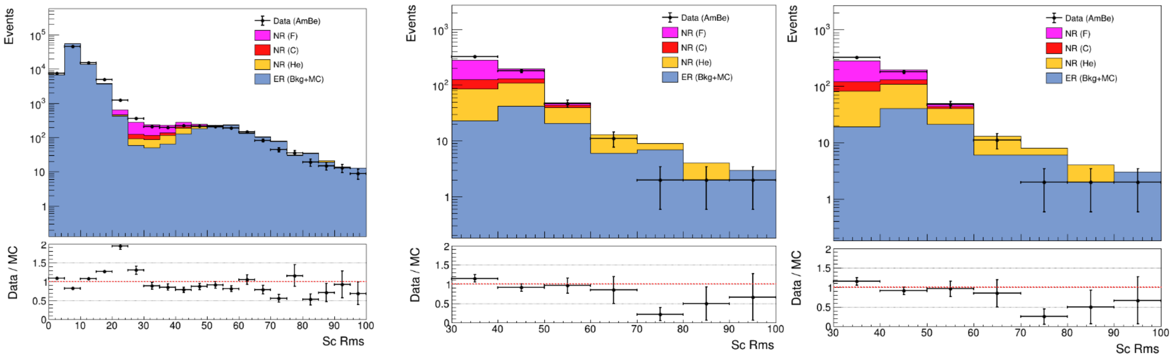

Figure 7.22: Comparison of `sc_rms` distributions between data and Monte Carlo for the three selections.

With the baseline selection, the simulation reproduces the shape of the RMS distribution remarkably well, with peaks around 10 and 50 pixels matching closely. The data/MC ratio remains near unity except around `sc_rms` $\approx$ 20 pixels, where the simulation highly underpredicts the observed rate.

The NR-enriched and high-purity selections show similar behavior, with good shape agreement but persistent normalization deficits affecting all RMS bins proportionally.

Figure 7.23 displays $\rho = \texttt{sc\_rms}/\texttt{sc\_nhits}$, a density-like measure highly effective for ER/NR discrimination.

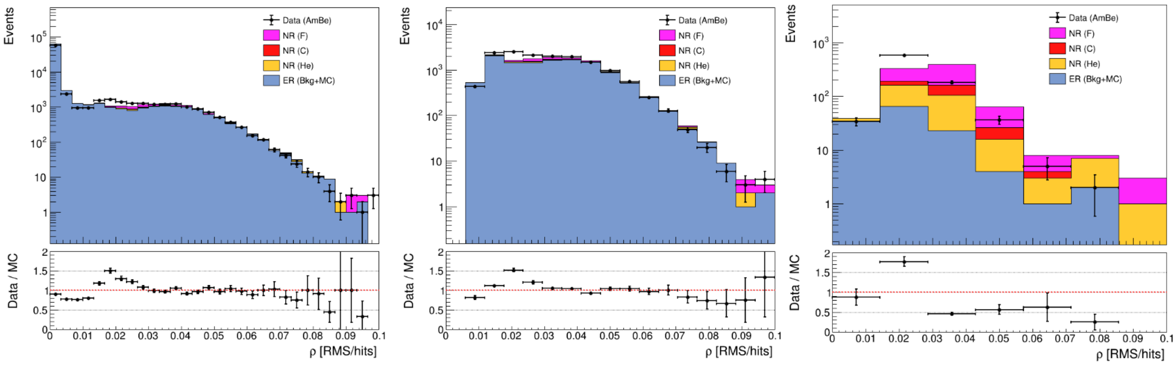

Figure 7.23: Comparison of track density parameter ρ between data and Monte Carlo for the three selections.

The baseline selection reveals one of the most significant discrepancies: simulation underpredicts data by 30-40% around $\rho \sim 0.02$, an intermediate-density regime where both ER and NR contribute. The high-density nuclear recoil region ($\rho > 0.05$) shows good agreement.

The NR-enriched selection maintains this deficit and the high-purity NR selection shows reasonable shape agreement with ratios between 0.5 and 1.5.

Figure 7.24 shows track length, providing direct measurement of maximum linear extent.

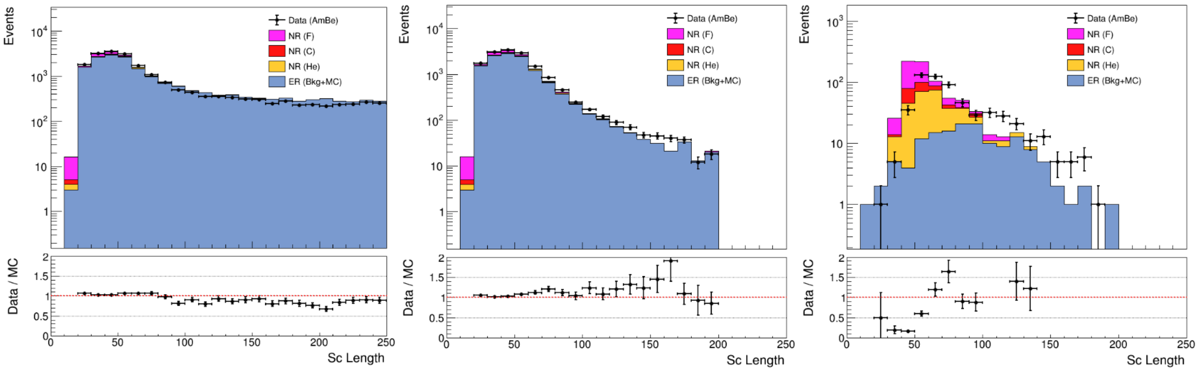

Figure 7.24: Comparison of `sc_length` distributions between data and Monte Carlo for the three selections.

For baseline selection, the simulation reproduces the distribution remarkably well, with the characteristic peak around 40-50 pixels matching closely. Data/MC ratio hovers around 1.0-1.1 across most length scales.

The NR-enriched selection maintains good agreement below 100 pixels. The high-purity NR selection shows correct shape modeling, with the data/MC ratio oscillating around unity.

It is worth noting that the track length is not affected by gain-saturation effects and should therefore be one of the most reliably reproduced features.

7.4.3.1 Discussion of data/MC discrepancies

The quantitative comparisons presented above reveal both strengths and limitations of the current simulation framework. While the overall agreement is encouraging (particularly for variables like `sc_length` and `sc_rms` where shape agreement is excellent), systematic discrepancies emerge that require careful consideration.

Environmental parameter variations A primary source of data/MC disagreement likely stems from environmental conditions that varied during data acquisition but remain fixed in the simulation. Gas pressure fluctuations, for instance, directly affect electron drift properties and recombination rates, influencing both the total light yield (`sc_integral`) and the spatial characteristics of ionization clouds. While humidity variations were identified and corrected during preprocessing (Section 7.2), other environmental factors such as gas purity and pressure were not accounted for.

The impact of these variations manifests differently across observables. For `sc_integral`-dependent quantities like `sc_density` and `sc_energy`, systematic shifts in light yield directly translate to the observed discrepancies, particularly visible in the energy spectrum comparisons where the simulation tends to underpredict low-energy events. For morphological variables like ρ, environmental variations affect gas diffusion properties, potentially explaining the observed differences.

Introducing an event-by-event smearing to mimic environmental parameter fluctuations could improve agreement. This approach would effectively broaden the simulated distributions to match the natural spread observed in data, particularly for variables sensitive to gas conditions.

Simulation framework limitations The current simulation employs the same digitization framework validated against ^{55}Fe electron recoil data (Chapters 5 and 6). While this framework successfully reproduces electron recoil characteristics at 5.9 keV, the AmBe data span a much broader range of energies (up to 1 MeV) and include nuclear recoils with fundamentally different ionization patterns. The digitization code described in Chapter 5, approximates certain physical processes rather than treating each particle interaction with the full detail of Geant4. This approximation becomes more critical for nuclear recoils, where ionization densities are higher.

Implications and outlook Despite these limitations, the level of agreement achieved is remarkable considering the complexity of the physical processes involved and the diversity of particle types, energies, and track morphologies present in the AmBe data. The simulation successfully reproduces the main features of the data across multiple observables and selection regimes, demonstrating qualitatively correct modeling of both electron and nuclear recoils.

This validation establishes confidence in using the Monte Carlo framework for several applications. Most importantly, the simulation provides a labeled dataset with particle-type truth information, precisely what is needed to develop and train multivariate discrimination algorithms. The qualitative agreement in feature space distributions, evident in the `sc_density` versus `sc_energy` comparisons, ensures that a machine learning model trained on simulation will learn decision boundaries that are physically meaningful and transferable to real data.

Future refinements could include systematic studies of environmental parameter correlations in the data, development of data-driven corrections for reconstruction efficiency as a function of track properties, and potential retuning of digitization parameters to better match the AmBe dataset.

Conclusions

The search for dark matter represents one of the most compelling challenges in contemporary physics. As discussed in Chapter 1, overwhelming astrophysical and cosmological evidence points to the existence of a non-luminous matter component constituting approximately 84% of the total matter in the Universe. Among the theoretical candidates proposed to explain this dark matter, Weakly Interacting Massive Particles (WIMPs) have received particular attention, also because their predicted interactions with ordinary matter could produce detectable nuclear recoils in terrestrial experiments.

The CYGNO experiment pursues a directional approach to dark matter detection using a gaseous Time Projection Chamber (TPC) with optical readout, as described in Chapter 3. The detector employs a He:CF_4 gas mixture at atmospheric pressure, combining sensitivity to both spin-independent and spin-dependent WIMP–nucleon interactions through the helium and fluorine content. The LIME prototype, the largest detector within the CYGNO development program featuring a 50-liter active volume, has been extensively characterized both at the Laboratori Nazionali di Frascati (LNF) and at the Laboratori Nazionali del Gran Sasso (LNGS), as detailed in Chapter 4.

A crucial requirement for rare event searches is the capability to accurately simulate the detector response to different particle interactions. This thesis has presented the development, optimization, and comprehensive validation of a Monte Carlo simulation framework for the CYGNO/LIME detector, demonstrating its capability to reproduce both electron recoil (ER) and nuclear recoil (NR) signatures with sufficient accuracy to enable discrimination between signal and background events.

Monte Carlo Simulation Framework

The simulation framework developed in this work, described in Chapter 5, consists of two main components. The first employs Geant4 to model particle interactions within the He:CF_4 gas mixture, generating detailed three-dimensional tracks with energy deposition information. For nuclear recoils, the simulation incorporates quenching factor corrections to account for the reduced ionization yield of recoiling nuclei compared to electrons, using parameters determined through SRIM simulations for helium, carbon, and fluorine recoils.

The second component is a comprehensive digitization algorithm that transforms Geant4 energy deposits into detector signals. This algorithm sequentially models all physical processes occurring in the actual detector: primary electron production, drift and diffusion in the gas volume, electron multiplication through the triple-GEM stack including gain fluctuations and saturation effects, scintillation light production, and finally the optical detection by the sCMOS camera system (Section 5.2). The GEM gain saturation model, detailed in Section 5.2.4, proved particularly important for accurately reproducing the detector response across the full energy range of interest.

Optimization and Validation with Electron Recoils

The simulation parameters were systematically optimized through detailed comparison with experimental data from ^{55}Fe calibration measurements at LNGS, as presented in Chapter 6. This optimization employed a simultaneous fit of the light integral as a function of both GEM voltage and drift distance, enabling the extraction of key parameters governing electron attenuation during drift (λ) and GEM amplification behavior (α). A dedicated low-density correction procedure was developed to account for systematic underestimation of track light yield in the low signal-to-noise regime.

The validation campaign demonstrated excellent agreement between simulation and experimental data across multiple observables. Energy linearity and resolution were reproduced within a few percent accuracy over the 3–45 keV range tested with various X-ray sources. Track shape variables, including length, width, and Gaussian profile parameters, showed consistent agreement between data and Monte Carlo predictions. Moreover, the simulation correctly captured the dependence of detector response on both GEM voltage and drift distance, validating the physical modeling of amplification and drift processes.

Stability Analysis and Environmental Effects

A comprehensive study of detector stability using daily ^{55}Fe calibration data revealed significant temporal variations in detector response (Section 6.1). A phenomenological model was developed to quantify the light collection profile as a function of drift distance, enabling systematic monitoring of attenuation effects related to gas contamination and environmental conditions. Strong correlations were identified between the attenuation parameter and both humidity levels and alpha particle rates, the latter suggesting radon-induced contamination mechanisms. These studies have been integrated into real-time monitoring systems and have informed operational mitigation strategies.

Validation with Nuclear Recoils

The ultimate validation of the simulation framework was achieved through comparison with AmBe neutron source data, as presented in Chapter 7. The AmBe source provides nuclear recoils that mimic the expected WIMP signatures, making it an ideal calibration tool for dark matter search experiments. The Monte Carlo study first validated the fundamental physics of neutron scattering in the detector medium, with theoretical predictions for neutron interaction probabilities showing excellent agreement with Geant4 results: fluorine-dominated interactions at approximately 75%, followed by carbon at 14% and helium at 10%.

Quantitative data/MC comparisons demonstrated the simulation's capability to reproduce the main features of AmBe data. Energy spectra showed good agreement in the 10–100 keV range with data/MC ratios around unity, while track morphology parameters including length, number of hits, and RMS were well reproduced. The track density parameter ρ and the composite morphology parameter η showed qualitatively correct separation between ER and NR populations, confirming that the simulation captures the essential topological differences between the two interaction types. The two-dimensional feature space analysis revealed that electron and nuclear recoil events occupy largely distinct regions, with the characteristic NR band structure at high density and low energy being successfully reproduced.

Conclusions and Outlook

This work has demonstrated the development and comprehensive validation of a Monte Carlo simulation framework for the CYGNO/LIME detector. The framework successfully reproduces both electron and nuclear recoil signatures with accuracy sufficient for physics studies, background estimation, and development of discrimination algorithms.

The level of agreement achieved between simulation and data, despite the complexity of the physical processes involved and the diversity of particle types, energies, and track morphologies, establishes confidence in using the Monte Carlo framework for several critical applications in the CYGNO experimental program. Future refinements could include systematic studies of environmental parameter correlations, development of data-driven corrections for reconstruction efficiency, and potential retuning of digitization parameters for specific energy ranges. However, for the primary objectives of understanding detector response and developing efficient ER/NR discrimination, essential requirements for a competitive dark matter search, the current simulation fidelity has been demonstrated to be sufficient.

The tools and methodologies developed in this work represent essential building blocks for the next phases of the CYGNO experiment, paving the way toward the construction of CYGNO_04 and ultimately CYGNO_30, which aims to probe unexplored regions of the dark matter parameter space through directional detection in a 30 m^3 scale detector.

Bibliography

[1] V. C. Rubin and W. K. Ford. "Rotation of the Andromeda Nebula from a Spectroscopic Survey of Emission Regions". In: *Astrophysical Journal* 159 (1970), p. 379.

[2] K. Begeman, A. Broeils, and R. Sanders. "Extended rotation curves of spiral galaxies: Dark haloes and modified dynamics". In: *Monthly Notices of the Royal Astronomical Society* 249 (1991), p. 523.

[3] R. Bandiera and R. Maiolino, eds. *Proceedings, 21st Texas Symposium on Relativistic Astrophysics (Texas in Tuscany): Florence, Italy, December 9-13, 2002.* World Scientific, River Edge, N.J., 2003. DOI: `10.1142/5373`.

[4] M. Bartelmann and P. Schneider. "Weak Gravitational Lensing". In: *Physics Reports* 340 (2001), pp. 291–472.

[5] M. Roos. "Astrophysical and Cosmological Probes of Dark Matter". In: *Journal of Modern Physics* 3 (2012), p. 1152. DOI: `10.4236/jmp.2012.329150`.

[6] M. A. Miville-Deschênes et al. "Planck 2018 results: VI. Cosmological parameters". In: *Astronomy and Astrophysics* 641 (2020), A6–A6.

[7] V. Springel et al. "Simulations of the formation, evolution and clustering of galaxies and quasars". In: *Nature* 435 (2005), pp. 629–636.

[8] S. D. M. White and M. J. Rees. "Core condensation in heavy halos: a two-stage theory for galaxy formation and clustering". In: *Monthly Notices of the Royal Astronomical Society* 183 (1978), pp. 341–358.

[9] M. Davis et al. "The evolution of large-scale structure in a universe dominated by cold dark matter". In: *Astrophysical Journal* 292 (1985), pp. 371–394.

[10] D. J. Fixsen. "The Temperature of the Cosmic Microwave Background". In: *Astrophysical Journal* 707.2 (2009), pp. 916–920.

[11] European Space Agency (ESA). *CMB temperature anisotropies measured by Planck.* `https://www.esa.int/Planck`. Image courtesy of ESA. Planck satellite data. 2013.

[12] Planck Collaboration. "Planck 2018 results. V. CMB power spectra and likelihoods". In: *Astronomy & Astrophysics* 641 (2020), A5. DOI: `10.1051/0004-6361/201936386`. arXiv: `1907.12875 [astro-ph.CO]`. URL: `https://arxiv.org/abs/1907.12875`.

[13] ATLAS Collaboration and CMS Collaboration. "Observation of a new particle in the search for the Standard Model Higgs boson with the ATLAS detector at the LHC". In: *Physics Letters B* 716 (2012), p. 1.

[14] J. Lesgourgues and S. Pastor. "Neutrino mass from Cosmology". In: *Advances in High Energy Physics* (2012), p. 608515.

[15] G. Bertone, D. Hooper, and J. Silk. “Particle dark matter: evidence, candidates and constraints”. In: *Physics Reports* 405 (2005), pp. 279–390.

[16] G. Jungman, M. Kamionkowski, and K. Griest. “Supersymmetric dark matter”. In: *Physics Reports* 267.5-6 (1996), pp. 195–373.

[17] J. L. Feng. “Dark Matter Candidates from Particle Physics and Methods of Detection”. In: *Annual Review of Astronomy and Astrophysics* 48 (2010), pp. 495–545.

[18] Y. Fukuda et al. “Evidence for oscillation of atmospheric neutrinos”. In: *Physical Review Letters* 81 (1998), pp. 1562–1567.

[19] A. Boyarsky, O. Ruchayskiy, and M. Shaposhnikov. “The role of sterile neutrinos in cosmology and astrophysics”. In: *Annual Review of Nuclear and Particle Science* 59 (2009), pp. 191–214.

[20] R. D. Peccei and H. R. Quinn. “CP Conservation in the Presence of Instantons”. In: *Physical Review Letters* 38 (1977), pp. 1440–1443.

[21] P. Sikivie. “Axion Dark Matter Detection Using Microwave Cavity Experiments”. In: *International Journal of Modern Physics A* 25 (2008), pp. 554–563.

[22] B. Holdom. “Two U(1)’s and Epsilon Charge Shifts”. In: *Physics Letters B* 166 (1986), pp. 196–198.

[23] M. Milgrom. “A Modification of the Newtonian Dynamics as a Possible Alternative to the Hidden Mass Hypothesis”. In: *Astrophysical Journal* 270 (1983), p. 365.

[24] G. W. Angus, B. Famaey, and D. A. Buote. “X-ray group and cluster mass profiles in MOND: Unexplained mass on the group scale”. In: *Monthly Notices of the Royal Astronomical Society* 387 (2007), p. 1470.

[25] Y. B. Zel’dovich and I. D. Novikov. “The Hypothesis of Cores Retarded during Expansion and the Hot Cosmological Model”. In: *Soviet Astronomy* 10 (1967), p. 602.

[26] Y. Sofue and V. Rubin. “Rotation curves of spiral galaxies”. In: *Annual Review of Astronomy and Astrophysics* 39 (2001), pp. 137–174.

[27] J. D. Lewin and P. F. Smith. “Review of mathematics, numerical factors, and corrections for dark matter experiments based on elastic nuclear recoil”. In: *Astroparticle Physics* 6.1 (1996), pp. 87–112.

[28] F. Mayet et al. “A review of the discovery reach of directional Dark Matter detection”. In: *Physics Reports* 627 (2016), pp. 1–49.

[29] Anna-Christina Eilers et al. “The Circular Velocity Curve of the Milky Way from 5 to 25 kpc”. In: *arXiv:1810.09466 [astro-ph.GA]* 871.1 (Jan. 2019), p. 120. DOI: `10.3847/1538-4357/aaf648`.

[30] T. Piffl et al. “The RAVE survey: The Galactic escape speed and the mass of the Milky Way”. In: *Astronomy & Astrophysics* 562 (2014), A91.

[31] Jo Bovy and Hans-Walter Rix. “A Direct Dynamical Measurement of the Milky Way’s Disk Surface Density Profile, Disk Scale Length, and Dark Matter Profile at 4 kpc $<$ R $<$ 9 kpc”. In: *arXiv:1309.0809 [astro-ph.GA]* 779.2 (Dec. 2013), p. 115. DOI: `10.1088/0004-637X/779/2/115`.

[32] Fabrizio Nesti and Paolo Salucci. “The Dark Matter halo of the Milky Way, AD 2013”. In: *Journal of Cosmology and Astroparticle Physics* 2013.07 (July 2013), p. 016. DOI: `10.1088/1475-7516/2013/07/016`. URL: `https://dx.doi.org/10.1088/1475-7516/2013/07/016`.

[33] Miguel Pato, Fabio Iocco, and Gianfranco Bertone. “Dynamical constraints on the dark matter distribution in the Milky Way”. In: *Journal of Cosmology and Astroparticle Physics* 2015.12 (Dec. 2015), p. 001. DOI: `10.1088/1475-7516/2015/12/001`. URL: `https://dx.doi.org/10.1088/1475-7516/2015/12/001`.

[34] M. Weber and W. de Boer. “Determination of the local dark matter density in our Galaxy”. In: *A&A* 509 (2010), A25. DOI: `10.1051/0004-6361/200913381`. URL: `https://doi.org/10.1051/0004-6361/200913381`.

[35] D. Baxter et al. “Recommended conventions for reporting results from direct dark matter searches”. In: *The European Physical Journal C* (2021). DOI: `10.1140/epjc/s10052-021-09655-y`.

[36] Moqbil S. Alenazi and Paolo Gondolo. “Phase-space distribution of unbound dark matter near the Sun”. In: *Phys. Rev. D* 74 (Oct. 2006), p. 083518. DOI: `10.1103/PhysRevD.74.083518`. URL: `https://link.aps.org/doi/10.1103/PhysRevD.74.083518`.

[37] Michael Kuhlen, Mark Vogelsberger, and Raul Angulo. “Numerical simulations of the dark universe: State of the art and the next decade”. In: *Physics of the Dark Universe* 1.1 (2012), pp. 50–93. ISSN: 2212-6864. DOI: `10.1016/j.dark.2012.10.002`. URL: `https://www.sciencedirect.com/science/article/pii/S2212686412000064`.

[38] M. Vogelsberger et al. “Phase-space structure in the local dark matter distribution and its signature in direct detection experiments”. In: *Monthly Notices of the Royal Astronomical Society* 395 (2009), pp. 797–811.

[39] M. Kuhlen et al. “Dark Matter Direct Detection with Non-Maxwellian Velocity Structure”. In: *JCAP* 02 (2010), p. 030. arXiv: `0912.2358`.

[40] Yao-Yuan Mao, Louis E. Strigari, and Risa H. Wechsler. “Connecting direct dark matter detection experiments to cosmologically motivated halo models”. In: *Phys. Rev. D* 89 (Mar. 2014), p. 063513. DOI: `10.1103/PhysRevD.89.063513`. URL: `https://link.aps.org/doi/10.1103/PhysRevD.89.063513`.

[41] M. Lisanti et al. “The Dark Matter at the End of the Galaxy”. In: *Phys. Rev. D* 83 (2011), p. 023519. arXiv: `1010.4300`.

[42] Annalisa Pillepich et al. “THE DISTRIBUTION OF DARK MATTER IN THE MILKY WAY’S DISK”. In: *The Astrophysical Journal* 784.2 (Mar. 2014), p. 161. DOI: `10.1088/0004-637X/784/2/161`. URL: `https://dx.doi.org/10.1088/0004-637X/784/2/161`.

[43] Iryna Butsky et al. “NIHAO project II: halo shape, phase-space density and velocity distribution of dark matter in galaxy formation simulations”. In: *Monthly Notices of the Royal Astronomical Society* 462.1 (July 2016), pp. 663–680. ISSN: 0035-8711. DOI: `10.1093/mnras/stw1688`. eprint: `https://academic.oup.com/mnras/article-pdf/462/1/663/18471899/stw1688.pdf`. URL: `https://doi.org/10.1093/mnras/stw1688`.

[44] Nassim Bozorgnia et al. “Simulated Milky Way analogues: implications for dark matter direct searches”. In: *Journal of Cosmology and Astroparticle Physics* 2016.05 (May 2016), p. 024. DOI: `10.1088/1475-7516/2016/05/024`. URL: `https://dx.doi.org/10.1088/1475-7516/2016/05/024`.

[45] Chris Kelso et al. “The impact of baryons on the direct detection of dark matter”. In: *Journal of Cosmology and Astroparticle Physics* 2016.08 (Aug. 2016), p. 071. DOI: `10.1088/1475-7516/2016/08/071`. URL: `https://dx.doi.org/10.1088/1475-7516/2016/08/071`.

[46] Jonathan D. Sloane et al. “ASSESSING ASTROPHYSICAL UNCERTAINTIES IN DIRECT DETECTION WITH GALAXY SIMULATIONS”. In: *The Astrophysical Journal* 831.1 (Oct. 2016), p. 93. DOI: `10.3847/0004-637X/831/1/93`. URL: `https://dx.doi.org/10.3847/0004-637X/831/1/93`.

[47] A. Drukier, K. Freese, and D. N. Spergel. “Detecting cold dark-matter candidates”. In: *Physical Review D* 33 (1986), pp. 3495–3508.

[48] J. Engel, S. Pittel, and P. Vogel. “Nuclear physics of dark matter detection”. In: *International Journal of Modern Physics E* 1 (1992), pp. 1–37.

[49] R. H. Helm. “Inelastic and elastic scattering of 187-MeV electrons from selected even-even nuclei”. In: *Physical Review* 104 (1956), pp. 1466–1475.

[50] M. T. Ressell et al. “Nuclear shell model calculations of neutralino-nucleus cross sections for ^{29}Si and ^{73}Ge”. In: *Physical Review D* 48 (1993), pp. 5519–5535.

[51] R. Bernabei et al. “On spin-dependent interaction with DAMA/NaI-1 results”. In: *Physics Letters B* 509 (2001), pp. 197–202.

[52] D. N. Spergel. “The motion of the Earth and the detection of WIMPs”. In: *Physical Review D* 37.6 (1988), pp. 1353–1355.

[53] W. Heitler. *The Quantum Theory of Radiation.* 3rd. Oxford: Oxford University Press, 1954.

[54] R. D. Evans. *The Atomic Nucleus.* New York: McGraw-Hill, 1955.

[55] O. Klein and Y. Nishina. “Über die Streuung von Strahlung durch freie Elektronen nach der neuen relativistischen Quantendynamik von Dirac”. In: *Zeitschrift für Physik* 52.11-12 (1929), pp. 853–868. DOI: `10.1007/BF01366453`.

[56] H. Bethe and W. Heitler. “On the stopping of fast particles and on the creation of positive electrons”. In: *Proceedings of the Royal Society of London A* 146.856 (1934), pp. 83–112. DOI: `10.1098/rspa.1934.0140`.

[57] E. Aprile and T. Doke. “Liquid xenon detectors for particle physics and astrophysics”. In: *Reviews of Modern Physics* 82 (2010), pp. 2053–2097.

[58] P. Sorensen and C. E. Dahl. “Nuclear recoil energy scale in liquid xenon with application to the direct detection of dark matter”. In: *Physical Review D* 83.6 (2011), p. 063501. DOI: `10.1103/PhysRevD.83.063501`.

[59] S. F. Mughabghab. *Atlas of Neutron Resonances: Resonance Parameters and Thermal Cross Sections.* 5th. Amsterdam: Elsevier, 2006.

[60] LUX Collaboration. “Radiogenic and muon-induced backgrounds in the LUX dark matter detector”. In: *Astroparticle Physics* 62 (2015), pp. 33–46. DOI: `10.1016/j.astropartphys.2014.07.009`. arXiv: `1403.1299 [astro-ph.IM]`.

[61] Glenn F. Knoll. *Radiation Detection and Measurements.* 4th ed. Hoboken, NJ: John Wiley & Sons, 2010.

[62] M. B. Chadwick et al. "ENDF/B-VIII.0: The 8th major release of the nuclear reaction data library with CIELO-project cross sections, new standards and thermal scattering data". In: *Nuclear Data Sheets* 148 (2018), pp. 1–142.

[63] J. I. Collar, F. T. Avignone, and B. R. Blaes. "Discrimination of nuclear recoils from alpha particles with superheated liquids". In: *Physical Review C* 53.4 (1996), pp. 1790–1799. DOI: `10.1103/PhysRevC.53.1790`.

[64] M. B. Chadwick, M. Herman, P. Obložinský, et al. "ENDF/B-VII.1 nuclear data for science and technology: Cross sections, covariances, fission product yields and decay data". In: *Nuclear Data Sheets* 112.12 (2011), pp. 2887–2996. DOI: `10.1016/j.nds.2011.11.002`.

[65] K. Shibata, O. Iwamoto, T. Nakagawa, et al. "JENDL-4.0: A new library for nuclear science and engineering". In: *Journal of Nuclear Science and Technology* 48.1 (2011), pp. 1–30. DOI: `10.1080/18811248.2011.9711675`.

[66] J. N. Bahcall. "Solar neutrinos: Where we are, where we are going". In: *Astrophysical Journal* 467 (1996), pp. 475–484. DOI: `10.1086/177624`. arXiv: `astro-ph/9505032`.

[67] J. N. Bahcall, M. H. Pinsonneault, and S. Basu. "Solar models: Current epoch and time dependences, neutrinos, and helioseismological properties". In: *Astrophysical Journal* 555.2 (2001), pp. 990–1012. DOI: `10.1086/321493`.

[68] D. Z. Freedman. "Coherent effects of a weak neutral current". In: *Physical Review D* 9.5 (1974), pp. 1389–1392. DOI: `10.1103/PhysRevD.9.1389`.

[69] D. Akimov et al. "Observation of coherent elastic neutrino–nucleus scattering". In: *Science* 357 (2017), pp. 1123–1126.

[70] K. Scholberg. "Prospects for measuring coherent neutrino-nucleus elastic scattering at a stopped-pion neutrino source". In: *Physical Review D* 73.3 (2006), p. 033005. DOI: `10.1103/PhysRevD.73.033005`. arXiv: `hep-ex/0511042`.

[71] J. Billard, L. Strigari, and E. Figueroa-Feliciano. "Implication of neutrino backgrounds on the reach of next generation dark matter direct detection experiments". In: *Physical Review D* 89 (2014), p. 023524.

[72] C. A. J. O'Hare. "New definition of the neutrino floor for direct dark matter searches". In: *Physical Review Letters* 127.25 (2021), p. 251802. DOI: `10.1103/PhysRevLett.127.251802`. arXiv: `2109.03116 [hep-ph]`.

[73] S. E. Vahsen et al. *CYGNUS: Feasibility of a nuclear recoil observatory with directional sensitivity to dark matter and neutrinos.* 2020. arXiv: `2008.12587 [physics.ins-det]`.

[74] H. Bethe. "Zur Theorie des Durchgangs schneller Korpuskularstrahlen durch Materie". In: *Annalen der Physik* 397.3 (1930), pp. 325–400. DOI: `10.1002/andp.19303970303`.

[75] H. Bethe and J. Ashkin. "Passage of radiations through matter". In: *Experimental Nuclear Physics* 1 (1953). Ed. by E. Segrè, pp. 166–357.

[76] B. Rossi. "High Energy Particles". In: *Prentice-Hall* (1952).

[77] A. Hitachi. “Effect of nuclear recoils on scintillation yields in liquid xenon”. In: *Astroparticle Physics* 24 (2005), pp. 247–256.

[78] J. Lindhard et al. “Integral equations governing radiation effects”. In: *Matematisk-fysiske Meddelelser udgivet af Det Kongelige Danske Videnskabernes Selskab* 33 (1963), p. 10.

[79] A. Manzur, A. Curioni, L. Kastens, et al. “Scintillation efficiency and ionization yield of liquid xenon for monoenergetic nuclear recoils down to 4 keV”. In: *Physical Review C* 81.2 (2010), p. 025808. DOI: `10.1103/PhysRevC.81.025808`. arXiv: `0909.1063 [physics.ins-det]`.

[80] XENON10 Collaboration. “A measurement of the scintillation efficiency of low-energy nuclear recoils in liquid xenon”. In: *Physical Review C* 84.4 (2011), p. 045503. DOI: `10.1103/PhysRevC.84.045503`. arXiv: `1104.3088 [physics.ins-det]`.

[81] P. Agnes et al. “Low-mass Dark Matter Search with the DarkSide-50 Experiment”. In: *Physical Review Letters* 121 (2018), p. 081307.

[82] T. Doke, A. Hitachi, J. Kikuchi, et al. “Absolute scintillation yields in liquid argon and xenon for various particles”. In: *Japanese Journal of Applied Physics* 27.7 (1988), pp. 1375–1381. DOI: `10.1143/JJAP.27.1375`.

[83] XENON Collaboration. “Response of the XENON100 dark matter detector to nuclear recoils”. In: *Physical Review D* 88.1 (2013), p. 012006. DOI: `10.1103/PhysRevD.88.012006`. arXiv: `1304.1427 [physics.ins-det]`.

[84] CYGNO Collaboration. “Negative ion time projection chamber operation with SF_6 at nearly atmospheric pressure”. In: *Journal of Instrumentation* 15.07 (2020), P07014. DOI: `10.1088/1748-0221/15/07/P07014`. arXiv: `2002.01821 [physics.ins-det]`.

[85] P. Sorensen. “A coherent understanding of low-energy nuclear recoils in liquid xenon”. In: *Journal of Cosmology and Astroparticle Physics* 2015.09 (2015), p. 033. DOI: `10.1088/1475-7516/2015/09/033`. arXiv: `1503.07308 [physics.ins-det]`.

[86] D. S. Akerib et al. “The LZ experiment”. In: *Nuclear Instruments and Methods in Physics Research A* 953 (2020), p. 163047.

[87] Particle Data Group. “Review of Particle Physics”. In: *Prog. Theor. Exp. Phys.* 2024 (2024). and references therein.

[88] J. A. Formaggio and C. J. Martoff. “Backgrounds to sensitive experiments underground”. In: *Annual Review of Nuclear and Particle Science* 54 (2004), pp. 361–412.

[89] L. Baudis. “Direct dark matter detection: the next decade”. In: *Physics of the Dark Universe* 4 (2014), pp. 50–59.

[90] G. Heusser. “Low-radioactivity background techniques”. In: *Annual Review of Nuclear and Particle Science* 45 (1995), pp. 543–590.

[91] D. M. Mei and A. Hime. “Muon-induced background study for underground laboratories”. In: *Physical Review D* 73 (2006), p. 053004.

[92] C. A. J. O’Hare et al. “Navigating the neutrino fog in direct detection”. In: *Physical Review D* 102.6 (2020), p. 063024. DOI: `10.1103/PhysRevD.102.063024`.

[93] LUX-ZEPLIN Collaboration. “First Dark Matter Search Results from the LUX-ZEPLIN (LZ) Experiment”. In: *Phys. Rev. Lett.* 131 (2023), p. 041002. arXiv: `2207.03764`.

[94] DAMA/LIBRA Collaboration. “First Model Independent Results from DAMA/LIBRA–Phase2”. In: *Nucl. Phys. At. Energy* 19 (2018), p. 307. arXiv: `1805.10486`.

[95] ANAIS-112 Collaboration. “ANAIS-112 three years data: a sensitive model-independent negative test of the DAMA/LIBRA dark matter signal”. In: *Phys. Rev. D* 106 (2022), p. 092005. arXiv: `2210.05143`.

[96] COSINE-100 Collaboration. “Three-year annual modulation search with COSINE-100”. In: *Phys. Rev. D* 106 (2022), p. 052005. arXiv: `2111.08863`.

[97] SABRE Collaboration. “The SABRE project and the SABRE Proof-of-Principle”. In: *Eur. Phys. J. C* 79 (2019), p. 363. arXiv: `1806.09340`.

[98] COSINUS Collaboration. “Detector development for the COSINUS direct dark matter experiment”. In: *J. Low Temp. Phys.* 199 (2020), p. 840.

[99] CRESST Collaboration. “First results from the CRESST-III low-mass dark matter program”. In: *Phys. Rev. D* 100 (2019), p. 102002. arXiv: `1904.00498`.

[100] SuperCDMS Collaboration. “Constraints on low-mass, relic dark matter candidates from a surface-operated SuperCDMS single-charge sensitive detector”. In: *Phys. Rev. D* 102 (2020), p. 091101. arXiv: `2005.14067`.

[101] PICO Collaboration. “Dark Matter Search Results from the Complete Exposure of the PICO-60 C_3F_8 Bubble Chamber”. In: *Phys. Rev. D* 100 (2019), p. 022001. arXiv: `1902.04031`.

[102] LUX Collaboration. “Results from a search for dark matter in the complete LUX exposure”. In: *Phys. Rev. Lett.* 118 (2017), p. 021303. arXiv: `1608.07648`.

[103] XENON Collaboration. “Observation of Excess Electronic Recoil Events in XENON1T”. In: *Phys. Rev. D* 102 (2020), p. 072004. arXiv: `2006.09721`.

[104] DAMIC Collaboration. “Constraints on Light Dark Matter Particles Interacting with Electrons from DAMIC at SNOLAB”. In: *Phys. Rev. Lett.* 123 (2019), p. 181802. arXiv: `1907.12628`.

[105] EDELWEISS Collaboration. “Searching for low-mass dark matter particles with a massive Ge bolometer operated above-ground”. In: *Phys. Rev. D* 99 (2019), p. 082003. arXiv: `1901.03588`.

[106] D. S. Akerib et al. “Limits on Spin-Dependent WIMP–Nucleon Cross Section Obtained from the Complete LUX Exposure”. In: *Phys. Rev. Lett.* 118.25 (2017), p. 251302. DOI: `10.1103/PhysRevLett.118.251302`. URL: `https://link.aps.org/doi/10.1103/PhysRevLett.118.251302`.

[107] CYGNUS Collaboration. “CYGNO: a gaseous TPC with optical readout for dark matter directional search”. In: *Eur. Phys. J. C* 82 (2022), p. 487. arXiv: `2110.02064`.

[108] J. B. R. Battat et al. “Reducing DRIFT Backgrounds with a Submicron Aluminized-Mylar Cathode”. In: *Nucl. Instrum. Meth. A* 755 (2014), p. 6. arXiv: `1403.2355`.

[109] P. Grothaus et al. “Directional Searches for Dark Matter Using the CYGNUS Detector”. In: *Phys. Dark Univ.* 39 (2023), p. 101166. arXiv: `2203.05990`.

[110] K. Miuchi et al. “First underground results with NEWAGE-0.3a direction-sensitive dark matter detector”. In: *Phys. Lett. B* 686 (2010), p. 11. arXiv: `1002.1794`.

[111] A. M. Green and B. Morgan. “Optimizing WIMP directional detectors”. In: *Astropart. Phys.* 27 (2007), p. 142. arXiv: `astro-ph/0609115`.

[112] P. Grothaus et al. “Directional Dark Matter Detection Beyond the Neutrino Bound”. In: *Phys. Rev. D* 90 (2014), p. 055018. arXiv: `1407.5558`.

[113] A. M. Green and B. J. Kavanagh. “Directional detectability of dark matter with matrix elements for elastic neutrino-nucleus scattering”. In: *Phys. Rev. D* 96 (2017), p. 043009. arXiv: `1706.02125`.

[114] T. Naka et al. “Fine grained nuclear emulsion for higher resolution tracking detector”. In: *Nucl. Instrum. Meth. A* 718 (2013), p. 519.

[115] T. Asada et al. “Extended track reconstruction for the future large-scale directional Dark Matter detector”. In: *PTEP* 2017 (2017), 063H01.

[116] T. Naka et al. “Nano Imaging Tracker: A new concept for neutrinoless double beta decay searches”. In: *Nucl. Instrum. Meth. A* 718 (2013), p. 519.

[117] T. Uchida et al. “Application of plasmonic resonances in nuclear emulsion detectors”. In: *Nucl. Instrum. Meth. A* 969 (2020), p. 163990.

[118] M. Yoshimoto et al. “Application of nanometric tracking for dark matter search”. In: *PTEP* 2020 (2020), 043H01.

[119] Walter Blum, Werner Riegler, and Luigi Rolandi. *Particle detection with drift chambers*. Springer Science & Business Media, 2008.

[120] F. Sauli. “Gaseous Radiation Detectors”. In: (2014).

[121] D. R. Nygren. “The Time Projection Chamber”. In: *Phys. Today* 31 (1978), p. 46.

[122] K. Miuchi et al. “Direction-sensitive dark matter search with gaseous tracking detector”. In: *Phys. Lett. B* 654 (2007), p. 58.

[123] D. Snowden-Ifft et al. “Discovery of multiple, ionization-created CS_2 anion species”. In: *Phys. Rev. Lett.* 84 (2000), p. 4760.

[124] F. A. F. Fraga et al. “The GEM scintillation in He-CF_4, Ar-CF_4, Ar-TEA and Xe-TEA mixtures”. In: *Nucl. Instrum. Meth. A* 513 (2003), p. 379.

[125] DRIFT Collaboration. “First Dark Matter Search Results from a Surface Run of the 10-L DRIFT-I Directional Dark Matter Detector”. In: *Astropart. Phys.* 23 (2005), p. 444.

[126] DRIFT Collaboration. “The DRIFT-II dark matter detector: Design and commissioning”. In: *Nucl. Instrum. Meth. A* 584 (2008), p. 219.

[127] DRIFT Collaboration. “Radon reduction in DRIFT-II, an underground TPC for dark matter searches”. In: *Nucl. Instrum. Meth. A* 707 (2013), p. 73.

[128] J. B. R. Battat et al. “First background-free limit from a directional dark matter experiment: results from a fully fiducialised DRIFT detector”. In: *Physics of the Dark Universe* 9-10 (2015), pp. 1–7. DOI: `10.1016/j.dark.2015.06.001`.

[129] MIMAC Collaboration. “MIMAC : A micro-tpc matrix for directional detection of dark matter”. In: *EAS Publ. Ser.* 53 (2012), p. 111. arXiv: `1106.0807`.

[130] J. Billard et al. “Measurement of the ionization of slow ions in micromegas detectors”. In: *Nucl. Instrum. Meth. A* 638 (2011), p. 76.

[131] J. Billard et al. “Exclusion limits from the MIMAC dark matter search with CF_4 at 0.5 mbar”. In: *Phys. Lett. B* 691 (2010), p. 156. arXiv: `1003.2949`.

[132] D. Santos et al. “MIMAC : MIcro-tpc MAtrix of Chambers for dark matter directional detection”. In: *EAS Publ. Ser.* 53 (2012), p. 25. arXiv: `1111.1566`.

[133] Q. Riffard et al. “First detection of tracks of radon progeny recoils by MIMAC”. In: *JINST* 11 (2016), P08011. arXiv: `1504.05865`.

[134] A. Fornali et al. “Measurement of the quenching factor of Na recoils in NaI(Tl) down to the sub-keV region”. In: *Phys. Rev. D* 102 (2020), p. 092003.

[135] L. Lebreton et al. “The COMIMAC facility: Measurements and simulations”. In: *Nucl. Instrum. Meth. A* 885 (2018), p. 80.

[136] D. Santos et al. “Directional direct dark matter detection”. In: *J. Phys. Conf. Ser.* 469 (2013), p. 012002.

[137] L. Lebreton et al. “First measurement of the carbon and fluorine quenching factors at energies between 50 and 500 keV”. In: *Nucl. Instrum. Meth. A* 884 (2018), p. 80.

[138] A. Dastgheibi-Fard et al. “Measurement of the ionization efficiency of nuclear recoils in CF_4 gas”. In: *Phys. Rev. D* 102 (2020), p. 062001.

[139] NEWAGE Collaboration. “Dark matter search experiment with gaseous tracking device NEWAGE-0.3b’”. In: *PTEP* 2015 (2015), 043F01.

[140] K. Miuchi et al. “Development of a micro-pixel chamber for detection of slow neutrons”. In: *Nucl. Instrum. Meth. A* 621 (2010), p. 667.

[141] T. Nakamura et al. “Detection of the low energy recoil nucleus with low-pressure gas detector”. In: *Nucl. Instrum. Meth. A* 579 (2007), p. 681.

[142] K. Miuchi et al. “Performance of the TPC with micro pixel chamber readout: micro-TPC”. In: *IEEE Trans. Nucl. Sci.* 50 (2003), p. 825.

[143] H. Nishimura et al. “Direction-sensitive dark matter search with gaseous tracking detector NEWAGE-0.3b"”. In: *Phys. Lett. B* 789 (2019), p. 45.

[144] K. Nakamura et al. “Direction-sensitive dark matter search results in a surface laboratory”. In: *PTEP* 2015 (2015), 043F01.

[145] K. Nakamura et al. “Spin-dependent WIMP-nucleon cross-section limits from the NEWAGE-0.3b’ directional detector”. In: *PTEP* 2015 (2015), 113F01.

[146] DMTPC Collaboration. “First Dark Matter Search Results from a 4-kg CF_4 DMTPC Directional Dark Matter Detector”. In: *Phys. Lett. B* 695 (2011), p. 124. arXiv: `1006.2928`.

[147] J. P. Lopez et al. “Directional Dark Matter Detectors”. In: *JINST* 9 (2014), p. C04014.

[148] J. B. R. Battat et al. “Low Threshold Results and Limits from the DRIFT Directional Dark Matter Detector”. In: *Astropart. Phys.* 91 (2017), p. 65. arXiv: `1701.00171`.

[149] J. B. R. Battat et al. “Dark Matter Search Results from the PICO-60 CF_3I Bubble Chamber”. In: *Phys. Rev. Lett.* 118 (2017), p. 021301.

[150] J. Dé Côté et al. “Demonstration of directional sensitivity to nuclear recoils at the percent level in liquid argon"”. In: *Phys. Rev. D* 102 (2020), p. 072001.

[151] D3 Collaboration. “A novel TPC concept for directional dark matter detection”. In: *Nucl. Instrum. Meth. A* 958 (2020), p. 162412.

[152] J. B. R. Battat et al. “Readout technologies for directional WIMP Dark Matter detection”. In: *Phys. Rep.* 662 (2016), p. 1. arXiv: `1610.02396`.

[153] O. López Gutiérrez et al. “Study of charge readout for a directional detector based on MPGD technologies”. In: *Nucl. Instrum. Meth. A* 958 (2020), p. 162412.

[154] F.D. Amaro et al. “The CYGNO Experiment”. In: *Instruments* 6.1 (2022). ISSN: 2410-390X. DOI: `10.3390/instruments6010006`.

[155] Jay N. Marx and David R. Nygren. “The Time Projection Chamber”. In: *Physics Today* 31.10 (1978), pp. 46–53. DOI: `10.1063/1.2994775`.

[156] D. R. Nygren. “The Time Projection Chamber: A New 4π Detector for Charged Particles”. In: *eConf C740805*. Ed. by J. Kadyk et al. 1974, p. 58.

[157] F. Sauli. “GEM: a new concept for electron amplification in gas detectors”. In: *Nuclear Instruments and Methods in Physics Research Section A* 386.2-3 (1997), pp. 531–534.

[158] David José Gaspar Marques. “3D Tracking with the CYGNO/INITIUM experiment”. PhD thesis. Gran Sasso Science Institute, June 2025. arXiv: `2509.10890 [hep-ex]`. URL: `https://arxiv.org/abs/2509.10890`.

[159] F. Sauli. “The gas electron multiplier (GEM): Operating principles and applications”. In: *Nuclear Instruments and Methods in Physics Research Section A* 805 (2016), pp. 2–24. DOI: `10.1016/j.nima.2015.07.060`.

[160] I. Abritta Costa et al. “CYGNO: Triple-GEM Optical Readout for Directional Dark Matter Search”. In: *Journal of Physics: Conference Series* 1498.1 (Apr. 2020), p. 012016. ISSN: 1742-6596. DOI: `10.1088/1742-6596/1498/1/012016`. URL: `http://dx.doi.org/10.1088/1742-6596/1498/1/012016`.

[161] V. C. Antochi et al. *A GEM-based optically readout TPC for direction-sensitive DM searches.* arXiv preprint. 2020. eprint: `2003.XXXX`.

[162] V. C. Antochi et al. “Combined readout of a triple-GEM detector”. In: *Journal of Instrumentation* 13.05 (2018), P05001. DOI: `10.1088/1748-0221/13/05/P05001`.

[163] M. M. F. R. Fraga et al. “The scintillation of CF_4 and Ar-CF_4 and its use in optical readout”. In: *Nuclear Instruments and Methods in Physics Research Section A* 504 (2003), pp. 88–92. DOI: `10.1016/S0168-9002(03)00784-5`.

[164] E. D. C. Freitas et al. “Secondary scintillation yield of CF_4”. In: *Journal of Instrumentation* 8 (2013), P07008. DOI: `10.1088/1748-0221/8/07/P07008`.

[165] A. Morozov et al. “Secondary scintillation in CF_4 gas”. In: *Journal of Instrumentation* 7 (2012), P02008. DOI: `10.1088/1748-0221/7/02/P02008`.

[166] K. Kurihara, K. Kasami, and T. Takahashi. “Emission spectra from CF_4-Ar gas mixtures”. In: *Journal of Physics D: Applied Physics* 33.17 (2000), pp. 2146–2151. DOI: `10.1088/0022-3727/33/17/314`.

[167] E. Baracchini et al. “Stability and detection performance of a GEM-based Optical Readout TPC with He/CF_4 gas mixtures”. In: *JINST* 15.10 (2020), P10001. DOI: `10.1088/1748-0221/15/10/P10001`. arXiv: `2007.00608 [physics.ins-det]`.

[168] R. Veenhof. “Garfield, a drift-chamber simulation program”. In: *Proceedings of the Workshop on Detector and Event Simulation in High Energy Physics (Vienna, 1993)*. 1993, pp. 66–71.

[169] R. Veenhof. “GARFIELD, recent developments”. In: *Nuclear Instruments and Methods in Physics Research Section A* 419.2 (1998), pp. 726–730. DOI: `10.1016/S0168-9002(98)00851-1`.

[170] V. C. Antochi et al. “Optical readout of a triple GEM detector in He–CF_4”. In: *Nuclear Instruments and Methods in Physics Research Section A* 999 (2021), p. 165209. DOI: `10.1016/j.nima.2021.165209`.

[171] A. Sharma. *Properties of some gas mixtures used in tracking detectors.* Technical note. 1998. URL: `http://consult.cern.ch/writeup/garfield/examples/gasmix/`.

[172] M. Reinking, H. W. Drawin, and R. G. Meyer. “Ionization and excitation in electron collisions with CF_4”. In: *Journal of Applied Physics* 60.2 (1986), pp. 499–508. DOI: `10.1063/1.337868`.

[173] Kazuya Ishida et al. “W-values for electron-ion pair production in gases and gas mixtures”. In: *Japanese Journal of Applied Physics* 31.5R (1992), pp. 1465–1472. DOI: `10.1143/JJAP.31.1465`.

[174] S. Agostinelli et al. “GEANT4—A simulation toolkit”. In: *Nuclear Instruments and Methods in Physics Research Section A* 506.3 (2003), pp. 250–303. DOI: `10.1016/S0168-9002(03)01368-8`.

[175] James F. Ziegler, M. D. Ziegler, and J. P. Biersack. “SRIM – The stopping and range of ions in matter (2010)”. In: *Nuclear Instruments and Methods in Physics Research Section B: Beam Interactions with Materials and Atoms* 268.11 (2010), pp. 1818–1823. ISSN: 0168-583X. DOI: `10.1016/j.nimb.2010.02.091`. URL: `https://www.sciencedirect.com/science/article/pii/S0168583X10001862`.

[176] Sagar Tripathy et al. *Studies on ion backflow and gain in multi-GEM detectors.* Preprint. 2021.

[177] E. Baracchini et al. “Electroluminescence in He:CF_4 and He:CF_4:iC_4H_10 mixtures for optical TPCs”. In: *Journal of Instrumentation* 15.08 (2020), P08018. DOI: `10.1088/1748-0221/15/08/P08018`.

[178] C. M. B. Monteiro et al. “Secondary scintillation yield in He-CF_4 and Ar-CF_4 mixtures”. In: *Physics Letters B* 714.1 (2012), pp. 18–23. DOI: `10.1016/j.physletb.2012.06.006`.

[179] B. Dominik, S. Kapusta, and A. Walenta. “Optical imaging of ionization in CF_4”. In: *Nuclear Instruments and Methods in Physics Research Section A* 278.3 (1989), pp. 779–787. DOI: `10.1016/0168-9002(89)91475-5`.

[180] Andy Rowlands. *Physics of Digital Photography.* IOP Publishing, 2017. ISBN: 978-0-7503-1242-4. DOI: `10.1088/978-0-7503-1242-4`.

[181] L. M. S. Margato et al. “Performance of an optical readout GEM-based TPC”. In: *Nuclear Instruments and Methods in Physics Research Section A* 535.1 (2004), pp. 231–235. DOI: `10.1016/j.nima.2004.07.126`.

[182] M. Marafini et al. “High granularity tracker based on a triple-GEM optically read by a CMOS-based camera”. In: *Journal of Instrumentation* 10.12 (2015), P12010. DOI: `10.1088/1748-0221/10/12/P12010`.

[183] N. S. Phan, E. R. Lee, and D. Loomba. “Imaging 55Fe electron tracks in a GEM-based TPC using a CCD readout”. In: *Journal of Instrumentation* 15.05 (2020), P05012. DOI: `10.1088/1748-0221/15/05/P05012`.

[184] Teledyne Digital Imaging Inc. *CCD vs CMOS (knowledge center)*. `https://www.teledynedalsa.com/en/learn/knowledge-center/ccd-vs-cmos/`. Accessed: 2023-10-10. 2023.

[185] H. Zhan, X. Zhang, and L. Cao. “Intrapixel effects of CCD and CMOS detectors”. In: *Journal of Instrumentation* 12.04 (2017), p. C04010. DOI: `10.1088/1748-0221/12/04/C04010`.

[186] Ajay Kumar Boyat and Brijendra Kumar Joshi. “A Review Paper: Noise Models in Digital Image Processing”. In: *Signal & Image Processing: An International Journal* 6.2 (2015). DOI: `10.5121/sipij.2015.6206`.

[187] Mikhail Konnik and James Welsh. *High-level numerical simulations of noise in CCD and CMOS photosensors: review and tutorial.* 2014. arXiv: `1412.4031 [astro-ph.IM]`.

[188] Hamamatsu Photonics K.K. *qCMOS®: Quantitative CMOS technology enabled by Photon Number Resolving.* White paper. 2023.

[189] João Almeida et al. “Low-noise optical readout for scintillation imaging with scientific CMOS”. In: *Measurement Science and Technology* 34.12 (2023), p. 125145. DOI: `10.1088/1361-6501/acf3d8`.

[190] Claus Grupen and Boris Shwartz. *Particle Detectors.* 2nd ed. Cambridge Monographs on Particle Physics, Nuclear Physics and Cosmology. Cambridge University Press, 2008. ISBN: 9780521677754.

[191] S. O. Flyckt and C. Marmonier. *Photomultiplier Tubes: Principles and Applications.* Photonis, 2002.

[192] I. Abritta Costa et al. “Performance of optically readout GEM-based TPC with a 55Fe source”. In: *Journal of Instrumentation* 14.07 (July 2019), P07011. DOI: `10.1088/1748-0221/14/07/P07011`. URL: `https://dx.doi.org/10.1088/1748-0221/14/07/P07011`.

[193] E. Baracchini et al. “Identification of low energy nuclear recoils in a gas time projection chamber with optical readout”. In: *Measurement Science and Technology* 32.2 (Dec. 2020), p. 025902. DOI: `10.1088/1361-6501/abbd12`. URL: `https://dx.doi.org/10.1088/1361-6501/abbd12`.

[194] Michela Marafini et al. “Study of the Performance of an Optically Readout Triple-GEM”. In: *IEEE Transactions on Nuclear Science* PP (Nov. 2017), pp. 1–1. DOI: `10.1109/TNS.2017.2778503`.

[195] G. Mazzitelli and the CYGNO Collaboration. *CYGNO_04 Technical Design Report.* Tech. rep. Internal report. INFN, 2023.

[196] J.-F. Castel et al. “TREX-DM: a low-background Micromegas-based TPC for low-mass WIMP detection”. In: *The European Physical Journal C* 79.9 (2019), p. 782. DOI: `10.1140/epjc/s10052-019-7269-0`.

[197] Giorgio Dho. “Optimisation of amplification and gas mixture for directional Dark Matter searches with the CYGNO/INITIUM project”. PhD thesis. arXiv preprint arXiv:2507.02474, 2025.

[198] Michael Willers et al. “The CRESST-III experiment: Status and perspectives”. In: *Proceedings of the 15th TAUP Conference.* 2017.

[199] R. Agnese et al. “Results from the SuperCDMS experiment at Soudan: Limits on low-mass WIMPs”. In: *Physical Review Letters* 119.18 (2017), p. 181302. DOI: `10.1103/PhysRevLett.119.181302`.

[200] F. D. Amaro et al. “Secondary scintillation yield in He:CF_4:iC_4H_10 mixtures”. In: *Instruments* 7.3 (2023), p. 56. DOI: `10.3390/instruments7030056`.

[201] H. Roque et al. “Electroluminescence in helium-based mixtures for optical TPCs”. In: *Journal of Instrumentation* 16.09 (2021), P09019. DOI: `10.1088/1748-0221/16/09/P09019`.

[202] F. D. Amaro et al. “A 50 l CYGNO prototype overground characterization”. In: *Eur. Phys. J. C* 83 (2023), p. 946. DOI: `10.1140/epjc/s10052-023-11988-9`.

[203] A. Di Gregorio et al. “Radon emanation measurements for low-background experiments”. In: *EPJ Techniques and Instrumentation* 10 (2023), p. 5. DOI: `10.1140/epjti/s40485-023-00109-1`.

[204] A. Di Gregorio. “Development of low-radioactivity molecular sieves for rare-event searches”. PhD thesis. University of Sheffield, 2022.

[205] J. Billard, F. Mayet, and D. Santos. “Markov chain Monte Carlo analysis to constrain dark matter properties with directional detection”. In: *Physical Review D* 83.7 (2011), p. 075002. DOI: `10.1103/PhysRevD.83.075002`.

[206] Samuel K. Lee and Annika H. G. Peter. “Probing the Local Velocity Distribution of WIMP Dark Matter with Directional Detectors”. In: *Journal of Cosmology and Astroparticle Physics* 2012.04 (2012), p. 029. DOI: `10.1088/1475-7516/2012/04/029`.

[207] Constantinos Skordis et al. “Large Scale Structure in Bekenstein’s Theory of Relativistic Modified Newtonian Dynamics”. In: *Physical Review Letters* 96 (2006), p. 011301. DOI: `10.1103/PhysRevLett.96.011301`.

[208] Ciaran A. J. O’Hare and Anne M. Green. “Directional detection of dark matter streams”. In: *Physical Review D* 90.12 (2014), p. 123511. DOI: `10.1103/PhysRevD.90.123511`.

[209] Daniele S. M. Alves, Sonia El Hedri, and Jay G. Wacker. “Dark matter in 3D”. In: *Journal of High Energy Physics* 2016.03 (2016), p. 149. DOI: `10.1007/JHEP03(2016)149`.

[210] Martin Ester et al. “A density-based algorithm for discovering clusters in large spatial databases with noise”. In: *Proceedings of the Second International Conference on Knowledge Discovery and Data Mining (KDD’96).* AAAI Press, 1996, pp. 226–231.

[211] E. Baracchini et al. “A density-based clustering algorithm for the CYGNO data analysis”. In: *Journal of Instrumentation* 15.12 (2020), T12003. DOI: `10.1088/1748-0221/15/12/T12003`.

[212] Pascal Getreuer. “Chan–Vese Segmentation”. In: *Image Processing On Line* 2 (2012), pp. 214–224. DOI: `10.5201/ipol.2012.g-cv`.

[213] F. Amaro, R. Antonietti, et al. “Directional iDBSCAN to detect cosmic-ray tracks for the CYGNO experiment”. In: *Measurement Science and Technology* 34 (2023). September.

[214] *ROOT*. `https://root.cern/`. Accessed: 2025-10-09. 2024.

[215] The Geant4 Collaboration. *GEANT4 Book For Application Developers*. Manual. 2023.

[216] The Geant4 Collaboration. *GEANT4 Physics Reference Manual*. Manual. 2023.

[217] Flaminia Di Giambattista. “Background study of the LIME prototype at underground LNGS for the CYGNO experiment”. PhD thesis. Gran Sasso Science Institute, 2022.

[218] P A Zyla and et al. (Particle Data Group). “Review of Particle Physics”. In: *Progress of Theoretical and Experimental Physics* 2020.8 (Aug. 2020), p. 083C01. ISSN: 2050-3911. DOI: `10.1093/ptep/ptaa104`.

[219] I. C. Wolfe. “Measurement of Work Function in CF4 Gas”. Master’s thesis. MA thesis. Massachusetts Institute of Technology, 2010.

[220] S. Vahsen et al. “Tests of gases in a mini-TPC with pixel chip readout”. In: *Nucl. Instrum. Meth.* A738 (2014), pp. 111–118. DOI: `10.1016/j.nima.2013.10.029`.

[221] Daniel P. Snowden-Ifft. “Discovery of Multiple, Ionization-Created Anions in Gas Mixtures Containing CS2 and O2”. In: (Aug. 2013).

[222] F. D. Amaro et al. “Enhancing the light yield of He:CF_4 based gaseous detector”. In: *Eur. Phys. J. C* 84 (2024), p. 1122. DOI: `10.1140/epjc/s10052-024-13471-5`.

[223] Davide Pinci. “A triple-GEM detector for the muon system of the LHCb experiment”. PhD thesis. Cagliari University, CERN-THESIS-2006-070, 2006. URL: `http://weblib.cern.ch/abstract?CERN-THESIS-2006-070`.

[224] S. Bachmann et al. “Charge amplification and transfer processes in the gas electron multiplier”. In: *Nucl. Instrum. Meth. A* 438 (1999), p. 376. DOI: `10.1016/S0168-9002(99)00820-7`.

[225] W. Bonivento et al. “A Complete Simulation of a Triple-GEM Detector”. In: *IEEE Transactions on Nuclear Science* 49(4) (2002), p. 1638. DOI: `10.1109/TNS.2002.805170`.

[226] F. D. Amaro et al. “Modeling the light response of an optically readout GEM based TPC for the CYGNO experiment”. In: *accepted for pubblication in EPJC* ().

[227] Matteo Folcarelli. “Characterization of the CYGNO experiment prototype during the underground campaign at LNGS”. Presented 23 Oct 2023. U. Rome La Sapienza (main), 2023. URL: `https://cds.cern.ch/record/2886640`.

[228] G. Mazzitelli et al. “A high resolution TPC based on GEM optical readout”. In: *2017 IEEE Nuclear Science Symposium and Medical Imaging Conference (NSS/MIC)*. 2017, pp. 1–4. DOI: `10.1109/NSSMIC.2017.8532631`.

[229] Thomas Goossens et al. "Vignetted-aperture correction for spectral cameras with integrated thin-film Fabry–Perot filters". In: *Applied optics* 58.7 (2019), pp. 1789–1799.

[230] Rajendra Nath Patra et al. "Measurement of basic characteristics and gain uniformity of a triple GEM detector". In: *Nucl. Instrum. Meth. A* 862 (Aug. 2017), pp. 25–30. ISSN: 0168-9002. DOI: `10.1016/j.nima.2017.05.011`.

[231] Hamamatsu Photonics K.K. *Photomultiplier Tube R7378A Datasheet.* Technical datasheet. Hamamatsu Photonics K.K., 2017.

[232] F. D. Amaro et al. "Bayesian network 3D event reconstruction in the Cygno optical TPC for dark matter direct detection". In: *European Physical Journal C* 85.11 (2025), p. 1261.

[233] S. Purushothaman et al. "Hyper-EMG: A new probability distribution function composed of Exponentially Modified Gaussian distributions to analyze asymmetric peak shapes in high-resolution time-of-flight mass spectrometry". In: *International Journal of Mass Spectrometry* 421 (2017), pp. 245–254. DOI: `10.1016/j.ijms.2017.07.014`.

[234] Hamamatsu Photonics K.K. *PMT Handbook: Basics and Applications.* 4th. Japan: Hamamatsu Photonics K.K., 2017.

[235] CAEN S.p.A. *Mod. V1742 32+2 Channel 12-bit 5 GS/s Switched Capacitor Digitizer.* Technical datasheet. 2023.

[236] CAEN S.p.A. *Mod. V1720 8 Channel 12-bit 250 MS/s Digitizer.* Technical datasheet. 2023.

[237] Luan Gomes Mattosinhos de Carvalho. "Characterization and simulation of photomultiplier tube signals for the CYGNO experiment". Trabalho de Conclusão de Curso (Graduação). Juiz de Fora, Brazil: Universidade Federal de Juiz de Fora, 2025.

[238] F. D. Amaro et al. "Simulation of the CYGNO Gaseous TPC Optical Readout". In: (2026). Submitted to JINST. arXiv: `2601.01435 [physics.ins-det]`.

[239] Samuele Torelli. *Feasibility of a directional solar neutrino measurement with the CYGNO/INITIUM experiment.* 2024. arXiv: `2408.03760 [physics.ins-det]`. URL: `https://arxiv.org/abs/2408.03760`.

[240] J. Fantidis. "Comparison of different geometric configurations and materials for neutron radiography purposes based on a ^{241}Am/Be neutron source". In: *Journal of Taibah University for Science* 11 (2017). (cit. on p. 52), pp. 1214–1220.